SCUOLA DI DOTTORATO
UNIVERSITÀ DEGLI STUDI DI MILANO-BICOCCA

Dipartimento di

Scienza dei Materiali

Dottorato di Ricerca in Scienza e Nanotecnologia dei Materiali Ciclo XXIX

Curriculum in scienza dei materiali (79R-13)

OPTIMIZATION STEPS OF GERMANIUM AS LIGHT EMITTER: STRAIN AND N-TYPE DOPING

Cognome Barget Nome Michael Reiner

Matricola 787864

Tutore Dott. Emiliano Bonera

Coordinatore: Prof. Gian Paolo Brivio

ANNO ACCADEMICO 2015/16

Abstract

The monolithic integration of photonic functionality into silicon micro-technology is a widely-sought goal with projected applications in data-communication and sensing for the near- and mid-infrared spectral range. The realization of integrated passive and active components with means of standard silicon manufacturing processes is already widely advanced. Yet there is no final solution for an effective, Si technology compatible, and electrically pumped light source. A lot of research effort focuses on germanium (Ge) on silicon (Si) hetero-structures. However, Ge is an indirect gap semiconductor with scarce quantum efficiency as compared to intrinsic direct gap materials. High tensile strain and heavy n-type doping have been proposed to enhance the carrier density in the Ge direct conduction band valley and are accepted as a route to achieve positive optical gain in Ge layers.

We introduce a top-down fabrication for external stressors made of SiGe nanostructures that is based on the lattice mismatch of SiGe and Ge. By means of micro-Raman spectroscopy we demonstrate that Ge is locally deformed and a uniaxial tensile strain of up to 4% is reached. However, the photoluminescence from the strained volume is scarce and the emission spectra are bulk like. To constrain the excited electrons to the highly strained regions, the insertion of a SiGe barrier below a shallow layer of Ge is investigated systematically by means of photoluminescence (PL) spectroscopy, showing that during thermalization carriers overcome the barrier by diffusion. To enlarge the strained volume and to have vacuum as the barrier, we transfer the SiGe stressors to a thin Ge micro-bridge and compare the obtained strain to the case of an attached bulk-like Ge layer. Absolute strain values are of the order of ~ 0.7% for both micro-bridge and bulk. However, the relative strain induced by the nanostructures in the micro-bridge is 1.3% due to the high sharing of elastic energy between nanostructures and bridge. Hence, the suspension doubles the strain value with respect to a bulk like system which could conversely allow a larger strained area in the suspended material at constant strain.

Moreover, we investigate the photoluminescence from phosphorous doped Ge selectively grown in SiO_2 windows on a Si substrate in dependence of the growth conditions. Investigated growth parameters comprise deposition temperature, in-situ dopant flux and postbake condition. By increasing the growth temperature from 325 °C to 400 °C, PL intensity can be increased by a factor of ×1.5. The variation of the dopant flux (phosphine PH_3 pressure) during in-situ doping at Ge deposition temperatures T_{dep} = 350 °C and 400 °C revealed that doping increases the PL intensity up to an optimum doping concentration resulting in maximum PL.

Relative enhancements of PL peak intensity with respect to an undoped sample were ×2.8 and ~ ×4.0 for the series with T_{dep} = 350 °C and that with T_{dep} = 400 °C, respectively. Varying the postbake temperature for fixed T_{dep} = 400 °C and fixed dopant flux from 500 - 800 °C, PL intensity is further increased by a factor of 2.0 - 2.5 due to further donor activation and improved crystal quality.

To elucidate the recombination dynamics in n-doped germanium we revert to a series of phosphorous doped Ge with different dopant concentrations. PL measurements at different temperatures and excitation powers are then compared with theoretical modeling. A self-consistent multi-valley effective mass numerical model for simulation of PL spectra is employed that considers the impact of dopants on the non-radiative recombination dynamics. To this aim we proposed a linear dependence of the defect-related recombination rate as a function of the donor density. We find that the Shockley-Read-Hall (SRH) mechanism dominates the non-radiative

recombination channel up to a donor density of ~ 5×10^{19} cm^{-3}. The observed increase and successive decrease of PL intensity as a function of doping could be accounted for by a drop of two orders of magnitude in the excess carrier density that is caused by a reduction of the non-radiative Shockley-Read-Hall lifetime. Our model proposes a lifetime reduction from ~ 30 ns in the intrinsic case to ~ 0.1 ns for doping in the 10^{19} cm^{-3} range.

The achievement of controlled high strain values and heavy doping in Ge layers as well as a proper understanding of the recombination dynamics are of high interest with the prospect to achieve a Ge-based laser.

Table of contents

1 Introduction

1.1 On-chip multi-function integration using silicon micro-technology

The advent of optical fibers also brought a miniaturization of optical components. The introduction of lithographic methods for the production of optical components lead to the development of micro-optics at the beginning of the 1970s.[1] The idea of integrating optical and opto-electronic systems came up just a little later. At the end of the 1980s the field of silicon photonics emerged, using silicon based materials to create photonic integrated circuits (PIC'S). It was fueled by the superior goal of integration of optics with advanced silicon electronics on the same substrate, i. e. without sacrificing the compatibility with standard Si technologies, leading to so-called optoelectronic integrated circuits (OEIC's). Abstreiter [2] and Soref [3] presented the idea of an OEIC "superchip", exploiting strained heteroepitaxial layers and quantum-confined structures made of group IV materials (Si, Ge, C , and Sn) already back in 1992 and 1993, respectively, see FIG. 1-1.

This idea is still up-to-date nowadays. In days of cloud computing and huge ("hyper-scale") data centers fast optical data links can establish high speed and power efficient optical communication between servers, replacing copper cables. On-chip optical communication may furthermore be part of future high performance computers.[4]

Further applications are forecasted in the field of miniaturized optical sensing systems. Sensing applications may comprise refractive index sensing, but also on-chip spectroscopy. The use of silicon photonics for absorption, fluorescence and Raman spectroscopy on a chip is already under investigation.[5] The final goal is to create an entire lab-on-a-chip (LoC) platform with applications in physics, chemistry, biology, and medical as well as environmental sciences.

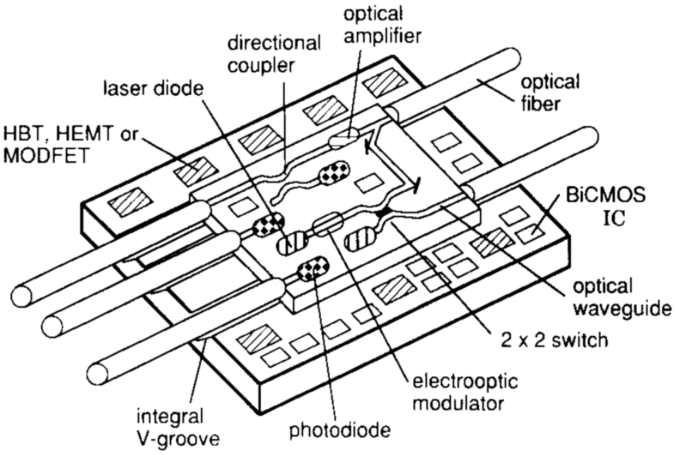

FIG. 1-1 An optoelectronic integrated circuit (OEIC) "superchip" integrating photonic and electronic functionality by means of standard silicon micro-technology, as proposed by Soref in 1993. Figure taken from Soref, Ref. [3].

1.2 A silicon integrated light source

Silicon photonics can make use of complementary metal-oxide-semiconductor (CMOS) process technology. This brings the advantages of existing factories and existing fabrication processes with high yields. Furthermore, the cost and reliability advantages of waferscale production and miniaturization may be exploited.

Moreover, monolithic integration of the single components of an optoelectronic integrated circuit is desired. Monolithic integration means that the different materials needed to realize the various functional components are grown on the Si substrate by material deposition. A contrary approach would be to prepare different components on different substrates and to bond several dies together. The monolithic approach – in contrast to hybrid integration – is thought to lead to more compact structures and less defective devices.[6]

The monolithic integration of photonic functionality into silicon microtechnology is widely advanced with the demonstration of optical modulators [7] and photodetectors.[8, 9] Silicon itself is an inefficient light emitter due to its indirect fundamental electronic band gap and there is no solution as yet for the realization of a monolithically integrated light source which hence is often termed the “holy grail” of silicon photonics. However, various approaches to obtain a lasing material for integration into Si-technology have already been proposed. These approaches include modified or structured Si, as well as other Si-related materials to be grown on a Si substrate. For instance, early attempts from the 1990s are that of Koshida and Koyama who reported visible electroluminescence from porous silicon,[10] Vogl et al. [11] who showed theoretically how SiGe quantum-well structures could obtain a direct electronic gap, or the work by Peng et al. who observed a direct electronic band structure in germanium quantum dots embedded in Si.[12] Very soon also the idea of employing erbium (Er) related light sources, that already succeeded in Er-doped fiber amplifiers and lasers, was considered, for instance by Zheng et al. who demonstrated electroluminescence from erbium-doped Si.[13]

More recent approaches comprise the demonstration of a Si Raman laser,[14, 15] dislocation emission from Si,[16, 17] or the work by Saito et al. who showed stimulated emission from an array of Si fin-shaped micro-structures.[18]

Two very promising approaches from which lasing has been reported are III-V quantum-dot lasers grown on Si (Ref. [19], electrical carrier injection at room temperature) and germanium-tin GeSn alloys (Ref. [20], optical pumping at low temperatures). Moreover, lasing under optical excitation (at low temperature) was also reported very recently from modified glassy Ge quantum dots.[21]

However, some of the proposed approaches are not compatible with CMOS technology and not all of the listed attempts led to lasing. The Si Raman laser was successful, but it was pumped optically. Lasing from GeSn and amorphous Ge quantum dots was only reported for cryogenic sample temperatures. InAs/GaAs quantum-dots grown on Si showed continuous-wave lasing at room-temperature with a threshold current density J_{th} as low as 64.3 A/cm^2.[19] However, the integration of III-V material on Si demanded a several micro-meter thick buffer layer which is unfavorable for the embedding of the laser source in the integrated circuit. Moreover, it is challenging to warrant the III-V material compability with standard micro-electronic fabrication processes.

1.3 Ge as active gain material for a Si integrated laser

A promising alternative solution is the use of Ge as active material and a lot of research effort focuses on germanium (Ge) on silicon (Si) heterostructures. Ge is compatible with standard complementary metal-oxide-semiconductor (CMOS) technology,[22] and is already in use in Si micro-technology. For instance, since the end of the eighties Ge is used as silicon germanium SiGe alloy in hetero-bipolar transistors (HBT) for RF systems in the GHz range.[23]

SiGe may also play a prominent role in 7 nm technology-node chips where it is forecasted as transistor channel material, as presented by researchers of IBM, Globalfoundries and Samsung at IEDM 2016.[24] Also germanium itself is rediscovered as transistor material.[25]

One major obstacle of Ge as an emission medium is that it is an indirect gap semiconductor like silicon. However, the electronic band structure of Ge features a local conduction band minimum at the Γ point which is only about 140 meV higher in energy than the overall minimum at L.[26] However, only about ~ 10^{-4} of excited electrons will be in the direct gap valley in point Γ due to the much larger density of states in the four-fold degenerate L valleys and electronic scattering from Γ into the indirect valleys.[27]

1.3.1 Challenges for a Ge-on-Si device

To increase the electron population in the Γ valley and to overcome the limitation of the indirect band gap to reach population inversion needed for lasing, Liu et al. proposed to apply tensile strain to the Ge layer to reduce the energy difference between Γ and L-valleys together with high levels of n-type doping to pre-fill the L-valleys with extrinsic carriers. A higher concentration of electrically active donors n_{act} induces an increase of the Fermi level in order to promote electrons into the zone-center valley Γ and to limit intervalley scattering out of it.[28, 29] Electrons from the Γ valley can then recombine directly with holes with a largely increased photon emission rate with respect to indirect gap recombination.

Subsequently, optical gain [30] as well as lasing from Ge under optical [31] and electrical [32, 33] pumping have been demonstrated.

However, only slightly strained (~ 0.2%) or even unstrained Ge layers have been used. The presented lasing devices suffered from high threshold current densities and low efficiencies. This can be traced back to high absorption losses (non-radiative recombination of excited carriers as well as emitted photons by free-carrier absorption) due to the high doping concentration and the strong pumping required.[28, 34]

In this regard, improvements can be made by decreasing the energy barrier between L and Γ. In fact, the doping concentration required for lasing can be reduced dramatically under increased tensile strain.[35-37] Sukhdeo et al. [62] report a rapidly reducing threshold current density for suspended Ge strained along the <100> axis when reaching a certain strain level. Approximately 3.2% uniaxial strain is required to achieve this threshold reduction in presence of 1×10^{19} cm^{-3} n-type doping. The threshold current density is calculated to drop by two orders of magnitude from ~ 100 kA/cm^2 to less than 1 kA/cm^2. Consequently, it is not necessarily essential to reach a complete indirect-to-direct bandgap transition. However, the required strain values are still higher than what has been used up until now. Hence, it is of vital interest to search for new methods to introduce tensile strain in the active Ge region.

1.3.2 Tensile strain creation

Note that strain is not a new concept in Si technology; it is already in use to tune electronic properties, above all carrier mobility to enhance transistor performance.[38, 39] Various methods have been applied in order to induce tensile strain in Ge. Camacho-Aguilera et al. used thermal strain in Ge for their lasing device, that is created through the difference in thermal expansion coefficient between the germanium layer and the Si substrate and Ge deposition at high temperature.[40] As already pointed out, this simple method leads only to a small tensile strain of about ~ 0.2%. Basic studies on Ge under higher strain values have been performed by straining bulk like Ge with a dedicated mechanical apparatus where the strain level can be adjusted by screws.[41] El Kurdi et al. controlled the mechanical tensile strain on a Ge membrane inflated by water pressure with an apparatus commonly used for bulge or blister test.[42] Sánchez-Pérez et al. [43] and Boztug et al. [44] investigated Ge membranes of nano-meter thickness by attaching it to a polymer membrane that is inflated by gas pressure. With this method they could reach tensile strain of over 2% in a membrane with 24 nm thickness.

These systems that rely on external hydraulic or pneumatic stress seem not to be suited for integration into a micro-chip. However, Boztug et al. [44] point out that nanomembranes could be strained using MEMS technology, as theoretically investigated by Lim et al..[29]

A more accessible method to create tensile strain in Ge layers may be the growth of Ge on substrates featuring a larger lattice parameter than Ge. Menéndez and Kouvetakis investigated theoretically Ge layers grown on GeSiSn [45] and Fang and coworkers from the same groups realized the growth of thin Ge films on GeSn substrates.[46] Jakomin et al. followed this approach by growing tensilely strained n-type doped Ge layers on an InGaAs buffer.[47] Fang et al. reported tensile strains up to 0.25% and Jakomin et al. could reach a tensile strain up to 0.5%.

A very common approach is that of plane external stressor layers deposited on Ge grounded, i. e. bulk-like layers [48, 49] as well as on suspended Ge structures.[50-53] In the work of Nam et al., Ref. [51], a tungsten layer deposited on Ge was used as stressor, whereas in the other works cited silicon-nitride SiN was used.

Guo et al. prepared strained Ge by defoliating and rolling-up a Ge layer deposited on a SiO_2 on Si substrate with the aid of a top chromium-layer deposited on Ge. They could reach 1% tensile strain.[54]

The highest strain values in Ge reported so far have been reached by the exploitation of a strain accumulation effect through shaping free standing pre-strained Ge layers.[55-58] Geometries realizing uniaxial strain resulted in up to 5.7% uniaxial strain [56] and in layer shapes leading to a biaxial strain up to 1.9% biaxial strain have been reported.[58]

In the first part of this thesis we are going to present an alternative method for creation of tensile strain in Ge. This method relies on the use of a patterned SiGe stressor layer to induce tensile strain in a Ge layer. For this purpose, SiGe is grown pseudomorphically on Ge, such that it is under tensile strain due to its smaller lattice constant with respect to Ge. Next, trenches are engraved into the SiGe layer, thereby creating a pattern of SiGe stripes. These stripes are free to elastically relax at their side walls, thereby compressing the Ge beneath a stripe.[59] At the same time, tensile strain is induced in the Ge inside a trench of the pattern, where SiGe was removed. This top down approach may be considered to be comparably easy to be fabricated.

We are going to present samples featuring bulk-like Ge on Si layers strained by SiGe stripe stressors. Micro-Raman spectroscopy was employed to determine the strain in Ge inside a trench and we revealed up to 4% tensile strain.[60] We found that the strain inside a trench increases with decreasing trench width. Using photo-luminescence (PL) measurements we investigate the emission properties of the strained Ge. However, as we will see, PL measurements turned out to be not straightforward and suffer from carrier diffusion into the unstrained regions of the samples. For this reason, we investigate the possibility to constrain excited carriers to the highly strained volume of the Ge layer. Moreover, the Ge volume strained by the stripe stressors is comparably small, the trench width for the highest strained samples is only 20 nm.

Motivated by the high strain values in suspended Ge reported in literature (as discussed above), as well as by simulations,[61] that show that SiGe stressors on suspended Ge can achieve high strain values using substantially larger gap widths, we transfer our SiGe stressor method from bulk-like material to suspended micro-bridges. In this thesis we are going to present SiGe stressors on Ge micro-bridges and compare the obtained strain to the case of attached bulk-like Ge. The pattern engraved into the pseudomorphically grown SiGe layer is that of a cross, that induces biaxial strain into the Ge layer as seen from simulations.[61]

1.3.3 Heavy n-type doping

Besides strain, substantially high n-type doping levels are needed to reach optical gain at reasonable threshold current densities, as shown in the calculations of Sukhdeo et al. with doping levels in the 10^{19} cm^{-3} range.[62] Hence, at first sight, doping appears to be a viable option to tackle the issue of the indirect band gap in germanium, however, the role of doping is less clear than that of strain, and results about the dependence of carrier lifetime on dopant concentration in Ge layers have been scarcely reported in the literature.[63]
As already stated previously, a higher doping concentration causes an up-shift of the Fermi level, easing the thermal excitation of electrons from the L_c valley to the Γ_c valley. On the other hand, the non-radiative recombination rate through the Auger mechanism is proportional to the third power of the total carrier concentration (i. e., equilibrium plus the excess carrier density δn),[64] therefore a high dopant concentration contributes to an enhancement of the non-radiative recombination rate which eventually may quench the radiative emission.
Furthermore, high doping levels may cause increased free carrier absorption limiting the gain in a laser cavity.

Moreover, also the Shockley-Read-Hall lifetime, related to non-radiative recombination through recombination centers with energy levels inside the Ge bandgap, is reduced with a higher doping concentration, leading to a further non-radiative recombination channel. Finally, a high total density of donors n_{tot} can decrease the non-radiative recombination time τ_{nr} through two different mechanisms:

(1) the reduced quality of the epitaxial material due to the increased density of point defects;
(2) the electron-hole non-radiative recombination via Coulomb scattering of electrons with charged dopant ions.

To minimize the detrimental effect of (1), high crystallinity Ge growth is required. Therefore, in this thesis, we investigate the photoluminescence from highly in-situ phosphorous doped Ge layers selectively grown in SiO_2 windows on a Si substrate in dependence of the growth conditions. Our goal is to reveal trends for the different growth parameters to find the relative most promising recipe for highly emitting Ge on Si heterostructures. Investigated growth parameters comprise Ge deposition temperature, dopant flux, and post-annealing condition. Moreover, we will discuss the effect of strain on PL emission, by applying a Si_3N_4 stressor layer to the Ge layers.

We find that, owing to the competitive mechanism discussed above, the PL signal is not a monotonic increasing function of the donor concentration. We obtained our best results for a P donor density of ~ $2 - 3 \times 10^{19}$ cm^{-3}. This is in agreement with Schwartz et al. [65] who have found that the electroluminescence (EL) intensity emitted by antimony (Sb) doped Ge diodes begins to quench above a doping level of ~ 3×10^{19} cm^{-3}. For this optimal doping concentration, we measure at room temperature an enhancement of the peak PL signal of ~ ×4 with respect to the undoped sample.

The proper understanding of the competition between these beneficial and detrimental effects is of paramount importance in view of the optimization of Ge as optical gain medium. For this reason, we present a study of the recombination dynamics in n-doped germanium:

The value of the non-radiative lifetime τ_{nr} has been largely overestimated in the literature. Liu et al. reported in their seminal work on Ge as gain medium a value of τ_{SRH} = 100 ns for a doping concentration of 7.6 ×10^{19} cm^{-3}.[28] Values of τ_{SRH} of the order of 10^2 ns may be realistic in high-quality intrinsic Ge layers, much faster rates are expected in heavily doped Ge, though, as for instance reported by Geiger et al..[66]

El Kurdi et al.,[67] estimated the photo-induced carrier concentration completely relying only upon Auger recombination as dominant mechanism and neglected the doping-induced reduction of the SRH rate. This is in contrast with Gaubas and Vanhellemont [68] who consider the Shockley-Read-Hall recombination mechanism to dominate at dopant concentrations of ~ 10^{19} cm^{-3}.

We point out that a proper consideration of a doping-induced reduction of the Shockley-Read-Hall (SRH) non-radiative lifetime τ_{SRH} allows for a correct evaluation of the excess carrier density and of its spatial distribution. This information is of great importance for the theoretical modeling of Ge-based lasers.

In order to contribute to a better understanding of the non-radiative recombination mechanism, we compare the results of photoluminescence (PL) experiments with a multi-valley self-consistent effective mass numerical model previously adopted to simulate PL in intrinsic tensile Ge layers,[69] that has been updated to take into account the influence of dopants on the non-radiative recombination dynamics.

We shall see that, using a proper calibration procedure of the model against experimental data, PL under steady excitation can be used to estimate the non-radiative lifetime τ_{nr} at the nanosecond scale.

We estimate that the SRH recombination rate is increased with respect to the intrinsic case by two orders of magnitude. Due to the negative impact of doping on the lifetime, the SRH recombination mechanism largely dominates over the Auger non-radiative dynamics not only in intrinsic samples, but also in all the heavily doped samples investigated in this work.

To sum up, the aim of this thesis is to study a novel and simple top-down approach to create tensile strain in Ge which is based on the transfer of elastic energy from highly strained SiGe patterns to a Ge layer and to investigate the effect of high phosphorous doping on the photo-luminescence properties of Ge layers selectively grown on silicon.

The structure of the thesis is as follows: In chapter 2 a brief introduction to the properties of the silicon-germanium material system and the theoretical concepts of strain, doping and recombination mechanisms is provided. In chapters 3 and 4 we then describe the two experimental methods applied in this work: micro-Raman spectroscopy to determine the strain in Ge and photo-luminescence spectroscopy to probe the emission efficiency of the prepared samples. The following chapters 5 to 10 report the details on the investigated samples and the results obtained. Finally, we summarize and conclude our work in chapter 11.

2 Theoretical aspects

The goal of this thesis is to investigate the main steps – tensile strain creation and heavy n-type doping – needed to optimize germanium as active material of a light source that is monolithically integrated into CMOS based micro-chips. Thereby monolithic integration will be accomplished by hetero-epitaxial growth on the Si substrate.
In this chapter the reader will find the specific theoretical aspects which are needed to follow our discussion. One of the beauties of our work is, that we are limited to the elemental semiconductors Ge and Si in the selection of exploited materials. Since our approach to induce tensile strain into a Ge layer relies on the action of external SiGe stressors, we also discuss the basic properties of the SiGe alloy.

2.1 Properties of the SiGe material system

The SiGe material system consists of the elements silicon and germanium, which belong to the fourth main group of the periodic table of elements (hence, using silicon and germanium for photonic applications, one refers to group IV photonics). Both are miscible at any molar fraction in both the liquid and solid state [70-72] and can form the binary alloy $Si_{1-x}Ge_x$ (with x the Ge molar fraction) which also has got semiconducting properties.

2.1.1 Crystal structure

Both silicon, element 14 of the periodic table, and germanium, element 32, crystallize in a diamond cubic crystal structure under ambient conditions, forming tetravalent bonds with the neighboring atoms. The diamond cubic crystal structure consists of a face-centered cubic (fcc) lattice with two tetrahedrally bonded atoms in its basis. This corresponds to two face-centered-cubic (fcc) lattices penetrating each other and mutually displaced by a quarter of the body diagonal. The cubic unit cell consists of 8 atoms, each of which has got four nearest neighbors at the corners of a tetrahedron, and twelve next-nearest-neighbors.

This crystal structure is also adopted by the alloy $Si_{1-x}Ge_x$ with any composition x. The Si and Ge atoms are randomly distributed on the lattice sites. The lattice parameters a are determined by the side length of the face centered translational cell (elementary fcc cube). The values for Si and Ge are given in Table 2-1. We find, that a_{Ge} is 4.17% larger than a_{Si}, a fact that will be of importance later on.

Table 2-1 Lattice parameters of Si, Ge and SiGe. The later is determined according to Vegard's law. Values for Si and Ge are taken from Ref. [73].

a_{Si} (at T_L = 295.7 K)	a_{Ge} (at T_L = 298.15 K)	$a_{Si_{1-x}Ge_x}$
5.43102018(34) Å	5.6579060 Å	$a_{Si} + x \cdot (a_{Ge} - a_{Si})$

The lattice parameter of $Si_{1-x}Ge_x$ can be well estimated by Vegard's law, which is a linear interpolation between the lattice parameter a_{Si} for Si and a_{Ge} for Ge.[74] The real lattice parameter of SiGe shows only a small deviation from Vegard's law, see FIG. 2-1.[75]

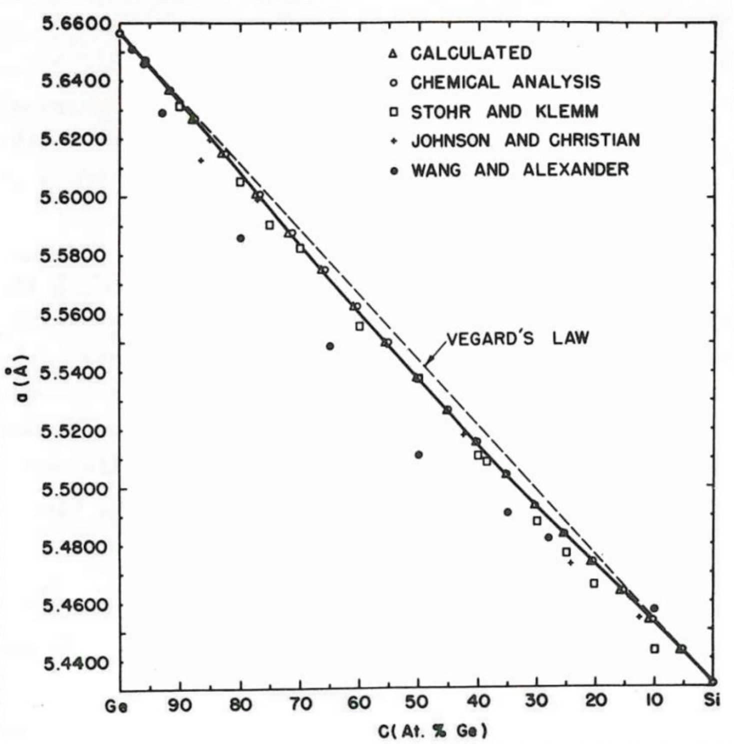

FIG. 2-1 Lattice parameter *a* of the alloy SiGe in function of the germanium molar fraction *x*, here denominated *C*. Figure taken from Dismukes et al., Ref. [75]. The presented theoretical and experimental data shows that the deviation from Vegard's law, i. e. a linear interpolation between the lattice parameters a_{Si} of silicon and a_{Ge} of germanium, is small.

The lattice parameter a is a function of lattice temperature T_L. The change with temperature can be expressed with the linear thermal expansion coefficients α(T) that also depend on temperature. Room temperature values for Si and Ge are $\alpha_{Si} = 2.92(6) \times 10^{-6}\ K^{-1}$ (at T = 293 K) and $\alpha_{Ge} = 5.90 \times 10^{-6}\ K^{-1}$ (T = 300 K).[73] The linear expansion coefficient of Ge is about twice that of Si at all relevant temperatures from $T_L = 0$ K to $T_L > 800$ K.[76] As we will see later, this has an important implication on hetero-epitaxial growth of Si and Ge.

The fcc lattice in real space leads to a bcc (body-centered cubic) lattice in reciprocal space (momentum space), so that the first Brillouin zone of Si, Ge and the alloy SiGe have got the shape of the Wigner-Seitz cell of the bcc lattice with a two atomic basis. The first Brillouin zone together with the nomenclature of the most interesting symmetry points and directions is depicted in FIG. 2-2.

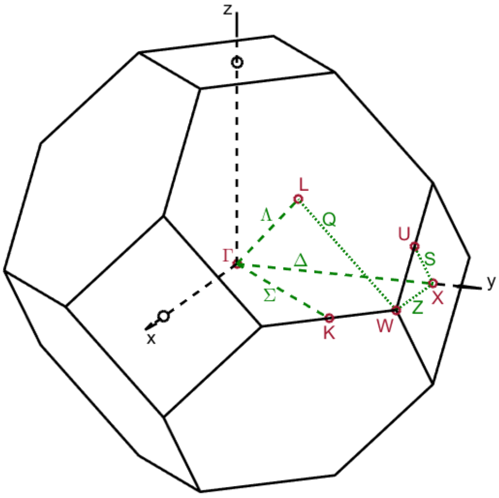

FIG. 2-2 First Brillouin zone of Si, Ge and the alloy SiGe. The nomenclature of the most important symmetry points and directions is plotted in color. The axes {x,y,z} correspond to the <100> crystallographic direction. The point L is along direction Λ which extends along <111>.

2.1.2 Phononic band structure

The phononic band structure, i. e. the dispersion curve of phonons, of a cubic lattice is characterized by six branches, three optical phonon modes and three acoustical ones. FIG. 2-3 reports the dispersion curves for Si and Ge along different symmetry lines of the crystal lattice obtained experimentally by thermal neutron spectrometry together with calculated curves. In both materials, the optical and acoustic branches are degenerate at $k = 0$. The frequency of the acoustical branches equals zero in this point, whereas the optical branches are non-zero. The frequency of the optical phonons in the center of the Brillouin zone are $\nu_{LTO}(\Gamma_{25'}) = 15.53 \times 10^{12}$ Hz for Si [77] and $\nu_{LTO}(\Gamma_{25'}) = 9.02 \times 10^{12}$ Hz for Ge,[78] at 300 K respectively.

In sec. 3 we will see, that we can probe the optical phonons with $k \approx 0$ using Raman spectroscopy. In Raman spectroscopy, wavenumbers $([\tilde{\nu}] = 1\,\mathrm{cm}^{-1})$ are used instead of frequencies. The frequencies of the normal optical modes of Si and Ge convert hence into $\tilde{\nu}_{Si} = 518.0\ \frac{1}{\mathrm{cm}}$ and $\tilde{\nu}_{Ge} = 300.9\ \frac{1}{\mathrm{cm}}$, respectively.

The high symmetry of the lattice leads to further degeneracy of phonons in special points of the Brillouin zone. Besides the degeneracy of the optical and acoustic phonon modes at $k = 0$ (Γ point), there is degeneracy of the longitudinal optical (LO) and longitudinal acoustic (LA) modes at the X_1 point with $\nu_{LAO}(X_1) = 12.44 \times 10^{12}$ Hz for Si and $\nu_{LAO}(X_1) = 7.14 \times 10^{12}$ Hz for Ge,[78] and moreover, the twofold degeneracy of both the transverse optical (TO) and the transverse acoustic (TA) modes along high-symmetry directions, e. g. Λ and Δ, see FIG. 2-3.

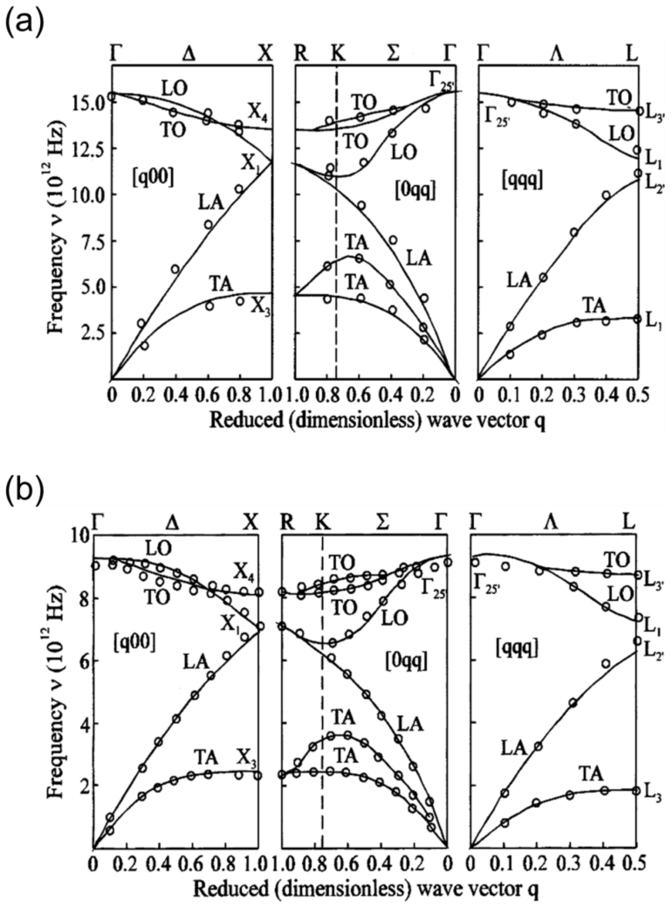

FIG. 2-3 Dispersion curves for acoustic and optical phonons of silicon (a) and germanium (b). Figures are taken from Ioffe Physico-Technical Institute, Ref. [79], with experimental data (○) taken from Dolling for Si, Ref. [77], and Nilsson and Nelin for Ge, Ref. [78], together with calculated dispersions from Tubino et al. for Si, Ref. [80], and Weber for Ge, Ref. [81].

2.1.3 Electronic band structure

Band structures of silicon and germanium

The location of the direct energy gap is at the center of the Brillouin zone in the Γ point with wavevector $k = 0$. FIG. 2-4 shows the reduced representations of the band diagrams of Si and Ge and gives the energy values at room temperature for the main conduction band valleys with respect to the top of the valence band. We find, that both Si and Ge are indirect gap semiconductors, i. e. the global minimum of the conduction band is not in point Γ where the maximum of the valence band is.

For Si, the minimum of the conduction band is along direction <100> (direction Δ) and the indirect band gap energy is $E_{\mathrm{ind}} = 1.12$ eV. Due to the crystal symmetry, this conduction band valley is six-fold degenerate. The direct gap energy in Si amounts to $E_{\mathrm{dir}} = 3.4$ eV.

In case of Ge, the absolute conduction band minimum is located in point L in direction <111> (Λ) at the border of the Brillouin zone. Hence, inside the first Brillouin zone there are – due to symmetry – eight half-valleys, thus the L valleys are four-fold degenerate. The indirect gap energy is $E_{\mathrm{ind}} = 0.66$ eV and the direct gap energy is $E_{\mathrm{dir}} = 0.80$ eV at room temperature. In contrast to Si, the energy difference between indirect gap and direct gap is quite small in Ge and is only ΔE = 140 meV. Hence, germanium is said to be a quasi-direct semiconductor and that is what makes germanium so interesting.

In both Si and Ge, the top of the valence band is located in point Γ (k = 0) and consists of degenerate light-hole (LH) and heavy-hole (HH) bands. Moreover, in both materials there is a split-off (SO) hole band at lower energies due to spin-orbit coupling.

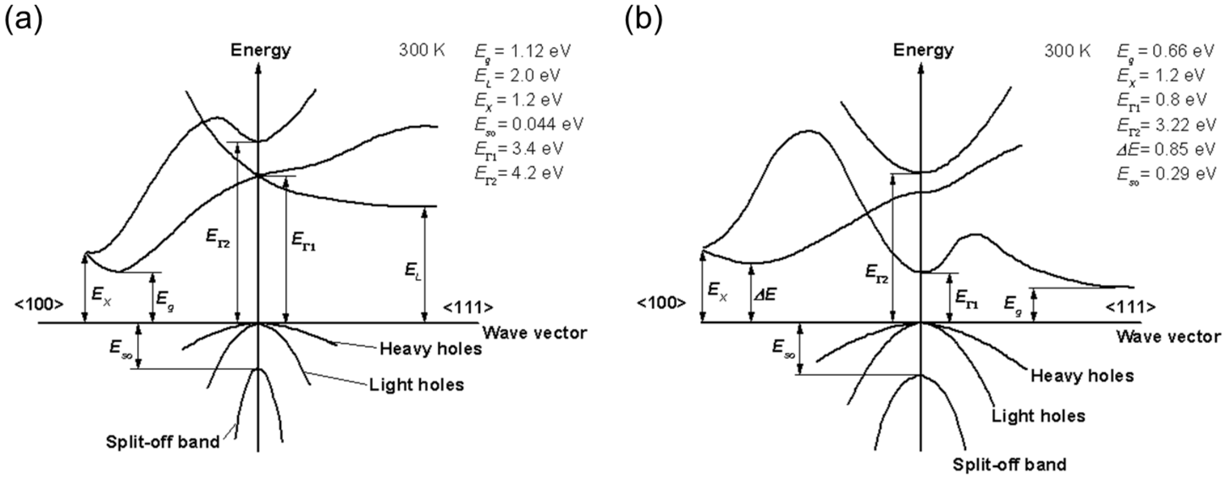

FIG. 2-4 Reduced representations of the electronic band diagrams of silicon (a) and germanium (b). Shown are the bands in directions <100> (Δ) and <111> (L). The most important gap energies are labelled and given. Both silicon and germanium are indirect gap semiconductors with the global conduction band minimum in a point of the Brillouin zone different from Γ (0, 0, 0). Figures are taken from Ioffe Physico-Technical Institute, Ref. [79].

The direct radiative transition $\Gamma_c \rightarrow \Gamma_v$ from the Γ valley of the conduction band (Γ_c) to the Γ valley of the valence band (Γ_v) is much more efficient than the indirect radiative transition from the L-valleys of the conduction band to the top of the valence band ($L_C \rightarrow \Gamma_v$). Liu et al. report recombination coefficients for the direct transition, $R_\Gamma = 1.3 \times 10^{-10}$ cm^3/s, and indirect transition, $R_L = 5.1 \times 10^{-15}$ cm^3/s.[28]

For this reason, we are interested in a high electron population of the Γ_c valley. However, since the L valleys constitute the energetical minimum of the conduction band and have got a much larger density of states, at room temperature only a fraction of 10^{-4} of excited electrons is located in the Γ_c valley.[27, 82] Hence, light emission from germanium is not efficient and in the course of this thesis we will present methods to improve it.

Detailed valence-band structure

When putting single atoms together to form a crystal, their atomic energy levels split and form the bands of the crystal. All atoms in a diamond-like lattice form a tetrahedron with their neighbors and the valence electrons hybridize into sp^3 orbitals. However, it turns out that the electronic states near the band-edges have the symmetries of the s- and p-like orbitals of the individual atoms. The states near the conduction-band minimum close to the center of the Brillouin zone (Γ, k = 0) are of s-like character (azimuthal quantum number l = 0), whereas the valence-band states close to the valence-band maximum are of p-like character (l = 1). At first, these valence band states are triply degenerate (neglecting the electron spin) with magnetic quantum numbers m_l = -1, 0, +1.

Taking into account also the spin $\vec{S}$ of an electron, its magnetic moment is $\vec{\mu}_S = g\frac{e}{2m}\vec{S}$, where g is the dimensionless g-factor, e is the electron charge, m is the electron mass, and $\vec{S}$ is the spin angular momentum. An electron moving in the stationary electric field $\vec{E}$ of the positively charged atomic nucleus with Z protons and charge $+Ze$ sees a magnetic field $\vec{B} = \frac{1}{c}\vec{E} \times \vec{v}$ due to the electric field $\vec{E}$ of the nucleus, where $\vec{v}$ is the velocity of the moving electron and c is the speed of light. The magnetic momentum of the electron interacts then with the magnetic field $\vec{B}$, this is the spin–orbit coupling.

Next, it can be shown that the valence band degeneracy at $\vec{k} = 0$ is lifted resulting in a four-fold degenerate state with total angular momentum quantum number $j = 3/2$ and projection of the total angular momentum on an arbitrary axis x $J_x = +3/2, +1/2, -1/2, -3/2$ and a doubly degenerate state with $j = ½$ and $J_x = +1/2, -1/2$ which is separated by the energy distance E_{SO} (often also denominated as Δ), the split-off energy due to the spin-orbit interaction.[83] Note, since the energy split-off E_{SO} depends on the spin-orbit coupling, which is higher for a higher magnetic field $\vec{B}$, and hence higher for a higher electric field $\vec{E}$ of the nucleus, E_{SO} is larger for atoms containing a larger number of protons Z. Indeed, we find for silicon E_{SO}(Si) = 44 meV and for germanium E_{SO}(Ge) = 290 meV, cf. FIG. 2-4.

Furthermore, as can be derived by means of the k·p method, for $\vec{k} \neq 0$ the four-fold degenerate band with $j = 3/2$ will be split into the heavy-hole band and the light-hole band. Both are doubly degenerate bands (the spin projection quantum number m_s can take values s = ± 1/2) and the projection of the angular momentum J on the direction of $\vec{k}$ (helicity) is ±3/2 in case of the heavy holes and ±1/2 for the light holes. For symmetry considerations in diamond- and zinc-blende-type semiconductors, the light hole band ($m_l = 0$) interacts with the s-like conduction band which results in a larger energy dispersion for $k \neq 0$ (larger curvature of the band) and consequently leads to the smaller effective mass of the light hole band compared to the non-interacting heavy-hole band, $m_{LH}^* < m_{HH}^*$.[84, 85]

Electronic band structure of SiGe

We conclude our discussion of the electronic band structures with some remarks on the band structure of SiGe, since we use SiGe as material for external stressors and we are also going to present an attempt to use SiGe to create a potential barrier in a Ge/SiGe heterostructure to confine excited carriers inside the Ge layer.

From the measurement of optical absorption in SiGe alloys over the entire range of alloy composition, Braunstein et al. could conclude that the $Si_{1-x}Ge_x$ band structure is characterized by an indirect energy band-gap for all compositions x. The determined band-gap shows a strong deviation in dependence of composition at about (1-x) = 15% of Si. Braunstein et al. could attribute this to a transition from a Ge-like conduction band with the lowest conduction band edge in L to a Si-like conduction band structure with indirect gap along direction Δ.[86] We replot their results regarding the indirect energy band-gap in FIG. 2-5 (a). Kline et al. [87] deduced the direct bandgap in SiGe from electroreflectance spectra and found a linear dependence on the molar composition of the alloy, see FIG. 2-5 (b).

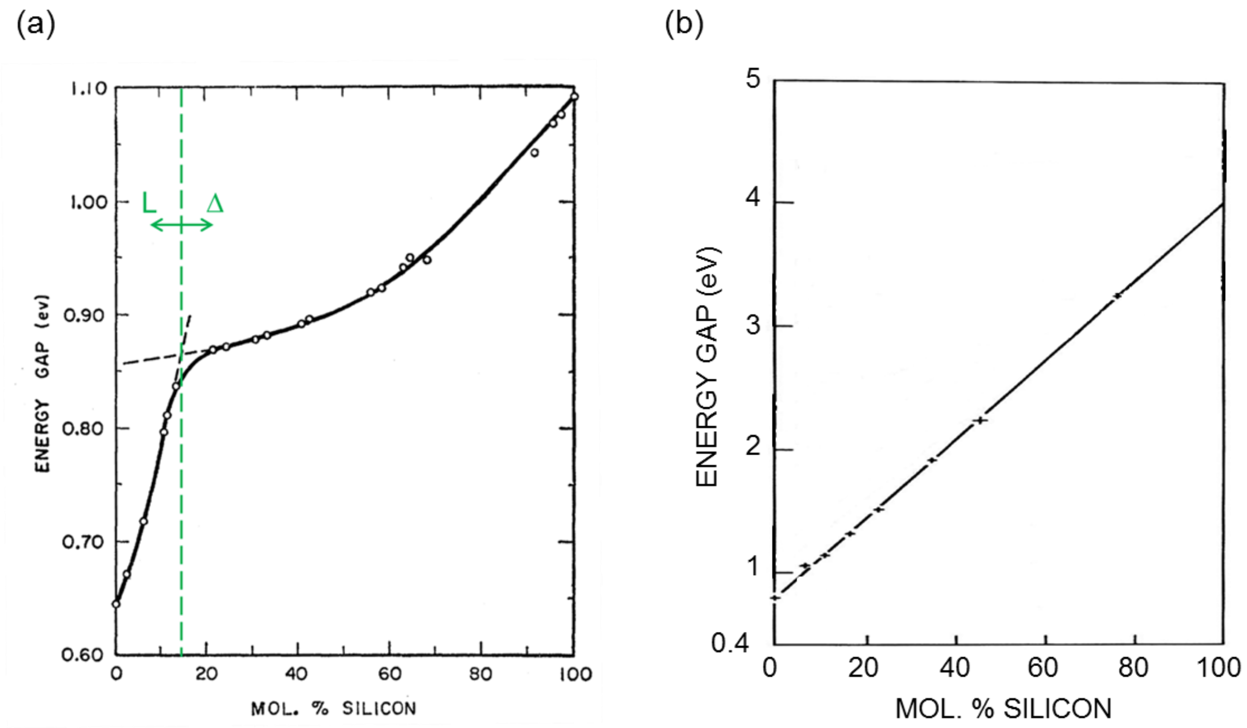

FIG. 2-5 (a) Indirect band gap in $Si_{1-x}Ge_x$ in dependence of the silicon molar fraction (1-*x*). At about 15% of Si (85% Ge) the nature of the indirect gap in the Brillouin zone changes from Ge-like (indirect gap in point L) to Si-like (indirect gap along direction Δ). Figure taken from Braunstein et al., Ref. [86].

(b) Direct bandgap E_0 in $Si_{1-x}Ge_x$ in dependence of the silicon molar fraction (1-*x*). The direct gap energy changes linearly from that of pure Ge to that of pure Si. Figure taken from Kline et al., Ref. [87].

2.2 Heteroepitaxy and strain relaxation

In this section we will give a short introduction to semiconductor heteroepitaxial growth and its implications. Hetero-epitaxial growth is different from e. g. growth of bulk single crystals.

2.2.1 Epitaxial growth

Epitaxy is the process in which a crystal is grown on top of another crystal (e. g. a bulk single crystal) and thereby adopts a preferred or specific crystallographic orientation related to the substrate, so that the process results in the formation of crystalline thin films. If the growth orientation is random, there is no epitaxial growth. The word *epitaxy* derives from ancient Greek, ἐπί meaning “upon”, “over” or "above", and τάξις meaning "in ordered manner", “arrangement”.
Epitaxial layers, i. e. the thin crystalline films created in an epitaxial process, are used in the creation of micro-electronic devices such as integrated circuits as well as optoelectronic devices and layer thicknesses usually range from less than one micron to several microns.
Chemical Vapor Deposition (CVD) and Molecular Beam Epitaxy (MBE) are two wide spread growth techniques that allow for epitaxial growth on a crystalline substrate. All samples presented in this thesis are prepared using CVD methods described in sec. 2.2.5.

We can distinguish between homo-epitaxy, that is the deposition of a film on a substrate of the same chemical composition (for example, a Ge film deposited on a bulk Ge crystal or a Ge film on a germanium on insulator substrate (GeOI)), and hetero-epitaxy in which the deposited film and the substrate are of different chemical composition. In this thesis, we are concerned with the hetero-epitaxial growth of Ge on Si as well as SiGe as a second epilayer grown on hetero-epitaxial Ge.

Materials of different chemical composition have got different crystal lattice parameters. In case of hetero-epitaxial growth there is a so-called lattice mismatch between the epilayer and the substrate the implications of which will be discussed later on.
For the growth of a crystalline film on a surface, there are three possible growth modes. We have taken the following information from the review of Venables et al., Ref. [88] The epitaxial growth proceeds through nucleation of material and successive growth stages. Processes involved are among others adsorption of atoms on the surface, surface diffusion and chemical binding.[88] The thermodynamics of adsorption and the kinetics of crystal growth determine the different growth modes.[88]
The three modes of crystal growth are:

- ☐ island, or Volmer-Weber mode:
    - ○ the nucleation of small clusters on the substrate leads to the growth of islands. In this case, the deposited atoms bond preferably to each other than to the substrate.
- ☐ layer, or Frank-van der Merwe mode:
    - ○ a complete monolayer is formed on the surface before a second layer is formed that binds less to the first than the first to the substrate. If the binding energy is further decreased for subsequent layers, the layer growth mode can be obtained also toward bulk-like thick crystals.
    - ○ The atoms bond more strongly to the substrate than to each other.
- ☐ layer plus island, or Stranski-Krastanov, growth mode:

- in this mode a first monolayer or a few monolayers are formed. Subsequent growth of layers is then unfavorable and islands are formed on top of the initially grown layers that are also called wetting layers. The layer plus island growth mode is hence the intermediate case between layer growth and island growth.
- The departure from layer growth and formation of islands can have several reasons. Decisive is a deviation from the steady reduction in binding strength when adding new layers that enabled layer growth.

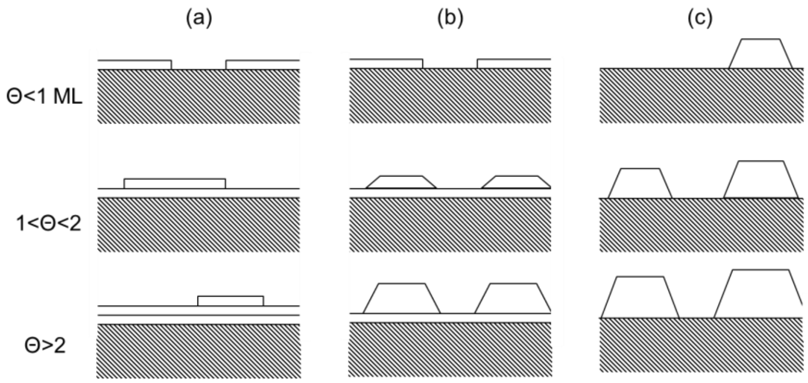

FIG. 2-6 Illustrations of the three crystal growth modes: (a) layer or Frank-van der Merwe, (b) layer plus island or Stranski-Krastanov, and (c) island or Volmer-Weber mode. Moreover, the coverage Θ in monolayers (ML) is indicated. Germanium on silicon growth occurs normally in the Stranksi-Krastonov mode. Figure adopted from Venables et al., Ref. [88]

Fig. FIG. 2-6 depicts these three growth modes. The growth of Ge on Si(100) normally happens in the Stranski-Krastanov growth mode. The deposition of Ge on Si is hetero-epitaxial and there is a difference in lattice constant of Ge and the Si substrate of about 4.2%. The first monolayers of Ge adopt to the lattice of Si and its smaller lattice parameter and are hence compressed. To accommodate this compressive strain, Ge deviates from the formation of additional layers during the further growth and results to form islands instead. However, also when the islands grow further, further strain is accumulated. We will see in the next section what this brings about and conclude here by mentioning the Stranski–Krastanov growth mechanism results in high surface roughness. Hence, one may seek to suppress it by intentional introduction of impurities like Sn [82] or growth of a seed layer below 390 °C.[89]

2.2.2 Lattice mismatch, critical thickness and plastic relaxation

As already discussed, in hetero-epitaxy the deposited material and the substrate are of different chemical composition and have got different lattice parameters in general. Thus, there will be strain when two layers are attached to each other. In hetero-epitaxy, initially, the deposit adopts to the lattice parameter of the substrate. This leads to a so called misfit strain that can be compressive or tensile as depicted in FIG. 2-7 and which is a biaxial in-plane strain.The misfit strain is equal to the lattice mismatch *f* defined as

$$f = \frac{a_s - a_l}{a_l} \qquad (2\text{-}1)$$

where a_l is the lattice parameter of the relaxed epilayer and a_s is the lattice parameter of the relaxed substrate. In the case of FIG. 2-7 (a), $a_l > a_s$ and hence $f < 0$, resulting in compressive strain in the epilayer, see FIG. 2-7 (b). An example for this is the growth of Ge on Si as already discussed above. The opposite case is shown in FIG. 2-7 (c) and (d), where the deposited material has got a lattice parameter $a_l < a_s$ so that the lattice mismatch $f > 0$ and the strain inside the epilayer is tensile.
In these cases, the epilayer extends the crystal lattice without any disruption and it is said that the epitaxial layer is “pseudomorphic” or “coherent”.

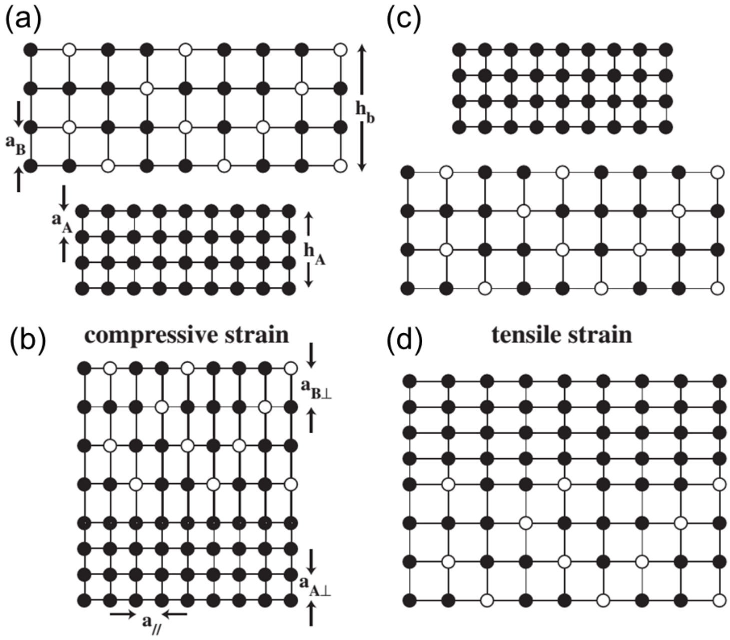

FIG. 2-7 Sketches of the crystal lattices of substrate and deposited material in a hetero-epitaxial process. (a) The material to be deposited has got a larger lattice constant a_B in its relaxed state than the substrate, a_A. (b) Deposition onto the substrate leads to compressive strain in the epilayer. An example would be SiGe on Si. (c) The deposit material has got a smaller lattice constant in its relaxed state than the substrate. (d) Deposition onto the substrate leads to tensile strain in the epilayer, e. g. Si on SiGe. Figure taken from Paul, Ref. [90].

In a strained layer, elastic energy proportional to the square of the strain ε^2 is stored. The thicker an epitaxial layer is grown, the more elastic energy is accumulated in it. At a certain layer thickness, it is energetically more favorable to break the perfect order of the crystal lattice and to reduce the accumulated strain energy. Consequently, some of the strain inside the epilayer is released. This is called plastic relaxation and happens through the introduction of dislocations into the lattice, i. e. extended defects, at which the bonds between atomic layers are broken. Fig. FIG. 2-8 (a) shows a sketch of a 90° misfit dislocation at the interface between two hetero-epitaxial layers.

In detail, a so-called misfit dislocation (MD) is nucleated as a loop at the surface of the growing epilayer and then migrates toward the epilayer/substrate interface, thereby creating a semi-loop which is connected to the surface through threading dislocations (TD), see. FIG. 2-8 (b). In Ge misfit dislocations are mostly directed along the <110> crystallographic directions and are of the 60° dislocation type, cf. FIG. 2-8 (b). The threading dislocations extending from the interface to the surface of the epilayer, form an angle of 60° with the interface, i. e. they glide on the Ge (111) lattice plane. In this way, the largest amount of strain can be released. A 60° dislocation can be divided into two so-called Shockley-partials, that is a 90° edge dislocation and a 30° dislocation, separated by a stacking fault, though. Indeed, it strongly depends on the actual growth conditions and strain levels which dislocations are formed.

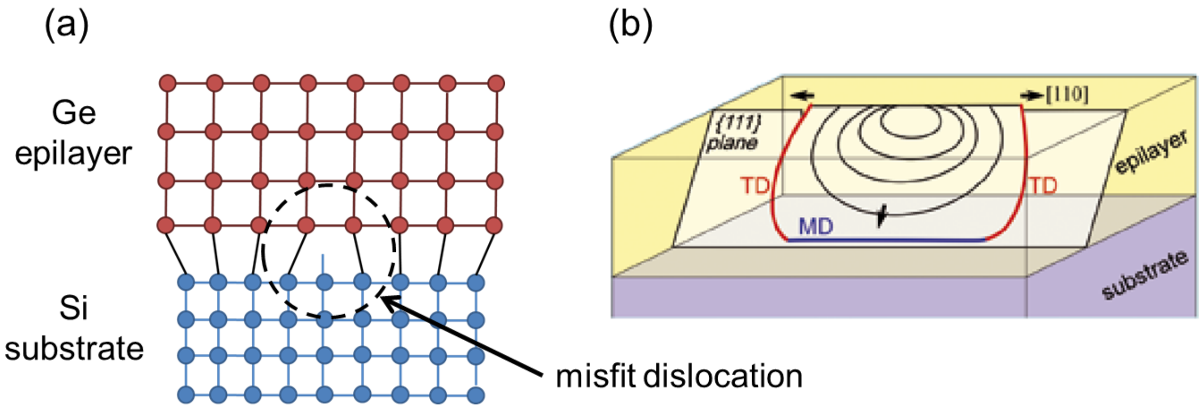

FIG. 2-8 (a) Schematic illustration of a 90° edge misfit dislocation at the interface of the Ge epilayer and the Si substrate caused by the lattice mismatch of deposited material and substrate.

(b) Misfit dislocations (MD) in the SiGe material system extend mostly along the <110> crystallographic directions. Misfit dislocations form segments that are connected to the surface through threading dislocations (TD). Figure taken from Miglio et al., Ref. [91].

Threading dislocations penetrating the epilayer are harmful to its electrical and optical performance. As we will discuss in matters of the photo-luminescence results presented in this thesis, TDs – and also MDs – can reduce the emitted luminescence intensity from a Ge epilayer. It is hence of great interest to reduce the threading dislocation density (TDD). One attempt is to extend the misfit section of the loop along the epilayer/substrate interface so that the threading dislocation reaches the edge of the wafer and the TDD at the epilayer surface is reduced. Typical values of TDD in Ge heteroepitaxial layers are 10^9 cm^2 that can be reduced to 10^7 cm^2 by thermal treatment (annealing, postbake). The dislocations in a Ge epilayer give raise to a crosshatch pattern on the layer surface.[90]

Hence, the strain induced in the epilayer persists only up to a certain critical thickness hc that depends on the lattice misfit and the elastic constants of the deposit material. Critical thicknesses were studied among others by van der Merwe [92] and Matthews and Blakeslee.[93]
FIG. 2-9 shows the critical thicknesses for the growth of pseudomorphic $Si_{1-x}Ge_x$ on a Si substrate in function of the Ge molar fraction x. For the growth of pure Ge on Si the critical thickness is only about ~ 2 nm. FIG. 2-9 displays also a metastable region in which h_c is exceeded but the introduction of dislocations is still delayed. At the beginning of metastability, the formation of dislocations is thermodynamically possible, but kinetically retarded, i. e. the system can fully relax the strain upon annealing when additional thermal energy is supplied to overcome the energy barrier for nucleation of dislocations.
The metastable region indicated in FIG. 2-9 corresponds to a growth with MBE at 550 °C, but a metastable state of the epilayer can be achieved also with other growth techniques at comparably low deposition temperatures. Indeed, as we will see in sec. 5, we deposited SiGe with Ge fractions of $x \approx 45\%$ and $x \approx 50\%$ on Ge exceeding the critical thicknesses and reaching metastable states. These highly strained and not plastically relaxed SiGe layers are then patterned into SiGe stressors that act on the Ge beneath.

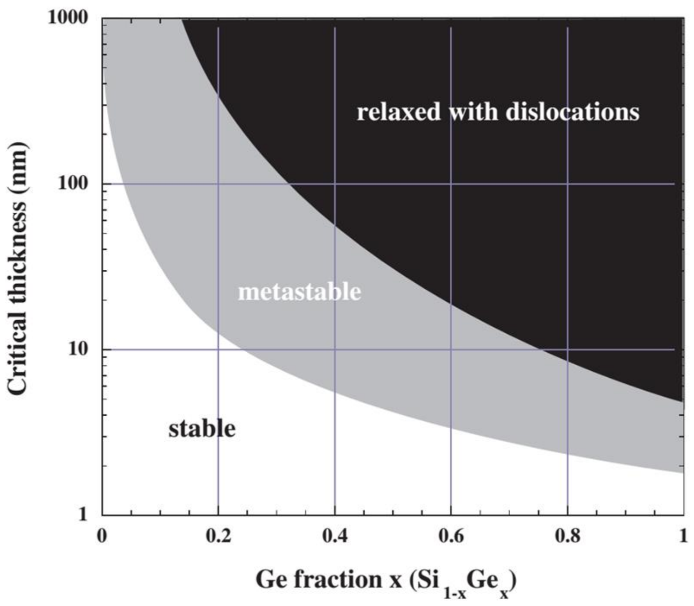

FIG. 2-9 Critical thickness h_c according to Matthews and Blakeslee, Ref. [93], for the growth of $Si_{1-x}Ge_x$ on a Si (100) substrate for different Ge molar fraction x. Moreover, the metastable region for MBE growth at 550 °C is indicated. Figure taken from Paul, Ref. [90].

2.2.3 Thermal strain

The traditional growth of Ge on Si in the Stranski-Krastonov mode would hence consist of growing islands, connected by a wetting layer. As the islands become larger, they accumulate elastic energy due to the misfit strain until part of the energy/strain is released by introducing dislocations into the islands. These steps are repeated during the further Ge deposition: The islands grow, releas the accumulated strain by dislocations, grow again and so forth.

At room temperature, Ge and Si have got a lattice mismatch of about ~ -4%. Hence, the hetero-epitaxial strain of Ge on Si should result in a compressed Ge layer or a plastically relaxed layer.

However, Ge on Si most often displays a slight tensile strain of about ~ 0.2%. This is due to the fact, that the thermal expansion coefficient α of Ge is larger than the one of Si at all temperatures, cf. sec. 2.1.1, and that epilayer deposition is carried out at temperatures higher than room temperature:

At the deposition temperature T_{dep} the Ge film is plastically relaxed by dislocations. Upon cooling to room temperature, Ge would shrink by a larger amount due to its larger thermal expansion coefficient than the Si substrate. Since the Ge film is attached to the Si substrate, though, it has to adopt to the lateral dimensions of the Si substrate that shrinks less when cooling to room temperature and as a result the Ge layer becomes tensilely strained.

2.2.4 Intermixing in Ge/Si heteroepitaxy

During growth of Ge on Si, Si atoms from the Si substrate can mix with the deposited Ge atoms. This is called intermixing or interdiffusion. Indeed, the wetting layer of the Stranski-Krastonov growth of Ge on Si is not composed of pure Ge. Intermixing may contribute in releasing small misfit strains in thin films.[89] Also during an annealing/postbake step there can be bulk diffusion of Ge and Si atoms leading to intermixing at the Ge/Si interface.

2.2.5 Growth techniques LEPECVD and RP-CVD

In general, the source material for the growth of epitaxial layers can be available in the solid, liquid, or gas phases. Different techniques for the layer deposition exist. In the course of this thesis we have already mentioned molecular beam epitaxy (MBE) and chemical vapor deposition (CVD), in both of which the epitaxial layer is deposited from a gas phase.

In this thesis samples are prepared by chemical-vapor deposition (CVD). Both low-energy plasma enhanced CVD (LEPECVD) and reduced-pressure CVD (RP-CVD) are utilized.

CVD is of comercial interest in the production of epitaxial layers, since CVD systems operating at atmospheric pressure (atmospheric-pressure CVD, APCVD) or reduced pressures in the range of 1 to 100 Torr are available (reduced-pressure CVD, RPCVD) and no ultra-high vacuum system is needed like it is in an MBE-reactor. A further difference between MBE and CVD is the source material: In MBE, the source material is present in its solid form and is evaporated in an effusion cell to form a beam of atoms. In CVD, gasous compounds of the material that shall be deposited (e. g., germane GeH_4 for Ge and silane SiH_4 for Si) serve as precursor gas. The precursors are deluted in a carrier gas N_2 or H_2.

In gas phase epitaxy the growth rate and layer thickness can be controlled by the gas flow of deposit material.

In chemical vapor deposition (CVD), the deposited material is hence produced in situ through a chemical reaction. FIG. 2-10 depicts the mechanism of epitaxial layer growth by a CVD system. The precursor gas, being a compound of the material to be deposited, enters the reactor through a gas inlet (step 1 in FIG. 2-10) and the gas flow brings it to the heated substrate (step 2). The precursor gas molecules adsorb to the substrate surface (3) and are decomposed due to the elevated substrate temperature (4). In the case of germanium growth with germane GeH_4 are precursor gas, the decomposition is given by the reaction equation

$$\mathrm{GeH_4} \xrightarrow{\text{heat}} \mathrm{Ge} + 2\mathrm{H_2}\uparrow$$

The single Ge atom can then move on the substrate surface by diffusion. The reaction byproduct is hydrogen H_2 which can be removed by the gas flow through the reactor. As we will discus in sec. 9.4, desorption of H_2 from the substrate depends on the substrate temperature.

The precursor gas for the growth of Si layers is silane SiH_4. In chapter 9 we are going to present phosphorous doped Ge layers grown on a Si substrate. The P-doping is achieved by co-deposition of P-atoms (in-situ doping) with phosphine PH_3 as precursor.

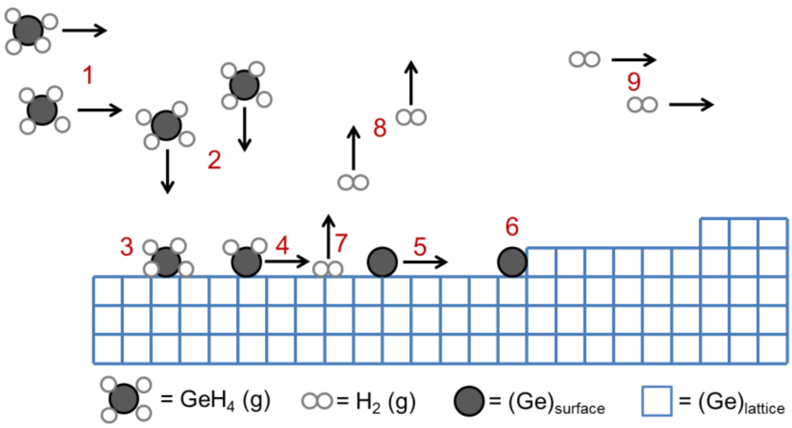

FIG. 2-10 Schematic illustration of the process steps occurring during the growth of thin films by chemical vapor deposition. Depicted is the growth of a germanium layer with GeH_4 as gaseous precursor. Steps 1 and 2 indicate the arrival of the precursor from the gas inlet, 3 is the adsorption to the growth surface. 4 presents the surface reaction that leads to the decomposition of GeH_4 in its elements Ge and H. 5 and 6 show surface diffusion of Ge atoms. 7 represents desorption of molecular hydrogen H_2 that is subsequently removed by the pump system (8 and 9). Figure adopted from Ref. [94].

LEPECVD

Low-energy plasma-enhanced chemical vapor deposition (LEPECVD) was used for all the samples featuring SiGe stressors on Ge and is a nonstandard growth technique described in detail in Refs. [95] and [96]. Worldwide there are only two reactors, both located at the LNESS institute in Como, Italy. It was developed with the aim of achieving high growth rates of Si, Ge, and SiGe. The main interest was in fast growth of thick SiGe buffer layers with gradually changing composition.
In this technique, the substrate is exposed to a high-density low-energy argon (Ar) plasma produced by an arc discharge with discharge voltage 30 V which is directed onto the substrate surface. The plasma energy is low enough to prevent damage of the sample surface by the impinging ions.

The precursor gas is introduced in the region of the plasma where it is decomposed into its constituents. Through this mechanism high growth rates of up to 10 nm/s can be achieved at temperatures as low as ~ 500 °C. The growth rate can thus be controlled by the plasma density, featuring a wide range of epitaxial growth rates independently of the substrate temperature in the range of 500–750 °C.[97]
High growth rates at comparably low temperatures (~ 500 °C) permits for out of equilibrium growth. As we have seen in 2.2.2, out of equilibrium conditions allow for metastable films in which dislocation nucleation is delayed. With LEPECVD record high thicknesses can be reached before the onset of plastic relaxation.[98]
The LEPECVD reactor is pumped to ultra-high vacuum (UHV) first, preventing contamination to the epitaxial film from the reactor, the pressure during growth being then in the order of 10^{-2} mbar.

The decomposition of the precursor gases in the plasma has got the additional advantage that the film composition, for example in the growth of SiGe, is strictly corresponding to the precursor gas mixture, whereas in a standard CVD process the decomposition of GeH_4 at the substrate surface is much faster than the SiH_4 decomposition due to the lower binding energy between surface-passivating hydrogen and germanium with respect to the Si case [97] and consequently Ge incorporation into the growing film is preferred.

We would like to end our excursus to LEPECVD by mentioning that the out of equilibrium growth with high growth rates is perfectly suited for the fabrication of vertical heterostructures on micrometer size Si pillar substrates, as shown for pure Ge “towers” in Ref. [99] and SiGe heterostructures in Ref. [100].

Reduced-pressure CVD

On the other hand, the samples in our doping optimization study, cf. sec. 9, were grown with a standard industrial RP-CVD system (ASM Epsilon-2000). There we are going to investigate the influences of the growth parameters deposition temperature, dopant flux, and postbake temperature on the PL intensity from Ge on Si layers.

The pressure in a RP-CVD reactor is sub-atmospheric and ranges from ~1-100 Torr. Are pressures in the mTorr range, the different technique of low-pressure CVD (LPCVD) is concerned.
The reduced pressures help to promote the reactions that take place at the sample surface and suppress unwanted reactions in the gas-phase that may lead to solid particles. In this way, the quality of the epitaxial film can be enhanced.
In contrast to CVD performed at atmospheric pressure (atmospheric pressure CVD, APCVD), the epilayer growth rate is limited by the surface reaction and not by the mass transport of material to be deposited, leading to uniform film thickness throughout the wafer. This allows furthermore to load the wafers laterally (and not horizontally as in APCVD).

In chapters 9 and 10 we are going to present germanium grown selectively on Si in SiO_2 windows with RP-CVD. To enable high phosphorous doping, growth temperature is in the range of 325 °C to 425 °C. To process Ge growth without assisting plasma to enable the dissociation of the precursor gas, the hydrogen termination of the Si substrate surface has to be removed by a prebake. The H-free Si surface is reactive so that GeH_4 can react on it. During further growth of the Ge epilayer, hydrogen desorption from the Ge surface starts from 300 °C on so that a reaction of GeH_4 on the Ge surface is also possible.

A typical deposition rate for epitaxial Si at ~ 1000 °C is ~ 100 nm/min [101] which is about one order less than the growth rates achieved with LEPECVD at twice the temperature.

2.3 Effect of strain

Before describing the effect of strain on the phononic and electronic band structure of a semiconductor, we will give a few notions on linear elasticity theory.

2.3.1 What is strain?

Mechanical stress σ is the force $\vec{F}$ per area A perpendicular to the direction of $\vec{F}$ acting on a body and causing its mechanical deformation. The stress can be tensile or compressive, depending on the direction of $\vec{F}$. The dimension of stress is N/cm^2 or Pa. The deformation ϵ caused by the stress is linked to the strain ε. In the following we apply the basic assumption of linear elasticity theory, that is, for small strain values the deformation of the body is elastic and within the elastic regime, i. e. the body relaxes to its original shape when the stress is released. In this regime, stress and strain are linearly dependent.

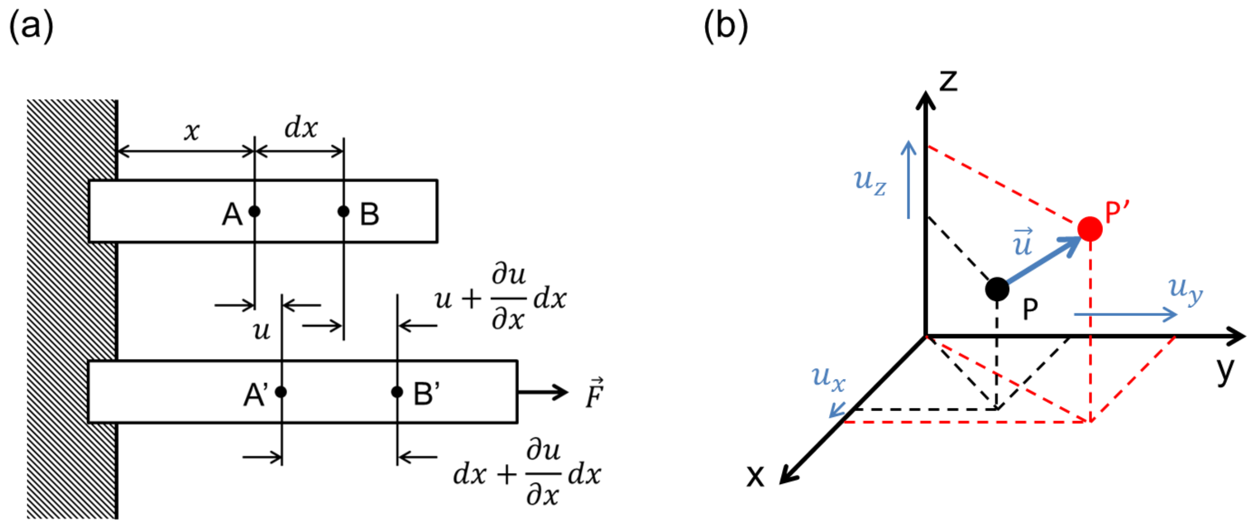

FIG. 2-11 (a) A force $\vec{F}$ acting on a rod and causing one-dimensional strain. (b) In a three-dimensional case point P in the unstrained state is shifted to point P' under strain. The displacement $\vec{u}$ is indicated.

Let us consider a rod that is uniformly elongated in one direction, see FIG. 2-11 (a). Point A in the original unstrained state is at distance x from the suspension, B is at x + dx. Under elongation, A is shifted by u to A'. Since the elongation is uniform, i. e. it is a linear function of the distance from the suspension, the shift from B to B' amounts to u $+ \frac{\partial u}{\partial x}$dx.

The deformation ϵ_x inside the rod can be expressed as the relative length change between points A and B:

$$\epsilon_x = \frac{\Delta L}{L} = \frac{\text{A'B'}-\text{AB}}{\text{AB}} = \frac{dx+\frac{\partial u}{\partial x}\text{dx}-\text{dx}}{dx} = \frac{\partial u}{\partial x} \qquad (2\text{-}2)$$

For the displacement u we obtain ∂u $= \epsilon_x$ ∂x.

We can generalize the displacement for a point P in an unstrained body to P‘ inside the strained body. This give a displacement vector u(x,y,z) with

$$\begin{aligned} \partial \mathrm{u_x} &= \epsilon_{\mathrm{xx}}\,\partial \mathrm{x} + \epsilon_{\mathrm{xy}}\,\partial \mathrm{y} + \epsilon_{\mathrm{xz}}\,\partial \mathrm{z} \\ \partial \mathrm{u_y} &= \epsilon_{\mathrm{yx}}\,\partial \mathrm{x} + \epsilon_{\mathrm{yy}}\,\partial \mathrm{y} + \epsilon_{\mathrm{yz}}\,\partial \mathrm{z} \\ \partial \mathrm{u_z} &= \epsilon_{\mathrm{zx}}\,\partial \mathrm{x} + \epsilon_{\mathrm{zy}}\,\partial \mathrm{y} + \epsilon_{\mathrm{zz}}\,\partial \mathrm{z} \end{aligned} \tag{2-3}$$

We can summarize to $\partial u_i = \epsilon_{ij}\partial x_j$ or $\epsilon_{ij} = \frac{\partial u_i}{\partial x_j}$. ϵ_{ij} are the coefficients of the deformation matrix that can be expanded into

$$\epsilon_{ij} = \frac{1}{2}\left(\epsilon_{ij} + \epsilon_{ji}\right) + \frac{1}{2}\left(\epsilon_{ij} - \epsilon_{ji}\right) \tag{2-4}$$

or

$$\epsilon_{ij} = \varepsilon_{ij} + \omega_{ij} \tag{2-5}$$

where $\varepsilon_{ij} = \frac{1}{2}\left(\frac{\partial u_i}{\partial x_j} + \frac{\partial u_j}{\partial x_i}\right)$ is the *strain tensor* and $\omega_{ij} = \frac{1}{2}\left(\frac{\partial u_i}{\partial x_j} - \frac{\partial u_j}{\partial x_i}\right)$ is the *rotation tensor*. These are second rank tensors, whereby ε_{ij} is a symmetric tensor and ω_{ij} is an antisymmetric tensor; the leading diagonal of ω_{ij} is always zero. The symmetry of the strain tensor results in no net momentum, e. g. translation or rotation of the body.

In the following we consider only the strain tensor, because in the samples investigated here no rotation is present. The diagonal terms represent the fractional change in length of volume elements along the axes *x*, *y*, and *z*, respectively, and are given by:

$$\varepsilon_{xx} = \frac{\partial u_x}{\partial x},\ \varepsilon_{yy} = \frac{\partial u_y}{\partial y},\ \text{and } \varepsilon_{zz} = \frac{\partial u_z}{\partial z} \tag{2-6}$$

The off-diagonal elements of the strain tensor constitute the *shear strains*:

$$\begin{aligned} \varepsilon_{xy} = \varepsilon_{yx} &= \frac{1}{2}\cdot\left(\frac{\partial u_x}{\partial y} + \frac{\partial u_y}{\partial x}\right), \\ \varepsilon_{yz} = \varepsilon_{zy} &= \frac{1}{2}\cdot\left(\frac{\partial u_y}{\partial z} + \frac{\partial u_z}{\partial y}\right), \\ \varepsilon_{zx} = \varepsilon_{xz} &= \frac{1}{2}\cdot\left(\frac{\partial u_z}{\partial x} + \frac{\partial u_x}{\partial z}\right). \end{aligned} \tag{2-7}$$

Within linear theory, we assume that the magnitude of all strain coefficients to be much smaller than unity, i. e. $\varepsilon_{ij} \ll 1$. The physical meaning of the shear strains is illustrated in FIG. 2-12, depicting a 2D case.

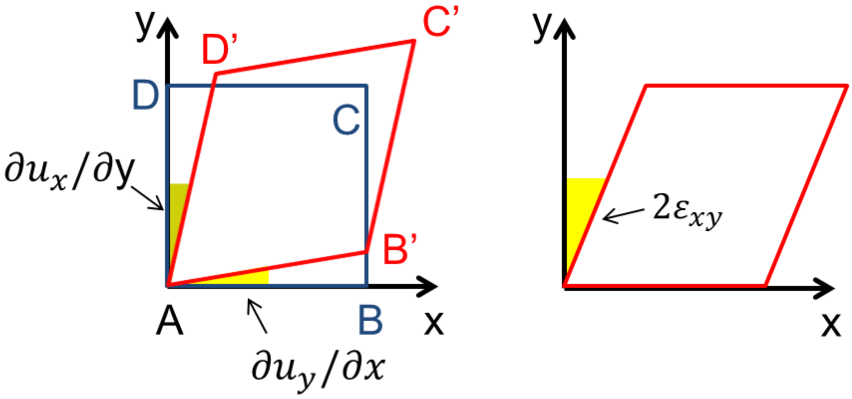

FIG. 2-12 Illustration of the action of shear strain. The shape of the body is deformed, but its volume is maintained.

The rectangle *ABCD* in the *xy* plane was strained into the shape *AB'C'D'*, thereby the original right angle between the sides *AB* and *AD* is decreased by $2 \cdot \varepsilon_{xy}$. The application of strain did not lead to a change in area. By rotating the rhombus *AB'C'D'* around point ***A***, it is seen that it has undergone a simple shear of $2 \cdot \varepsilon_{xy}$.

Also the stress can be expressed as a second rank tensor and be written in matrix form:

$$\sigma = \begin{pmatrix} \sigma_{xx} & \sigma_{xy} & \sigma_{xz} \\ \sigma_{yx} & \sigma_{yy} & \sigma_{yz} \\ \sigma_{zx} & \sigma_{zy} & \sigma_{zz} \end{pmatrix} \tag{2-8}$$

The stress tensor has to be symmetric to have no net momentum that would lead to a macroscopic movement of the body (translation and rotation): $\sigma_{ij} = \sigma_{ji}$. The single components of the stress tensor and their respective directions are illustrated in FIG. 2-13.

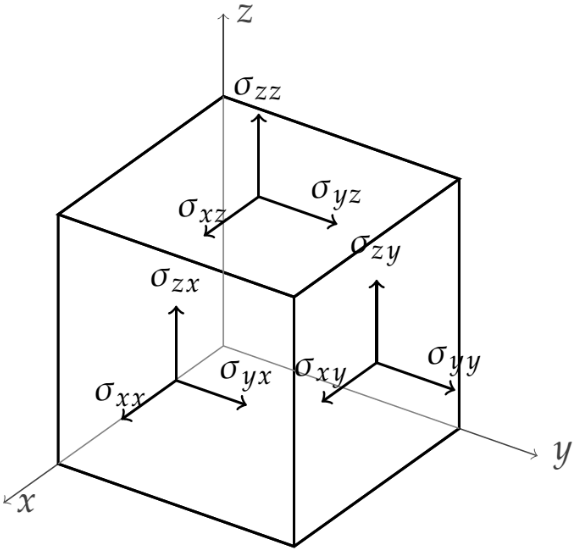

FIG. 2-13 Illustration of the components of the stress tensor. The different components act on the surface of a cube along a certain direction. Stress tensor components with directions parallel to a surface result in shear strain.

The relationship between the second rank tensors stress σ and strain ε is then given by a fourth rank tensor, the *compliance tensor* $\underline{S}$:

$$\underline{\varepsilon} = \underline{S} \cdot \underline{\sigma} \text{ or } \varepsilon_{ij} = S_{ijkl}\sigma_{kl} \tag{2-9}$$

The forth rank tensor has got 9 × 9 terms. However, both stress $\underline{\sigma}$ and strain $\underline{\varepsilon}$ are symmetric tensors with only six independent terms, each. This reduces the number of independent terms in $\underline{S}$ from 81 to 36.
These 36 components can be written in Voigt notation as a 6 × 6 matrix. Because of considerations about the energy related to strain, it is found that this 6 × 6 has to be symmetric, too, and the number of independent terms is reduced to 21.

In case there is symmetry also in the material being deformed, the number of coefficients is even further reduced. In the simplest anisotropic case, that of cubic symmetry – like the crystal lattice of silicon and germanium – only three independent elements remain. In the Voigt notation we can write:

$$\begin{bmatrix} \varepsilon_{xx} \\ \varepsilon_{yy} \\ \varepsilon_{zz} \\ 2\varepsilon_{yz} \\ 2\varepsilon_{zx} \\ 2\varepsilon_{xy} \end{bmatrix} = \begin{bmatrix} S_{11} S_{12} S_{12} & 0 & 0 & 0 \\ S_{12} S_{11} S_{12} & 0 & 0 & 0 \\ S_{12} S_{12} S_{11} & 0 & 0 & 0 \\ 0 \;\; 0 \;\; 0 & S_{44} & 0 & 0 \\ 0 \;\; 0 \;\; 0 & 0 & S_{44} & 0 \\ 0 \;\; 0 \;\; 0 & 0 & 0 & S_{44} \end{bmatrix} \cdot \begin{bmatrix} \sigma_{xx} \\ \sigma_{yy} \\ \sigma_{zz} \\ \sigma_{yz} \\ \sigma_{zx} \\ \sigma_{xy} \end{bmatrix} \qquad (2\text{-}10)$$

In the case of an isotropic material, i. e. a material that behaves the same in any orientation, the matrix relationship simplifies further and there are only two independent quantities left. All coefficients may be expressed using Young's modulus *E*, and the shear modulus *G*, or alternatively *E* and Poisson's ratio ν. The following relations are established:

$$\mathrm{S}_{11} = 1/\mathrm{E}, \text{ and} \qquad (2\text{-}11)$$

$$\mathrm{S}_{44} = 2(\mathrm{S}_{11} - \mathrm{S}_{12}) = \frac{1}{\mathrm{G}}, \qquad (2\text{-}12)$$

or alternatively, using Poisson's ratio ν,

$$\mathrm{S}_{12} = -\frac{\nu}{E}, \qquad (2\text{-}13)$$

$$\text{so that } \nu = \frac{\mathrm{E}}{2\mathrm{G}} - 1. \qquad (2\text{-}14)$$

The stress/strain relations becomes

$$\begin{bmatrix} \varepsilon_{xx} \\ \varepsilon_{yy} \\ \varepsilon_{zz} \\ 2\varepsilon_{yz} \\ 2\varepsilon_{zx} \\ 2\varepsilon_{xy} \end{bmatrix} = \frac{1}{E} \begin{bmatrix} 1 & -\nu & -\nu & 0 & 0 & 0 \\ -\nu & 1 & -\nu & 0 & 0 & 0 \\ -\nu & -\nu & 1 & 0 & 0 & 0 \\ 0 & 0 & 0 & 2+2\nu & 0 & 0 \\ 0 & 0 & 0 & 0 & 2+2\nu & 0 \\ 0 & 0 & 0 & 0 & 0 & 2+2\nu \end{bmatrix} \cdot \begin{bmatrix} \sigma_{xx} \\ \sigma_{yy} \\ \sigma_{zz} \\ \sigma_{yz} \\ \sigma_{zx} \\ \sigma_{xy} \end{bmatrix} \qquad (2\text{-}15)$$

Using above equation and considering the case of a normal strain, e. g. along axis *x*, the relation between the applied stress σ_{xx} and the resulting strain ε_{xx} parallel to the stress, is given by Hooke's law $\sigma_{xx} = E\varepsilon_{xx}$. Considering a real 3D material, one finds a contraction for the perpendicular directions *y* and *z* which is proportional to ε_{xx}:

$$\varepsilon_{yy} = -\nu \cdot \varepsilon_{xx} \text{ and } \varepsilon_{zz} = -\nu \cdot \varepsilon_{xx}. \qquad (2\text{-}16)$$

The Poisson ratio ν hence relates the strain parallel and perpendicular to the axis of applied stress:

$$\nu = -\varepsilon_{\perp}/\varepsilon_{\parallel} \qquad (2\text{-}17)$$

Cerdeira et al. [102] give values for the elements of the *compliance tensor* $\underline{S}$ for germanium:

$S_{11} = 0.973 \cdot 10^{-12} \frac{\mathrm{cm}^2}{\mathrm{dyn}}$,

$S_{12} = -0.267 \cdot 10^{-12} \frac{\text{cm}^2}{\text{dyn}}$, and

$S_{44} = 1.49 \cdot 10^{-12} \frac{\text{cm}^2}{\text{dyn}}$.

The inverse relation of Eq. (2-9), linking the stress to the observed strain, is, written in Voigt notation as

$$\begin{bmatrix} \sigma_{xx} \\ \sigma_{yy} \\ \sigma_{zz} \\ \sigma_{yz} \\ \sigma_{zx} \\ \sigma_{xy} \end{bmatrix} = \begin{bmatrix} C_{11} & C_{12} & C_{12} & 0 & 0 & 0 \\ C_{12} & C_{11} & C_{12} & 0 & 0 & 0 \\ C_{12} & C_{12} & C_{11} & 0 & 0 & 0 \\ 0 & 0 & 0 & (C_{11} - C_{12})/2 & 0 & 0 \\ 0 & 0 & 0 & 0 & (C_{11} - C_{12})/2 & 0 \\ 0 & 0 & 0 & 0 & 0 & (C_{11} - C_{12})/2 \end{bmatrix} \cdot \begin{bmatrix} \varepsilon_{xx} \\ \varepsilon_{yy} \\ \varepsilon_{zz} \\ 2\varepsilon_{yz} \\ 2\varepsilon_{zx} \\ 2\varepsilon_{xy} \end{bmatrix}, \qquad (\text{ 2-18 })$$

where $\underline{C}$ is the *elasticity tensor* or *stiffness tensor*, with $\underline{S} = \underline{C}^{-1}$, and $C_{44} = (C_{11} - C_{12})/2$. The stiffness tensor elements C_{11}, C_{12}, and C_{44} are linked to the compliance tensor elements S_{11} and S_{12} through

$$C_{11} = \frac{S_{11}+S_{12}}{(S_{11}-S_{12})(S_{11}+2S_{12})}, \qquad (\text{ 2-19 })$$

$$C_{12} = -\frac{S_{12}}{(S_{11}-S_{12})(S_{11}+2S_{12})}, \text{ and} \qquad (\text{ 2-20 })$$

$$C_{44} = \frac{1}{S_{44}} \qquad (\text{ 2-21 })$$

Values for the stiffness tensor elements for germanium can be found in Ref. [73], for example.

The volume V of a small volume element of the deformed body is changed by the strain to

$$V + \Delta V = V \cdot (1 + \varepsilon_{xx}) \cdot \left(1 + \varepsilon_{yy}\right) \cdot (1 + \varepsilon_{zz})$$

The fractional change in volume is the dilatation Δ:

$$\Delta = \frac{\Delta V}{V} \cong \varepsilon_{xx} + \varepsilon_{yy} + \varepsilon_{zz}$$

which is the trace of the strain tensor.

In the discussion of the effect of strain on the phonon frequencies and energy levels, we will see that it is useful to decompose any stress tensor into two parts, leading to the concepts of hydrostatic pressure (strain) and deviatoric stress. The hydrostatic component conserves the geometrical shape of the body but changes its volume. The deviatoric stress changes the shape of the body, but its volume change equals zero. The hydrostatic pressure is also called mean stress tensor (σ_m) that contains only pure tension or compression:

$$\begin{pmatrix} \sigma_{xx} & \sigma_{xy} & \sigma_{xz} \\ \sigma_{yx} & \sigma_{yy} & \sigma_{yz} \\ \sigma_{zx} & \sigma_{zy} & \sigma_{zz} \end{pmatrix} = \begin{pmatrix} (\sigma_{xx} - p) & \sigma_{xy} & \sigma_{xz} \\ \sigma_{yx} & (\sigma_{yy} - p) & \sigma_{yz} \\ \sigma_{zx} & \sigma_{zy} & (\sigma_{zz} - p) \end{pmatrix} + \begin{pmatrix} p & 0 & 0 \\ 0 & p & 0 \\ 0 & 0 & p \end{pmatrix} \qquad (2\text{-}22)$$

where $p = \frac{1}{3}\left(\sigma_{xx} + \sigma_{yy} + \sigma_{zz}\right)$. Above expression can also be written using the Kronecker delta notation as $\sigma_{ij} = \sigma_{ij}^{\mathrm{dev}} + \sigma_{ij}^{\mathrm{hyd}} = \sigma_{ij}^{\mathrm{dev}} + p\delta_{ij}$.

2.3.2 Strain-induced change of phonon frequencies

Strain changes the distances between atoms in a crystal lattice and hence their bonding strengths, thus changing the frequency of lattice vibration. Cerdeira et al., Ref. [102], discuss the stress-induced shifts of optical phonons at wavevector $k = 0$, that – as we will see in sec. 3 – play an important role in Raman spectroscopy. For the sake of completeness, we will recall the main arguments of Cerdeira et al. here:

In a cubic lattice, the optical phonons are triply degenerate at $k = 0$ (longitudinal and two transversal optical phonons). For a diamond-type material with two atoms in the unit cell, the dynamical equations in presence of strain have the form

$$\mathrm{\bar{m}\ddot{u}_i} = -\sum\nolimits_{\mathrm{k}} \mathrm{K_{ik}u_k} = -\left(\mathrm{K_{ii}^{(0)}u_i} + \sum\nolimits_{\mathrm{klm}} \frac{\partial \mathrm{K_{ik}}}{\partial \varepsilon_{\mathrm{lm}}} \varepsilon_{\mathrm{lm}} \mathrm{u_k}\right) \qquad (2\text{-}23)$$

where the indices *i*, *k*, *l*, and *m* refer to *x*, *y* or *z*, the axes of the coordinate system.[102] The following parameters occur in the above equation:

- $\mathrm{u_i}$: i-th component of the relative displacement of the two atoms in the unit cell;
- $\bar{m}$: reduced mass of the two atoms in the unit cell;
- $K_{ii}^{(0)} = \bar{m}\omega_0^2$: effective spring constant in the absence of strain;
- $\frac{\partial K_{ik}}{\partial \varepsilon_{lm}} \varepsilon_{lm} = K_{iklm}^{(1)} \varepsilon_{lm} = K_{ikml}^{(1)} \varepsilon_{ml} = K_{kilm}^{(1)} \varepsilon_{lm} = K_{kiml}^{(1)} \varepsilon_{ml}$: change in spring constant due to an applied strain ε_{lm};

Like stated above, the strain influences the bonding between atoms, which is represented by the change in spring constant in the dynamical equation, Eq. (2-23). In a cubic crystal the tensor $K^{(1)}$ has only got three independent components due to thermodynamic and symmetry considerations. In a coordinate system with $\hat{x} = 1 = [100]$, $\hat{y} = 2 = [010]$, and $\hat{z} = 3 = [001]$ these are:

$$K_{1111}^{(1)} = K_{2222}^{(1)} = K_{3333}^{(1)} = \bar{m}p,$$

$$K_{1122}^{(1)} = K_{2233}^{(1)} = K_{1133}^{(1)} = K_{2211}^{(1)} = K_{3322}^{(1)} = K_{3311}^{(1)} = \bar{m}q, \text{ and} \qquad (2\text{-}24)$$

$$K_{1212}^{(1)} = K_{2323}^{(1)} = K_{1313}^{(1)} = K_{2121}^{(1)} = K_{3232}^{(1)} = K_{3131}^{(1)} = \bar{m}r$$

The coefficients *p*, *q*, and *r* are called *deformation potentials* and describe the changes in the “spring constant” of the $\vec{k} \approx 0$ optical phonons with strain ε.

Eq. (2-23) constitutes a homogeneous linear differential equation system:

$$\bar{m}\begin{pmatrix}\ddot{u}_1\\ \ddot{u}_2\\ \ddot{u}_3\end{pmatrix} = A \cdot \begin{pmatrix}u_1\\ u_2\\ u_3\end{pmatrix} \qquad (\text{ 2-25 })$$

which can be solved with the eigenvalues and eigenvectors of the Matrix A:

$$A = -\bar{m} \cdot \begin{pmatrix} \frac{K_{11}^{(0)}}{\bar{m}} + p\varepsilon_{11} + q\varepsilon_{22} + q\varepsilon_{33} & r\varepsilon_{12} + r\varepsilon_{21} & r\varepsilon_{13} + r\varepsilon_{31} \\ r\varepsilon_{12} + r\varepsilon_{21} & \frac{K_{22}^{(0)}}{\bar{m}} + p\varepsilon_{22} + q\varepsilon_{11} + q\varepsilon_{33} & r\varepsilon_{23} + r\varepsilon_{32} \\ r\varepsilon_{13} + r\varepsilon_{31} & r\varepsilon_{23} + r\varepsilon_{32} & \frac{K_{11}^{(0)}}{\bar{m}} + p\varepsilon_{11} + q\varepsilon_{22} + q\varepsilon_{33} \end{pmatrix} \qquad (\text{ 2-26 })$$

The characteristic equation is

$$\det(A - \lambda \cdot E) = 0 = \begin{vmatrix} p\varepsilon_{11} + q\varepsilon_{22} + q\varepsilon_{33} + \frac{K_{11}^{(0)}}{\bar{m}} - \lambda & \\ & \ddots & \\ \cdots & & \ddots \end{vmatrix} \qquad (\text{ 2-27 })$$

Under the simplifying assumption that the shear strain values ε_{ij} with $i \neq j$ are equal to zero, the characteristic equation reduces to

$$\left(p\varepsilon_{11} + q\varepsilon_{22} + q\varepsilon_{33} + \frac{K_{11}^{(0)}}{\bar{m}} - \lambda\right) \cdot \left(p\varepsilon_{22} + q\varepsilon_{33} + q\varepsilon_{11} + \frac{K_{22}^{(0)}}{\bar{m}} - \lambda\right) \cdot \left(p\varepsilon_{33} + q\varepsilon_{11} + q\varepsilon_{22} + \frac{K_{33}^{(0)}}{\bar{m}} - \lambda\right) = 0 \qquad (\text{ 2-28 })$$

This condition is fulfilled if any of the three factors equals zero; for the third factor one obtains

$$p\varepsilon_{33} + q\varepsilon_{11} + q\varepsilon_{22} + \frac{K_{33}^{(0)}}{\bar{m}} - \lambda_3 = 0 \qquad (\text{ 2-29 })$$

with λ_3 the third eigenvalue. The eigenvalues can be identified with the square of the phonon frequency under strain, ω^2, and $\frac{K_{33}^{(0)}}{\bar{m}} = {\omega_0}^2$ is the frequency without strain. The above equation becomes

$$p\varepsilon_{33} + q\varepsilon_{11} + q\varepsilon_{22} + {\omega_0}^2 = \omega^2 \qquad (\text{ 2-30 })$$

and solving for ω

$$\sqrt{\left(\frac{p\varepsilon_{33} + q\varepsilon_{11} + q\varepsilon_{22}}{{\omega_0}^2} + 1\right)} \cdot \omega_0 = \omega \qquad (\text{ 2-31 })$$

Using the approximation $\sqrt{x+1} \approx 1 + \frac{1}{2}x, x \ll 1$ we get

$$\left(1+\frac{1}{2}\cdot\frac{p\varepsilon_{33}+q\varepsilon_{11}+q\varepsilon_{22}}{{\omega_0}^2}\right)\cdot\omega_0=\omega \tag{2-32}$$

or

$$\omega=\omega_0+\frac{1}{2\omega_0}\cdot(p\varepsilon_{33}+q\varepsilon_{11}+q\varepsilon_{22}). \tag{2-33}$$

As we will see in sec. 3.3, p, q, and r are negative values, hence a positive strain, i. e. a tensile strain, decreases the phonon frequency under strain, ω, with respect to ω_0. In Raman spectroscopy, we can relate the inelastic scattering of a photon to the phonon frequency. The eigenvector corresponding to λ_3 is parallel to direction i = 3. With a sample orientation $\hat{x}$ = [100], $\hat{y}$ = [010], and $\hat{z}$ = [001] and an experimental geometry with excitation and collection along $\hat{z}$, the above equation is that for the longitudinal-optical (LO) phonon.

We would like to point out the following: As discussed, the k = 0 optical phonons are triply degenerate in a material with diamond lattice. The application of a uniaxial stress along any direction breaks the cubic symmetry of the lattice and lifts the degeneracy of the triplet. As we have seen at the beginning of this section in Eq. (2-22), any stress tensor can be decomposed into a hydrostatic pressure and deviatoric stress, see sec. 2.3.1. Hence, in applying uniaxial strain to a semiconductor crystal, there is a shift of phonon frequency due to the hydrostatic pressure and a split of the degenerate triplet into a singlet and a doublet. This situation is depicted in FIG. 2-14.

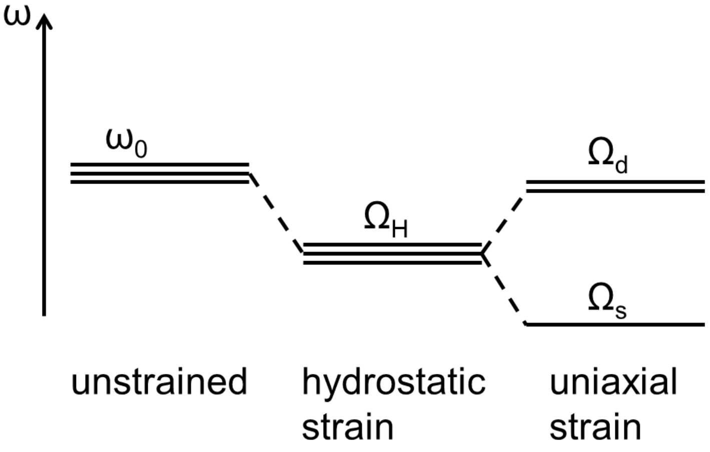

FIG. 2-14 Shift of the phonon frequencies of triply degenerate phonons due to hydrostatic strain and splitting of the degeneracy due to uniaxial strain.

2.3.3 Strain-induced change in the electronic band structure

The band structure, i. e. the energy dispersion in momentum space, is related to the arrangement of atoms in real space. On this note, the Schrödinger equation for an electron in the crystal contains a periodic potential related to the positions of the atoms in the crystal and its solution, the Bloch waves have also the periodicity of the lattice. Hence, a deformation of the crystal lattice and consequently the change of position of the atoms affects the energy band structure of the crystal.

Maybe the most common approach to describe the effect of strain on the band structure is the use of deformation potentials with which the energy shifts at symmetry points of the Brillouin zone can be calculated. The concept of deformation potentials was introduced by Bardeen and Shockley.[103] At the end of the 1980’s and in the 1990’s it was used to calculated the band alignment of semiconductor hetero-structures (see for example Refs. [104, 105]) or to calculate carrier mobilities of strained semiconductors (Ref. [106]). In the following we want to list the equations for the band edge energies in the symmetry points important for germanium as used by El Kurdi et al. [107] and in the recent work by Guilloy et al. [108]:

$$\delta E_{c\Gamma} = a_{c,dir}\mathrm{Tr}(\varepsilon) \tag{2-34}$$

$$\delta E_{cL} = \left(\Xi_d + \frac{1}{3}\Xi_u\right)\mathrm{Tr}(\varepsilon) \tag{2-35}$$

$$\delta E_{vLH} = a_v Tr(\varepsilon) - \frac{1}{6}\Delta_0 + \frac{1}{4}\delta E_v + \frac{1}{2}\sqrt{\Delta_0{}^2 + \Delta_0\delta E_v + \frac{9}{4}\delta E_v{}^2} \tag{2-36}$$

$$\delta E_{vHH} = a_v Tr(\varepsilon) - \frac{1}{3}\Delta_0 + \frac{1}{2}\delta E_v \tag{2-37}$$

using $\delta E_v = 2b\left(\varepsilon_\perp - \varepsilon_{||}\right)$.

$a_{c,dir}$, Ξ_d, Ξ_u, and b are deformation potentials, Δ_0 is the spin-orbit splitting energy, $\varepsilon_{||}$ and $\varepsilon_\perp$ are the strains parallel to the stress direction and perpendicular to the stress, respectively.

$\delta E_{c\Gamma}$ corresponds to the shift of the Γ valley conduction band edge, δE_{cL} to the energy shift in point L of the conduction band. δE_{vLH} and δE_{vHH} are the energy shifts of the light hole band and the heavy hole band, respectively. Note, that for zero strain, these bands are degenerate and the two formulae give the same value. Upon application of strain, the valence band degeneracy is broken and the light hole band (LH) and heavy hole band (HH) are split into separate energy levels.

Again, like in the case of the phonon frequencies, we find that the effect of strain can be divided into two contributions on the band edge energies. A mean energy shift due to the hydrostatic component of the stress and a split of energy bands due to breaking the symmetries, see FIG. 2-15.

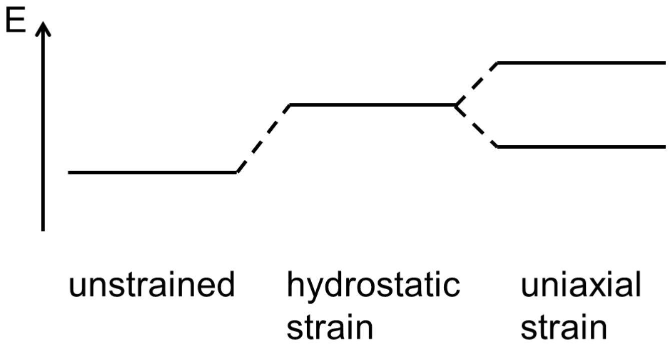

FIG. 2-15 Illustration of the effect of hydrostatic and deviatoric strain on a doubly degenerated energy band. For instance, the degenerate light hole (LH) and heavy hole (HH) bands are split in two energy levels in strained germanium.

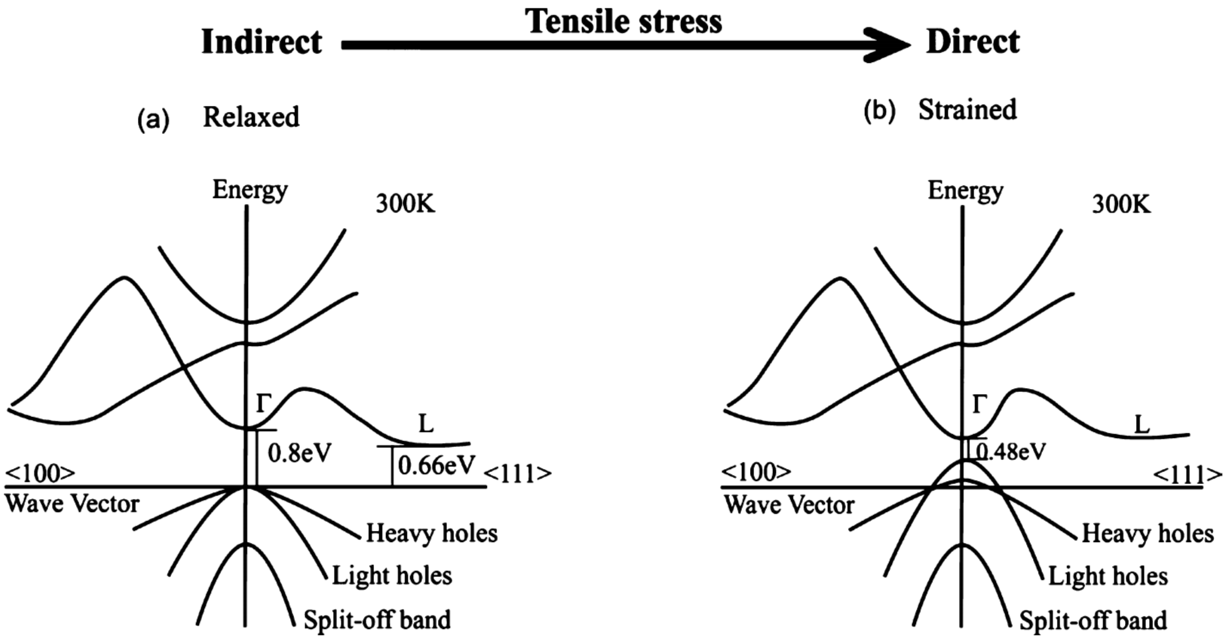

FIG. 2-16 Effect of (001) in-plane tensile strain on the band structure of germanium. (a) Relaxed germanium. (b) Strained germanium. The energy difference between the L and Γ conduction band valleys, $\Delta E_{\Gamma L}$, is reduced, and Ge becomes a direct gap material eventually. Boztug et al. calculated an in-plane strain $\varepsilon_{||} = 1.9\%$ for the indirect/direct gap transition. The degeneracy of light hole (LH) and heavy hole (HH) valence bands is lifted. The direct bandgap energy is reduced from 0.8 eV in the unstrained case to 0.48 eV under strain. Figure taken from Boztug et al., Ref. [109].

Boztug et al. [44, 109] discuss the case of biaxial tensile strain in Ge in a {100} plane. In FIG. 2-16 we replot one of their figures to illustrate the effect of strain on the Ge band structure. The direct energy bandgap is lowered relative to the indirect bandgap. Thereby, the energy difference from the Γ conduction band to the L conduction band valleys, $\Delta E_{\Gamma L}$ is reduced. At a strain of about 1.9% Ge is transformed into a direct-bandgap material.
The degeneracy of the light hole (LH) and heavy hole (HH) bands is broken, resulting in a LH valence band edge. Moreover, all band edge energies are shifted toward the bandgap center resulting in a smaller bandgap energy. The direct bandgap of the strained material is reduced considerably from 0.8 eV to 0.48 eV at the indirect/direct gap transition.[109]

Due to the reduction of the barrier between L and Γ, $\Delta E_{\Gamma L}$, population of the Γ valley is facilitated. The excess carrier density to reach population inversion (transparency) is decreased and optical gain becomes obtainable.

As seen in FIG. 2-16, tensile strain lifts the LH band above the HH band. Hence, at high tensile strain most of the holes created in the valence band thermalize into the LH band.[44] Photons emitted from recombination to the LH band in strained Ge have predominantly got a linear polarization perpendicular to the plane of the biaxially strained layer (transverse magnetic (TM)).[29, 109] On the other hand, the polarization of photons recombining with holes from the HH band are exclusively linearly polarized in the direction parallel to the plane of the biaxially strained layer (transverse electric (TE)).[109]

The TM polarized luminescence propagates in plane of the Ge layer. A standard geometry for photo-luminescence experiments is a backscattering configuration with the Ge surface perpendicular to the excitation and collection path. Consequently, the TM polarized luminescence cannot be collected in these measurements. The experimental direct gap luminescence band is hence dominated by the recombination to the HH band (Γ_c → HH).

In fact, the tensile strain can cause an anti-crossing of the hole states, that is, bands mix and the LH band is energetically higher than the HH band for all wavenumbers as depicted in FIG. 2-17. Vitiello et al. [110] could observe a dominating light hole contribution in the room temperature direct gap PL of p-type doped Ge featuring only low tensile strain of about ~ 0.2% and could resolve the Γ_c → LH transition also for intrinsic and n-type Ge at low temperatures by analyzing the circular polarization of the direct gap emission. With increasing temperature, the hole quasi-Fermi level E_{Fv} is pushed toward lower energies and the contribution of the recombination with the heavy holes (HH) increases, so that direct gap emission from intrinsic and n-type material is dominated by Γ_c → LH at room temperature.

The fact that the LH band is lifted above the HH band and the resulting importance of radiative recombination to the LH band in Ge under tensile strain has got another important effect for Ge as gain material. Since the LH density of states (DOS) is low, the effective DOS of strained Ge is reduced so that the quasi-Fermi levels can be changed more quickly which allows to reach population inversion more easily.[29, 109] As a matter of fact, the LH and Γ_c effective masses can be compared with those of III-V compound semiconductors which are known as very efficient light emitters.[109]

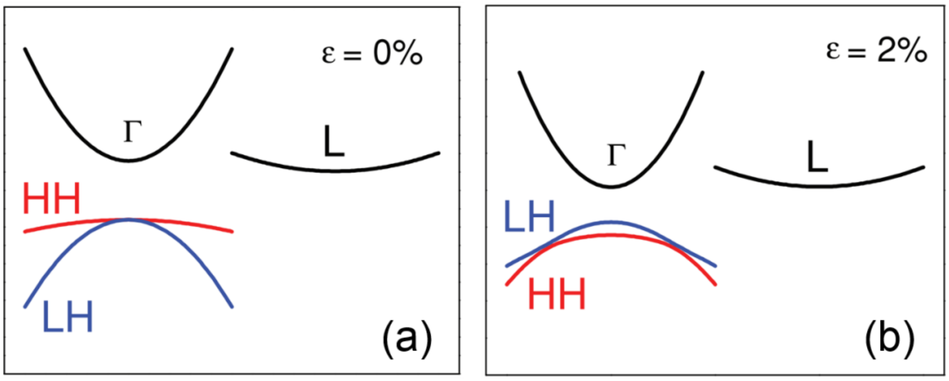

FIG. 2-17 Schematic representations of the electronic band structure of germanium. (a) relaxed Ge with L as conduction band minimum and degenerate light-hole and valence hole bands. (b) Ge under tensile strain. As discussed in FIG. 2-16, the light hole (LH)/heavy hole (HH) degeneracy is lifted. However, LH and HH bands do not cross (anti-crossing). Figure taken from Ref. [44].

In general, the effect of strain on the band structure depends on the direction of strain with respect to the crystal orientation. To discuss the different cases, we rely on the work of Liu et al. [111] and replot in our FIG. 2-18 their Figs. 2 and 3. Liu et al. calculated the change in the Ge band structure in different biaxial and uniaxial tensile strain configurations. To do so, they used density functional theory (DFT). The biaxial cases treated are biaxial in-plane strain in the (001), (110), and (111) planes and the results of Liu et al. regarding the direct and indirect band gap (denominated in the figure as E_g^{Γ} and E_g^{L}, respectively) are shown in the left hand panel of FIG. 2-18. The panel on the right hand side shows their results obtained for the uniaxial cases with strain along the [001], [110], and [111] directions.

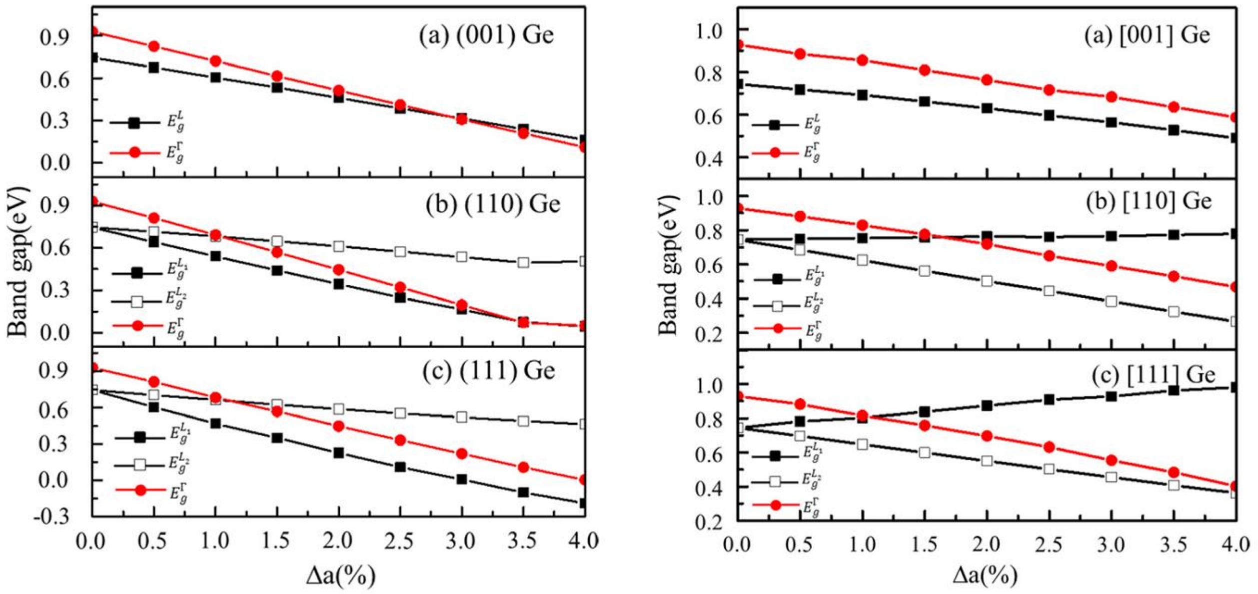

FIG. 2-18 Band gap energies in germanium for the direct gap E_g^Γ and the indirect gap E_g^L in function of the strain Δa(%) of the material. The left-hand panels show calculations for biaxial strain in the lattice planes (a) (001), (b) (110), and (c) (111). Right-hand panels present calculations for uniaxial strain along the crystallographic directions (a) [011], (b) [110], and (c) [111]. For appropriate strain configurations a reduction in the energy difference $E_g^\Gamma - E_g^L$ and eventually a crossover of the direct and indirect gap are observed. Ge becomes a direct gap semiconductor. Figure taken from Liu et al., Ref. [111].

In cases that are favorable for our application, namely to lower the energy barrier between the L and the Γ valleys, the conduction band edge in point Γ is shifted toward lower energies with increasing strain. This happens more quickly than for the conduction band edge in L so that (1) the energy difference between the L and the Γ valleys is reduced, and (2) at a certain point there is a crossover of the energy levels in Γ and L, Γ is now the global minimum of the conduction band and we have obtained a direct gap semiconductor. One prominent example for this behavior is biaxial strain in the (001) plane.

We want to point out, that the band gap energy is reduced under tensile strain in any case. This may have technological implications. The direct gap of unstrained Ge has got an energy of 0.8 eV which corresponds to 1549 nm and hence would match the C-band of optical communication fibers (1530 nm to 1565 nm). The reduced band gap of strained Ge may thus lead to alternative applications of a Ge based laser. Typically, the emission wavelengths of tensilely strained Ge will be in the shortwave mid-infrared spectral region with many significant applications in the areas of biochemical sensing and spectroscopy.[112]

Besides this “favorable” case, we also observe “unfavorable” cases. In these cases, strain is applied with respect to the crystal orientation in such a way, that the symmetry of the L-valleys and hence their degeneracy are broken. Examples are biaxial strain in the (111) plane or uniaxial strain in the [110] direction. Here the split of the L-degeneracy lead to two sets of L-valley related energy bands, denominated $E_g^{L_1}$ and $E_g^{L_2}$ in FIG. 2-18. From Liu et al.’s calculations, we can observe that there is a crossover of the Γ band with one of the L bands at quite low strain values, but the crossover of the Γ band with the lowest L-valley related band happens only at much higher strain values or never. Table 2-2 summarizes the threshold strain values needed for the Γ/L crossover in the conduction band of Ge that are published in literature and obtained using different theoretical approaches. Generally accepted is, that the threshold strain for biaxial strain in the (001) plane is slightly less than 2% tensile and that for uniaxial strain in direction [100] is > 4% uniaxial tensile. For this reason, in this thesis, we will present SiGe stressors grown on Ge that create biaxial strain in plane (001) and along [100]. However, as we will see in sec. 5.2, due to the Raman selection rules, it is not possible to apply Raman spectroscopy to our system creating tensile strain in direction [100]. To demonstrate the principal potential of our system of SiGe stressors, we will also present a system that creates uniaxial tensile strain in direction [110].

Table 2-2 Recent calculations of the threshold tensile strain necessary for an indirect/direct conduction band cross-over in Ge for uniaxial and biaxial strain applied in different crystallographic directions.

strain type	direction	threshold strain (%)	reference
uniaxial	<111>	4.2%	Zhang et al., Ref. [115]
	<100>	4.6%	Aldaghri et al., Ref. [116]
	<001>	3.05%	Tahini et al., Ref. [117]
	<110>	1.71%	Tahini et al., Ref. [117]
	<111>	1.05%	Tahini et al., Ref. [117]
	<100>	8.56%	Liu et al., Ref. [111]
	<111>	5.69%	Liu et al., Ref. [111]
	<100>	4.6%	Sukhdeo et al., Ref. [62]
biaxial	(001)	1.61%	Chang and Chuang, Ref. [118]
	(001)	2%	Lim et al., Ref. [29]
	(001)	1.9%	El Kurdi et al., Ref. [107]
	(001)	1.6%	Virgilio et al., Ref. [27]
	(001)	1.9%	Boztug et al., Ref. [44]
	(001)	2.5%	Sukhdeo et al., Ref. [36]
	(001)	2.91%	Liu et al., Ref. [111]
	(110)	~ 3.5%	Liu et al., Ref. [111]
	(001)	1.67%	El Kurdi et al., Ref. [119]

As calculations of optical gain from Ge show, e. g. Refs. [29] and [44], a direct gap Ge is not mandatory to obtain carrier population inversion and optical gain in germanium, but that strain values less but close to the L/Γ transition are sufficient. For doped Ge, Sukhdeo et al. [62] showed in their more recent paper that also a strong threshold reduction for lasing in n-type Ge can be obtained with strain values less than the crossover threshold.

Moreover, from the equations containing the deformation potential (Eqs. (2-34) to (2-37)), we see that the change in band edge energy is linear with the strain. Guilloy et al. [108] prepared suspended Ge beams in which they could reach uniaxial strain along direction [100] up to 3.3%. They determined the direct band gap energy using electroabsorption spectroscopy and revealed a nonlinear relation between direct bandgap energy and strain and introduce second-order deformation potentials to correct for the non-linearity.

At this point it would be interesting to know if their material is still within the regime of elastic deformation or if plastic deformation already set in where deformation is permanent and there is no linear stress/strain relation anymore. A hint may be the fact, that in the growth of Ge on Si – where initially about 4% compressive strain are generated due to the lattice mismatch of both materials – after only a few nanometers dislocations are formed. Eventually, high stress/strain leads to fracture of the material. For direction [100], Ruoff reports an ultimate strain of 18.3% (at 14.7 GPa stress) [113] and Roundy and Cohen calculated 20% (at 14 GPa stress) for the [111] direction.[114]

We conclude by noting that the reduction of the electronic band-gap in Ge through tensile strain is considerably. Sukhdeo et al. have calculated the emission wavelength in <100> uniaxially strained Ge lasers in dependence of tensile strain and n-type doping.[62] Solutions that result in lasing threshold current densities less than 1 kA/cm^2 will emit at wavelengths in the mid-infrared spectral range (> 3000 nm). This would result in a vast variety of mid-IR applications as for example presented by Soref in Ref. [112].

To match transmission windows of fiber-optic communication, emission wavelengths should not be longer than 1675 nm (U band). Peschka et al. simulated a Ge laser strained to not more than $\varepsilon_{bi} = 0.7\%$ (which roughly corresponds to a uniaxial strain of $\varepsilon \approx 1.4\%$) and found a laser emission wavelength of ~ 1700 nm.[120] They optimized the laser cavity design to reduce the threshold current density, but still calculated necessary current densities of ~ 50 kA/cm^2. Further improvements to or alternative cavity designs (e. g. germanium microdisks with circular Bragg reflectors, Ref. [121]) may be one solution to improve performance of Ge based lasers with short emission wavelength.

2.4 Effect of n-type doping

2.4.1 Lift of Fermi level and L-valley filling

The effect of n-type doping is schematically depicted in FIG. 2-19. The energy levels of the dopant impurities (donors) are close to the conduction band edge. In case of high dopant concentrations, the wave functions of the donor electrons overlap and the impurities do not constitute discrete, localized energy levels but form a continuous band with delocalized electron states that is merged with the conduction band. This transition is referred to as Mott transition. The semiconductor is said to be degenerate. For phosphorous doping of Ge, the critical shallow donor concentration N_c is 2.5 $\times 10^{17}$ cm^{-3}.[122]

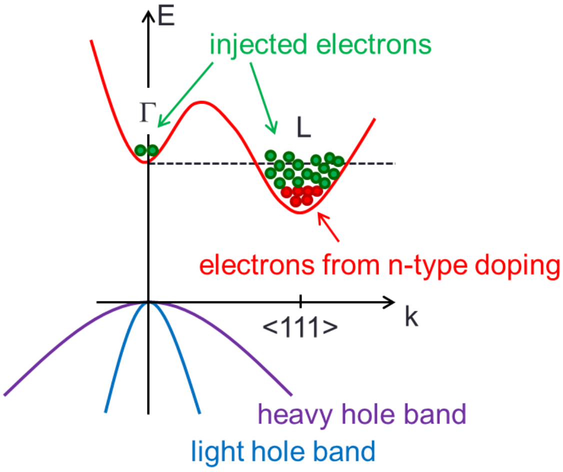

FIG. 2-19 Schematic illustration of the Ge band structure and the effect of heavy n-type doping. Extrinsic electrons originating in ionized dopant atoms (donors) fill the L-valley states and raise the Fermi level E_F. Excess electrons – photo-excited or injected electrically into the conduction band – experience a smaller energy barrier between L and Γ valleys and the electron population in the Γ valley is enhanced. Figure adopted from Liu et al., Ref. [28].

The n-type dopants are easily ionized and the conduction band minimum, the valleys in point L, is filled with the extrinsic electrons stemming from the ionized donors. The Fermi level E_F is shifted toward higher energies, i. e. electrons photo-excited from the valence band or electrically injected experience a lower energy difference between L and Γ valleys. Through this band filling effect the electron population in Γ_c is enhanced. Moreover, another effect of high doping is a reduced scattering from electrons out of Γ into the L valleys.[29, 123] Consequently, the possibility of direct gap radiative transitions is enhanced which eventually increases the light emitting efficiency of Ge. Several groups reported an increase of photoluminescence with increasing doping densities, for instance Sun et al., Ref. [124], and El Kurdi et al., Ref. [67].

2.4.2 Band-Gap Narrowing and active donor concentration

The many-body interactions of the free carriers and carrier-impurity interactions cause a narrowing of the band-gap (*band-gap narrowing*, BGN). According to Haas, BGN as a function of doping concentration is nearly the same for the L and Γ valleys so that high n-type doping does not affect the shape of the conduction band and the energy difference between the L and Γ band edges is not changed.[125]

As pointed out by Camacho-Aguilera there is an interesting side effect of BGN due to doping, helping to fill the L-valleys with extrinsic electrons: The reduced conduction band edge energy due to BGN in return results in a lower dopant concentration needed for degeneracy, i. e. to lift the Fermi level E_F above the conduction band energy than without this effect. For Ge with 0.25% biaxial strain, the doping level needed to push the Fermi level E_F to the Γ_c energy is reduced from ~ 6.2×10^{19} cm^{-3} to ~ 3.5×10^{19} cm^{-3}.[126]

Jain and Roulston discussed the various contributions to band-gap narrowing at dopant concentrations higher than 1×10^{18} cm^{-3} and figured out that there are four major contributions:[127]

(1) shift $\Delta E_{ex(maj)}$ of the majority band edge due to exchange interaction
(2) shift $\Delta E_{cor(mino)}$ of the minority band edge due to carrier-carrier or electron-hole interaction (correlation energy shift)
(3) shift $\Delta E_{im(maj)}$ of the majority band edge due to carrier-impurity interactions
(4) shift $\Delta E_{im(mino)}$ of the minority band edge due to carrier-impurity interactions.

$\Delta E_{ex(maj)}$ and $\Delta E_{cor(mino)}$ are shifts due to many-body interactions. Jain and Roulston point out that all shifts contribute to a decrease of the band gap energy and that the total band gap narrowing BGN is given by the sum of the single contributions:[127]

$$\mathrm{BGN} = \Delta \mathrm{E}_{\mathrm{ex(maj)}} + \Delta \mathrm{E}_{\mathrm{cor(mino)}} + \Delta \mathrm{E}_{\mathrm{im(maj)}} + \Delta \mathrm{E}_{\mathrm{im(mino)}} \qquad (2\text{-}38)$$

Jain and Roulston then could derive analytical formulae for BGN as a function of the concentration of free carriers N. Hence, N corresponds to the concentration of ionized, i. e. electrically activated dopants n_{act}.

In the experiments presented in this thesis, we are going to link the BGN determined from photo-luminescence spectra to the number of activated donors n_{act}. We rely on the empirical approach introduced by Camacho-Aguilera et al..[126] Camacho-Aguilera et al. determined the total and activated donor concentration of highly phosphorous doped Ge films grown on Si with SIMS and Hall effect measurements and linked it to the band-gap narrowing observed with photo-luminescence measurements.

Camacho-Aguilera et al. investigated Ge sample with n_{act} between 5×10^{18} cm^{-3} and 4.5×10^{19} cm^{-3} and give a phenomenological formula by performing a linear fit of the obtained data for BGN versus activated donor concentration n_{act}:

$$\mathrm{BGN} = E_g(n_{act} = 0) - E_g(n_{act}) = E_{BGN} + \Delta_{BGN} \cdot n_{act} \qquad (2\text{-}39)$$

With the active dopant concentration n_{act} in units of [cm^{-3}]. E_{BGN} is the y-intercept (n_{act} = 0) of the linear fit ("BGN turn-on offset energy reduction") and Δ_{BGN} is the slope of the linear fit ("BGN coupling parameter"). Camacho-Aguilera et al. give the values $E_{\mathrm{BGN}} = 0.013$ eV and $\Delta_{\mathrm{BGN}} = 10^{-21}$ eV/cm^{-3}.

This approach of Camacho-Aguilera et al. is a phenomenological approach and includes also the effect of strain, since the investigated Ge on Si films showed thermal strain of ~ 0.25%.

The linear fit is justified by the large number of data points showing linear behavior. The formula of Camacho-Aguilera et al. is hence restricted to the range of investigated high doping concentrations.

Active donor concentration can alternatively also be derived from four-point-probe measurements of the sheet resistance and from Hall measurements. Hartmann et al. point out that the active donor concentration derived from the sheet resistance measured with a four-point probe may be underestimated because an artificially high resistivity might be measured due to worse crystal quality.[128]

We would like to note, that BGN is not only due to doping. The following situations lead to a reduction of the electronic band gap:

- Doping (as discussed here)
- strain (see 2.3.3)
- Increase in lattice temperature (Ref. [129])
    - "implicit" (anharmonic) term of the thermal expansion.
    - "explicit" (harmonic) effect of the electron-phonon interaction (electron-phonon scattering) (Ref. [130])
- Electronic strain due to sample irradiation and electron-hole pair creation (Refs. [131] and [132])

To capture the effect of doping on BGN only, it is important that different samples feature the same strain and photo-luminescence is measured under the same conditions.

2.5 Recombination processes and loss mechanisms in semiconductors

In a semiconductor, the ground state of an electron is within the valence bands. Due to different excitation mechanisms, the energy of an electron can be increased so that the electron occupies a state in the conduction band of the semiconductor. The excitation can be – amongst others – due to thermal energy, the absorption of a photon (like we will see happens in photo-luminescence experiments), or the energy exchange with another electron (like in cathodo-luminescence experiments where an electron beam is used for electron excitation). The excitation of an electron to the conduction band creates a hole in the valence band. Both electrons in the conduction band and holes in the valence band are excited carriers. They tend to return into their energetic ground state, i. e. to relax. Hence, electrons and holes have got a limited lifetime in their excited states. Relaxation – i. e. the transition from an excited state into the ground state – occurs by the recombination of an excited electron with a hole. Hence, carrier lifetime corresponds to a mean time between generation and recombination of excited carriers. The shorter the lifetime, the faster and more effective is the related mechanism.

There are different recombination mechanisms which we will outline in the following and which are depicted in FIG. 2-20. In a radiative recombination process, the electron and hole relax in a recombination that is accompanied by the emission of a photon. The energy of the emitted photon $\hbar\omega$ is equal to the energy difference between excited and ground state of the electron. On the other hand, in a non-radiative recombination process, no photon is emitted, the energy of the excited electron is eventually transferred into lattice vibrations (phonons), i. e. into heat. As we will discuss, non-radiative recombinations occur much more frequently in hetero-epitaxially grown material, i. e. they have got a higher rate than radiative recombination processes. In every attempt to create an efficient light emitter one tries to maximize radiative recombinations with respect to non-radiative recombinations. We have seen that the application of tensile strain and n-type doping helps to increase radiative recombinations. In sec. 9 we are going to investigate the influence of various sample growth parameters on the photo-luminescence intensity, i. e. radiative transitions after photo-excitation, of Ge layers grown on a Si substrate.

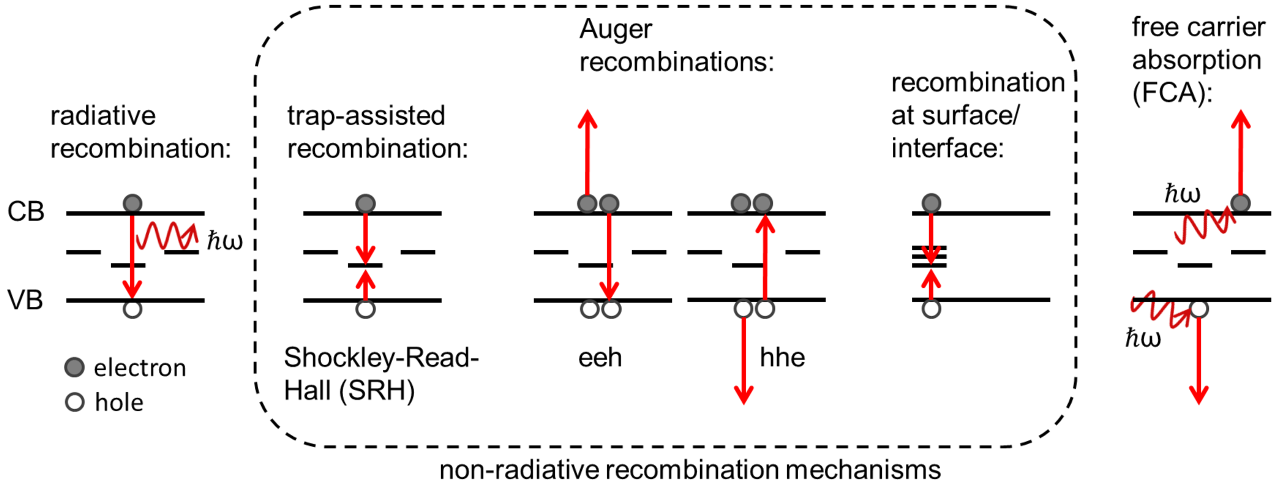

FIG. 2-20 Band diagrams illustrating relaxation mechanisms of conduction band (CB) electrons in semiconductors to the valence band (VB). Additionally, the mechanism of free carrier absorption (FCA) is depicted. Associated to each single relaxation mechanism is a rate R and a lifetime $\tau \sim 1/R$. Non-radiative recombination mechanisms reduce the internal quantum efficiency through a reduction of excess carriers, whereas free carrier absorption may constitute a main loss in highly doped and highly excited germanium lasers and hence reduces the external quantum efficiency of the system.

2.5.1 Radiative electron-hole recombination

For band-to-band recombination an excited electron and a hole are needed, hence the recombination rate depends on the density of electrons n in the conduction band and holes p in the valence band and since both types must be available the rate is proportional to the product of n and p. With the proportionality constant B, we can write the recombination rate as

$$R_{rad} = -\frac{dn}{dt} = -\frac{dp}{dt} = Bnp, \tag{2-40}$$

which gives the number of recombining electrons and holes per unit time and per unit volume. Thus, B is the recombination probability for radiative recombination. In thermal equilibrium the net recombination rate equals zero, since there is no net emission or absorption. Hence, the rate for radiative recombination R_{rad} equals the equilibrium (thermal) generation rate G_{eq}:

$$G_{\mathrm{eq}} = Bn_0p_0 \tag{2-41}$$

The net or excess recombination rate R_{exc} under external carrier excitation is hence

$$R_{\mathrm{exc}} = R_{rad} - G_{\mathrm{eq}} = B(np - n_0p_0) = B(np - n_i^2). \tag{2-42}$$

When additional carriers are injected into the semiconductor, the product np is larger than n_0p_0, the case of thermal equilibrium, and the net recombination rate will be positive, i. e. there will be net light emission.

We can decompose the carrier densities n and p into the values in thermal equilibrium, n_0 and p_0, and the excess-carrier densities δn and δp created through external excitation:

$$n = n_0 + \delta n \tag{2-43}$$
$$p = p_0 + \delta p \tag{2-44}$$

The excess recombination rate becomes then

$$\begin{aligned} R_{\mathrm{exc}} = B(np - n_i^2) = B\left((n_0 + \delta n)\cdot(p_0 + \delta p) - n_i^2\right) = B(n_0p_0 + p_0\delta n + n_0\delta p + \delta n\delta p - n_i^2) \\ = B(p_0\delta n + n_0\delta p + \delta n\delta p) \end{aligned} \tag{2-45}$$

In the case of a small neutral excitation we find $\delta n = \delta p \ll n_0, p_0$ and we can neglect the last term in the excess recombination rate:

$$R_{\mathrm{exc}} = -\frac{d}{dt}\delta n = B(p_0 + n_0)\delta n \tag{2-46}$$

The solution of this differential equation gives the decay of excess carriers with time and is given by

$$\delta n(t) = \delta n_0 e^{-B(p_0+n_0)t} \tag{2-47}$$

with δn_0 the excess carrier density at time t = 0. We can now introduce a carrier lifetime defined as $\tau = \frac{1}{B(p_0+n_0)}$ and write Eq. (2-47) as $\delta n(t) = \delta n_0 e^{-t/\tau}$.

In case of n-type doped semiconductors, we can state that n_0 is much larger than p_0, $n_0 \gg p_0$ and the net recombination rate for n-type material is governed by the excess-hole density δp:

$$R_{\text{exc}} = B(n_0 \delta p) \tag{2-48}$$

We can then identify the minority carrier lifetime τ_p as $\tau_p = \frac{1}{Bn_0} = \frac{1}{BN_D}$. The minority carrier lifetime is thus a function of the doping concentration and decreases with increasing doping. On the other hand, the related radiative recombination rate increases with doping.

Values for the constant B at 300 K are $B_{\text{Ge}} = 0.034 \times 10^{-12}$ cm^3/s for germanium and $B_{\text{Si}} = 0.002 \times 10^{-12}$ cm^3/s for silicon (values from Ref. [133]), compared to $B_{\text{GaAs}} = 200 \times 10^{-12}$ cm^3/s (Ref. [134]). This illustrates how scarce light emitters Ge and Si are compared to a classic III-V laser material.

2.5.2 Defect-related non-radiative recombination

Non-radiative recombination at defects inside the crystal is the most common non-radiative mechanism in semiconductors, since defects cannot be avoided in a crystal. Electrically active defects may be dislocations and other crystal defects (vacancies, interstitials) or impurity atoms. Even the purest semiconductors still have got an impurity concentration of about 10^{12} cm^{-3}. Especially extended defects like misfit and threading dislocations are luminescence killers. As we have seen in sec. 2.2.2, misfit dislocations are present at the interface of a hetero-epitaxial structure, but threading dislocations pervade also the bulk of the crystal.

The energy levels related to these defects are located inside the semiconductor bandgap as sketched in FIG. 2-20. These energy states constitute efficient recombination centers. The process of recombination via defect related recombination centers has been discussed by Hall [135] and by Shockley and Read [136] and is commonly known as Shockley-Read-Hall (SRH) recombination.

The motivation of Hall, Shockley, and Read has been that the observed recombination rate in germanium power rectifiers was linear with the carrier concentration and not proportional to the square of the carrier concentration as it would result, if recombination of electrons and holes would be dominated by a two-body collision mechanism.
Consequently, Shockley, Read, and Hall considered recombinations that are mediated through recombination centers distributed throughout the material. These recombination centers act like traps and electron capture, electron emission, hole capture, and hole emission are taken into account as the basic processes involved in recombination through these defect states.

Shockley, Read, and Hall determined then the rate of recombination for steady-state conditions under continuous carrier excitation. It is supposed that electrons and holes are generated in pairs and the concentrations of electrons in the conduction band and holes in the valence band are $n = n_0 + \delta n$ and $p = p_0 + \delta p$, respectively. Under steady-state conditions, the net rate of electron capture and hole capture must be equal and the net rate of recombination through the Shockley-Read-Hall process, R_{SRH}, is given by

$$R_{SRH} = \frac{np - {n_i}^2}{\frac{1}{C_p}\cdot(n+n_1) + \frac{1}{C_n}\cdot(p+p_1)} \tag{2-49}$$

where C_n and C_p represent the probabilities per unit time that an electron (hole) of the conduction (valence) band is trapped in the case that all traps are empty, and $n_1 = N_c e^{(E_t - E_c)/kT}$ gives the number of electrons in the conduction band in the case in which the Fermi level coincides with the energy level of the trap E_t. N_c is the effective density of levels for the conduction band. p_1 is defined like n_1 for the corresponding number of holes in the valence band.

Following Shockley and Read,[136] we can write $C_n = N_t\langle c_n\rangle$ and $C_p = N_t\langle c_p\rangle$ with N_t the density of traps and $\langle c_n\rangle$ ($\langle c_p\rangle$) the average of c_n (c_p) over the states in the conduction (valence) band. c_n(E) (c_p(E)) is the average of $v_n\sigma_n$ ($v_p\sigma_p$) for states of energy E with v_n (v_p) the speed of the electron (hole) and σ_n (σ_p) the capture cross section for electrons.

$\frac{1}{C_n}$ and $\frac{1}{C_p}$ can be identified with the lifetimes for electrons τ_n when the traps are completely empty and that for holes τ_p with all traps occupied by electrons.[135] These lifetimes are equal to the minority carrier lifetimes in case of doped semiconductors and show that the Shockley-Read-Hall recombination rate R_{SRH} is limited by the trapping of minority carriers.[134] We can write R_{SRH} as

$$R_{SRH} = \frac{np - {n_i}^2}{\tau_p\cdot(n+n_1)+\tau_n\cdot(p+p_1)} \tag{2-50}$$

and under high excitation levels, $n \approx \delta n = \delta p \gg n_0, p_0, n_1, p_1$, the rate is linear in the carrier density:

$$R_{SRH} \cong \frac{n}{t_n + t_p} = An \tag{2-51}$$

As pointed out by Hall, the lifetime τ_{SRH} related to R_{SRH} should be reduced with impurity content, see FIG. 2-21.[135] We shall see in sec. 10 that we can explain the variation of PL intensity of Ge on Si heterostructures with different levels of n-type doping very well with a model that accounts for a change in τ_{SRH} lifetime with the concentration of total impurities. Comparing our PL data to a numerical model, we found that the SRH related lifetime became shorter than the lifetime related to the non-radiative Auger recombination mechanism that is going to be discussed in the next section.

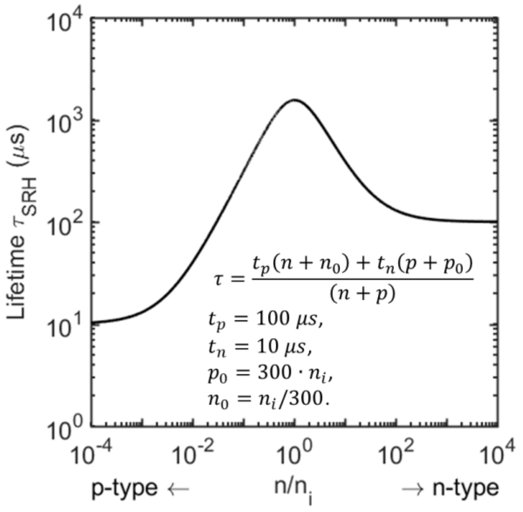

FIG. 2-21 Variation of the defect related lifetime τ_{SRH} with doping concentration according to Hall. Figure adopted from Hall, Ref. [135].

Finally, we would like to note, that Pezzoli et al. showed that at cryogenic temperatures, carriers are trapped effectively at dislocation levels and even dislocation related luminescence can be observed in Ge with a sub-bandgap emission wavelength.[137]

2.5.3 Auger recombination

Auger recombination is a three body process. The energy released by the recombination of an excited electron with a hole is transferred to a second excited electron or hole. In the case of a second electron, we face the process labelled eeh in FIG. 2-20 and the second electron is promoted high into the conduction band. It then thermalizes back to the conduction band edge by scattering/emission of phonons. The other case is that of a second hole which absorbs the dissipated energy of the electron-hole recombination and is transferred to a lower energy level in the valence band (process ehh in FIG. 2-20). It then thermalizes back to the valence band edge. The recombination rates associated with the eeh and ehh processes are given by

$$R_{Auger} = C_n n^2 p \text{ and } R_{Auger} = C_p n p^2, \tag{2-52}$$

respectively. Since either two electrons or two holes are involved in the processes, the electron density or hole density enter the rates squared.

C_n and C_p are coefficients that are different in general, because during Auger scattering energy and momentum conservation must be obeyed. Hence, the probability of an Auger scattering depends on the effective masses, the density of states and the bandgap width. This gives rise to different events in the conduction and valence band.[138] Liu et al. use the values $C_\text{n} = 3.0 \times 10^{-32}$ cm^6/s and $C_\text{p} = 7.0 \times 10^{-32}$ cm^6/s for their calculations of gain in germanium layers.[28] Conradt and Aengenheister roughly estimate $C_\text{p} \approx 10^{-31}$ cm^6/s.[139]

For an n-type semiconductor with a large electron density in the conduction band, the eeh process is more probable. However, in case of high external excitation, i. e. the excess carrier density is much larger than the equilibrium carrier density, $\delta n = \delta p \gg n_0$, we can merge both equations to

$$R_{Auger} = (C_n + C_p) n^3 = C n^3 \tag{2-53}$$

with C the Auger coefficient. Values for C can be found in Ref. [34], $C = 3.2 \pm 0.3 \times 10^{-30}$ cm^6/s (extracted from mid-IR reflection spectra), and Ref. [119], $C = 0.9 \times 10^{-30}$ cm^6/s (obtained from comparison of numerical data with experiment). El Kurdi et al. estimate the Auger recombination related lifetime to be $\tau_{Auger} = \frac{1}{Cn^2} \approx \frac{1}{C{N_D}^2}$. With $N_\text{D} = 1 \times 10^{19}$ cm^{-3} they obtain $\tau_{Auger} = 14\ ns$.[119]

Mroziewicz et al. pointed out, that the Auger recombination rate is the higher, the smaller the bandgap energy of the material is.[138] This raises the question, if in Ge gain calculations a strain dependent Auger coefficient has to be employed.

Like the radiative recombination, also the Auger process is an intrinsic property of the material that cannot be avoided.

2.5.4 Recombination at surfaces and interfaces

The periodicity of the crystal lattice is broken at surface. Other electronic states occur inside the bandgap of the semiconductor. Moreover, dangling bonds, i. e. loose, half-filled electron orbitals from the atoms located at the surface, also create energy levels inside the electronic band gap; this levels can be acceptor- or donor-like. Furthermore, surface reconstruction can also lead to the creation of energy levels different from the bulk crystal.
Carrier recombination at a surface is characterized by a surface recombination velocity, S. For Ge, the surface recombination velocity, S, of a bare surface is S = 143 cm/s.[140]

Also an interface terminates the volume of the sample. As discussed in the section on hetero-epitaxy, cf. sec. 2.2.2, due to the lattice mismatch and plastic relaxation the interface of epitaxial layers may be very defective.
Recombination at an interface may – like a surface – be expressed by a surface lifetime τ_S and a surface recombination velocity S. In case that the recombination at the interface is dominating and the recombination at the real surface is negligible, we can write

$$\tau_s \cong \frac{H}{S}$$

with H the thickness of the sample and $(S \cdot H)/D < 0.1$, where D is the diffusion constant.[141]

Grzybowski et al. reason that fast recombination at a surface (or interface) brings the excess carrier densities in the L and Γ conduction band valleys out of thermal equilibrium and with that could explain the unexpected high photo-luminescence intensity ratio of direct and indirect gap recombination $I_{\mathrm{dir}}/I_{\mathrm{ind}}$ in Ge films grown on Si.[82] Non-radiative recombination reduces the overall excess carrier density in the conduction band, but due to its comparably long radiative lifetime, in first place the indirect L valleys are affected, so that the ration $I_{\mathrm{dir}}/I_{\mathrm{ind}}$ is increased.

Geiger et al. identified non-radiative recombination at the Ge/Si interface as the main lifetime limitation in Ge on Si layers.[66] However, for vertical Ge hetero-structures (“towers”) with a high aspect ratio of the height of the structure to the base area, when increasing the temperature from cryogenic temperatures to room temperature, non-radiative recombination at the surface becomes more important than non-radiative recombination at the interface.[142]

2.5.5 Rate equation for excess carrier density

We have seen, that radiative recombination of excited carriers and Auger recombination are intrinsic properties of the material. We stated moreover, that also crystal defects are merely avoidable. Hence, there are several recombination channels for excited carriers. For bulk like material, in which surface recombination is negligible, we can form the following rate equation for excited electrons:

$$\frac{dn}{dt} = G - A \cdot n - B \cdot n \cdot p - C \cdot n^3 \qquad (2\text{-}54)$$

with the generation rate G of excited carriers and $A \cdot n$, $B \cdot n \cdot p$, and $C \cdot n^3$ the rates of SRH-like recombination, radiative recombination, and Auger recombination, respectively, as discussed previously. In a dynamic equilibrium under continuous optical pumping it is $\frac{dn}{dt} = 0$.

In a photo-luminescence experiment, the generation rate G depends on the flux I of photons impinging on the sample, their energy $\hbar\omega$, and their absorption inside the material $\alpha(\hbar\omega)$.

In sec. 10 we are going to study the scaling of the PL intensity as a function of the excitation power density W. W is directly proportional to the flux I and to the generation rate G. Using the rate equation (2-54) we can deduce the change in PL intensity with excitation power W. Due to the very small value of B, the rate equation which describes the excess carrier dynamics is governed by the non-radiative rates R_{SRH} and R_{Auger}. In the following, we will discriminate different cases of dominant non-radiative recombination mechanism for intrinsic and n-type doped material.

Scaling of PL intensity as a function of excitation power: intrinsic material

For an intrinsic sample, we found that the radiative recombination rate is $R_{rad} = Bnp$. The detected PL intensity will be proportional to this radiative recombination and is hence roughly proportional to the product of the excess electron and hole densities $\delta n \cdot \delta p$.
Now, in case, that the Shockley-Read-Hall mechanism is the fastest non-radiative recombination mechanism and dominates the excess carrier equilibrium, we can neglect the Auger term and find

$$\frac{dn}{dt} = G - A \cdot (n_0 + \delta n) = 0 \tag{2-55}$$

The excess carrier density δn varies thus linearly with the generation rate G and we can conclude that the PL intensity varies with the pump power W as PL $\propto W^2$.

On the other hand, in case that Auger recombinations are dominating, we neglect R_{SRH} and write

$$\frac{dn}{dt} = G - C \cdot (n_0 + \delta n)^3 = 0 \tag{2-56}$$

The rate equation for the excess carriers contains now terms in δn up to the third power and we can assume $\delta n^3 = \frac{G}{\text{const.}}$, and consequently $\delta n \propto W^{1/3}$. Since $I_{PL} \propto \delta n \cdot \delta p = \delta n^2 \propto W^{2/3}$, it follows that in intrinsic materials the integrated PL scales sublinearly with the excitation density, as ~ $W^{2/3}$.

Scaling of PL intensity as a function of excitation power: n-type material

In case of an n-type doped material, we have seen that the radiative recombination rate is governed by the excess-hole density δp (which is equal to the excess electron density δn, since electrons and holes are created in pairs):

$$R_{\mathrm{exc}} = B(n_0 \delta p) \tag{2-57}$$

Hence, in this case, we have $I_{PL} \propto \delta p = \delta n$ for the PL intensity. In case that Shockley-Read-Hall is the dominating mechanism, the rate equation which describes the excess carrier dynamics is linear in δn, as seen previously. Consequently, $W \propto G \propto \delta n$ and it follows $I_{PL} \propto W$, thus PL intensity increases linearly with excitation power, the scaling exponent for the integrated PL as a function of the excitation power W is 1.

Is the Auger mechanism the fastest one and dominates the excess carrier dynamic equilibrium, we find – like in the intrinsic case – $\delta n \propto W^{1/3}$. Consequently, also the PL intensity scales with $W^{1/3}$.

2.5.6 Carrier lifetime and internal quantum efficieny

In typical Ge on Si heterostructures, carrier recombination due to the non-radiative channels is much faster than radiative recombination. We can write a total carrier lifetime τ due to radiative and non-radiative processes:

$$\frac{1}{\tau} = \frac{1}{\tau_{SRH}} + \frac{1}{\tau_{rad}} + \frac{1}{\tau_{Auger}} \qquad (2\text{-}58)$$

For instance, minority carrier lifetimes at room temperature for bulk Ge samples with low doping concentrations n_{tot} ($n_{tot} < 10^{15}$ cm^{-3}) are of the order of hundreds of microseconds.[68] In sec. 10 we are going to investigate the effect of high phosphorous doping with $n_{tot} \geq 10^{19}$ cm^{-3} on the carrier lifetime.

The probability of a radiative recombination event is given as the relative probability of radiative recombination to non-radiative recombination. It corresponds to the internal quantum efficiency:

$$\eta_{int} = \frac{\frac{1}{\tau_{rad}}}{\frac{1}{\tau_{rad}} + \frac{1}{\tau_{nr}}} \qquad (2\text{-}59)$$

with $\frac{1}{\tau_{nr}} = \frac{1}{\tau_{SRH}} + \frac{1}{\tau_{Auger}}$. In the research on Ge as light emitter, one tries to shorten the radiative lifetime of excited carriers, i. e., bring all electrons into the Γ valley from which electrons and holes can quickly recombine radiatively, and to increase the non-radiative lifetimes, e. g. by improved sample growth.

Not all photons emitted inside the semiconductor can be detected externally. Some of them are lost due to self-absorption in the Ge layer (see also sec. 4.2.2) or free-carrier absorption (FCA) which is an important loss mechanism to be tackled in the realization of a Ge based light emitter, reducing its external quantum efficieny.

2.5.7 Free carrier absorption

We complete our discussion with free carrier absorption (FCA), that is one main loss mechanism to be considered in a laser cavity. FCA is the absorption of a photon by a free carrier that is then excited to a higher energy. When an electron is excited to a higher state in a parabolic band, it changes its wavenumber and hence its momentum, whereas the momentum of the absorbed photon is very small. To conserve momentum, scattering by an acoustic phonon, optical phonon, or by an impurity can be involved.[143] This kind of absorption mechanism is strongest for photon energies lower than the bandgap energy and increases with increasing wavelength λ of the photon with λ^p, where the exponent p depends on the scattering mechanism involved. Values for p are $p = 1.5$, $p = 2.5$, and $p = 3$ or 3.5 for scattering with an acoustic phonon, optical phonon, or impurity, respectively.[143] Impurity scattering depends on the impurity species and for n-type germanium Spitzer et al. obtained $\alpha_f(\mathrm{As}) > \alpha_f(\mathrm{P}) > \alpha_f(\mathrm{Sb})$.[144]

In their calculation of gain in heavily n-type Ge, Liu et al. [28] estimate the loss due to free carrier absorption with a linear dependence on the total (i.e., equilibrium plus excess) electron and hole densities *N* and *P*:

$$\alpha_f(\lambda) = AN\lambda^a + BP\lambda^b. \tag{2-60}$$

By evaluating free carrier absorption data in heavily n- and p-type Ge published in the 1960s, they obtain $A = -3.4 \times 10^{-25}$, $a = 2.25$, $B = -3.2 \times 10^{-25}$, and $b = 2.43$. For tensile Ge on Si layers due to thermal strain ($\varepsilon = 0.25\%$) and a total n-type dopant density $n_{\mathrm{tot}} = 7.6 \times 10^{19}\ \mathrm{cm}^{-3}$, they determine transparency for an injected carrier density of $\Delta n_{\mathrm{trans}} = 3.5 \times 10^{18}\ \mathrm{cm}^{-3}$ and obtain a net gain of ~ 400 cm^{-1} at an injection level $\Delta n = 9 \times 10^{18}\ \mathrm{cm}^{-3}$.

Carroll et al. [34] presented gain measurements and absorption data obtained from reflection spectra of Ge on Si layers with thermal strain ($\varepsilon \approx 0.25\%$) and low doping or unstrained material and high doping ($n_{tot} = 2.5 \times 10^{19}\ \mathrm{cm}^{-3}$). They found that no net-gain is obtainable due to strong pump-induced absorption of 7000 cm^{-1}, mainly caused by a vertical heavy hole to split off (HH → SO) hole transition in the valence band. Their results started a controversy if optical amplification in Ge is possible at all.[35]

3 micro-Raman spectroscopy

A common method for the investigation of the effects of strain in the Si/Ge material system is micro-Raman spectroscopy, in which the shift of the scattered Raman signal is linked to the strain in the material.[145-147]

The Raman effect was discovered in 1928 independently within a few months by Raman and Krishnan who discovered the effect first in liquids [148, 149] and Landsberg and Mandelstam who discovered a change of wavelength in light scattering by a quartz crystal.[150] Light/matter interaction can be absorption, transmission, emission, or scattering of the light. The largest amount of scattered light has got the same frequency than the incident light, i. e. it is scattered elastically. However, a much smaller quantity of the light (one photon out of 10^{12}) undergoes inelastic scattering by the matter.[151] The inelastic scattering can involve the interaction of photons with phonons. Hence, Raman spectroscopy is suited to obtain information about the lattice vibration frequencies of a crystal and is therefore sensitive to strain in the material.

3.1 Raman effect

The Raman effect is the inelastic scattering of a photon by a crystal: an incoming photon scatters by the crystal and thereby creates or annihilates a phonon in the crystal. The scattered photon thus gains or loses energy. The Raman effect is hence a process involving an incident and a scattered photon. It is also a second-order inelastic scattering process, and hence its probability is much lower as compared to a first-order scattering like the elastic Rayleigh scattering.
In the first-order Raman effect one phonon is involved in the scattering and the selection rules are $\omega = \omega' \pm \Omega$ and $\vec{k} = \vec{k}' \pm \vec{K}$ for the angular frequency and wave vector of the incoming and scattered photon ($\omega, \vec{k}$ and $\omega', \vec{k}'$, respectively). Ω and $\vec{K}$ are the frequency and wavevector of the created or annihilated phonon. Creation of a phonon constitutes the Stokes process with frequency of the scattered light $\omega' = \omega - \Omega$ and the annihilation of a phonon results in the anti-Stokes process that with $\omega' = \omega + \Omega$. Both processes are depicted in FIG. 3-1. In a second-order Raman process two phonons are involved in the inelastic scattering.
The energy and hence angular frequency Ω of the involved phonons are small as compared to the energies of photons typically used in Raman spectroscopy, so that the frequencies of incident, ω, and scattered light, ω' differ only slightly. We will see that special light filters are required to separate the Stokes lines from the elastically scattered Rayleigh lines.

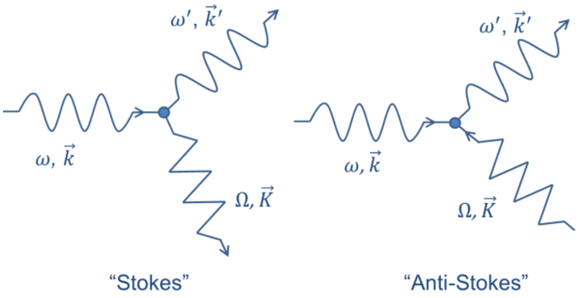

FIG. 3-1 Raman scattering of a photon by a crystal under emission ("Stokes") or annihilation (absorption, "Anti-Stokes") of a crystal phonon.

The intensities of the Stokes and anti-Stokes line depend on the matrix elements for creation and annihilation of a phonon, respectively. These are in turn proportional to $n_{\vec{K}} + 1$ and $n_{\vec{K}}$, where $n_{\vec{K}}$ is the initial occupation number of the respective phonon mode given by the Bose-Einstein particle-energy distribution.[152] For the intensity ratio between anti-Stokes and Stokes line we hence obtain

$$\frac{I(\omega+\Omega)}{I(\omega-\Omega)} = \frac{n_{\vec{K}}}{n_{\vec{K}}+1} = e^{(-\hbar\Omega/k_B T)} \qquad (3\text{-}1)$$

Taking the degenerate energy value of the optical phonons of Ge in the center of the Brillouin zone (Γ) at 300 K ($\hbar\Omega = 37.3$ meV [78]), we obtain an intensity ratio of about ~ ¼. Hence, at room temperature, the Raman Stokes line of Ge is clearly more intense than the anti-Stokes line. The same holds true for Si, where the optical phonons in Γ have got the energy $E_{LO/TO} = 64.1$ meV [77] at room temperature and the intensity ration between the Stokes and anti-Stokes lines results to be as small as 1/12. Hence, it is easier to probe the Stokes lines of the Raman spectra in the Si/Ge material system at room temperature.

The wave vector of a photon is given by $\vec{k} = 2\pi/\lambda$ whit λ the wavelength of the photon. In typical Raman experiments with Si and Ge wavelength in the visible region of the photonic spectrum are used, e. g. λ = 532 nm corresponds to ~ 5 $\times 10^3$ Å. On the other hand, the wave number at the border of the Brillouin zone is $k = |\vec{k}| = \pm 2\pi/a$ with a the lattice parameter that is of the order of 5 Å for Si and Ge. Consequently, to respect the momentum selection rule, the wave number of the created or annihilated phonon has to be k ≈ 0. Hence, Raman scattering involves the optical modes of the phononic band structure close to the center of the Brillouin zone.

The Raman effect is enabled through the dependence of the electronic polarizability α on the lattice vibration. Hence, there are also selection rules linking the polarization of incident and scattered light. The Raman scattering efficiency *I* depends of the polarization of the incident and scattered light. With $\vec{e}_i$ the polarization vector of the incident and $\vec{e}_s$ the polarization vector of the scattered light, *I* is given by

$$I = C \sum_j \left| \vec{e}_i \cdot \overleftrightarrow{R}_j \cdot \vec{e}_s \right|^2 \qquad (3\text{-}2)$$

where *C* is a constant and *Rj* is the Raman tensor of the phonon *j*.[151]

The Raman tensor is a second rank tensor with elements R_{kl} proportional to $\left(\frac{\partial \chi_{kl}}{\partial Q} Q\right)$ where χ_{kl} is the susceptibility tensor and *Q* the normal coordinate of the lattice vibration. For Si, Ge, and SiGe, that have got a diamond lattice, there are three Raman tensors. In a crystal coordinate system *x* = [100], *y* = [010], and *z* = [001] these are

$$\overleftrightarrow{R}_x = \begin{pmatrix} 0 & 0 & 0 \\ 0 & 0 & d \\ 0 & d & 0 \end{pmatrix}, \overleftrightarrow{R}_y = \begin{pmatrix} 0 & 0 & d \\ 0 & 0 & 0 \\ d & 0 & 0 \end{pmatrix}, \text{and } \overleftrightarrow{R}_z = \begin{pmatrix} 0 & d & 0 \\ d & 0 & 0 \\ 0 & 0 & 0 \end{pmatrix} \qquad (3\text{-}3)$$

The Raman tensors are then used to calculate selection rules regarding which vibrations can be probed with incident light with a certain polarization.

In this thesis, we are going to present Raman measurements obtained in a backscattering geometry on (001) sample surfaces. With the crystal coordinate system as introduced, R_x and R_y correspond to scattering by transverse optical (TO) phonons that are polarized along *x* and *y*, respectively, and R_z corresponds to scattering by longitudinal optical (LO) phonons that are polarized along the *z*-axis.[151] Note, that the characterization as longitudinal or transverse phonon depends on the direction of the incident light beam. In case of backscattering from (001), the *z*-axis extends longitudinally to the incident light beam. Examining the Raman tensors for the three phonon modes, we find that in the special experimental configuration of backscattering from (001) only scattering by the LO phonon leads to a non-zero scattering intensity *I*. With the incident light beam polarized, e. g., along $\vec{e}_i$ = [010], the polarization of the light scattered at the LO phonon is rotated to $\vec{e}_s$ = [100].

To probe the other phonons, one has to change the geometry of the experiment. For instance, in a configuration of backscattering from (110) and an incident polarization of $\vec{e}_i$ = [1-10], it is possible to probe the phonons along axes *x* and *y*.

3.2 Raman spectra of Si, Ge and Si$_{1-x}$Ge$_x$

In the Si$_{1-x}$Ge$_x$ alloy, Ge-Ge, Ge-Si, and Si-Si vibrational modes are present. The appearance and frequency of these vibrations depend on the alloy composition.

FIG. 3-2 replots the Raman spectra of pure Ge, Si$_{1-x}$Ge$_x$ for different compositions *x*, and pure Si calculated by Pagès et al.[153] The inset shows the Raman spectra of pure Ge that exhibits a single band at about 300 cm-1, and that of pure Si with a single band at about 520 cm^{-1}. These two bands are attributed to the Ge-Ge and Si-Si vibrational modes, respectively. Upon alloying with Si, the Ge-Ge mode of Ge rich SiGe shifts to lower wavenumbers and decreases in intensity. At the same time, a two-peaked band at about ~ 400 cm^{-1} occurs. This band is attributed to the Ge-Si vibrational modes in which mainly the vibration of a Ge atom bonded to a Si atom is involved. Its frequency is sensitive to its environment, comprising first and second neighbors. The Ge-Si vibration at 390 cm^{-1} can be attributed to the Si local vibrational mode (LVM) that is also visible at Si concentrations as low as 1.3%, and the second Ge-Si vibration at 400 cm^{-1} can be attributed to nearest-neighbor pairs of Si atoms.[154]

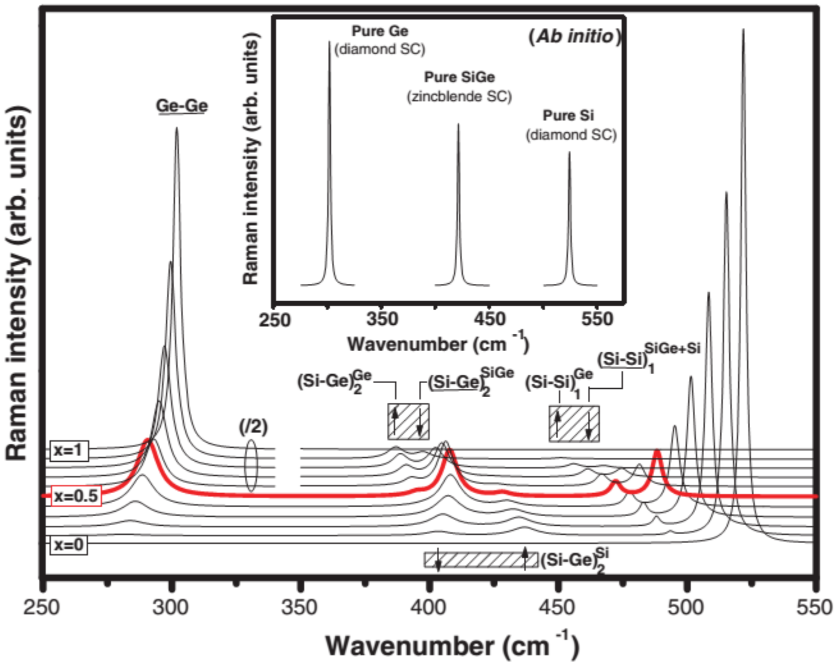

FIG. 3-2 Calculated optical active modes in Si$_{1-x}$Ge$_x$ visible in Raman spectra. Plotted are the spectra for Si$_{1-x}$Ge$_x$ alloys with different Ge molar fraction *x*. The evolution of the single peak intensities as a function of *x* is hence visible. The inset shows the three vibrational modes Ge-Ge, Si-Ge, and Si-Si for pure Ge, pure Si, and Si$_{50}$Ge$_{50}$ with the Si and Ge atoms distributed in a zincblende lattice. Figure taken from Ref. [153].

With further increased Si content in the SiGe alloy, also the Si-Si vibrational mode starts to develop at ~ 475 cm^{-1} that shifts toward the value for pure Si at ~ 520 cm^{-1} for an increasing amount of Si in the alloy. Like the Si-Ge mode, the Si-Si mode is sensitive to its nearest neighbors and several weak Raman peaks can be found between 400 cm^{-1} and 500 cm^{-1}. These modes originate in localized Si-Si vibrations in the neighborhood of one or more Ge atoms.[155] They are not generated by second-order Raman processes or long-range ordering.[155]

Pezzoli et al. determined the change of peak position of the most intense peaks of the Ge-Ge, Si-Ge and Si-Si modes.[156] They found a linear decrease in Raman shift for the Ge-Ge and the Si-Si mode, whereas the Si-Ge peak first shifts to higher Raman frequencies and then back to lower frequencies, as depicted in FIG. 3-3. In a following study, Pezzoli et al. additionally considered the effect of biaxial in-plane strain on the three Raman modes of epitaxial SiGe layers and derived the following relationships:[157]

$$\omega^{Ge-Ge}(x,\varepsilon) = 280.3 - 19.4 \cdot x - 450 \cdot \varepsilon \tag{3-4}$$

$$\omega^{Si-Ge}(x,\varepsilon) = 400.1 + 24.5 \cdot x - 4.5 \cdot x^2 - 33.5 \cdot x^3 - 570 \cdot \varepsilon \tag{3-5}$$

$$\omega^{Si-Si}(x,\varepsilon) = 520.7 - 66.9 \cdot x - 730 \cdot \varepsilon, \tag{3-6}$$

where x denotes the germanium molar fraction of the SiGe alloy and ε the in-plane strain.

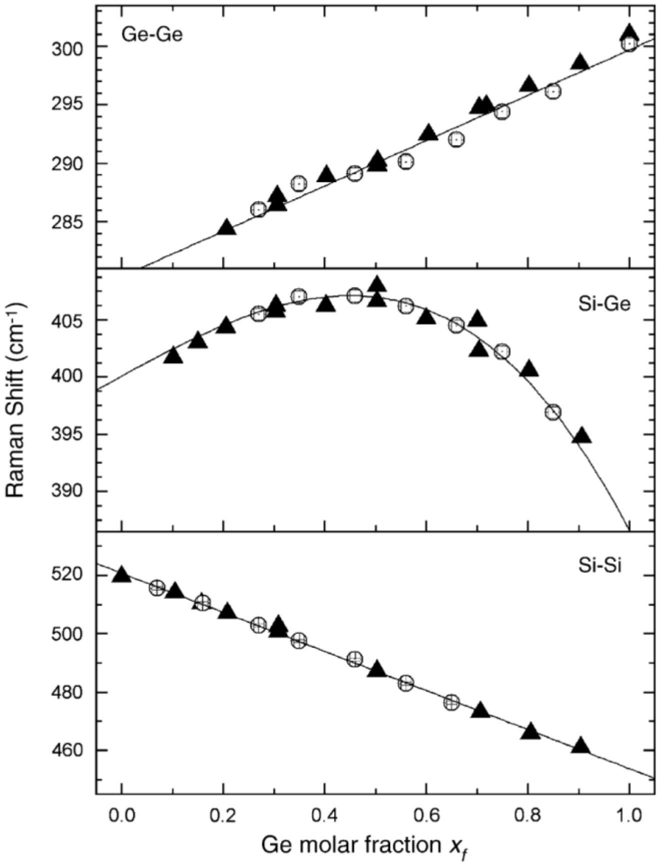

FIG. 3-3 Peak positions of the Raman modes Ge-Ge, Si-Ge, and Si-Si (top down) of $Si_{1-x}Ge_x$ as a function of the Ge molar fraction x. Figure taken from Ref. [156].

3.3 Relation between relative Raman shift Δω and strain ε

In sec. 2.3.2 we have established the effect of strain on the phonon frequency and we have seen that the frequency ω_0 of the relaxed material changes under strain to

$$\omega = \omega_0 + \frac{1}{2\omega_0} \cdot (p\varepsilon_{33} + q\varepsilon_{11} + q\varepsilon_{22}) \tag{3-7}$$

with p and q the phonon deformation potentials. In a Raman spectroscopy set-up for strain measurements, the system is calibrated to the relaxed material with frequency ω_0 and the frequency ω of a sample under strain load is measured. We thus can determine the relative Raman shift $\Delta\omega = \omega - \omega_0$ from Eq. (3-7):

$$\Delta\omega = \frac{1}{2\omega_0}\left(p\varepsilon_{zz} + q\left(\varepsilon_{xx} + \varepsilon_{yy}\right)\right) \tag{3-8}$$

where *z* is the growth direction of the epilayer and corresponds to <001>. In their fundamental work on Raman spectroscopy in diamond- and zinc-blende-type semiconductors, Cerdeira et al. [102] give values for the parameters *p*, *q*, and *r* as well as the Grüneisen mode parameter γ. However, some of them are reported only implicitly. From $(p-q)/(2\omega_0^2) = 0.23$ and $\gamma = -(p+2q)/(6\omega_0^2) = 0.89$, we obtain the deformation potentials $q = -1.93 \cdot \omega_0^2$, $p = -1.47 \cdot \omega_0^2$, and $r = -10.87 \cdot \omega_0^2$.

3.3.1 Case: biaxially strained epitaxial layer

From the geometry of the stressors we know which stress directions are present and which entries of the stress tensor can be set to zero.

Let us assume that in case of biaxial in-plane strain the epitaxial layer is exposed to stress forces in the directions x and y: $\sigma_{xx} \neq 0$ and $\sigma_{yy} \neq 0$. One example for this case is the *thermal strain* which remains in a Ge epitaxial layer after the growth on a Si substrate at temperatures higher than room temperature. The residual stress tensor elements equal to zero. The stress-strain relation (Eq. (2-10) results in

$$\begin{bmatrix} \varepsilon_{xx} \\ \varepsilon_{yy} \\ \varepsilon_{zz} \\ 2\varepsilon_{yz} \\ 2\varepsilon_{zx} \\ 2\varepsilon_{xy} \end{bmatrix} = \begin{bmatrix} S_{11} \cdot \sigma_{xx} + S_{12} \cdot \sigma_{yy} \\ S_{12} \cdot \sigma_{xx} + S_{11} \cdot \sigma_{yy} \\ S_{12} \cdot \sigma_{xx} + S_{12} \cdot \sigma_{yy} \\ 0 \\ 0 \\ 0 \end{bmatrix} \tag{3-9}$$

with S_{11} and S_{12} elements of the compliance tensor. Since in the biaxial in-plane strain the stresses along x and y are equal, $\sigma_{xx} = \sigma_{yy}$, we find $\varepsilon_{xx} = \varepsilon_{yy} = \varepsilon$. ε_{zz} can then be expressed in terms of ε_{xx} and ε_{yy} as $\varepsilon_{zz} = \left(2S_{12}/(S_{11} + S_{12})\right) \cdot \varepsilon$. Hence, we can write Eq. (3-8) as

$$\Delta\omega = \varepsilon \cdot \frac{1}{\omega_0} \cdot \left(\frac{S_{12}}{(S_{11}+S_{12})} \cdot p + q\right) = \varepsilon \cdot \frac{1}{\omega_0} \cdot \left(-\frac{C_{12}}{C_{11}} \cdot p + q\right) = \varepsilon \cdot b \tag{3-10}$$

where C_{11} are C_{12} elements of the stiffness tensor and *b* the biaxial strain shift coefficient. Using the deformation potentials p and q and the compliance tensor elements S_{11} and S_{12} from Cerdeira et al.

[102], see sec. 2.3.1, we can calculate b and obtain $b = -1.27 \cdot \omega_0$. For Germanium we use $\omega_0 = 300.3\ \mathrm{cm}^{-1}$ in this work and which would result in $b = -413\ \mathrm{cm}^{-1}$. However, using the stiffness tensor elements given by Madelung,[73] we obtain $b = -1.44 \cdot \omega_0$ and $b = -433\ \mathrm{cm}^{-1}$. We will see that the difference in strain obtained with these two values for b is negligible compared to the experimental error in Raman spectroscopy. In this thesis, though, we will rely on the experimentally determined biaxial strain shift coefficient $b = -450\ \mathrm{cm}^{-1}$ obtained by Pezzoli et al., Ref. [145].

3.3.2 Case: Uniaxially strained epitaxial layer

Also in this case, from the geometry of the stressors we know which stress directions are present and which entries of the stress tensor can be set to zero.

In case of uniaxial in-plane strain, the epitaxial layer is subject to a stress force in direction x only: $\varepsilon_{xx} \neq 0$. The residual stress tensor elements equal zero. The stress-strain relation (2-10) results in

$$\begin{bmatrix} \varepsilon_{xx} \\ \varepsilon_{yy} \\ \varepsilon_{zz} \\ 2\varepsilon_{yz} \\ 2\varepsilon_{zx} \\ 2\varepsilon_{xy} \end{bmatrix} = \begin{bmatrix} S_{11} \cdot \sigma_{xx} \\ S_{12} \cdot \sigma_{xx} \\ S_{12} \cdot \sigma_{xx} \\ 0 \\ 0 \\ 0 \end{bmatrix} \tag{3-11}$$

Here, we want to discuss the special case of uniaxial strain created by SiGe stripe stressors in a Ge layer attached to a Si substrate. This case will be examined in this thesis and results are presented in sec. 5. It is not a real uniaxial case, but we can reasonably assume the following for the strain values in y- and z-direction:

- the epitaxial layer has infinite length in direction y such that strain in this direction can be neglected and we can set $\varepsilon_{yy} = 0$.
- the strain in z-direction ε_{zz} results from the Poisson ratio.

We can express ε_{zz} in terms of ε_{xx} as $\varepsilon_{zz} = (S_{12}/S_{11}) \cdot \varepsilon_{xx}$. The relation between relative Raman shift and strain becomes then ($\varepsilon_{xx} = \varepsilon$)

$$\Delta\omega = \frac{1}{2\omega_0}\left(p\frac{S_{12}}{S_{11}} \cdot \varepsilon + q \cdot \varepsilon\right) = \varepsilon \cdot \frac{1}{2\omega_0} \cdot \left(p\frac{S_{12}}{S_{11}} + q\right) = \varepsilon \cdot u \tag{3-12}$$

with u the uniaxial strain shift coefficient. With the deformation potentials p and q and the compliance tensor elements S_{11} and S_{12} from Cerdeira et al. [102] we can calculate u and obtain $u = -0.76 \cdot \omega_0$. For germanium, we calibrate our system to $\omega_0 = 300.3\ \mathrm{cm}^{-1}$ in this work, which would result in $u = -228\ \mathrm{cm}^{-1}$. We note, that the value for u is about half of the value of the biaxial strain shift coefficient b. Hence, for the conversion of relative Raman shift into uniaxial strain we use half of the experimental value $b = -450\ \mathrm{cm}^{-1}$ from Pezzoli et al., [145] i. e. $u = -225\ \mathrm{cm}^{-1}$.

3.4 Non-linearity of the Raman shift/strain relationship at high strain values

Gassenq et al. [158] recently compared micro-Raman measurements performed on uniaxially strained suspended micro-bridges with synchrotron based microdiffraction strain measurements. They found that for strain values > 2.5% the relative Raman shift $\Delta\omega$ is not linear anymore to the measured strain. It deviates from the linear relationship so that lower strain values are obtained.

Note that the linear relationship between relative Raman shift $\Delta\omega$ and strain ε, as derived for instance by Cerdeira et al.,[102] is per se an approximation as it was made in Eq. (2-32) in sec. 2.3.2.

The suspended micro-bridges of Gassenq et al. are different from our system of SiGe stressors that we are going to present in sec. 5; in our case, uniaxial strain is created in Ge layers attached to a Si substrate using the perimeter of SiGe stripes on top of Ge, that can be assumed to have an infinite length (along direction *y*), whereas the micro-bridges of Gassenq et al. have micro-meter dimensions in direction *y*. To estimate the effect of the non-linearity of the Raman shift/strain relation on our results, we go back to Eq. (2-30) and write it as

$$p\varepsilon_{zz} + q\left(\varepsilon_{xx} + \varepsilon_{yy}\right) = \omega^2 - {\omega_0}^2 \qquad (\,3\text{-}13\,)$$

For instance, we have seen in the example of an uniaxially strained material in the previous sec. 3.3.2 that we can express the perpendicular strain values ε_{yy} and ε_{zz} in terms of the uniaxial strain ε_{xx}. In general, we may then resolve () for ε_{xx} and can write

$$\varepsilon_{xx} = \frac{\omega^2 - {\omega_0}^2}{(\dots)} \qquad (\,3\text{-}14\,)$$

where the bracket (…) in the denominator will contain the deformation potentials p and q as well as the elements of the compliance tensor. Next, we can express the numerator in terms of Δω:

$$\varepsilon_{xx} = \frac{\omega^2 - {\omega_0}^2}{(\dots)} = \frac{2\omega_0}{(\dots)} \cdot \Delta\omega + \frac{1}{(\dots)} \cdot \Delta\omega^2 \qquad (\,3\text{-}15\,)$$

Note that the factor to the term in first order of Δω corresponds exactly to the uniaxial strain shift coefficient *u* as derived in sec. 3.3.2. Hence, the factor $\frac{1}{(\dots)}$ of the second-order correction to the linear relationship between relative Raman shift Δω and strain ε_{xx} is proportional to the strain shift coefficient *u*. This meets our expectation that the correction has to be different in different systems under strain. Adjusting the correction factor of Gassenq et al. [158] in this way to our system, we can estimate an overestimation of about ~ 0.8% in our sample with the highest uniaxial strain which is about twice the error that we give for our result.

3.5 Probing depth

The sample volume probed by Raman spectroscopy in a micro-setup is – to a first approximation – defined by the diameter of the focused laser spot on the sample surface and the penetration depth of the laser source into the sample. This second quantity is dependent on the wavelength of the laser radiation and the sample material composition. Humlíček et al. [159] and Humlíček [160] have derived the real and imaginary parts of the pseudodielectric function of $Si_{1-x}Ge_x$ for different compositions *x* from ellipsometric measurements. From this data, the absorption coefficient and hence the penetration depth of different wavelengths λ into $Si_{1-x}Ge_x$ can be obtained. We show the penetration depths as a function of the germanium content *x* for the wavelengths 457.9 nm, 532 nm, and 1064 nm that can be typically found in a spectroscopy laboratory in FIG. 3-4. With the various wavelengths, quite different penetration depths can be reached. Hence, different laser sources can be used to probe different volumes of a sample.

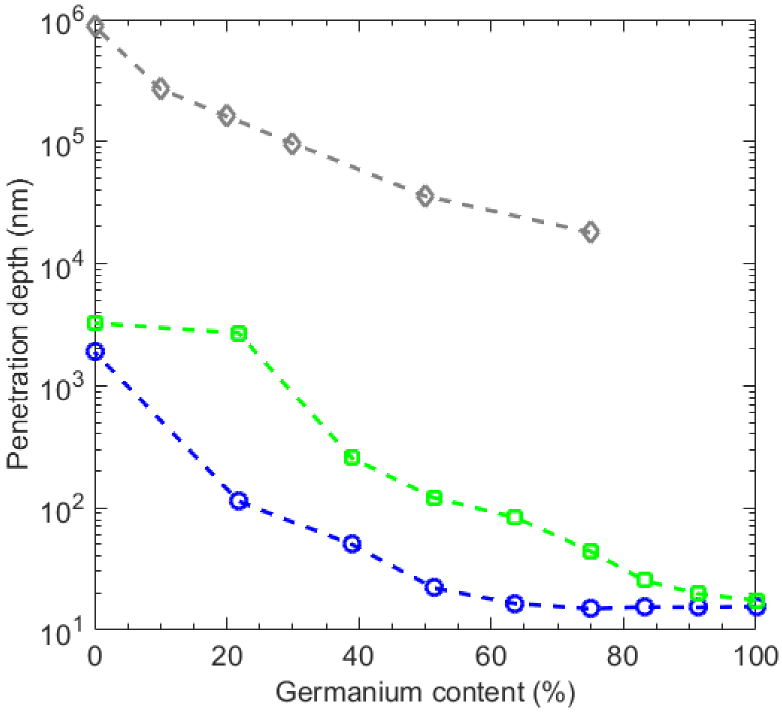

FIG. 3-4 Penetration depth into SiGe as a function of its germanium content for light with typical laser wavelengths λ available in spectroscopy laboratories: λ = 457.9 nm (blue, circles), λ = 532 nm (green, squares), and λ = 1064 nm (IR, diamonds).

3.6 Effect of sample heating

The peak position in a Raman spectrum is sensitive to the sample temperature. An increased lattice temperature due to heating with the excitation laser would cause local thermal expansion of the crystal lattice and shift the Raman peaks of Ge and Si toward lower wavenumbers. Hence, the same effect than with tensile strain would be observed. Burke and Herman measured the linear Raman shift in dependence of the sample temperature in the range of 295 K to 900 K. They determined the change in wavenumber with temperature $d\omega/dT$ for Si to be $d\omega/dT = -0.0247\ \mathrm{cm^{-1}/K}$ and for Ge $d\omega/dT = -0.0200\ \mathrm{cm^{-1}/K}$.[161]

Consequently, to accurately determine the Raman shift due to strain, thermal artefacts from the heating of the sample have to be ruled out. This can be done to reduce the excitation power until no further changes in wavenumber are observed.

3.7 Apparatus for measuring the Raman scattered radiation

In this thesis, different experimental set-ups were used, that are equal in their principles. FIG. 3-5 shows a sketch of the principle Raman set-up. A laser source serves as excitation source. We used the 457.9 nm (blue) line of an argon ion (Ar^+) gas laser and a frequency doubled Nd:YAG solid-state laser with 532 nm (green). A special requirement is asked to the solid state laser the cavity of which has to be designed to allow for one longitudinal mode only. The laser light is polarized linearly. To filter spurious laser lines, a filter with transmission only at the desired wavelength is used at the exit of the laser (laser clean-up filter). The light beam is directed by mirrors and/or prisms and a beam splitter into the objective. The beam splitter allows to collect the scattered light in the backscattering geometry. In this thesis, short working distance objectives with a magnification of ×100 and numerical aperture N. A. = 0.90 are used that focus the light beam to a spot with sub-micron diameter on the sample. The polarization of the incident laser light on the sample was controlled. The sample is mounted on a movable stage to be able to select different patterns on the sample. Furthermore, the stage is motorized so that automated line scans can be performed. The scattered light is collected by the objective and the beam splitter divides the collection path from the excitation path. Inside the collection path, there is the possibility to select the polarization of the scattered light through a polarizer. As shown previously in sec. 3.1 this allows for the probing of a selected phonon.

Since the actual Raman signal is very low compared to the Rayleigh scattered light, but very close to it in terms of frequency, one needs dedicated equipment to reject the Rayleigh-scattered light and to select the Stokes lines only. In the early days of Raman spectroscopy, this was done with double monochromators. Since the beginning of the 2000's, razor edge filters are available. In this thesis, we used a razor edge filter to block the Rayleigh and anti-Stokes lines. A razor edge filter is a low pass filter with a very steep absorption edge of less than 100 cm^{-1}. The very intense laser line (Rayleigh line) and the anti-Stokes lines are blocked so that only the Stokes lines can be observed.

After that, the light from the Stokes line is dispersed by a monochromator and registered by a CCD camera. In this thesis, we used a 800 mm additive double Czerny Turner grating monochromator for high-resolution Raman measurements with a resolution of the Raman shift of 0.4 cm^{-1}/pixel at a excitation wavelength of 457.9 nm. Moreover, we had a single grating monochromator at our disposal which resulted in a resolution of about 0.7 cm^{-1}/pixel.

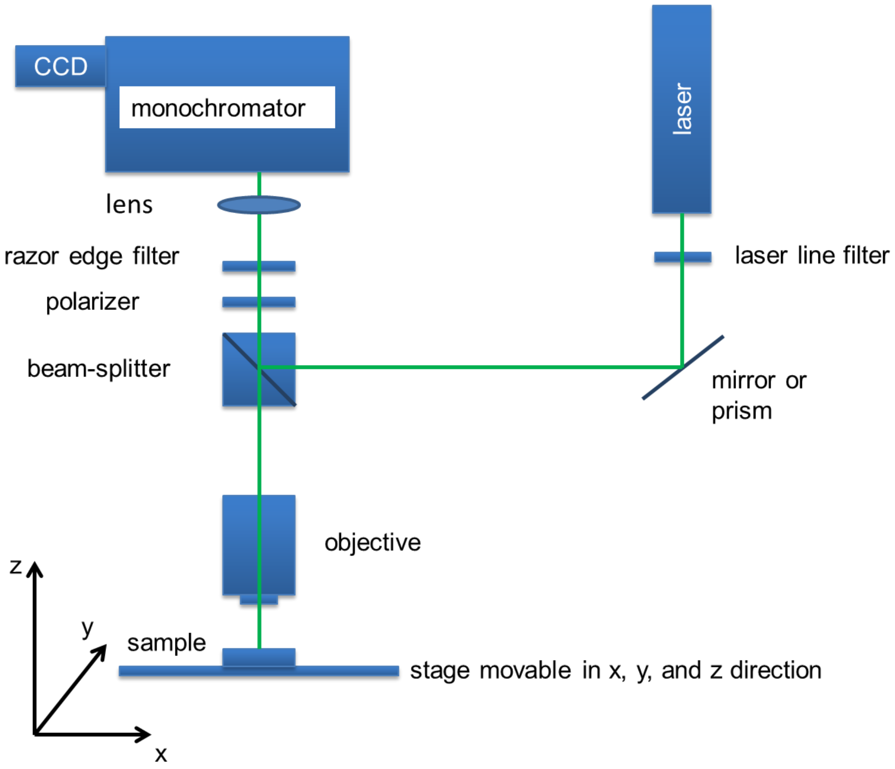

FIG. 3-5 Illustration of a modern micro-Raman spectroscopy set-up utilizing a laser source, microscope objective, razor edge filter for selection of the Stokes-line, monochromator, and detector (CCD).

4 micro-Photoluminescence spectroscopy of Ge

4.1 Photoluminescence emission

Photoluminescence (PL) spectroscopy is an experimental technique in which luminescence emitted from a sample is collected. As already discussed in sec. 2.5, by means of an excitation mechanism, an electron is brought from the valence band to the conduction band of the semiconductor. In case of a photo-luminescence experiment, the luminescence emission collected occurs after excitation of electrons in the semiconductor by absorption of photons that possess energy higher than the bandgap energy. The photons are typically supplied by a laser beam impinging on the sample. To obey momentum conservation in the absorption process, the electrons are excited vertically inside the band structure, i. e. the wavenumber k of the electron in its ground state in the valence band and that in its excited state in the conduction band does not change. In most cases, the energy of the absorbed photons is clearly higher than the band gap faced in a vertical excitation. The excess energy that remains after lifting the electron from the valence band into the conduction band is converted into the kinetic energy of the electron. A non-equilibrium ensemble of high-energy carriers is referred to as hot electrons. Since these electrons are not in equilibrium with each other, we cannot ascribe a temperature to them. Electron-electron and hole-hole scattering brings the electron and the hole gas into equilibrium conditions, each, with an electron gas temperature Te and a hole gas temperature Th. Eventually, both electron gas and hole gas reach thermal equilibrium through electron–hole scattering with a common carrier gas temperature Tc. These Carrier–carrier scattering processes happen on a timescale of 10^{15}– 10^{12} s.[162]

On a similar time scale of tens and hundreds of femtoseconds, intervalley scattering occurs in germanium, that is electrons in the zone center Γ valley are scattered to the four L and six X side valleys through long wave vector phonons.[162] Electrons in X are immediately scattered into the L valleys,[123, 163] so that in the case of Ge mainly the L valleys, which constitute the absolute energy minimum of the conduction band, are populated.

Besides intervalley scattering, electrons also scatter with LO phonons, remaining inside the same valley. This is called intravelley scattering. The carrier gas transfers energy through inter- and intravalley to the crystal lattice and is thereby cooled. Eventually, equilibrium with the crystal lattice is reached. Roskos et al. determined the cooling time of the photoexcited carriers to be 7 ps.[164] Electrons and holes are now situated at the band edge of the conduction and valence band, respectively. Radiative recombination involves electrons and holes from the band edges.

4.2 Photo-luminescence spectrum of Ge

In FIG. 4-1 we present the photo-luminescence spectrum of a germanium crystal, recorded in two different ways. The first spectrum (blue line) was acquired in a macro-like set-up, that is without using an objective to focalize the laser beam on a sub-micron spot and to collect from a limited spatial area (as discussed later on, we did not use a real macro-set-up, but used an objective with only low magnification (×5)). The second spectrum was collected in a micro-set-up, using a microscope objective to restrict the area of excitation and collection. The principal differences between both techniques are summarized in Table 4-1. In sec. 4.2.2 we are going to discuss the differences in photoluminescence spectra of Ge obtained with a macro- and micro-PL set-up.

Both experimental set-ups result in a Ge spectrum that consists mainly of two bands: the direct gap transition Γ_c to Γ_v with peak spectral energy at about ~ 800 meV at room temperature and the indirect gap transition L_c to Γ_v with peak energy at ~ 700 meV. In case of the macro-set-up, the peak intensity of both direct and indirect gap band is comparable, whereas in a micro-set-up the spectrum is dominated by the direct gap emission band. The direct gap transition is a first-order process in which momentum conservation is given. The indirect gap transition is a second-order process and a third particle has to be involved for momentum conservation.

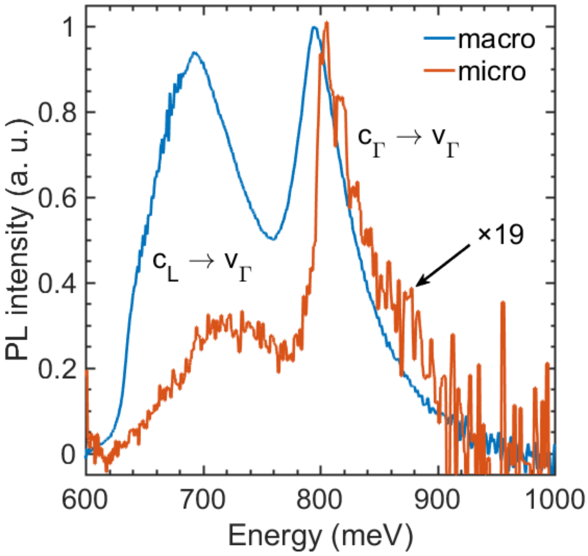

FIG. 4-1 Photo-luminescence spectra of a Ge bulk crystal acquired at room temperature using a ×5 objective (macro) and a ×50 objective (micro). The laser output power is chosen such to produce the same excitation power density of $W = 2.7 \times 10^5$ W/cm^2 close to the external surface. The "micro" spectrum is enlarged by a factor of ×19.

Table 4-1. Main differences in the optical set-up of the measurement apparatus in macro-PL and micro-PL. The spot size given for the macro-set-up is that produced with a low refractive lens.

	macro-PL	micro-PL (objective ×100)
spot-size (µm)	~ 50	≤ 1
depth of focus (µm)	limited by carrier diffusion (for Ge: up to ~ 20)	~ 2

4.2.1 Indirect gap radiative recombinations in Ge

To fulfill momentum conservation in an indirect gap radiative recombination, electronic transitions can be assisted by phonons that belong to different branches of the vibrational spectrum. This process is an inelastic scattering and a phonon is created or annihilated. In the case of Ge, due to symmetry arguments,[165] the longitudinal acoustical (LA) and transverse acoustical (TA) phonons are much more frequently involved than the longitudinal optical (LO) and transverse optical (TO) phonons. Moreover, as seen in the phononic band structure shown in FIG. 2-3 of 2.1.2, the TA and LA phonons have a lower energy in point L of the Brillouin zone than the LO and TO phonons. The respective energies of the TA, LA, LO and TO phonons are ~ 8 meV, ~ 28 meV, ~ 30 meV, and ~ 36 meV, respectively.[166-168] Lieten et al. [168] report PL spectra of intrinsic and doped bulk Ge acquired at 7 K and 4.3 K and showed that the indirect gap emission is dominated by intense luminescence peaks that can be attributed to phonon-assisted recombination involving the creation of TA, LA, and TO phonons in point L of the Brillouin zone. At room temperature, the number of phonons in the crystal is increases and indirect-gap transitions under the annihilation of a phonon are also possible.

Besides the inelastic scattering with a phonon, also elastic scattering events can occur to conserve momentum in indirect-gap transitions. Inelastic scattering can happen at charged impurities in doped samples,[168] but also electron-electron scattering can assist indirect-gap transitions.[125]

4.2.2 Bulk Ge: micro vs. macro-PL

The first papers on luminescence of germanium reported a spectral distribution with a maximum at 1800 nm wavelength (690 meV). Haynes was one of the first to present a “new radiation resulting from recombination of holes and electrons in germanium” with intensity maximum at wavelength $\lambda = 1500$ nm (830 meV).[169] This “new radiation” is originating in direct gap transitions. Haynes used a macro-photoluminescence apparatus without collecting luminescence with an objective. Since germanium PL-spectra appear differently in macro- and micro-PL, it is important to detail how data was acquired when discussing PL results. For this reason, we compare macro- and micro-PL from an undoped Ge (001) wafer in a short study. We discuss the spectral shape and the peak intensity ratio $I_{\mathrm{dir}}/I_{\mathrm{ind}}$ of the direct gap and indirect gap luminescence in function of excitation power density W.

The laser output power is chosen such to produce the same excitation power density of $W = 2.7 \times 10^5$ W/cm^2 close to the external surface. The resulting spectra are shown in FIG. 4-1, where we enlarged the spectrum obtained in the micro-set up by a factor of ×19. The ×5 objective produces a spot with a diameter of 6.5 µm on the sample surface, whereas the spot diameter in case of the ×50 objective is only 1.0 µm. Hence, a much larger volume is excited with the same power density in case of the macro set-up, explaining the difference in PL intensity.

However, the aim of our discussion is the intensity ration between direct and indirect transitions. From FIG. 4-1 we can clearly see, that in case of the macro-set up, direct and indirect gap emission have got comparable intensity, whereas in case of the micro-set up the direct gap emission is much stronger. The explanation for this discrepancy was given by Haynes in 1955,[169] but to fully understand, we stress the role of the objective.

In case of a macro-set up (like Haynes used it), we collect luminescence from a huge volume of the sample. This volume is mainly given by the depth of focus (D. O. F.) achieved by the optical components used. The D. O. F. is the depth inside the sample which is in sharp focus at the same time. We estimated the D. O. F. of the ×5 objective to be about 100 µm. On this length scale, the direct gap emission, which is energetically above the indirect gap of Ge, can be re-absorbed inside the Ge crystal before escaping the crystal and being detected. Hence, the direct gap intensity is strongly reduced by this self-absorption mechanism. In a real macro-set up, it is even possible that direct gap emission is not detected at all.

On the other hand, the D. O. F. of the ×50 objective is estimated to be only 2 µm. Consequently, we collect luminescence only from the surface region of the bulk crystal. Self-absorption is negligible and the PL spectrum of bulk Ge has got the typical shape of a spectrum from a Ge film with a strong direct gap emission band considerably larger in intensity than the indirect gap emission.

Next, we would like to compare PL spectra obtained at room temperature under different excitation power densities in the “macro-” and “micro-”set up. FIG. 4-2 (a) reports the spectra obtained in the macro-set up with excitation power densities ranging from 0.027 MW/cm^2 to 0.27 MW/cm^2. As can be expected, the emitted intensity is continuously increased with increasing excitation power density. We want to point out a second effect, that becomes more visible from panel (b) where we normalized all spectra to the intensity of the indirect gap emission band. We observe an increase of the direct gap emission intensity with respect to indirect gap luminescence when increasing the excitation power density. The peak intensity ratio $I_{\mathrm{dir}}/I_{\mathrm{ind}}$ changes from ~ 0.7 at 0.027 MW/cm^2 to ~ 1.1 at 0.27 MW/cm^2.

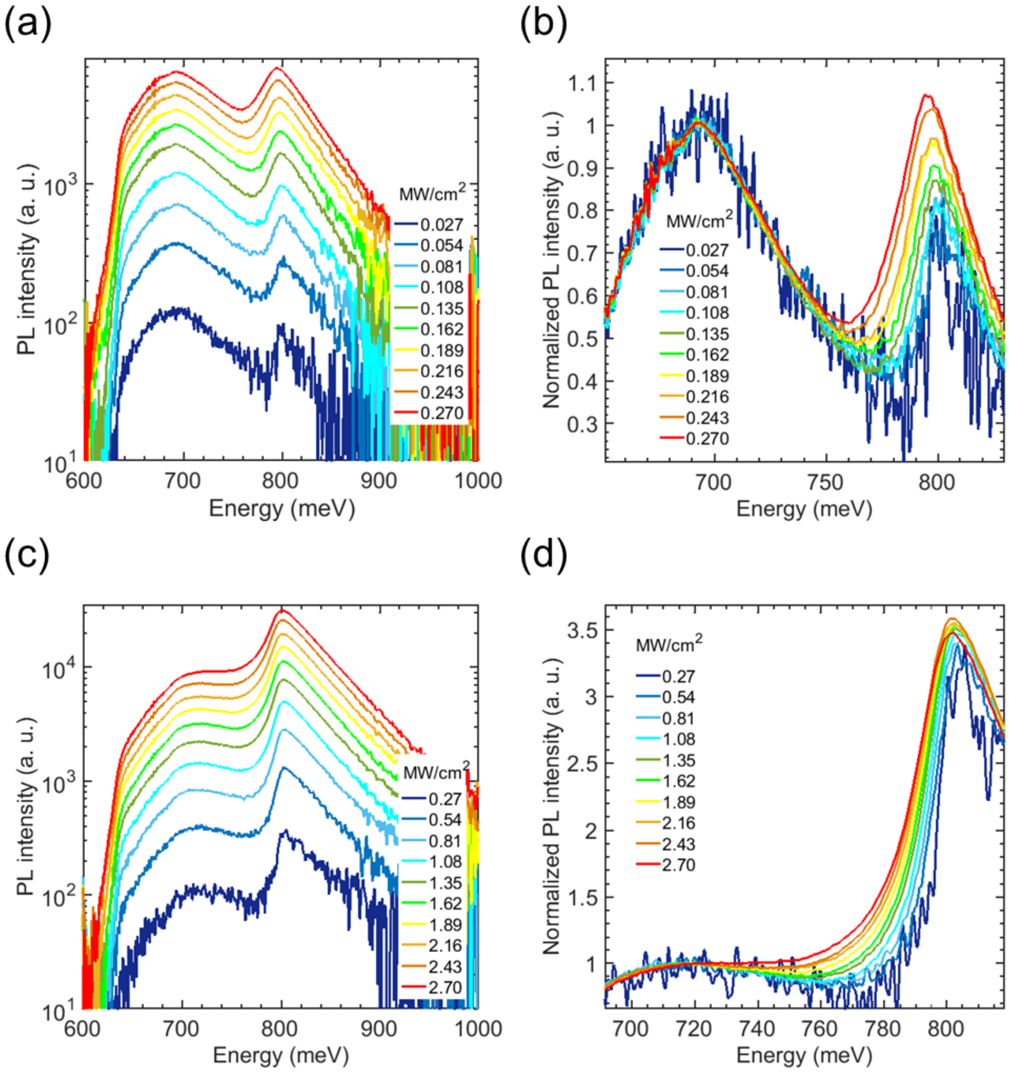

FIG. 4-2 Room temperature PL spectra from bulk Ge in dependence of the excitation power density *W*. Spectra obtained in a macro-set-up (a). To evidence the change in direct gap to indirect gap intensity ratio, $I_{\mathrm{dir}}/I_{\mathrm{ind}}$, spectra are normalized to the indirect gap intensity (b). In the macro-set-up, $I_{\mathrm{dir}}/I_{\mathrm{ind}}$ is increased with excitation power density.

Micro-PL spectra are shown in panel (c), and normalized to the indirect gap intensity in panel (d). The intensity ratio $I_{\mathrm{dir}}/I_{\mathrm{ind}}$ is not increased in case of the micro-PL-spectra.

For comparison we report the data for the micro-set up in panels (c) (spectra) and (d) (normalization to indirect gap intensity). We find that the ratio $I_{\mathrm{dir}}/I_{\mathrm{ind}}$ is constant in this room temperature measurements increasing the excitation power density from 0.27 MW/cm^2 to 2.7 MW/cm^2. This observation can be explained as follows:

The enhanced excitation power density leads to an enhanced excess electron density n_{ex} pumped into the conduction band which leads also to a lift of the quasi-Fermi level E_{Fc} in the conduction band. It seems that this does not lead to an enhanced population in Γ_{c}, since then the ration $I_{\mathrm{dir}}/I_{\mathrm{ind}}$ should also be increased in case of the micro-set up. We propose another explanation: the increase quasi-Fermi level E_{Fc} leads to a bleaching of the indirect gap self-absorption which – as shown previously – plays an important role in a macro-set up and consequently the direct gap emission intensity in the macro-set up is increased. Since in the micro-set up self-absorption is negligible due to the fact that luminescence is only collected from ~ 2 μm below the surface, the ratio $I_{\mathrm{dir}}/I_{\mathrm{ind}}$ does not change.

It is important to stress, that these measurements were carried out at room temperature, where micro-PL spectra are dominated by the direct gap emission band. In sec. 10.8 we investigate excitation power dependent measurements at 190 K and 100 K for Ge on Si films and find that above observation is not true anymore, since at these temperatures the spectra are dominated by the indirect gap feature at low excitation power density and I_{dir}/I_{ind} can be increased with increasing pump power.

4.2.3 PL dependence on excitation wavelength λ_{ex}

Like in Raman spectroscopy, we can use different laser sources for photo-excitation of carriers inside the sample. There, we have seen that different excitation wavelength, or energies, result in different penetration depths. That is still true for photo-luminescence experiments: Different wavelength have got a different absorption length. Hence, using different laser sources, the carriers are excited in differently large volumes inside the sample. In case of photo-luminescence spectroscopy on germanium, however, we would like to point out another effect of different excitation wavelengths: The energy of the exciting photons may or may not be resonant to optical transitions in the germanium band structure. For germanium, this can be clearly seen at low lattice temperatures in which thermal excitation plays a minor role.

For purposes of Raman spectroscopy at Università degli Studi di Milano-Bicocca we often use the 457.9 nm line of an argon-ion gas laser. This laser line can also be used for excitation in micro-PL experiments in Milano-Bicocca. Its wavelength corresponds to 2.71 eV. For this reason, we compare the spectrum under excitation with this wavelength with that obtained with λ_{ex} = 1064 nm stemming from a Nd:YAG solid state laser. FIG. 4-3 shows the micro-PL spectra obtained from a slightly p-type doped Ge bulk crystal acquired at a lattice temperature T_L = 77 K using both wavelengths. Whereas the indirect gap transition $L_c \rightarrow \Gamma_v$ intensity is comparable in both cases, the direct gap transition $\Gamma_c \rightarrow \Gamma_v$ is completely quenched in case of λ_{ex} = 457.9 nm, but strong in case of λ_{ex} = 1064 nm.

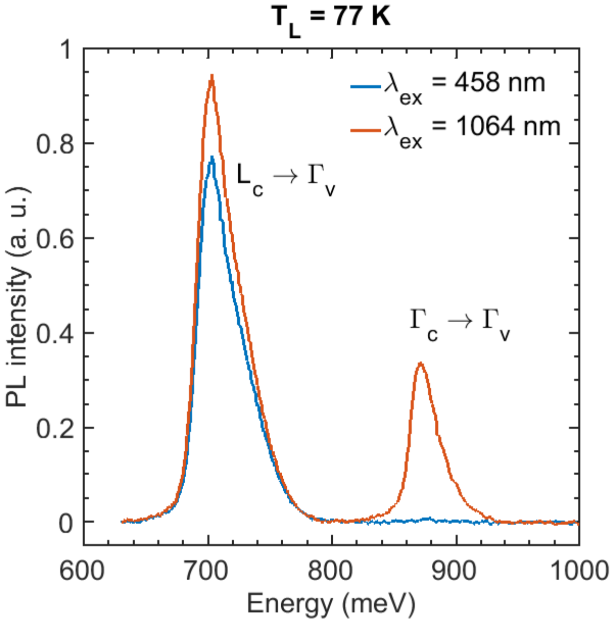

FIG. 4-3 Micro-photoluminescence spectra of a germanium bulk crystal taken at a lattice temperature of T_L = 77 K. Excitation is with 457.9 nm (2.7 eV) or with 1064 nm (1.2 eV) and results in no direct-gap emission or strong direct-gap emission, respectively.

This can be explained as follows: The energy of the excitation wavelength λ_{ex} = 1064 nm is E_{ex} = 1.16 eV which is close to the direct gap energy of 0.80 eV at room temperature or ~ 0.88 eV at 77 K. Hence, there is a resonant transition from the valence band to the conduction band near the

Brillouin zone center. Consequently, after photo-excitation, it is very probable that a large fraction of the excited electrons thermalizes into the conduction band Γ valley Γ_c. The fact, that the indirect gap transition $L_c \rightarrow \Gamma_v$ is the most intense spectral feature, shows that also in case of resonant pumping with the direct transition, most electrons scatter into the L valleys which constitute the global minimum in the conduction band. Indeed, the intervalley scattering from Γ to X (and then into L) or to L is very fast (about a few hundred femtoseconds). Only a very little fraction can then be backscattered into Γ (especially in doped samples).[123]

On the other hand, Sakamoto et al.[170] point out that in the band structure of Ge in direction Λ of the Brillouin zone the conduction band edge and the bands of the heavy (HH) and light (LH) holes run in parallel. Parallel energy bands constitute M1-type van Howe singularities in the band diagram and Sakamoto et al. argue that in the mentioned case of germanium the density of these singularities is peculiarly high. They show, that hence a large joint density of states (JDOS) for vertical transitions at these M1-type van Hove singularities is present. Sakamoto et al. determine the resonance energies for excitation within this joint density of states at 0 K to be 2.33 eV for the transition from the HH band to the conduction band and 2.5 eV for the transition from the LH to the conduction band, respectively.[170]

A standard laser in many spectroscopy laboratories is the frequency-double Nd:YAG laser with 2.33 eV radiation (λ_{ex} = 532 nm, green). Hence, the transition from the valence band to the conduction band would be in resonance with this excitation source. As Sakamoto et al. showed, these van Howe singularities are along Λ half way between Γ end L. Since L is the energetically deeper level, photo-excited electrons relax to the band edge of the L valleys. Hence, electrons are directly pumped into the L-valleys of the conduction band.

For E_{ex} = 2.7 eV there is no resonant absorption, especially there is no resonant transition which would pump electrons into the conduction band Γ valley. The next highest resonance energy would be at 3.0 eV for the transition from the top of the valence band to the Γ2 conduction band. Therefore, it is most likely that the use of a 2.71 eV pump in PL experiments leads to off-resonant carrier excitation and electrons thermalize to the global conduction band minimum, i. e. the L-valleys. Indeed, direct gap emission from bulk Ge is completely quenched in case of photo-excitation with λ_{ex} = 458 nm, cf. FIG. 4-3.

We point out that a high Γ valley population may be obtained only when electrons are directly excited into the conduction band edge in Γ. For instance, with an UV laser it may be possible to excite electrons resonantly to the Γ2 valley at $E_{\Gamma 2}$ = 3.22 eV. However, during thermalization to the band edge excited carriers will scatter to the global conduction band minimum in L, as also observed experimentally.

The calculations of Sakamoto et al., Ref. [170], are performed for T_L = 0 K. It might be that resonance energies are changed at room temperature, as well as JDOS for the transitions due to the different temperature behavior of the Γ and L-valley energies. In sec. 5.5.3 we perform PL measurements on Ge grown on Si at different lattice temperatures from 80 K to 445 K using a green (λ_{ex} = 532 nm) and an IR (λ_{ex} = 1064 nm) laser. We can conclude that the 532 nm excitation leads to population of the L valleys at all T_L and the use of the 1064 nm pump to population of the Γ valley.

4.2.4 PL spectrum of strained Ge

As we have seen in sec. 2.3.3, the application of strain lifts the degeneracy of the light-hole (LH) and heavy-hole (HH) band in point Γ. Thus, in strained material, direct gap transitions Γ_c → LH and Γ_c → HH are possible. Both transitions are characterized by different energies. In case of tensile strain, the LH energy is lifted and the recombination of electrons with light holes becomes energetically lower than the recombination of electrons with heavy holes. Moreover, in case of strong optical excitation also electrons from the split-off band SO may be excited into the conduction band. Hence, a recombination Γ_c → SO may be visible in the spectrum.

4.3 Spectral shape of direct gap emission and fitting procedure for band-gap determination

The spectral dependence of the direct gap photoluminescence emission in semiconductors is theoretically given by the rate of spontaneous emission R_{sp} in function of photon energy $\hbar\omega$. In literature two ways to determine $R_{sp}(\hbar\omega)$ can be found:

- Van Roosbroeck and Shockley [171] used a so called detailed balance approach: in thermal equilibrium the emission and absorption of photons is balanced, i. e. there is no net emission. This situation can be expanded to the case of external pumping sources acting on the sample.
- Bebb and Williams [172] follow a semiclassical approach which puts joint-density of states in first place.

Both methods lead to the same result. We follow the derivation of Bebb and Williams. Starting from Fermi’s golden rule and considering transitions between continuous energy bands this leads to a recombination rate $R_{sp}(\hbar\omega)$ for spontaneous emission proportional to the direct gap joint density of states ($\propto E^{1/2}$) times the Boltzmann factor accounting for occupation of the energy bands:

$$R_{sp}(\hbar\omega) = A \cdot \left(\hbar\omega - E_g\right)^{\frac{1}{2}} \cdot \exp(-(\hbar\omega - E_g)/k_B T) \qquad (4\text{-}1)$$

with the fit parameters A, E_g and T, where A is an arbitrary pre-factor accounting for intensity, E_g is the direct gap energy and T is the temperature characteristic for the occupation of the energy bands with excited carriers. T can significantly differ from the lattice temperature T_L.[173]

The direct-gap energy in our Ge samples was determined from a fit of the direct-gap luminescence band with Eq. (4-1). We are going to make frequently use of this in order to quantify the renormalization of the band gap energy due to doping, see sec. 2.4.2. FIG. 4-4 shows Eq. (4-1) fitted to a room temperature PL spectrum of doped Ge together with the two factors entering the formula.

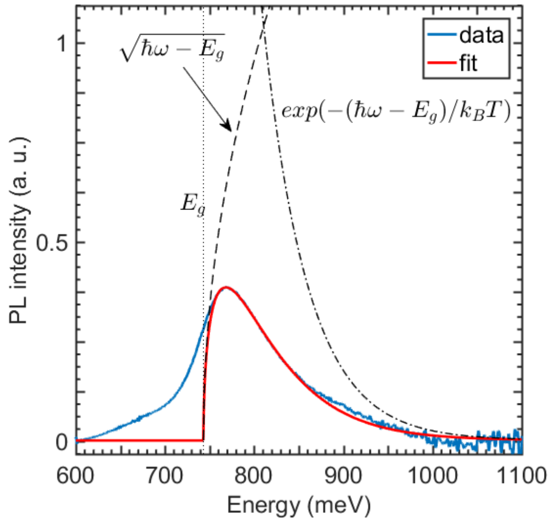

FIG. 4-4 Fit of experimental data with the formula for the spontaneous recombination rate R_{sp} (Eq. (4-1)) and decomposition into the single factors of the formula.

4.4 Apparatus for measuring the recombination radiation

A typical apparatus for measuring the recombination radiation spectra of semiconductor samples as it was used in this thesis is illustrated in FIG. 4-5. It consists roughly speaking of a laser source for sample excitation that is directed by several prisms and a microscope objective on the sample. We work in a back-scattering geometry, that is, the radiation from the sample is collected by the same objective. A beam-splitter then divides excitation and collection path. The radiation from the sample is directed along the collection path and is coupled through a lens into the monochromator. The centerpiece of the monochromator is a diffraction grating which separates the single spectral contributions of the radiation that are eventually registered by the detector. The detector is an extended InGaAs photo-diode array with 512 pixels.

We recorded photo-luminescence spectra in Bicocca and Frankfurt (Oder). The two set-ups differ in the following equipment:

- Laser lines:
  - Bicocca:
    - 457.9 nm (Ar-Ion gas laser)
    - 1064 nm (Nd:Yag)
  - Frankfurt (Oder):
    - 532 nm (frequency doubled Nd:Yag)
    - 1064 nm (Nd:Yag)
- Objective:
  - Bicocca: 50× objective with numerical aperture of 0.42
  - Frankfurt (Oder): 50× objective with numerical aperture of 0.65
- diffraction grating:
  - Bicocca: 70 grooves/mm
  - Frankfurt (Oder): 300 grooves/mm and 600 grooves/mm
- Cryostat:
  - Bicocca: Cryostat for liquid nitrogen allows measurements at temperatures as low as 77 K.
  - Frankfurt (Oder): LINKAM cryostat in the 80 K - 430 K range within a ±5 K accuracy

When presenting experimental data, we will state which objective and cryostat has been used. In Frankfurt (Oder) we used highly diffracting gratings with 300 grooves/mm or 600 grooves/mm. To obtain the whole spectrum of Ge, we stitched several spectral segments together.

In Bicocca, we faced the problem that the background radiation recorded by the extended-InGaAs photo-diode array (PDA) was varying considerably with time. This radiation is mainly heat radiation and its variation may be linked to the air conditioning system of the laboratory. PL spectra are obtained after recording a spectrum which contains the luminescence from the sample and the background radiation. The background is then to be subtracted from the recorded spectrum. To improve the spectral quality, we introduced a shutter in the excitation path, which allowed us to record only a few seconds of background and background plus luminescence shortly after each other. Within this short time, the background was stable. The background was subtracted immediately from the acquired spectrum containing the luminescence from the sample. To gain a higher intensity of the luminescence, we repeated this procedure several times. With this approach, we could improve the signal-to-noise (S/N) ratio of the sample luminescence tremendously.

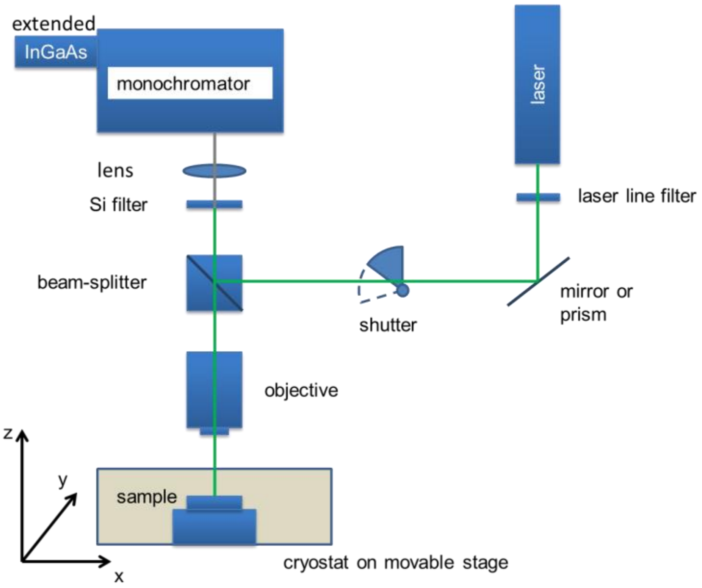

FIG. 4-5 Apparatus to collect the emission luminescence from germanium in a backscattering geometry. Shown is a set-up for micro-photo-luminescence measurements in which the luminescence is collected with a microscope objective.

5 $Si_{1-x}Ge_x$ stripe stressors for tensile strain creation in bulk Ge:

5.1 Functional principle of strain creation with SiGe stressors and sample preparation

The functional principle of the external SiGe stressors that are exploited to create tensile strain inside a germanium layer can be visualized with the analogy of a rubber strap under tensile strain: When it is scored or even cut completely, it immediately shrinks at the scratch or slit that has been created. This shrinkage is due to a driving force that tends to relax the strap.

In the samples investigated in this thesis, the strained rubber band is realized as highly tensile layer made of SiGe grown on Ge. FIG. 5-1 shows sketches in cross section of the sample preparation and functional principle of SiGe stressors on a bulk-like Ge virtual substrate.

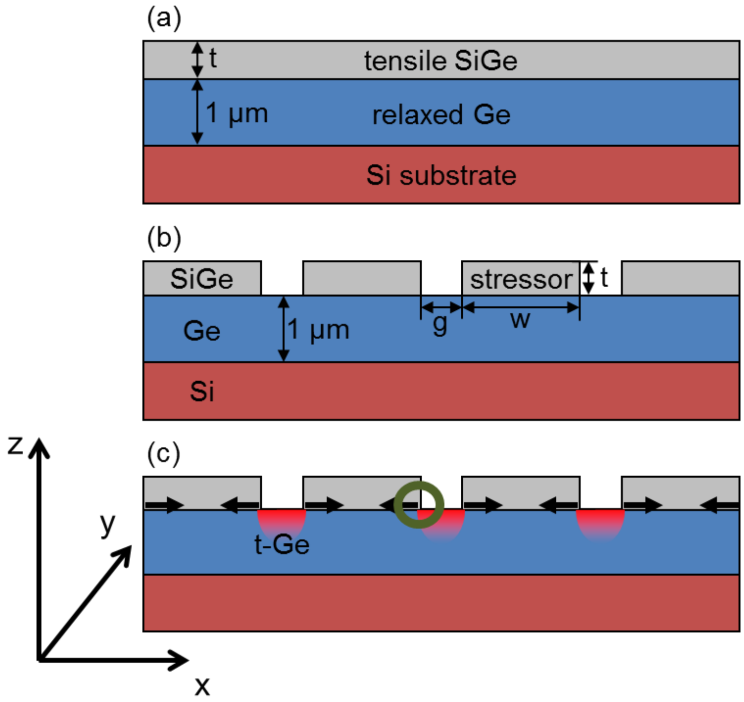

FIG. 5-1 Sketches of the preparation and functional principle of the system of SiGe stressors on Ge. (a) Coherent hetero-epitaxial growth of SiGe with thickness *t* on a Ge virtual substrate results in a highly tensile SiGe layer. (b) Patterning of the tensile SiGe layer in stripe stressors with thickness *t* and width *w*. Adjacent stressors are separated by a gap with width *g*. (c) The patterning permits the SiGe stressors to relax along direction *x* at the created gap. The restoring forces acting at the perimeters of the stripes are indicated by arrows. They constitute pulling forces on the Ge inside a gap that have largest magnitude at the junction of SiGe with Ge directly at the gap; this region is highlighted with a circle. Ge inside a gap results to be tensile (t-Ge, distinguished with red color).

A 1 µm thick germanium virtual substrate is grown on a Si(001) substrate. It is characterized by complete plastic relaxation. On top of germanium, SiGe is grown so that it adapts its lattice constant to that of the germanium virtual substrate. Since SiGe has got a smaller lattice constant than Ge, it results in a layer under tensile strain which is the crucial prerequisite to work as stressor. In this thesis, we investigate SiGe alloys with nominal germanium molar fractions of $x = 50\%$ and $x = 40\%$ that have got a lattice constant 2.1% and 2.5% smaller than germanium, respectively. At this point, it is important to remind that coherent hetero-epitaxial growth is limited by the critical thickness and the region of metastability. Consequently, the SiGe layer thicknesses t (cf. FIG. 5-1 and Table 5-1) that can be reached when using SiGe with 50% or 40% germanium, are limited and different from each other, since in the layer with 40% germanium a larger amount of elastic energy is stored due to the higher misfit strain with Ge.

In the next step, the SiGe layer is patterned into stripe stressors. This is done by etching trenches in it that then result in the gaps between two stripe stressors. The gap width *g* is varied from 18 nm to 45 nm in different samples. Relaxation of the SiGe stripe stressors takes place at their sidewalls (perimeters). Thereby, the Ge under a SiGe stripe stressors is compressed. However, the restoring force inside the SiGe stressor acts as a pulling force on Ge inside a gap between two stressors. This force is highest at the very junction of SiGe and Ge, see FIG. 5-1 For this reason, to maximize the pulling force on Ge, it is of outstanding importance that the trench inside SiGe is etched down exactly to the interface with Ge. If the etch would stop before the interface, the highest forces would act on a remaining shallow SiGe layer and not on Ge. In addition, also a too deep etch that corrodes the Ge inside the gap is harmful since it removes that portion of Ge which would otherwise be subject to the highest strain values.

We point out that with this method of SiGe stressors, strain is created locally inside the Ge virtual substrate. The strained Ge volume depends on the gap width between two stripe stressors. This will lead to implications discussed later in this thesis.

For our method it is crucial that the SiGe layer is coherently grown onto the Ge layer beneath and is thus highly tensile. Coherent hetero-epitaxial growth of SiGe with high Si content on a Ge virtual substrate can be achieved by low energy plasma-enhanced chemical vapor deposition (LEPECVD).[98]

We start our investigation with SiGe stressors on 1 μm thick Ge layers that can be considered bulk like from a structural point of view. Table 5-1 summarizes the samples under investigation and their main features. Further specific details will be given in the subsequent sections.

Table 5-1. Details of samples featuring SiGe stripe stressors on bulk-like Ge virtual substrates.

wafer	dies	$Si_{1-x}Ge_x$ composition	$Si_{1-x}Ge_x$ thickness
9184	E9, G6, G7	x = 52.39%	56 nm
9431	C8a, C8b, C9	x = 45.39%	28 nm

5.2 SiGe stressors along <100>

As seen in sec. 2.3, uniaxial tensile strain in direction <100> reduces the energy barrier between L and Γ valleys in the conduction band and can eventually lead to a crossover of the direct gap with the indirect gap. This situation would be favorable in terms of enhancing the excited electron population in Γ and increasing the rate of radiative emission.

We prepared samples with $Si_{50}Ge_{50}$ and $Si_{60}Ge_{40}$ stripe stressors along <100>. The uniaxial strain induced into the Ge layer is perpendicular to the longitudinal axis of the stressor stripes, and hence also in a direction belonging to the <100> family.
However, we were not able to detect a Raman signal from the Ge inside the gaps between the stripe stressors. This is due to the Raman selection rules and the peculiar geometry of stripes and can be explained as follows:

We found, that the stripe pattern acts as a grid polarizer, i. e. light with the polarization in parallel to the stripes is blocked by the stripes pattern and light with the polarization perpendicular to the stripes can pass.

To probe the Ge inside the gaps, we thus have to select the laser polarization to be perpendicular to the stressors. Let us assume that the longitudinal axis of the stripes is along y = [010]. Then, the uniaxial stress on Ge would be applied in direction x = [100] and also the laser polarization has to be in direction x.

However, the Raman selection rules for polarization, cf. sec. 3.1, lead to a rotation of 90° of the scattered light with respect to the incident light, i. e. the Raman signal originating in Ge is polarized along direction y and consequently blocked by the stripe pattern acting as a grid polarizer. We are not able to detect it.

A rotation of the sample by 45°, so that the polarizer is in the intermediate position, did not lead to a detectable signal.

To be able to prove the effectiveness of the stripe stressors, we decided to prepare the stripe pattern along the crystallographic directions <110>. In this case, there is no rotation of the polarization of the scattered light due to the Raman selection rules.

However, by applying tensile strain along <110>, no crossover between direct and indirect gap can be reached. Tahini et al. [117] report a crossover for 1.71% tensile strain in this direction, but their calculations can be doubted, since it seems that the split of the L valley degeneracy has been neglected. But it is this split, that prevents the direct/indirect gap crossover, as seen in the results from Liu et al. [111] replotted in FIG. 2-18.

In the following, we present our results on stripe stressors along <110>.

5.3 $Si_{50}Ge_{50}$ stressors along <110>

In a previous work we have already investigated the strain created by SiGe stripe stressors with 50% of Ge directed along <110>.[60] The results are reported in the following:

5.3.1 Sample preparation of $Si_{50}Ge_{50}$ stressors on bulk germanium

The SiGe/Ge stack is grown on a Si(001) substrate with the low-energy-plasma enhanced chemical vapor deposition technique (LEPE-CVD) at L-NESS in Como. Details to this non-standard growth method are given in sec. 2.2.5. Growth of the Ge virtual substrate is accomplished at a deposition temperature of about ~ T_{dep} = 500 °C, followed by cyclic annealing between ~ 600 °C and 800 °C to reduce the threading dislocation density in the Ge layers. The SiGe layer of nominally 50% germanium was deposited at about 500 °C and has got a layer thickness of 56 nm.

After the growth the SiGe layer is patterned to form the SiGe stressors. Nanostructuration was performed by the team of Dr. Bollani in Como. The samples with bulk-like Ge feature stripe SiGe stressors along <110> that are obtained by etching parallel trenches into the SiGe layer. To this aim, a mask of poly(methyl methacrylate) (PMMA) is applied on top of the hetero-structure and the desired pattern is transferred to the mask using electron-beam lithography (EBL). Subsequently, the actual etching of SiGe is performed with reactive-ion etching (RIE). We want to stress again that the etching process is crucial for the strain transfer from the tensile SiGe stressors to the Ge between two stressors. FIG. 5-2 (a) shows a micrograph of the sample in which different regions can be identified. Besides the actual stripe pattern of dimensions 25 µm × 25 µm, the sample features a flat part containing the original SiGe/Ge/Si stack and a Ge window in which the SiGe top layer was removed down to the Ge virtual substrate. Panel (b) shows a scanning electron micrograph of the stripe stressors of a representative pattern engraved into the Si$_{50}$Ge$_{50}$ layer. Samples with gap width g = (20 ± 5) nm to g = (45 ± 5) nm have been realized. The length of the stripes is 25 µm along direction y in FIG. 5-1.

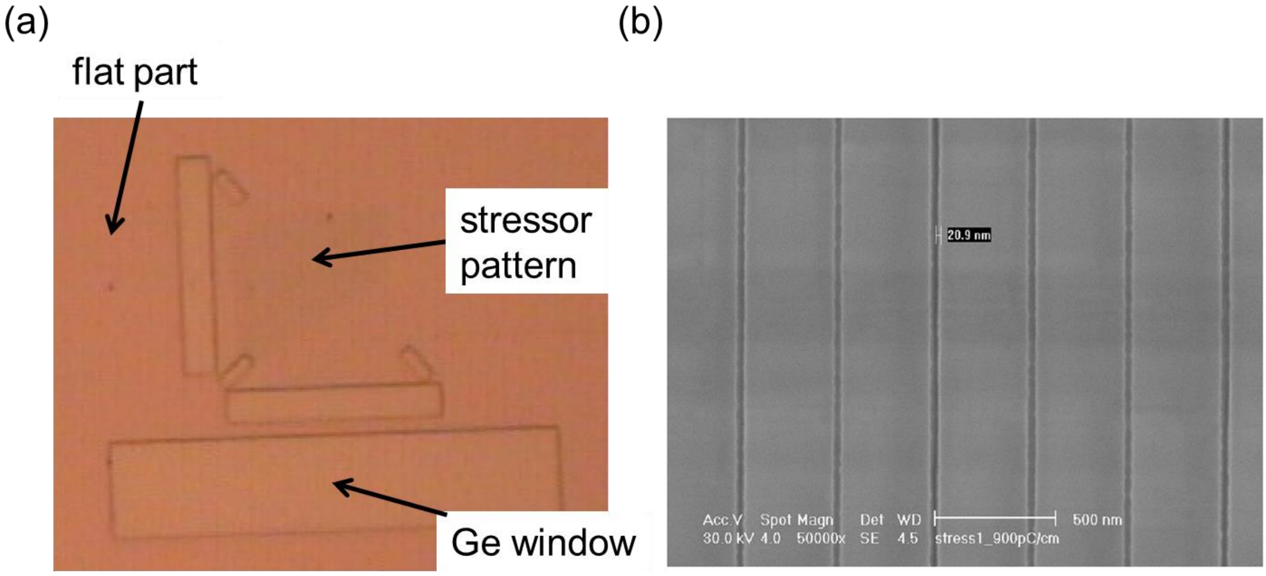

FIG. 5-2 (a) Micrograph of the sample showing the different regions. The stressor pattern can be recognized in the middle of the image. (b) Scanning electron micrograph (SEM) of a representive pattern of Si$_{50}$Ge$_{50}$ stripe stressors on a Ge virtual substrate extending along the <110> crystallographic direction (sample 9184-G6). The etched gap between two SiGe stripe stressors is (21 ± 5) nm.

5.3.2 Samples with Si$_{50}$Ge$_{50}$: XRD analysis

High resolution X-ray diffraction (XRD) around the (0 0 4) and grazing-incidence (2 2 4) Bragg peaks was employed to determine strain and chemical composition (germanium content x) of the SiGe/Ge stack after growth and before creation of the SiGe stressors. This task was executed by Dr. Chrastina from Politecnico di Milano in Como. The germanium content x_{VS} of the Ge virtual substrate is determined to be $x_{VS} =$ 99.32% and a slight tensile strain of $\varepsilon_{||}$ = 0.1369% is revealed in it. The tensile strain can be explained with the growth and annealing of Ge on Si at temperatures higher than room temperature and the different thermal expansion coefficient of Ge and Si.[40] For the SiGe layer we obtain a Ge content $x_{\text{stressor}} =$ 52.39%. The strain measured in this layer amounts to $\varepsilon_{||}$ = 2.0755%, corresponding to an in-plane stress of $\sigma_{||}$ = 3.3217 GPa. The SiGe layer showed signs of relaxation (x-ray peak laterally broadened, no thickness fringes) with an estimated relaxation β ~ 5% with respect to the Ge-VS. Hence, there might be defects at the SiGe/Ge interface. However, the estimated relaxation β ~ 5% of the SiGe layer is not significant and the layer is still highly strained, the prerequisite to act as SiGe stressor.

5.3.3 Raman strain analysis Si$_{50}$Ge$_{50}$ stressors

The challenge in the determination of the strain created by the SiGe stressors is that the gap between the stressors is of a size of a few nano-meters. The micro-X-ray diffraction system employed in Como has got a spot diameter in the micro-meter range. Also with more advanced X-ray technologies like diffraction with synchrotron radiation, it is not possible to resolve the nano-meter gaps between the SiGe stressors. Since SiGe stressors induce tensile strain only locally and due to the complete penetration of the sample by the X-rays, also the Ge portion under the SiGe stressors, which is compressed, and the vast relaxed bulk material are probed and it is unlikely that the strain induced by the SiGe stressors can be discriminated. For this reason, we employ micro-Raman spectroscopy to investigate the action of the SiGe stressors. Micro-Raman spectroscopy has been performed using the setup described in section 3.7. The scattered laser radiation was the 457.9 nm line of an argon-ion laser and the objective had a magnification of 100× with numerical aperture N. A. = 0.90. The system was calibrated with a relaxed Ge crystal to a Raman shift of 300.3 cm^{-1} and the laser fluence was controlled to prevent heating artefacts. The power incident on the sample was of the order of 1 mW for all these measurements.

In the diffraction limit, the laser is focused to a spot with diameter of about ~ 600 nm, a value still larger than the gaps between the SiGe stressors. However, the penetration depth of the blue laser light into the 56 nm thick $Si_{50}Ge_{50}$ stressors is 22 nm. Hence, the SiGe stressors are opaque for the laser and with Raman spectroscopy we only probe the Ge inside a gap between two SiGe stressors. Nevertheless, the Ge-Ge mode of the Raman signal originating in the $Si_{50}Ge_{50}$ stressors is closely located to the Raman signal from the strained Ge and has to be subtracted from the overall spectrum obtained in a measurement. This subtraction will be described in detail in the discussion of the Raman spectra from samples with $Si_{60}Ge_{40}$ stressors, see sec. **Errore. L'origine riferimento non è tata trovata.**.

FIG. 5-3 shows calculations by the finite element method (FEM) of the strain distribution around the gap between two stripe stressors for different gap width *g*.

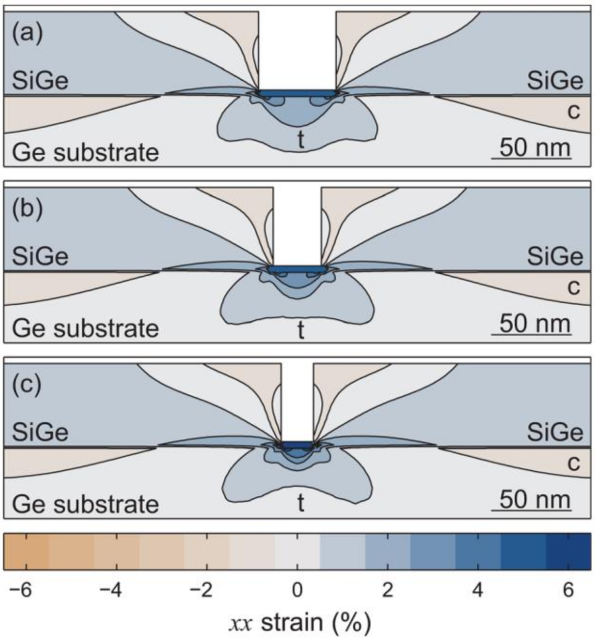

FIG. 5-3. Calculations of the strain distribution inside a Ge virtual substrate and SiGe stripe stressors with Ge molar fraction *x* = 50%. Calculations are performed with the finite element method (FEM). Shown are stripe stressors separated by gaps of (a) *g* = 45 nm, (b) *g* = 30 nm, and (c) *g* = 20 nm. The stripe relaxation is the same in all three cases. Since the highest stress on the Ge substrate is reached close to the perimeter of a stripe, the highest strain induced into Ge is achieved with the narrowest gap of *g* = 20 nm. (Figure taken from Bollani et al. [60])

When the width of the SiGe stripe exceeds a certain limit, its relaxation does not depend on its with anymore. In the three cases displayed by FIG. 5-3, we can assume that the single stripe stressors exert the same force on the Ge virtual substrate and induce each a certain strain in it. Since the strain field of adjacent stripe stressors overlaps additively, the reached strain value is higher when the gap is smaller.

This behavior could also be detected with micro-Raman spectroscopy. FIG. 5-4 shows the Raman signal originating in the flat $Si_{50}Ge_{50}$/Ge stack and these of stripe patterns with gap widths g = 45 nm, 30 nm and 20 nm. The Raman wavenumber for the flat part is at about 300.0 cm^{-1} and therefore slightly shifted to lower Raman shift values with respect to the calibration with relaxed Ge. This is in agreement with the X-ray strain analysis that revealed a slight tensile strain in the Ge virtual substrate. Note, in order to obtain the Raman signal from the flat stack, we had to use a 532 nm laser line for which the $Si_{50}Ge_{50}$ layer is transparent. The measurements on the stressor patterns are then carried out with 457.9 nm excitation as discussed above. Their results show decreasing Raman shift values for decreasing gap width, meaning that the Ge inside the smallest gaps is strained the most.

The strain in the 25 µm long gaps induced by two adjacent stressors is of uniaxial nature. The conversion of Raman shift into strain is hence done by using the uniaxial strain shift coefficient discussed in section 3.3.2. However, due to the thermal strain of the Ge virtual substrate, there is also a small strain component longitudinal to the gap. We took account of this by using an offset of -0.3 cm^{-1} for the relative Raman shift induced by the stripe stressors.[60] Hence, we applied the following formula for the Raman shift/strain conversion: $\Delta\omega(\varepsilon_{xx}) = -225 \cdot \varepsilon_{xx}\ \mathrm{cm}^{-1} - 0.3\ \mathrm{cm}^{-1}$.

The obtained strain values are displayed on the top axis of FIG. 5-4 which is reprinted from Bollani et al..[60] Note that the peak value for the sample with stripe stressors separated by a gap of 20 nm reaches about 5% tensile strain which would overcomes the strain value needed for a transition of the electronic band structure of germanium into a direct gap one.

The obtained Raman scattering from the Ge inside the stripes is broadened significantly with respect to the Raman spectrum of the flat part. This is due to the inhomogeneous strain distribution created by the stressors as calculated by FEM and depicted in Fig. FIG. 5-3. We extract the strain distribution along the vertical direction from the Ge surface down to the bulk from the FEM calculation. To account for the attenuation of the penetrating laser probe, the frequency of the strain values is weighted with an exponential function with characteristic length $d_p/2$, where d_p is the penetration depth into Ge. The strain distribution is then plotted in a histogram with a $\Delta\varepsilon = 0.5\%$ strain interval. The histograms for different gap sizes are also shown in FIG. 5-4 together with the corresponding Raman spectra. The good agreement underlines that with the method of subtraction of the SiGe contribution from the complete Raman spectrum of the stripe pattern, we obtain a true Raman spectrum from Ge inside the gap.

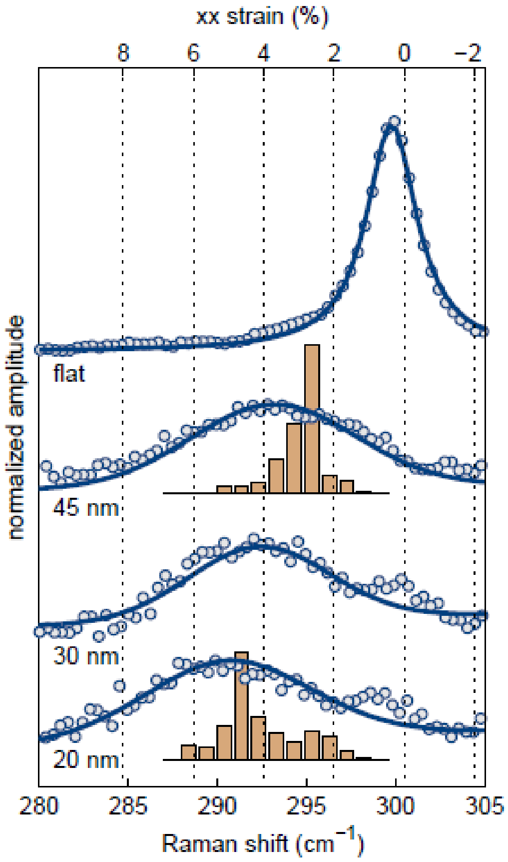

FIG. 5-4 Raman signal originating in Ge from (top to bottom) the flat $Si_{50}Ge_{50}$/Ge stack, a stripe stressor pattern with gap width g = 45 nm, g = 30 nm, and g = 20 nm. The top axis features a scale of strain values obtained by conversion of Raman shift into strain. The Ge spectra for the 45 nm gap and the 20 nm gap are compared with the strain histograms extracted from FEM calculations, cf. FIG. 5-3. (Figure taken from Bollani et al. [60])

5.4 $Si_{60}Ge_{40}$ stressors along <110>

As shown, we have obtained highly strained Ge with $Si_{50}Ge_{50}$ stressors separated by a 20 nm wide gap. These 20 nm of highly strained material correspond only to a small volume of strained Ge in terms of exploitation of Ge as active material for potential light emitting or detecting applications.

The separation of the stripe stressors and hence the strained Ge volume may be enlarged if the pulling force at the stressor perimeter was increased. This pulling force originates in the elastic relaxation of the SiGe layer under tensile strain upon patterning the stripes. It may be increased by increasing the tensile load in the SiGe layer. For this purpose, we have prepared samples with a $Si_{60}Ge_{40}$/Ge stack with germanium content x = 40% in the SiGe top layer. In this case, the lattice mismatch of SiGe and Ge amounts to 2.5% compared to 2.1% with a $Si_{50}Ge_{50}$ alloy with x = 50%.

However, due to the higher lattice mismatch between virtual substrate and epitaxial layer, the critical thickness before onset of plastic relaxation in the SiGe layer is reduced with respect to the 50% alloy. Scopece et al. have simulated the strain induced into bulk Ge by SiGe stripe stressors and found that the strain decreases with decreasing stressor thickness. Hence, the advantage by the higher mismatch strain could be undone by the lower stressor thickness in $Si_{60}Ge_{40}$ stressors. On the other hand, the lower thickness of the $Si_{60}Ge_{40}$ layer might be advantageous in terms of etching the trenches, since less deep trenches have to be etched. The fact that the trenches will be less deep could also facilitate the probe of the Ge inside the trenches in the sense that the exciting wavefront is less attenuated by the more shallow trenches.

5.4.1 $Si_{60}Ge_{40}$ stressor preparation

We have prepared samples with $Si_{60}Ge_{40}$ stripe stressors by growing a Ge virtual substrate on a Si(001) wafer with LEPECVD followed by the growth of the SiGe layer on Ge. The growth of the Ge virtual substrate is performed with the same recipe than in the previous case of samples with $Si_{50}Ge_{50}$ stressors (deposition temperature T_{dep} = 500 °C, followed by cyclic annealing between ~ 600 °C and 800 °C). The modified germanium content of the stressor $x_{\text{stressor}} = 40\%$ needs an adjustment in growth temperature to reach maximum thick layers before plastic relaxation sets in. For this reason, the deposition temperature for $Si_{60}Ge_{40}$ was 400 °C. The deposited stressor layer thickness is estimated to be 28 nm.

Stripe stressors were created by etching trenches into the SiGe layer. The trenches are defined in a mask of PMMA applied on top of the hetero-structure by electron-beam lithography (EBL). Subsequently, the trenches are etched with reactive-ion etching (RIE). We want to stress again that the etching process is crucial for the strain transfer from the tensile SiGe stressor to the Ge between two stressors. For this reason, different etching times are tested for the $Si_{60}Ge_{40}$ stressors.

The created stripes are parallel to the <110> crystallographic direction. Several patterns with different stripe widths w and gap widths g between adjacent stripes have been realized ranging from $w = (373 \pm 5)$ nm to (488 ± 5) nm and $g = (18 \pm 5)$ nm to (35 ± 5) nm, cf. FIG. 5-1 for a sketch of the samples with indication of the geometric dimensions. FIG. 5-5 (a) depicts the different regions of the samples and panel (b) shows a scanning electron micrograph of the stripe stressors of a representative pattern. The length of the trenches engraved into the $Si_{60}Ge_{40}$ layer is 25 µm along direction y in FIG. 5-1.

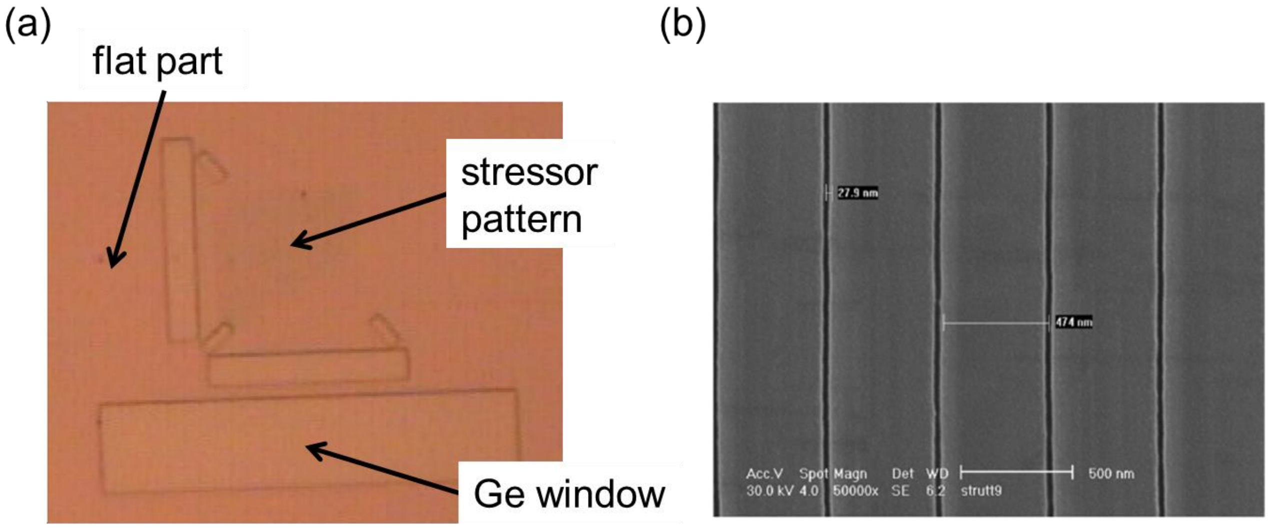

FIG. 5-5 (a) Different regions of the sample: stressor pattern, flat part containing the flat stack of $Si_{60}Ge_{40}$/Ge/Si, and Ge window with the SiGe layer removed. (b) Scanning electron micrograph (SEM) of a representative pattern of $Si_{60}Ge_{40}$ stripe stressors on Ge extending along the <110> crystallographic direction. The gap width is g = 27.9 nm.

5.4.2 Samples with $Si_{60}Ge_{40}$: XRD analysis

High resolution x-ray diffraction (XRD) around the (0 0 4) and grazing-incidence (2 2 4) Bragg peaks revealed a germanium content of $x_{VS} = 99.78\%$ in the Ge virtual substrate and an in-plane strain $\varepsilon_{||,VS} = 0.1654\%$ in line with growth and annealing of Ge on Si at elevated temperatures. The germanium content in the SiGe layer is determined to be $x_{\text{stressor}} = 45.39\%$. The in-plane strain $\varepsilon_{||}$ is equal to $\varepsilon_{||,\text{stressor}} = 2.4961\%$ which corresponds to a stress of $\sigma_{||} = 4.0624$ GPa. Hence, the SiGe layer is fully strained (sharp x-ray peak with thickness fringes, relaxation β ~ 1%) and thus coherently grown on Ge, so there should not be any defects at the SiGe/Ge interface.

5.4.3 Raman strain analysis $Si_{60}Ge_{40}$ stressors

Micro-Raman spectroscopy has been performed using the setup described in section 3.7. The scattered laser radiation was the 457.9 nm line of an argon-ion laser focused to a spot of about ~ 600 nm in diameter by a 100× objective with numerical aperture N. A. = 0.90. The laser fluence was controlled to prevent heating artefacts. The system is calibrated for a Raman signal of relaxed Ge at 300.3 cm^{-1}.

The new challenge in these measurements is that the 28 nm thick $Si_{60}Ge_{40}$ stripe stressors are not thick enough to prevent complete penetration through the excitation laser and hence work as a blocking layer to prevent probing of Ge beneath the stripes. We thus expect, that in the Raman spectrum acquired on a stripe pattern, besides the Ge inside the gaps there is also a contribution from the Ge beneath the stripes. However, the Ge beneath the stripes is expected to be slightly compressed or relaxed, as one can see from the sketch of FIG. 5-1 and the FEM calculations in FIG. 5-3 so that we are still able to discriminate the effect of the stripe stressor on the material inside the gaps.

We start our analysis by verifying the small thermal strain remaining in the Ge virtual substrate after growth. FIG. 5-6 (a) shows the Raman spectrum of a relaxed Ge bulk crystal used for calibration of the system together with the spectrum originating in a region of the sample where the top $Si_{60}Ge_{40}$ has been removed so that we can directly probe the Ge virtual substrate, cf. FIG. 5-5. The band of the Ge virtual substrate of the sample is shifted to lower Raman shifts by -0.6 cm^{-1}, i. e. it is under tensile strain. This strain is due to the growth procedure and hence of biaxial nature so that we can use the biaxial strain shift coefficient $b = 450\ cm^{-1}$, as discussed in sec. 3.3.1. We obtain a strain $\varepsilon_{||} = (0.13 \pm 0.09)\%$ confirming the X-ray diffraction analysis after growth. The barely lower strain value might be explained by the fact that the Raman measurement was performed in a window etched in $Si_{60}Ge_{40}$. The surrounding $Si_{60}Ge_{40}$ is tensile and tends to shrink at the perimeter of the window. The contracting perimeter might exert a compressing force on the Ge inside the window.

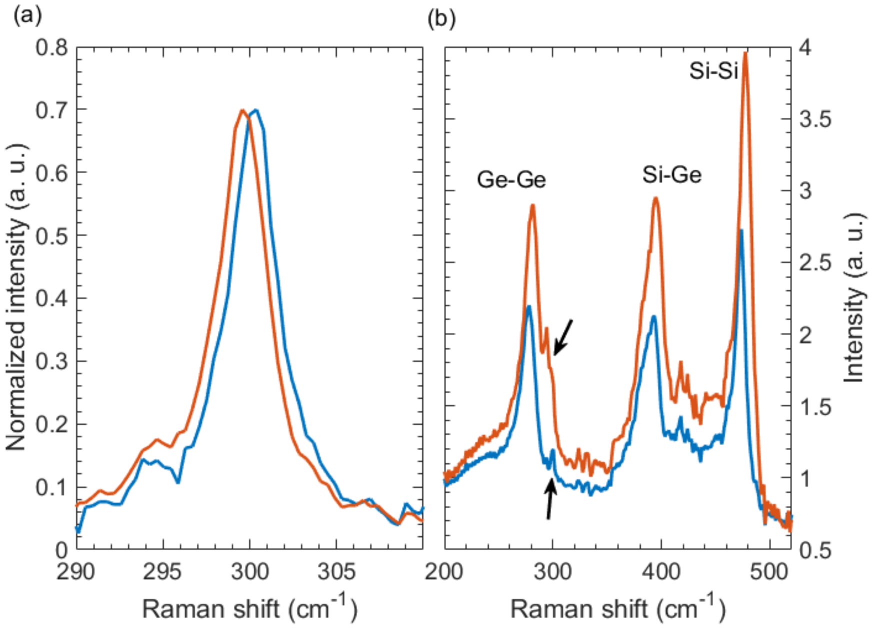

FIG. 5-6 (a) Calibration of the apparatus to collect the Raman spectra has been performed with a relaxed Ge crystal to obtain the Ge Raman mode at a wavelength of $\omega(\mathrm{Ge_{rel}}) = 300.3\ \mathrm{cm^{-1}}$ (blue curve). The probed Raman mode of the Ge virtual substrate of the stressor samples is shifted to lower wavenumbers indicating slight tensile strain (orange curve). (b) Raman spectra of the flat (blue curve) and stripe-patterned (orange curve) $Si_{60}Ge_{40}$/Ge stack. The three Raman modes typical for SiGe are present: Ge-Ge, Si-Ge and Si-Si. The $Si_{60}Ge_{40}$ is not completely opaque to the excitation wavelength so that in addition the Ge virtual substrate is probed in the flat part of the sample (small feature at 300 cm^{-1} indicated by an arrow). The Raman signal originating in the Ge inside the gaps in the stripe pattern constitutes a shoulder to the Ge-Ge mode of the SiGe stressors (indicated by an arrow).

Fig. FIG. 5-6 (b) shows representative Raman spectra originating in the flat $Si_{60}Ge_{40}$/Ge stack and the one of the stressor pattern. Both spectra show the characteristic three Raman modes of the SiGe alloy: Ge-Ge, Si-Ge and Si-Si. Since in the alloy the Si content is higher than the Ge content, the Si-Si mode is more intense.

We further note the small peak in the spectrum from the flat part at 300 cm^{-1} that is present in all samples (indicated by an arrow in FIG. 5-6) and can be attributed to the Ge virtual substrate. As pointed out previously, the SiGe layer in these samples is not completely opaque anymore to the excitation wavelength.

In all spectra from the stressor patterns, we can identify a shoulder at the high wavenumber side of the Ge-Ge mode. This shoulder is not present in the spectra from the flat stack and originates in the strained Ge inside the gaps between the stressors. Our expectation, that in the $Si_{60}Ge_{40}$ samples the excitation power inside the gap is higher than in the case of $Si_{50}Ge_{50}$ stressors, where the trenches that constitute the gap between the stressors is deeper, is matched.

From the peak positions of these three bands we can determine the composition x and strain ε of the SiGe layer.[157] Both composition and strain influence the peak wavenumber $\omega(x, \varepsilon)$ of the three SiGe Raman modes. By plotting all three mode equations in an ε-x space, the intersect of the three curves gives the strain and composition of the alloy in question. For the flat part we obtain $x = (43.3\ \pm 3.2)\%$ and $\varepsilon_{||} = (2.50\ \pm 0.24)\%$ averaged over all samples in very good agreement with XRD.

We note that the Raman modes in the spectrum from the stressor pattern are shifted with respect to the flat stack. This is due to the partial relaxation of the SiGe stressor layer when elastic energy is transferred from SiGe to Ge. The relaxation of the stripe stressors starts from its sidewalls created during the etch. Hence, the strain field inside a stripe stressor is highly non-uniform, cf. FIG. 5-3. The degree of relaxation of the stripes should therefore depend on its width w. A narrower stripe may be relaxed to an higher degree than a wider stripe.

The relaxation of the stripe stressor is along its transversal direction, hence it is uniaxial. We can discuss the relaxation of the stripe stressors in two ways. First, we can give a value for the uniaxial strain relaxation β by comparing the peak positions of the Ge-Ge mode in the stripe pattern and on the flat part of the sample. Pezzoli et al. [145] showed that the biaxial strain-shift coefficient is constant for all SiGe compositions. We can assume that this holds true for the uniaxial strain shift coefficient as well. With a uniaxial strain shift coefficient u = -225 cm^{-1} (cf. sec. 3.3.2) we can derive the uniaxial strain relaxation β by solving $\omega_{\text{stressor}} - \omega_{\text{flat}} = u \cdot \beta$.

The obtained values are reported in Table 5-2. Roughly, we can distinguish two groups: the samples with etching times of 52 s and 58 s have got similar relaxation with average value $\beta = -(1.6 \pm 0.4)\%$. Samples with etching time 46 s have got a slightly lower relaxation of about $\beta = -(1.3 \pm 0.5)\%$.

Both values are a distinct reduction in strain compared to the as-grown $\text{Si}_{60}\text{Ge}_{40}$ layer. This underlines the concept of a SiGe stressor: Elastic energy stored in the grown flat SiGe layer is transferred to the Ge beneath upon patterning of the SiGe layer. Relaxation values are independent of the stressor width w from which we conclude that w = 380 and w = 480 are both too large to discriminate differences in their relaxation.

The second approach would be to use the methods of the intersection of the three Raman modes in the composition/strain space. This method is strictly speaking valid only for biaxial strains. Since the relaxation of the stripe stressors takes place in one direction only, the in-plane strain values ε_{xx} and ε_{yy} differ and the strain is not biaxial anymore. The application of this method leads then to equivalent biaxial strain values $\varepsilon_{\text{stressor,equ.}}$. Results are reported in Table 5-2.

For etching times of 58 s and 52 s, the remaining strain in the stripes stressors is about $\varepsilon_{\text{stressor}} = (1.8 \pm 0.2)\%$. For a shorter etch time of 46 s we find a slightly higher remaining strain of $\varepsilon_{\text{stressor}} = (2.1 \pm 0.2)\%$. For the same etching time, the strain inside the stripe stressors is the same within its error for stripes of widths $w \approx 380$ nm and $w \approx 480$ nm. The observation that the samples with 46 s show slightly higher remaining strains $\varepsilon_{\text{stressor,equ.}}$ is probably an indication that the etch is not reaching down to the SiGe/Ge interface. The sidewalls of the SiGe stressors are thus lower and relaxation of the SiGe stripe stressor is less. This should also reduce the strain created inside Ge in the gap between two stripes, the analysis of which is discussed in the following.

5.4.4 $\text{Si}_{60}\text{Ge}_{40}$ stressors: strain inside Ge

In FIG. 5-6 (b) we have seen that the $\text{Si}_{60}\text{Ge}_{40}$ layer is not completely opaque and also the Ge material beneath the SiGe top layer is probed. To extract the Raman scattered light originating in the Ge of the gaps between the stripe stressors only, the method of subtracting the spectrum of the flat part from the spectrum of the stripe pattern is considered the appropriate approach. In FIG. 5-6 (b) we have furthermore seen that the Raman modes in the spectra from the flat part and the pattern are not in the same peak positions. Moreover, since the $\text{Si}_{60}\text{Ge}_{40}$ layer possesses an inhomogeneous strain distribution, the bands of its Raman spectrum are broader than in the case of the flat stack. It proved very helpful to perform the subtraction with a spectrum of the flat part of the sample in close proximity to a stripe pattern. In this part, the Raman modes of the SiGe alloy result to have nearly the same width as in the stripe pattern (not shown). In this way, the Raman spectrum of the flat part only has to be shifted to higher wavenumbers and adjusted to match the intensity of the Ge-Ge mode of the Raman spectrum of the pattern as demonstrated in FIG. 5-7 (a). Then the subtraction can be executed easily and the difference signal is attributed to the Raman scattering from the Ge inside the gaps. A representative result is shown in FIG. 5-7 (b). This difference spectrum is fitted with a mixed Lorentzian-Gaussian to determine its peak position ω_{Ge}.

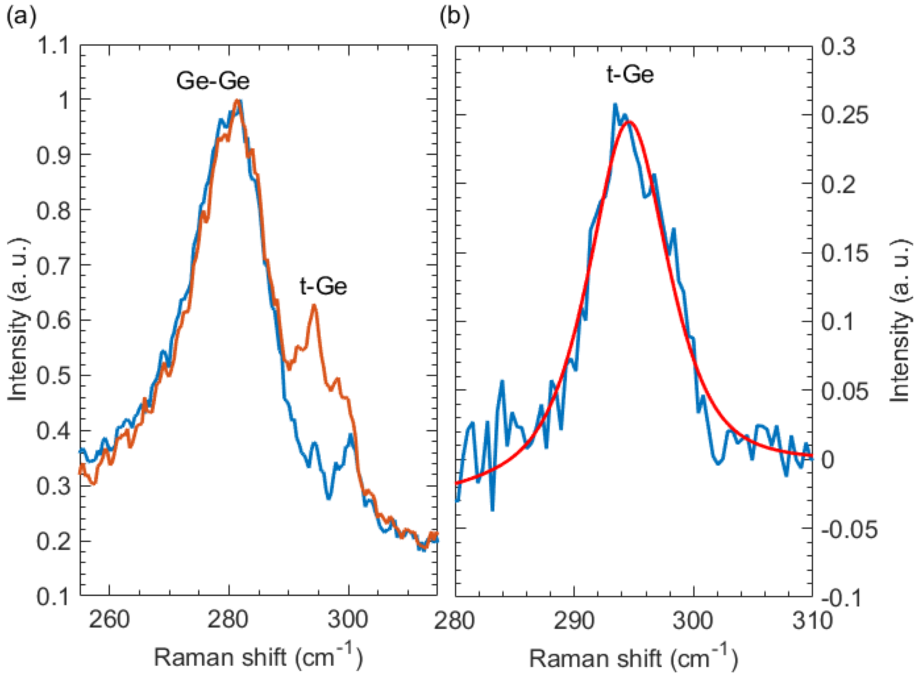

FIG. 5-7 (a) Details of the Raman spectra obtained from the flat stack (blue) and the stripe pattern (orange). Both spectra show the Ge-Ge mode of the SiGe top layer. In the spectrum from the flat stack, a small peak at 300 cm-1 can be identified that originates in the Ge virtual substrate below the SiGe layer. The spectrum from the stripe pattern shows a clear peak from tensile Ge inside the gap between two SiGe stripe stressors. (b) Difference spectrum of the spectra in (a), corresponding to the spectral contribution from Ge strained by SiGe stripe stressors. The difference spectrum is fitted to quantify the induced relative Raman shift.

The peak wavenumbers obtained for the different samples are listed in Table 5-2 together with an estimated error that takes into account the following error sources:

- error in the subtraction of spectra: 0.6 cm^{-1}
- error of the fit: 0.2 cm^{-1} to 0.6 cm^{-1}
- resolution of the apparatus: 0.5 cm^{-1}
- error of the apparatus calibration: 0.5 cm^{-1}

Since these are independent error sources, we estimate the final error for the measurement results as the root of the sum of squares. This error is also given in the table.

The Ge virtual substrate is already pre-strained through the thermal strain originating in the growth of Ge on Si. In the previous discussion we found that for this reason the Raman shift of the Ge virtual substrate is already shifted by -0.6 cm^{-1} with respect to relaxed Ge. To calculate the strain that is caused by the presence of the stripe stressors only, we have to take this strain bias into account. Again we use an uniaxial strain shift coefficient of -225 cm^{-1} (cf. section 3.3) and obtain the stressor induced strain by using the relation $\Delta\omega(\varepsilon_{xx}) = -225 \cdot \varepsilon_{xx}\,\mathrm{cm}^{-1} - 0.6\,\mathrm{cm}^{-1}$. The strain values are reported in Table 5-2.

The highest strain value reached is that of ε_{Ge} = (2.80 ± 0.44)% for a 21 nm wide gap. This value comes short in comparison with the value of 4.3% obtained with $Si_{50}Ge_{50}$ stressors of a comparable gap width. As we can see from the results obtained and tabulated in Table 5-2, for the same gap width the strain created in Ge depends on the etching time. As discussed in section 5.1, the etch of the trenches to create the stripe stressors is a crucial process step. From the fact that with a 28 nm gap higher strain is reached with 58 s etching than with 52 s etching, we conclude that the former is the better etching time. A sample with 21 nm gap and 58 s etch is thus suspected to outplay the

2.8% strain obtained with 52 s. Inside a set of samples with the same etching time, the strain increases with decreasing gap width, as expected. On the other hand there is no dependence on whether the gap width is ~ 380 nm or ~ 480 nm. FIG. 5-8 reports the dependence of strain on the gap width for the different etching times. As seen in the discussion of the relaxation of the stressor stripes, both stressor widths w are too long to discriminate differences and can be considered infinitely large and no appreciable increase of strain is expected.[61]

Table 5-2 Sample details and results of the Raman analysis. Time of reactive-ion etching t_{etch} and obtained gap and stressor widths, g and w, respectively. Uniaxial relaxation and equivalent biaxial strain values of the $Si_{60}Ge_{40}$ stressors, β and $\varepsilon_{stressor,equ.}$. Raman shifts ω_{Ge} of the tensile Ge inside the gap as well as calculated uniaxial strain ε_{Ge} obtained in Ge.

die	pattern	t_{etch} (s)	g (nm)	w (nm)	β (%)	$\varepsilon_{stressor,equ.}$ (%)	ω_{Ge} (cm^{-1})	ε_{Ge} (%)
C8a	3	58	28 ± 5	376 ± 5	-1.47 ± 0.36	1.80 ± 0.20	294.6 ± 0.9	2.27 ± 0.40
C8a	9	58	28 ± 5	474 ± 5	-1.47 ± 0.36	1.82 ± 0.20	294.5 ± 1.0	2.31 ± 0.44
C8b	3	52	28 ± 5	380 ± 5	-1.64 ± 0.36	1.80 ± 0.20	294.7 ± 1.0	2.22 ± 0.44
C8b	7	52	28 ± 5	474 ± 5	-1.64 ± 0.36	1.84 ± 0.20	294.8 ± 1.0	2.18 ± 0.44
C8b	9	52	21 ± 5	481 ± 5	-1.64 ± 0.36	1.80 ± 0.20	293.4 ± 1.0	2.80 ± 0.44
C9	2	46	18 ± 5	373 ± 5	-1.11 ± 0.36	2.07 ± 0.20	294.5 ± 1.1	2.31 ± 0.49
C9	6	46	21 ± 5	373 ± 5	-1.29 ± 0.36	2.05 ± 0.20	295.7 ± 1.1	1.78 ± 0.49
C9	8	46	21 ± 5	488 ± 5	-2.00 ± 0.36	1.66 ± 0.20	296.7 ± 1.1	1.33 ± 0.49
C9	12	46	18 ± 5	484 ± 5	-0.71 ± 0.36	2.19 ± 0.20	295.3 ± 1.1	1.96 ± 0.49

Moreover, from the point of strain simulations there is no increase in strain expected in the $Si_{60}Ge_{40}$ samples with respect to the $Si_{50}Ge_{50}$ samples. The fact, that the misfit between Ge virtual substrate and SiGe stressor is higher in the $Si_{60}Ge_{40}$ samples is mitigated by the reduce height of the stressors that can be realized. As shown by Scopece et al. [61] by means of FEM simulations, higher stressors transfer a higher strain into Ge. For a 20 nm gap, the 56 nm thick $Si_{50}Ge_{50}$ stressors should create about ~ 5% strain, a value close to what could be revealed by our measurements in section 5.2. On the other hand, the expected strain in a 20 nm gap with 28 nm thick $Si_{60}Ge_{40}$ stressors is about ~ 4% (for this estimation we took the Ge content $x_{stressor} \approx 45\%$ as determined by XRD and Raman).

As we have seen in sec. 3.2, alloying of Ge with Si downshifts the Raman wavenumber. However, we can exclude that the Raman shifts measured in this study are affected by a significant level of Ge-Si intermixing during growth of the SiGe layer using LEPECVD with which the intermixing has been shown to be negligibly low.[174]

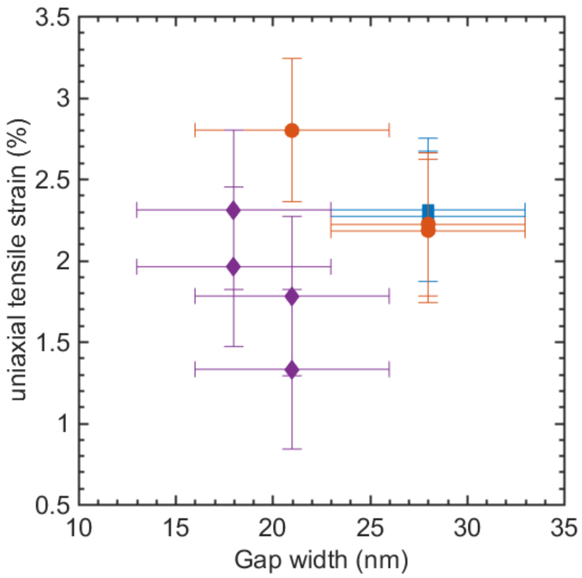

FIG. 5-8 Induced tensile strain through the $Si_{60}Ge_{40}$ stripe stressors in function of the gap width *g* between the stripe stressors. The gaps were etched using RIE for 46 s (◊), 52 s (○), and 58 s (□).

5.5 Photoluminescence of Ge strained by SiGe stripe stressors

In the previous sections we have introduced our concept of SiGe stressors and have presented bulk-like Ge grown on Si with SiGe stripe stressors. The Raman strain analysis of SiGe stripe stressors with nominal compositions $Si_{50}Ge_{50}$ and $Si_{60}Ge_{40}$ has shown that we reach high strain values exceeding 4% strain uniaxial.
In the following we are presenting our main results of the investigation of these samples by means of photoluminescence spectroscopy. The expectations for the investigation of tensile Ge are:

(1) the band-gap energy (indirect as well as direct gap) shrinks with tensile strain; the spectral features in the PL spectrum should be shifted to lower energies.
(2) due to the tensile strain, the energy barrier between L valleys and the Γ valley is reduced; the concentration of excess carriers in Γ should increase, which in turn should increase the intensity of the radiative recombination across the direct gap in strained Ge.

As discussed in sec. 5.2, micro-Raman measurements on SiGe stripe stressors have only been possible in samples with the stripes oriented along direction <110>. It is to be assumed that strain in this direction does not lead to a crossover of the direct and indirect conduction band valleys. However, to verify the strain obtained by Raman spectroscopy, we revert again to stripe stressors along <110>. The above mentioned enhancement in direct gap PL due to the decreased barrier $E_{\Gamma L}$ cannot be expected in this case. Nevertheless, the bandgap energies should be reduced also in this case. Aldaghri et al.[116] calculated the behavior of direct and indirect valleys in Ge under tensile strain and found that for Ge grown in indirection (001) and strained in direction <110> the direct bandgap is solely 0.47 eV at room temperature for 4% tensile strain. With our apparatus equipped with an extended-InGaAs photodiode array with cut-off energy at about 0.56 eV we are not able to detect a signal from Ge with such a high tensile strain.

The strain distribution inside the strained Ge virtual substrate is not homogeneous, though, as we have seen in FIG. 5-3. We thus might be able to distinguish a photo-luminescence signal originating in the strained Ge region that extends into the detectable region. In a first trial with our highest strained samples in which we revealed uniaxial strains of ~ 4%, we were not able to identify a luminescence band that could be unobjectionably attributed to the strained volume of Ge.

For this reason, we have chosen to further investigate the SiGe stripe pattern 9 of die 9184-G6. The SiGe stripes are made of $Si_{50}Ge_{50}$ and there are gaps of 45.3 ± 5 nm between them. Raman measurements determined the strain in Ge inside the gaps between the stripe stressors to be $\varepsilon_{Ge} = (3.5 \pm 0.8)$ %. This strain value corresponds to a direct gap energy $E_{dir} = 0.52 \pm 0.06$ eV. The direct bandgap of this sample is now close to the detector cut-off and since the stripe stressor samples inherently have got a large strain gradient due to the stressor geometry, we should be able to detect a signal originating in the strained Ge volume close to the cut-off wavelength of our detector. With this respect, the wider gap size of about 45 nm may be helpful to have a larger area for excitation and collection. A strong and narrow peak like observed by de Kersauson et al. [50] from the strained portion of a Ge wire cannot be expected, admittedly.
We have chosen a comparative approach and compare the spectrum from the stressor pattern with the spectrum from the flat, unpatterned part of the sample.

PL measurements were performed at Università degli Studi di Milano-Bicocca as well as at IHP GmbH in Frankfurt (Oder). In both cases we have used a micro-setup. The spot diameter on the sample surface on which the laser is focused depends on the actual objective and laser source used. In the experiments presented in the following, we have used different laser sources which have a different influence on the excitation of carriers in Ge. For this reason, we will give the detailed experimental conditions in the discussion of the results. However, the laser spot diameter is at most ~ 3 µm. The carriers are therefore excited within the region of the stripe stressors only, which has an area of about 25 µm × 25 µm. By changing the width of the entrance slit of the monochromator and observing the intensity of the collected signal, we can estimate the size of the image on the sample from which we collect. For a Ge bulk crystal we estimate an image of less than ≤ 20 µm in diameter. However, the diffusion of carriers in an inhomogeneously strained region complicates the prediction of the region of recombination, but it is not expected to be enlarged due to "funneling" toward the lower bandgap energies of the strained region. Hence, we can assume that collection is restricted to the stripe stressors when we excited in the middle of the pattern. This allows us to employ a comparative approach to reveal the effect of the stripe stressors on the PL of Ge. We acquired spectra from the following regions of the sample, depicted in FIG. 5-2 of sec. 5.2:

- Ge window: the SiGe top layer is removed from the Ge virtual substrate
- Flat stack of SiGe/Ge/Si
- Stressor pattern etched into SiGe

5.5.1 2.7 eV excitation, room temperature

We start our investigation using the 457.9 nm laser line of an argon-ion laser. This wavelength corresponds to 2.7 eV and it is the same laser with which we have performed the micro-Raman measurements. As explained in the corresponding section about these measurements, the penetration of this wavelength into germanium is limited to less than 20 nm. Hence, carriers are excited close to the germanium surface where the highest strain is created by the SiGe stressors. The hope is that with this approach excited carriers are generated in the strained region and recombine there. The lower band-edge values in strained Ge may create a potential sink for electrons and holes in the conduction and valence band, respectively ("funneling" effect). However, electrons excited with 2.7 eV possess high kinetic energy and we hence have to compromise between depth of excitation and kinetic energy.

FIG. 5-9 shows the micro-PL spectra from the Ge window, the flat stack and the stressor pattern. All spectra feature the intensity maximum at about 800 meV. This emission band originates in the bulk Ge virtual substrate – unaffected by the stripe stressors in case of the measurement on the stressor pattern. The three spectra showed different intensities so that we normalized intensity to the maximum at ~ 800 meV for better comparability, since we are interested in spectral shape only. We would like to stress that different intensities are expected since the surfaces of the three sections of the sample are different: without SiGe top layer, with flat layer and with patterned layer. This influences the excitation power arriving in Ge. In our study it is important, though, to identify a distinct spectral feature in the spectrum from the stressor pattern that we can ascribe to the strained Ge volume.

We find that the spectra from the stressor pattern and from the flat stack differ from the spectrum of the Ge window. This is expected due to the additional presence of the SiGe layer in the former sections of the sample: the lower intensity ratio between the direct-gap emission from bulk Ge at ~ 800 meV and the indirect-gap band at ~ 740 meV may be due to the fact that most exciting photons are absorbed in the SiGe top layer and reach the Ge layer only by diffusion which may favor injection into the L valleys of Ge.

To detect the contribution from the strained Ge, we have to compare the spectrum of the stressor pattern with that one of the flat stack. Here, we can identify only marginal differences between both spectra. The Ge direct-gap band from the stressor pattern is slightly red-shifted which in principle may be a signature for higher tensile strain. However, the spectrum from the stressor pattern does not show any distinct band of emission from tensile Ge that would not be present in the spectrum from the flat stack and that should be close to the detector cut-off.

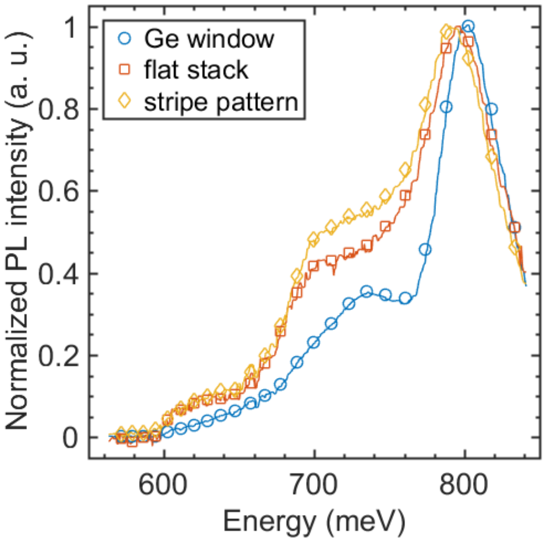

FIG. 5-9 Photoluminescence spectra of the three parts of the sample (Ge window, flat stack and stressor pattern) at room temperature. The spectra have been normalized to the direct-gap emission originating in the bulk-like Ge virtual substrate. No marked difference in spectral shape between the flat stack spectrum and the stressor spectrum can be observed.

5.5.2 2.71 eV excitation, 77 K

It might be helpful to perform measurements at low temperature: the emission bands for direct and indirect gap radiative transition may be narrower since broadening of energy states should be lower. This may help in efficient radiative recombination. On this note, also the first report of lasing from GeSn was only at temperatures below 90 K.[20] In addition, at low temperatures, all band-gap energies are shifted to higher values: If the strained Ge should have a band-gap out of the detection limits at room temperature, its higher band-gap at low temperatures should be shifted toward the detectable range.

We perform the micro-PL measurements with the 2.7 eV excitation source at 77 K. The acquired spectra for the three parts of the sample are shown in FIG. 5-10. Has the direct-gap emission from the bulk-like Ge virtual substrate been the strongest source of emission at room temperature, it is now reduced strongly at 77 K. In the spectrum from the Ge window there is still a clearly detectable emission band at about 850 meV, whereas in the other two spectra the direct-gap emission is merely a shoulder of the much higher emission in the range from ~ 700 meV to 800 meV. The emission band at about ~ 720 meV is present in all three samples and we can attribute it to the indirect-gap emission $L_c \rightarrow \Gamma_v$ from the germanium virtual substrate. Rowell et al.[175] measured the PL of SiGe alloys with different composition at 8 K and from their measurements we conclude that the peak at ~ 780 meV present in the spectra of the flat stack and the stressor pattern originates in the top SiGe layer. In addition, all spectra show strong dislocation luminescence below 650 meV.

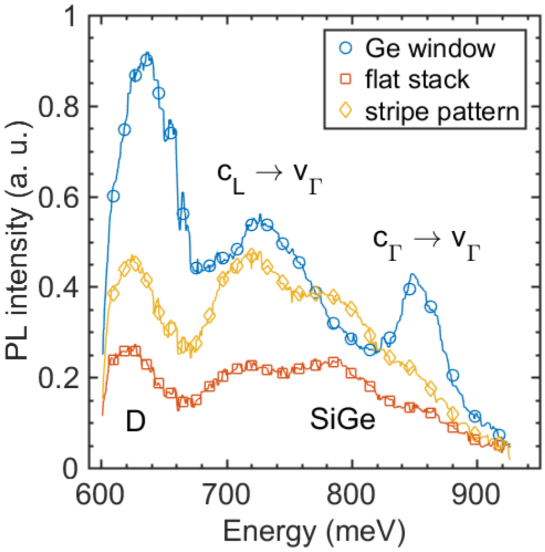

FIG. 5-10 Photoluminescence spectra of the three parts of the sample (Ge window, flat stack and stressor pattern) at a lattice temperature T_L = 77 K. The direct-gap emission at ~ 850 meV from the Ge virtual substrate is strongly suppressed.

Again, the spectral shape of the luminescence from the stressor pattern and the flat stack is identical. The strongly reduced or even absent direct-gap emission from the Ge virtual substrate is explained as follows: in the bulk Ge, characterized by a small thermal strain, the L valleys constitute the global minima of the conduction band, hence carriers thermalized to the band edges after photo-excitation may end up preferably in the L-valleys. Moreover, scattering of electrons from the direct-gap valley in Γ into the side valleys in L (and those along the Δ-direction) is much faster than backscattering into Γ.[123] Moreover, at low temperatures thermal promotion of excited electrons to the Γ valley is absent. This leads to the low direct gap emission.

Sakamoto et al. [170] point out that there could even be resonant pumping of electrons into the L valleys of relaxed Ge. With respect to our objective of enhancing the emission from the strained Ge volume, pumping into the L valleys is highly disadvantageous since we cannot assume to have reached direct-gap Ge in which the Γ valley would be the global conduction band minimum and could act as a sink for excited electrons (“funnel effect”). For this reason, we will present a study on the effect of the excitation source on the PL from the different parts of our sample in the next section. Note, that the calculations by Sakamoto et al. are performed for relaxed Ge at 0 K. The strong transition from the valence band directly into L relies on the large joint-density of state (JDOS) of parallel valence and conduction band edges. This symmetry may be broken in strained Ge.

5.5.3 PL intensity dependence on lattice temperature T_L and excitation energy

In the previous two sections we have seen that there is no spectral difference between the stressor pattern and the flat part of the sample. We know – cf. section 4.2.3 – that excitation with 457.9 nm (2.71 eV) results foremost in population of the L-valleys in Ge.

Sakamoto et al. [170] have calculated the resonance energies for the different vertical transitions in the Ge band structure. They showed, that excitation with a 532 nm line (2.33 eV) leads to direct pumping of electrons into L, hence phenomenologically the same result than with 457.9 nm excitation.

However, the micro-PL measurements by Süess et al. [55], carried out at room temperature with a 532 nm laser source, showed that there is a "funneling" effect: Süess et al. prepared a Ge bridge under tensile load and measured the photoluminescence spectra for different excitation positions starting in the center of the bridge and translating the point of excitation off the bridge. Thereby, the region of high tensile strain which is reached on the bridge, is left. However, also the spectrum acquired with excitation off the bridge in a region with only slight strain, had its emission maximum at that spectral energy where the main contribution from the highly strained bridge has been. The conclusion is, that the lower energy levels of the energy bands of the highly strained Ge might act as a sink for excited carriers so that carrier diffusion into the highly strained region may exceed normal diffusion of carriers. This has not proven true for our sample.

Sakamoto et al. [170], on the other hand, explain that the 1064 nm line (1.16 eV) of a Nd:YAG laser is close to the resonance for the transition from the top of the valence band into the Γ-valley. Direct pumping into Γ may help to enhance the "funneling" in the sense of the simple view that excited carriers are already in Γ from the beginning.

Temperature dependent PL spectra

In the following, we want to analyze the micro-PL spectra obtained from our sample with both 532 nm (2.33 eV) and 1064 nm (1.16 eV) excitation in a lattice temperature range T_L = 83 K to 448 K. The power output for the laser sources has been set in such a way that the excitation power on the sample surface is ~ 20 mW in both cases. FIG. 5-11 shows the acquired spectra for the Ge window, the flat part of the sample and the stressor pattern. The difference in excitation with 532 nm and 1064 nm is the absence and presence of the spectral feature at about 830 meV, respectively, at low temperatures (83 K to 163 K). We can attribute this luminescence band to direct gap transitions in the bulk-like – in first order – relaxed Ge virtual substrate. In case of the stressor pattern, this is the large volume of the Ge substrate that is not influenced by the stressors that create the strain close to the Ge surface as we have seen in the previous section.

For excitation with 532 nm this feature is only evolving at higher lattice temperatures. In both cases it is red-shifted with increasing T_L in agreement with a shrinking energy gap according to Varshni.[129]

Moreover, we notice that the spectral intensity of the Ge window is higher than that of the flat part and the stressor pattern. We can explain this by the removal of the SiGe top layer in case of the Ge window. Thereby the excitation energy impinging on the Ge window is higher than in the other two cases.

Ge window, flat part and stressor pattern show luminescence below 650 meV at low lattice temperatures for both excitation sources. Since this feature is present also in the Ge window and the flat part, it cannot be originating in the strained Ge created by the stripe stressors. Most probably this emission stems from dislocations at the Ge/Si interface or from those inside the Ge virtual substrate.[176] For excitation with 532 nm this dislocation related feature is the most intense spectral feature in the low temperature spectra.

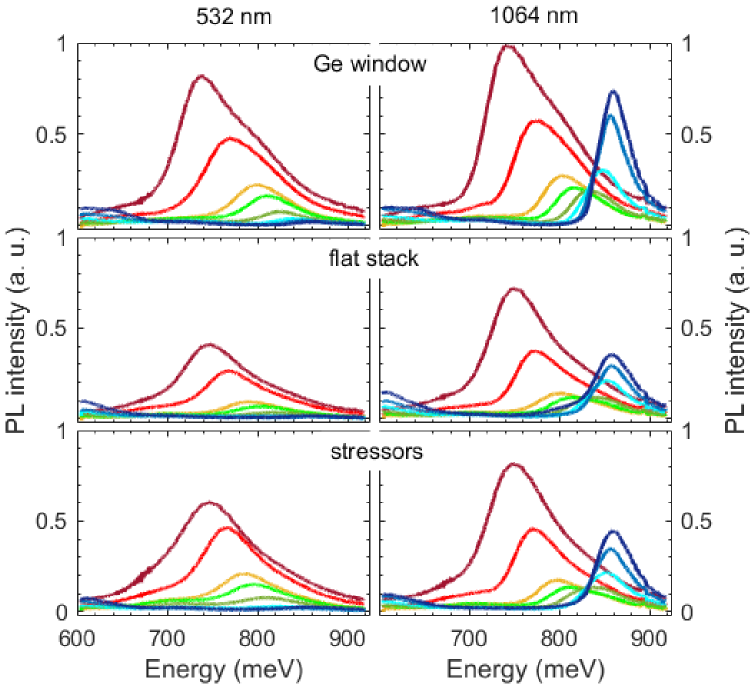

FIG. 5-11 Luminescence spectra collected with a micro-setup after photo-excitation with a 532 nm laser line (left) and a 1064 nm laser line (right). The Ge window, the flat part and the stressor pattern have been probed at lattice temperatures T_L = 83 K, 113 K, 163 K, 213 K, 263 K, 298 K, 373 K and 448 K (spectra in dark blue to dark red).

Contour plot representation of the temperature dependent spectra

The different evolution of spectral intensity distribution with temperature for photo-excitation with 532 nm and 1064 nm can be well appreciated in contour plots in which the spectral intensity is coded by a color. The contour plots corresponding to FIG. 5-11 are shown in FIG. 5-12. At low temperatures with 532 nm, the emission from defects is the strongest contribution to the spectrum, whereas with the 1064 nm pump there is a strong emission band from the direct gap transition. For lattice temperatures from 200 K to 350 K we can discriminate a spectral band around 700 meV in all cases depicted in FIG. 5-12. This band originates foremost in the indirect gap transition of the bulk Ge virtual substrate. For excitation with 532 nm, this band is also present at low temperatures. As already mentioned, contrarily to excitation with 532 nm, in case of 1064 nm at low temperatures, emission from Ge stems from the direct gap transition and indirect gap emission increases to detectable intensities only at higher temperatures. Electrons are pumped directly into Γ and at low temperatures the L valleys are efficiently emptied through defect-mediated non-radiative recombination, see discussion below.

On the other hand, in the case of the 532 nm pump, the direct gap transition from bulk Ge increases noticeably with temperature: At higher temperatures carriers in L have got a higher thermal energy to overcome the energy barrier between L and Γ; moreover, this barrier is reduced with increasing lattice temperatures. At temperatures higher than 350 K then, all spectra (of all sample parts investigated as well as with 532 nm and 1064 nm pump) are then dominated by the direct gap transition from bulk Ge.

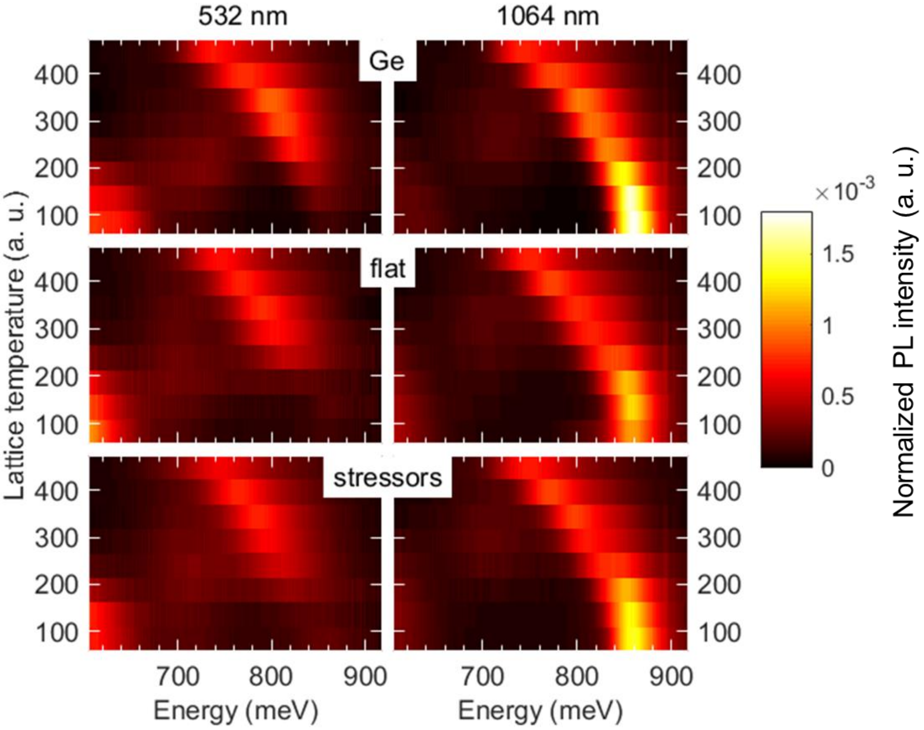

FIG. 5-12 Contour plots of the spectra acquired at different lattice temperatures T_L with 532 nm (left hand panels) or 1064 nm (right hand panels) laser source. The spectral intensity is coded by color. Excitation with 532 nm and 1064 nm lead to a different spectral intensity distribution foremost at low temperatures. With 1064 nm pump source, direct gap emission from Ge is strongly enhanced.

Integrated intensity as a function of temperature

We would like to have a closer look at the behavior of the photoluminescence intensity of Ge with change in lattice temperature, since this has been explained in different manners in literature. We start this excursion with FIG. 5-13 that shows the Arrhenius plots of the integrated intensity versus $\beta = 1/k_BT$ of all regions of the sample under 532 nm and 1064 nm excitation. Integration was carried out over the direct and indirect-gap luminescence bands as identified previously. The luminescence stemming from dislocations was excluded.

The three regions of the sample show the same curve progression for integrated intensity as a function of β with an intensity off-set that can be explained by the presence or absence of the SiGe layer, i. e. the Ge window without SiGe layer shows highest intensity. The absence of the SiGe layer causes a higher excitation power density arriving at the Ge virtual substrate.

Moreover, the intensity behavior as a function of lattice temperature T_L depends strongly on the energy of the exciting photons. Whereas in the region of high temperature, i. e. $\beta < 0.04$, the intensity behavior is identical for the 532 nm laser and the 1064 nm laser, a striking difference can be seen at low lattice temperatures, $\beta > 0.04$. For the 532 nm laser, the intensity is about one order of magnitude lower in this region.

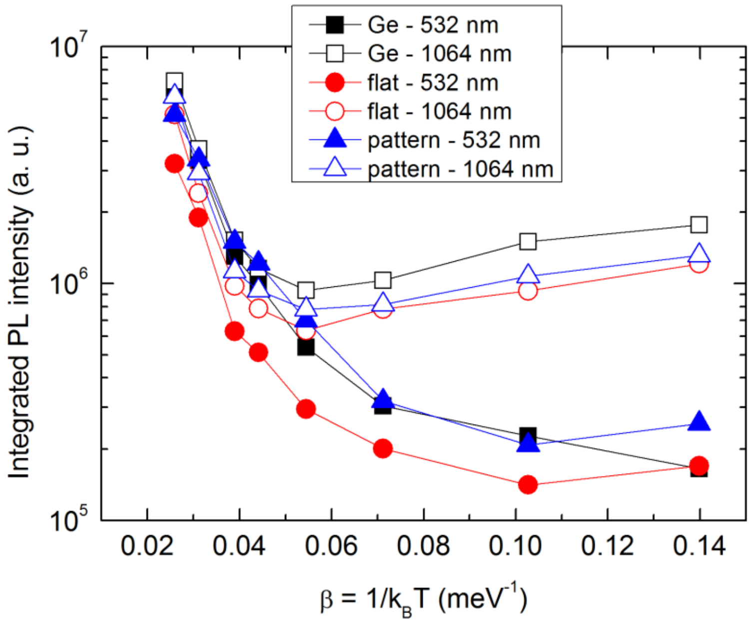

FIG. 5-13 Integrated PL intensity of the spectra of the temperature ramp from 83 K to 448 K acquired under 532 nm (2.33 eV, full symbols) and 1064 nm (1.16 eV, open symbols) photo-excitation for the Ge window (○), flat stack (□) and stressor pattern (△). Intensity values are plotted against $\beta = 1/k_B T$.

As can be seen from FIG. 5-11 and FIG. 5-12, the low temperature spectra with 532 nm excitation have similar direct and indirect gap intensities, $I_{\mathrm{dir}} \approx I_{\mathrm{ind}}$, with a strongly quenched direct gap luminescence compared to the excitation with 1064 nm. We conclude, that with 532 nm excitation the indirect L-valleys are populated. Due to its very long radiative lifetime for indirect recombinations $L_c \rightarrow \Gamma_v$, the population in L is strongly affected by non-radiative recombination which can be mediated by the Shockley-Read-Hall mechanism. Moreover, with 532 nm, the penetration depth of the laser into Ge is less than 20 nm and excited carriers are created close to the surface. For this reason, surface recombination may be more important in case of 532 nm than in case of 1064 nm which has got a much longer penetration depth, see 3.5.

Increasing the lattice temperature T_L, the Γ valley is populated by thermal excitation of carriers from the L valleys. Indeed, from 298 K to 448 K the runs of the integrated intensity curves of all three regions of the sample are linear in the Arrhenius plot and their slopes correspond to an energy of about ~ 120 meV. This energy values fits very well with the energy difference of the L valleys and the Γ valley in slightly strained germanium. This supports the view of thermal promotion of electrons into the Γ valley as pointed out by Virgilio et al. in Ref. [69].

The same behavior for this high temperature interval can be found for excitation with 1064 nm. However, the run of the 1064 nm curves differs from the temperature dependent behavior of the intensity under 532 nm excitation. As we have seen in the spectra of FIG. 5-11 and the intensity contour plots of FIG. 5-12, at 83 K all regions of the sample show a strong direct-gap transition luminescence originating in the Ge virtual substrate. Consequently, the integrated intensity at high values of β is distinctively higher than in the case of 532 nm excitation. In addition, differently to the 532 nm case, integrated intensity decreases at first with increasing temperature and all regions of the sample and has its intensity minimum at T_L = 213 K. Then, with further increasing T_L, the integrated intensity increases steeply and follows exactly the linear behavior of the 532 nm excitation.

Pezzoli et al. also observed an initial PL intensity quenching with increasing temperature followed by a steep intensity increase in Ge [137] and GeSn [177] hetero-structures and attributed this behavior to the presence of dislocations. To have a complete picture, we discuss their findings in the following.

In a dislocation free Ge wafer and a dislocation free GeSn epitaxial layer, respectively, they observed highest PL at the lowest lattice temperature (6 K) that was then quenched successively with increasing temperature. This is the PL temperature behavior often ascribed to direct gap material and the quenching is explained by increasing non-radiative recombination rates.

It is important to stress that Pezzoli et al. measured indirect gap material in both cases and thereby illustrated that the observed PL quenching is not unique to direct gap material.

They continued their discussion with observing the temperature dependent PL of hetero-epitaxial structures in which dislocations are present and observed an initial PL intensity decrease up to a certain temperature which is followed by a steep increase, in agreement with our results shown in FIG. 5-13. It is important to note that the PL intensity of the samples with dislocations was much reduced with respect to the dislocation-free samples and may reach comparable intensity levels only at high temperatures ($T_L \geq \mathrm{RT}$).

In the work of Ref. [137], Pezzoli et al. then apply a phenomenological “barrier model” developed originally by Morrison [178] and Figielski [179] to explain recombination of electrons and holes at dislocations and to discuss photoconductivity phenomena in plastically deformed Ge and Si. According to this model, dislocations establish isolated energy levels inside the electronic band-gap of germanium. At low temperatures, these levels can act efficiently as traps for the photo-excited carriers. An excess carrier (electron or hole) trapped at a dislocation level cannot contribute to interband radiative transitions; the PL intensity from samples with dislocations is much lower than that without dislocations at low temperatures. Carriers trapped by dislocations can recombine radiatively or non-radiatively from the dislocation level. The former recombination process leads to the dislocation related emission in the PL spectra, visible at ~ 600 meV. With increasing lattice temperature, hence, the PL is quenched like in the samples without dislocations. At a certain temperature, however, the thermal energy of carriers is high enough to overcome the potential barrier of the trap states and photo-excited carriers trapped are promptly released again to the conduction and valence band. As a consequence, they are available to contribute to interband radiative transitions. This mechanism hence can account for the steep increase in integrated PL intensity in the high temperature regime. Eventually, the PL quenching effect of dislocation related traps is less strong and at sufficient temperatures samples with and without dislocations will have the same integrated PL intensity, as also shown by Pezzoli et al. in Ref. [177].

From the model of Figielski [179] it follows that the temperature with minimum integrated intensity corresponds to the transition temperature T_t in which the excess concentrations of holes in the valence band δp equals the charges trapped at the dislocations δm, $\delta p = \delta m$. It constitutes the transition from the temperature range in which the density of trapped charges δm is larger than the free excess holes in the valence band, to the range in which most of the excess carriers stay in the valence band (or conduction band, respectively) and do not leak into the dislocation energy levels.

For excitation with 1064 nm, we find from FIG. 5-13 that T_t is about 213 K which is larger than the temperatures reported in Ref. [137] (125 K) and Ref. [177] (120 K and 90 K). An increase in this transition temperature with increasing dislocation density is also in accordance with the modelling of Figielski.[179] This may be explained with the expected higher dislocation density in our sample compared to the vertical Ge hetero-structures or the GeSn layers that are in a state at the onset of plasticity investigated by Pezzoli et al. (the threading dislocation density is estimated to be about ~ 10^7 cm^{-3} in our samples). Figuratively, at a higher dislocation density more excited carriers are trapped in average. The positive effect of temperature on integrated PL intensity starts to appear when the average number of excited carriers in the conduction/valence band is larger than the average trapped number of excited carriers, i. e. $\delta p > \delta m$. To reach this inversion with a higher dislocation density, a higher temperature which leads to a higher release rate, is necessary.

In case of 532 nm excitation, PL from the Ge window shows no intensity minimum, flat stack and stripe pattern only show a weak decrease from 83 K to 113 K. As discussed previously, PL intensity is already quenched strongly at low lattice temperatures and may explain the absence of a pronounced PL intensity minimum in dependence on temperature. Moreover, we would like to add, that with 532 nm excitation the excitation power density was 2.7×10^6 W/cm^2 which is to be considered a high excitation power level. The expressions for carrier capture through dislocations derived by Figielski [179] though, are derived for low excitation powers so that higher order terms in excitation power can be neglected for derivation of the excess carrier densities. Furthermore, the leakage of carriers from the electronic bands into the dislocation energy states is governed by the charge of a dislocation which in turn depends on the excess carrier density. A high excess carrier density would increase the ratio of free excess holes to captured holes $\delta p/\delta m$ and may also explain the fact that the slight intensity minimum in case of 532 nm excitation is at a lower temperature T_t compared with 1064 nm excitation. We conclude, that the application of the barrier model to the data with 532 nm should be done with suspicion.

Detailed comparison of spectra obtain under 532 nm (2.33 eV) and 1064 nm (1.16 eV) excitation.

Finally, we would like to compare selected spectra of the Ge window under 532 nm and 1064 nm excitation in a single figure. FIG. 5-14 shows the spectra at lattice temperatures T_L = 298 K and 448 K. We find, that at both temperatures the spectra acquired with 532 nm are red-shifted with respect to the 1064 nm spectra. Moreover, the spectra with 532 nm pump at 298 K is observably broader than the corresponding spectrum under 1064 nm excitation. It is probable that due to the higher kinetic energy of the electrons in case of the 532 nm pump the crystal lattice is heated locally when the carriers thermalize. This could explain the red-shift of the spectrum. Also the broadening may be due to the higher temperature of the electron gas, since, depending on the actual excitation mechanism under the use of a 532 nm laser (vertical transition from the top of the valence band or vertical transition at the singularities along the Λ-direction (cf. Sakamoto et al. for the later, Ref. [170])), the carriers excited with 2.33 eV pump have got the higher kinetic energy $E_{\text{kin}} = E_{\text{pump}} - E_{\text{gap}}$.

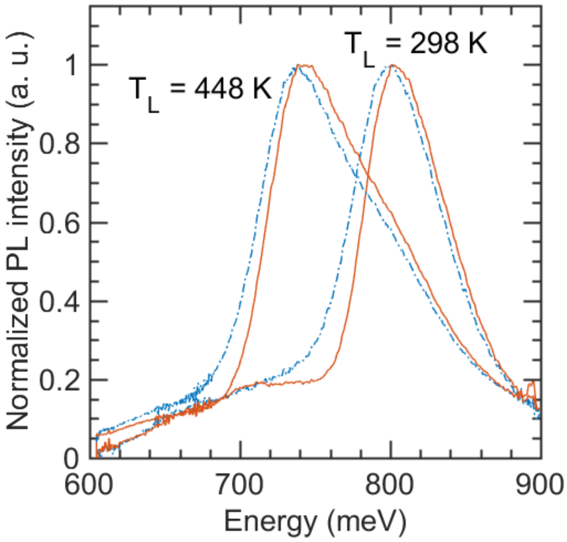

FIG. 5-14 Normalized PL spectra of the Ge window at lattice temperatures T_L = 298 K and 448 K for photo-excitation with 532 nm (2.33 eV, dash-dotted line) and 1064 nm (1.16 eV, solid line). Excitation with the higher energy leads to a red-shift and broadening of the emission bands.

The fact, that the same excitation power is focused to a smaller spot size in the case of 532 nm radiation and hence the power density in this case is about 4× times larger than in the 1064 nm case, should not matter for the red-shift in the sense that PL is not collected from the point of incidence only, but from a larger volume due to carrier diffusion. In this respect, the 1064 nm source might have the advantage that the photo-excited carriers have lower kinetic energy. This could help, because we can expect more thermalized carriers close to the surface, the phonon drag may be lower.

For this reason and since electrons are pumped directly into the Γ valley, we hence conclude, that for our purposes the use of a 1064 nm excitation source may be better suited.

5.5.4 micro-PL with 1064 nm (1.16 eV) excitation at 77 K

We have seen in the previous discussion that pumping with a 1064 nm laser source led to strong direct gap emission from the Ge virtual substrate at low temperature. Emission from the indirect transition $L_c \rightarrow \Gamma_v$ was not observable. Hence, this experimental condition may allow us to probe the direct band-to-band transition in Ge only. Emission originating in the strained Ge volume created by the SiGe stressors should be shifted toward lower energies with respect to the relaxed bulk-like material, since the direct band gap shrinks with the application of tensile strain.

We repeated PL measurements of the three parts of the sample (Ge window, flat stack and stressor pattern) under these conditions. FIG. 5-15 compares the obtained spectra. All three spectra have got a strong emission band from the bulk Ge virtual substrate at 850 meV, like expected, as well as pronounced dislocation luminescence below 650 meV. Moreover, the spectrum from the stressor pattern shows a distinct feature at about 740 meV that is not present in the other spectra. Hence, we conclude that it originates in the strained Ge volume created by the SiGe stripe stressors.

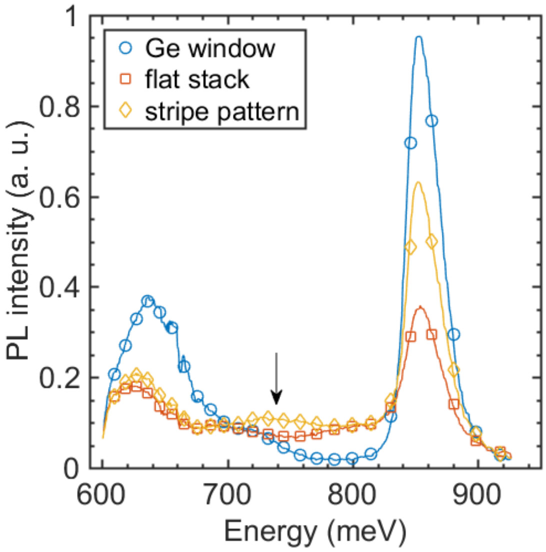

FIG. 5-15 Micro-photoluminescence spectra from the three parts of the sample: Ge window, flat stack and stressor pattern acquired with 1064 nm excitation at 77 K lattice temperature. The broad spectral feature marked with an arrow is unique in the spectrum originating in the stressor pattern and we can ascribe it to the strained Ge created by the SiGe stressors.

Calculations for the band gap of strained Ge are only available for room temperature. For a simple estimation, we can proceed by assuming that the band-gap of the strained region will change with temperature by the same amount than the band-gap of the bulk Ge virtual substrate. The emission from the Ge bulk is also visible at room temperature, thus the change in band-gap with temperature can be retrieved from the measurements. Doing so, we find a band gap of 670 meV at room temperature for the peak of the strain related feature in FIG. 5-15. According to Aldaghri et al. [116] this corresponds to 1.6% uniaxial strain.

This strain value comes short compared to the 3.5% determined by Raman spectroscopy. However, we have to bear in mind that with Raman spectroscopy we can only probe a volume close to the Ge surface proportional to the penetration depth of the excitation source into Ge which is less than 20 nm. On the other hand, in PL experiments, due to carrier diffusion after excitation, the probed volume is much larger. Indeed, the fact, that emission from dislocations that are mainly localized at the Ge/Si interface demonstrates, that with PL a depth up to 1 µm (which corresponds to the thickness of the Ge virtual substrate) is probed. In consequence, the emission band that we attribute to the strained Ge could emerge from the entire strain gradient present in the sample and the peak value represents a mean of the strain created by the SiGe stripe stressors. If we wanted to probe the highly strained volume only, we should think about strategies to constrain the photo-excited carries into this volume. We will do so in the next section.

5.5.5 micro-PL of <100> oriented stressors with 1064 nm (1.16 eV) excitation

Even though we were not able to detect a Raman signal from the strained Ge region inside the gap between SiGe stripe stressors oriented along <100>, as discussed in sec. 5.2, it is interesting to investigate these samples with means of photo-luminescence, since the emitted luminescence is not polarized and hence should be detectable.

The strain induced in the Ge virtual substrate by SiGe stressors oriented along <100> should be different from that created by <110> stripe stressors in general, because the elastic constants depend on the crystallographic orientation. We can assume in good approximation that they differ only slightly. Hence, for a stripe pattern on the same die, prepared with the same etching time and featuring the same gap width between stripes, we can expect a similar strain for <100> stressors as for <110> stressors. Aldaghri et al. have calculated that the resulting direct band gap energy is slightly less in the <100> case.[116]

We have chosen to investigate structure 12 of die 9184-G6 which features stripes stressors along <100> separated by a gap of 45 nm. Thus, it corresponds to the <110> stripe pattern presented previously (structure 9) where we determined the strain in Ge inside the gaps between the stripe stressors to be $\varepsilon_{Ge} = (3.5 \pm 0.8)$ %. Hence, we assume also for structure 12 the same strain level. According to Aldaghri et al. this strain results in a $E_{dir} \sim 0.54$ eV direct gap energy (for <110> we found $E_{dir} \sim 0.52$ eV).[116]

Since in the previous PL studies we have found, that sample excitation with 1064 nm is most suited to reveal luminescence from the strained volume in the Ge virtual substrate, FIG. 5-16 shows the micro-PL spectra from the flat SiGe/Ge stack and the stripes stressor pattern acquired at room temperature and at 75 K using this laser line. As found previously for the <110> sample, the spectra at room temperature are dominated by the direct gap emission from unstrained Ge. However, this time we can identify a clear difference in the spectrum from the stripe pattern that is not present in the flat stack spectrum. We thus can attribute it to the strain created by the stripe stressors inside the Ge virtual substrate. Due to the detector cut-off the spectral intensity is reduced to zero at 600 meV and it is not unambiguously possible to determine the peak energy of this band, but it is estimated to be at about ~ 620 meV. The calculations of Aldaghri et al. [116] link this direct gap energy to $\varepsilon_{Ge} \sim 2.2\%$. This strain value and the broad spectral distribution may well be in line with the inhomogeneous strain field generated by the stripe stressors.

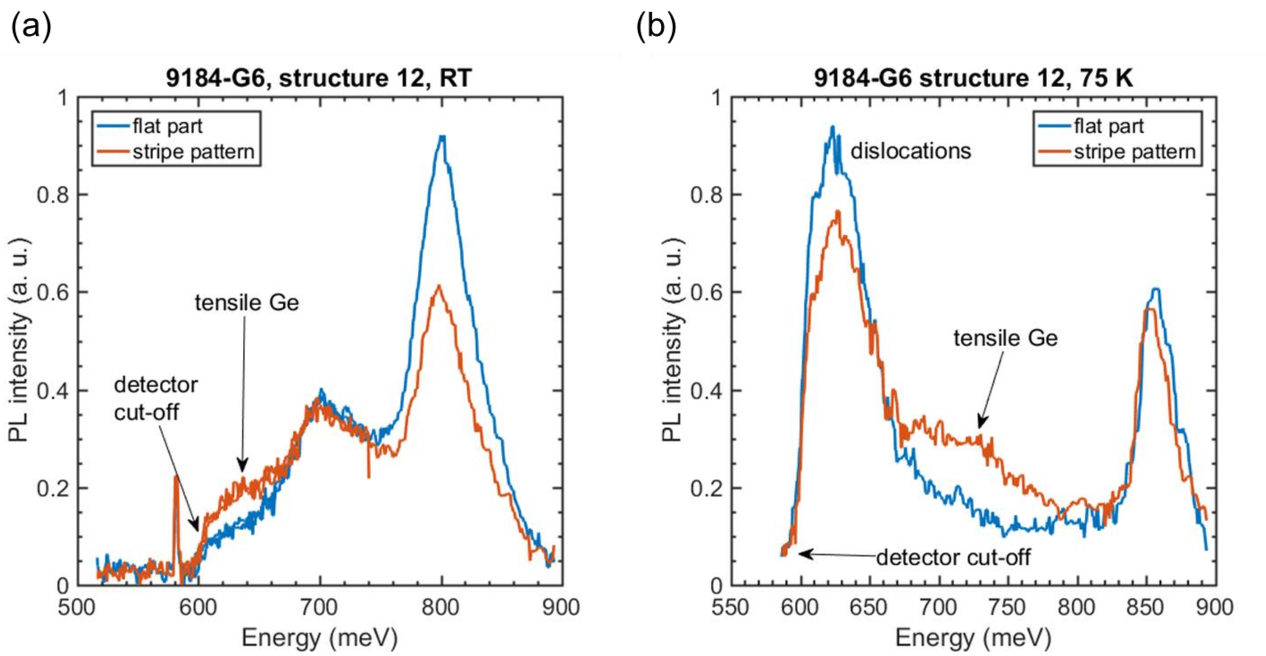

FIG. 5-16 Micro-photoluminescence spectra of a <100> oriented stripe pattern with *g* = 45 nm gap width obtained under 1064 nm laser excitation.

- **(a) Spectra of the flat SiGe/Ge stack and the stripes pattern at room temperature. In both spectra, the most intense luminescence at 800 meV originates in direct gap transitions in the vast bulk Ge virtual substrate, that is unaffected by the stripe pattern. The intensity peak at 700 meV is attributed to indirect gap emission in unstrained Ge. In the spectrum from the stripe pattern, a clear spectral difference is visible at ~ 620 meV that we ascribe to the tensile strain created in Ge. The sharp peak at ~ 580 meV is caused by the second-harmonic of the excitation laser.**

- **(b) Spectra of the flat SiGe/Ge stack and the stripe pattern acquired at 75 K. The emission band from direct gap transitions in the unstrained Ge virtual substrate is shifted to higher energies (~ 860 meV) with respect to the room temperature measurement. The strong emission band peaked at ~ 620 meV arises from dislocations at the Ge/Si interface. A distinct spectral difference is observable between the stripe stressor spectrum and that of the flat stack. The emission band peak at ~ 720 meV can hence be attributed to the tensile strain induced into Ge by the SiGe stressors.**

Panel (b) of FIG. 5-16 reports the PL spectra obtained at 75 K. It is thus comparable with FIG. 5-15. Like in FIG. 5-15 we find that the strongest luminescence band arrise from the direct gap transitions in the unstrained Ge virtual substrate (band at ~ 860 meV) and in dislocations from the Ge/Si interface (~ 620 meV). In the present case of FIG. 5-16 an even clearer spectral difference between stripe pattern and flat SiGe/Ge stack can be observed than in the case of <110> oriented stressors of FIG. 5-15. This emission band, present only in the spectrum from the stressor pattern, is attributed to the tensile strain induced into the Ge virtual substrate by the SiGe stressors. It is peak at about 720 meV in good agreement with the findings of the stripes along <110>. Moreover, it is blueshifted with respect to the tensile Ge emission at RT, giving further support to the asignment to the tensilely strained volume in Ge. The fact, that the emission from tensile strain is more intense in the case of <100> than that of <110> suggests that by straining Ge uniaxially along <100> the energy difference between the conduction band L valley and the Γ valley is reduced, resulting in a higher Γ_c electron population. To conclude our discussion of PL from samles featuring stripe stressors,

6 SiGe barrier for carrier confinement in photoluminescence experiments

6.1 Sample preparation

From FEM strain simulations we know that the high tensile strain created inside Ge by the stripe stressors is limited to less than ~ 20 nm below the Ge surface.[61] The PL analysis of the previous stripe stressor samples showed that it is important to constrain the photo-excited carriers to the highly strained region in the Ge virtual substrate.

In the following we investigate the possibility to confine the excited carriers to this region by a potential barrier introduced by a SiGe layer below a Ge top layer. For this purpose we have prepared dedicated samples by means of LEPECVD the layout of which is shown in FIG. 6-1. The common structure of the samples consists of a stack of a 30 nm Ge top layer grown on 1 μm thick $Si_{10}Ge_{90}$ on a silicon substrate. Two of the samples feature additionally a barrier made of a 30 nm thick layer of $Si_{10}Ge_{60}$ introduced directly below the Ge layer or 500 nm below the Ge surface, resulting in a sample with shallow and deep barrier, respectively. Note, that the Ge layer in all three samples has got the same thickness insuring comparability of the photoluminescence intensity originating in this layer.

The $Si_{10}Ge_{90}$ virtual substrate is grown at a temperature of 500 °C on a Si(001) substrate, followed by six annealing cycles between 600 and 850 °C. The growth of the barrier and the top Ge layer is then carried out at 400 °C.

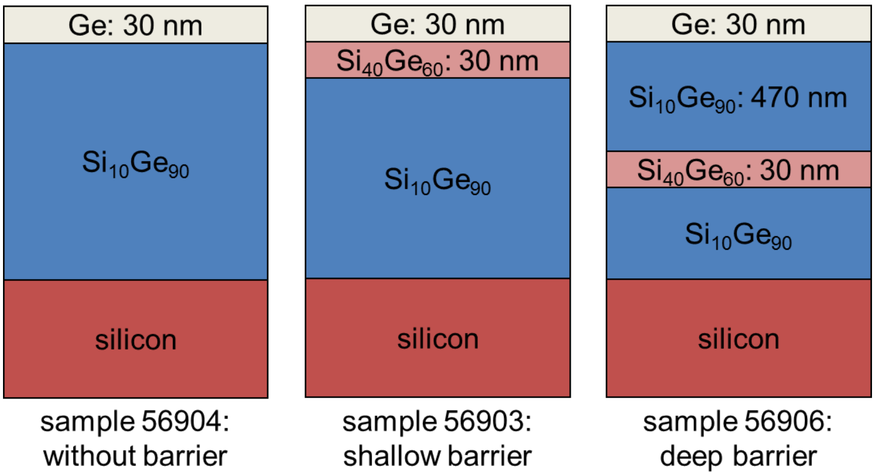

FIG. 6-1 Sample layouts of the samples under investigation featuring a thin Ge top layer on $Si_{10}Ge_{90}$ with optionally no $Si_{10}Ge_{60}$ barrier, a shallow $Si_{10}Ge_{60}$ barrier or a deep $Si_{10}Ge_{60}$ barrier.

The compositions of the different sample layers as well as their strain values are determined by X-ray diffraction. Furthermore, we use Raman spectroscopy to verify the strain value of the top Ge layer of the sample with the shallow barrier. Raman measurements are carried out in a backscattering geometry using a micro-setup with 100× objective with numerical aperture of 0.9 and a 532 nm laser line. The fluence is controlled to prevent heating artefacts. Photoluminescence measurements are performed with a micro-setup using as a laser source the 457.9 nm laser line of an argon-ion laser and focused on the samples with a 50× objective with numerical aperture of 0.42. All measurements were done at room temperature.

6.2 X-ray Diffraction analysis SiGe barrier samples

Table 6-1 reports the germanium fraction *x* and strain values ε of the different layers in the investigated samples. All three samples have got a slightly tensile $Si_{10}Ge_{90}$ layer with strain ε ≈ 0.1% which can be explained by thermal strain due to the difference in thermal expansion coefficient of the silicon substrate and the epitaxial layer. The following layers, i. e. the barrier (in case of the samples with barrier) and the Ge top layer are then coherent to $Si_{10}Ge_{90}$. For this reason the Ge layer is slightly compressed.

In the sample with the deep barrier (sample 56906), there are two layers of $Si_{10}Ge_{90}$: the first grown on the Si substrate, the second one grown on top of the barrier. With the X-ray diffraction measurements we cannot distinguish both layers and have to report single values for composition and strain for both $Si_{10}Ge_{90}$ layers.

Table 6-1 Germanium content *x* and strain ε obtained by X-ray diffraction for the different epilayers.

	56904 (without barrier)	56903 (shallow barrier)	56906 (deep barrier)
x_{Ge}	98.98%	98.56%	98.70%
ε_{Ge}	-0.1736%	-0.2127%	-0.2410%
$x_{Si_{40}Ge_{60}}$		60.26%	60.24%
$\varepsilon_{Si_{40}Ge_{60}}$		1.4641%	1.4491%
$x_{Si_{10}Ge_{90}}$	92.65%	92.36%	92.89%
$\varepsilon_{Si_{10}Ge_{90}}$	0.1273%	0.1101%	0.1059%

6.3 Micro-Raman strain analysis SiGe barrier samples

To confirm the compressive strain state of the top Ge layer we performed micro-Raman analysis on the sample with the shallow barrier (sample 56903). Considering the effects of strain and composition on the relative Raman shift Δω according to Ref. [157] we obtain a strain value $\varepsilon = -(0.22 \pm 0.02)$ % for the top Ge layer in very good agreement with the XRD data.

6.4 Band-alignment of the SiGe barrier

To estimate the band-alignment of the Ge/$Si_{40}Ge_{60}$/$Si_{10}Ge_{90}$ stack which is comparable in strain and composition for all the samples under investigation, we refer to the work of Virgilio and Grosso [180] who have calculated the band-alignment of strained $Si_{1-x}Ge_x$ epitaxial layers on relaxed $Si_{1-y}Ge_y$ substrates using an sp3d5s* nearest neighbor tight-binding Hamiltonian.
Their calculations are for systems at temperature 0 K. We follow their approach to first determine the valence band offset and obtain the conduction band offset by comparing the conduction band edges of the different layers that are obtained by simply adding the band-gap energies to the position of the valence band edges determined by the valence band offsets. We assume that the

valence band offset is not changed by temperature and can use the formula given by Virgilio and Grosso.[180]

From the XRD and Raman data we can assume the stack of our samples to be coherent, consequently in the estimation of the band-alignment we can refer both the $Si_{40}Ge_{60}$ barrier as well as the Ge top layer to the $Si_{10}Ge_{90}$ layer. Next, we take the band-gap energies for the strained barrier and Ge layer at 0 K from Virgilio and Grosso and estimate the room temperature values interpolating Varshni's laws for germanium and silicon for the composition of the layer in question. In all this estimation, we used the average experimental compositions of the investigated samples, i. e. x = 98% for the top Ge layer, x = 60% for the barrier and x = 93% for the $Si_{10}Ge_{90}$ layer. The obtained band alignment is of type I and is reported in FIG. 6-2.

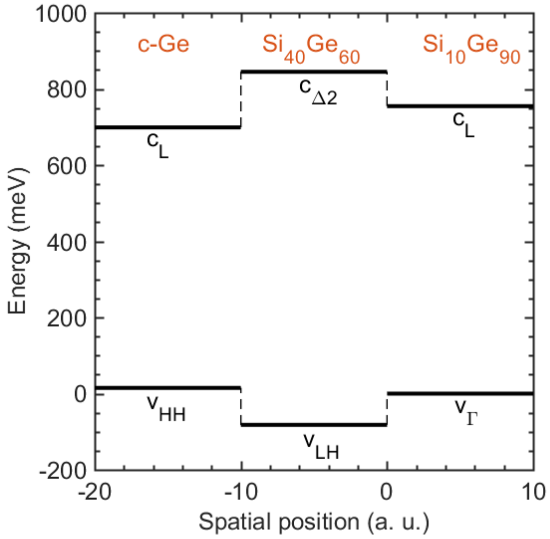

FIG. 6-2 Band-alignment of the samples featuring a $Si_{40}Ge_{60}$ barrier. The alignment of the top Ge layer with respect to the $Si_{40}Ge_{60}$ barrier is of type I. Hence, electrons and holes at the band-edges of Ge are confined.

6.5 Micro-PL analysis SiGe barrier samples

For the PL analysis we have chosen a 457.9 nm laser line to excite the samples. In this case, absorption of the exciting photons takes place in the top germanium layer, only. FIG. 6-3 (a) shows the PL spectra of the three samples obtained with an excitation power density of about 3.5 $\times 10^{5}$ W/cm^{-2}. The sample without barrier shows a PL maximum at an spectral energy of about 830 meV. We identify this band with the direct gap band-to-band transition of the top Ge layer. The band is shifted to higher energies with respect to bulk germanium due to the compressive strain in the Ge layer which leads to an increase in the direct band-gap energy. Below 800 meV we expect several contributions to the PL spectrum: The indirect-gap energy of the compressive Ge layer is estimated to be 680 meV, cf. FIG. 6-2. However, the luminescence band of the indirect gap transitions is broadened because of the variety of indirect-gap transitions; it's peak energy is expected to be $2k_BT$ above the band-gap energy, that is at about 730 meV. On the other hand, it is questionable if indirect-gap luminescence from a 30 nm thin layer can be detectable at all.

Besides the Ge indirect gap, also the $Si_{10}Ge_{90}$ indirect gap luminescence has got spectral energies below 800 meV. The indirect-gap energy for relaxed material has an estimated energy gap of 755 meV. Using deformation potentials, we estimate the indirect band-gap for tensile strain $\varepsilon = 0.12\%$ to be $E_{ind} = 761$ meV.

Considering in addition that the luminescence peak will again occur at an energy higher than the band-gap energy, we can assign the spectral feature at about ~ 760 meV that occurs as a shoulder in the PL spectrum of the sample without barrier, to the indirect-gap luminescence of the $Si_{10}Ge_{90}$ virtual substrate.

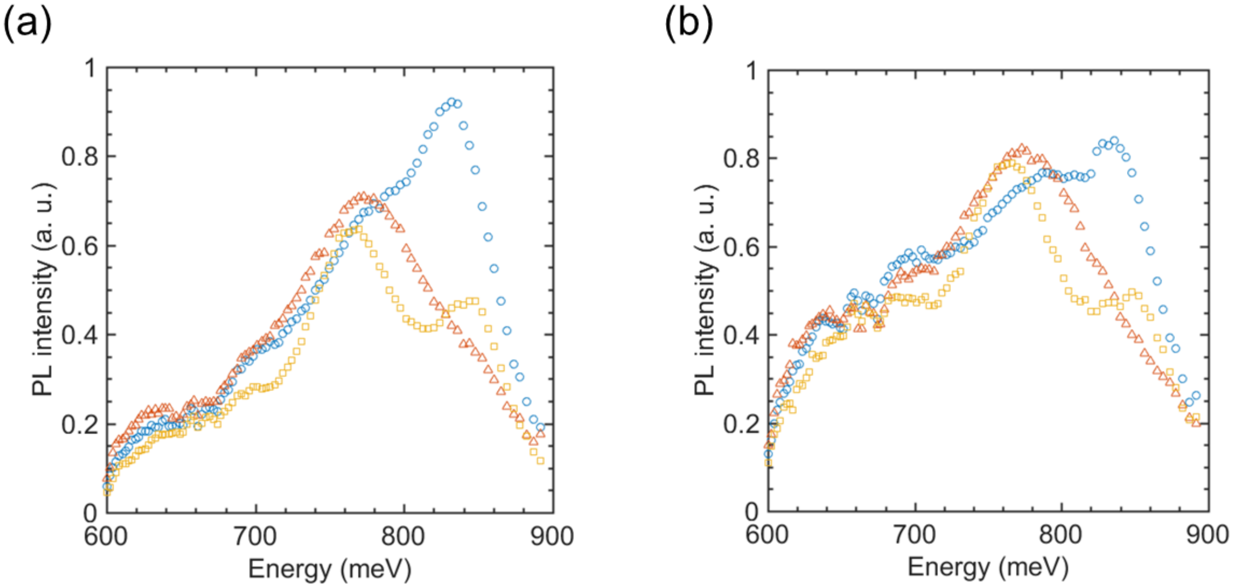

FIG. 6-3 Photoluminescence spectra of the samples without barrier (○), shallow barrier (barrier 30 nm below the Ge surface, △) and deep barrier (barrier 500 nm below the Ge surface, □) for excitation power densities of (a) 3.5 ×10^5 W/cm^{-2} and (b) 1.8 ×10^5 W/cm^{-2}. In both cases, the Ge related signal is reduced through the introduction of a barrier.

This feature even constitutes the most intense band in the PL spectrum of the sample with shallow barrier. From this observation we can immediately tell that the shallow barrier works in a detrimental way: the luminescence from the Ge top layer at 830 meV is reduced strongly, whereas the luminescence from $Si_{10}Ge_{90}$ remains at the same level.

The spectrum of the sample with deep barrier also shows a contribution from the Ge layer at about 830 meV with only slightly higher intensity to that one of the sample with shallow barrier. Regarding the PL intensity of the Ge layer, the deep barrier brings only a slight improvement with respect to the shallow barrier. Still the Ge direct luminescence is reduced strongly with respect to the sample without barrier.

The spectral position of the second dominant band is shifted to lower energies with respect to the other two samples. We cannot explain this from a point of view of the bandgap energies that differ only by a view meV. However, in the sample with the deep barrier, the $Si_{40}Ge_{60}$ barrier is sandwiched between two $Si_{10}Ge_{90}$ layers. From a photoluminescence study of samples with SiGe virtual substrates of different germanium content, we found that room temperature PL spectra of SiGe resemble in shape the low temperature spectra reported by Rowell et al. [175], but are shifted to lower energies. The deviating spectral positions in the sample with deep barrier could consequently be due to a stronger contribution of luminescence from the $Si_{40}Ge_{60}$ barrier.

FIG. 6-3 (b) depicts the PL spectra obtained at half the excitation power density with respect to FIG. 6-3 (a). Again, the sample without barrier shows the strongest Ge signal. We can identify all peaks that are also present in the spectra with higher excitation power density. However, the intensity ration between luminescence from the top Ge layer and SiGe related PL is decreased.

After optical excitation the carriers possess enough energy to overcome the SiGe barrier. Since absorption of the exciting photons is within the top germanium layer (absorption length is estimated

to be ~16 nm for 458 nm wavelength. In the case of compressed material absorption may be reduced slightly because of the larger band-gap of compressed germanium resulting in a little longer absorption length that still can be assumed to be ~20 nm), diffusion of carriers during thermalization is the only way to overcome the barrier. The thermalization time τ_{therm} of photo-excited carriers in Ge amounts to about ~ 7 ps (cf. Ref. [164] and sec. 4.1). For a first estimation we use the ambipolar diffusion coefficient for already thermalized carriers in Ge from Grzybowski et al. [82] with value $D = 65$ cm^2 s^{-1} and obtain a diffusion length $L = 213$ nm.
Hence, it is not surprising that hot carriers overcome the shallow barrier (30 nm deep) during thermalization. The thermalized carriers are then kept on the $Si_{10}Ge_{90}$ side by the barrier, because also between $Si_{40}Ge_{60}$ and $Si_{10}Ge_{90}$ the band-alignment is of type I (cf. FIG. 6-2) so that both electrons and holes are confined by a potential barrier.

On the other hand, with the diffusion length L estimated, the 500-nm-deep barrier should be appropriate to block the thermalized carriers. However, the deep-barrier-sample shows only a slight increase in Ge luminescence: the deeper position of the barrier allows more carriers to thermalize before the appearance of the barrier – that can then diffuse back to the Ge top layer, but most of them still overcome it. Consequently, the diffusion length of hot carriers is longer than the estimated 213 nm. This can be explained by an increased diffusion coefficient for hot carriers like done by Othonos.[162] Furthermore, Othonos shows that the carrier temperature depth profile is not following the carrier concentration profile, but that due to carrier-carrier scattering the carrier temperature is elevated on a larger length scale, so that also the increased diffusion coefficient is valid on a larger length scale. From our result we can conclude that the diffusion length for hot carriers is larger than 500 nm.

The changed intensity ratio between Ge related and SiGe related PL intensity observed in FIG. 6-3 (b) may also be related to the important role of carrier diffusion during thermalization: The thin Ge top layer (30 nm thick) needs an adequate pumping to show PL and PL is weak when the excitation power is reduced. The thick SiGe virtual substrate on the other hand is less dependent on pump power and due to the strong carrier diffusion during thermalization the carrier concentration is still sufficient also at low excitation powers.

Note, that the above given thermalization time of Roskos et al. [164] has been extracted from pump-probe experiments with short pump pulses. In contrast to this, our measurements are performed under continuous excitation of the sample. The permanent photo-excitation could lead to a steady state in which the carrier gas is not completely thermalized but electrons and holes possess temperatures higher than the sample lattice temperature: $T_{\mathrm{e,h}} > T_{\mathrm{L}}$ and hence have got elevated kinetic energies. Consequently, in our samples the time constant to reach equilibrium may be different from the ~ 7 ps of Roskos et al. and the constant elevated carrier gas temperature may lead to an increased diffusion coefficient over a wide spatial range.

Furthermore, as Virgilio and Grosso point out, the conduction band offset of the $Si_{40}Ge_{60}$ alloy with respect to alloys $Si_{1-x}Ge_x$ with $x > 0.8$ is not consistent in literature and calculations also resulted in negative offsets.[180] A negative conduction band offset means that the conduction band edge of the $Si_{40}Ge_{60}$ barrier lies below the top Ge layer as well as the $Si_{10}Ge_{90}$ bulk. Electrons would not be confined by the barrier.

However, the conduction band minimum in the barrier is constituted by two-fold valleys in direction Δ whereas the conduction band minima in the top Ge layer are in the L valleys along direction <111> of the Brillouin zone so that an electron in L would first have to change momentum to scatter into the Δ2 valleys which could limit this channel through the barrier. Considering only the L valleys of the Ge layer and the barrier, electrons still experience a potential barrier by the $Si_{40}Ge_{60}$ layer.

The work of Pezzoli et al. shows that a SiGe barrier can be successfully applied in Ge systems.[137] They introduced 10 nm thick $Si_{0.25}Ge_{0.75}$ barriers 2 µm, 4 µm and 6 µm below the top of Ge towers grown on patterned 2 x 2 µm Si substrates. They used a 1064 nm laser for photo-excitation that results in a larger penetration depth and less excess kinetic energy of the photo-excited carriers. Nevertheless, from the fact, that the barrier 2 µm below the tower top already brings an improvement with respect to a reference samples without barrier, we conclude that the energetic position of the Δ2 valleys is not the main issue, since also the alloy $Si_{0.25}Ge_{0.75}$ with 75% germanium features the conduction band minimum along direction Δ.[86] Moreover, Pezzoli et al. observe, that the deeper barriers perform better, supporting our view that the barriers in our samples are overcome during thermalization of the carriers.

7 Effect of surface etching on photoluminescence from germanium

The SiGe stripe stressors are fabricated by etching trenches into a SiGe layer on top of Ge by means of reactive-ion etching, see the preparation details in sections 5.3.1 and 5.4.1. It is inevitable in this fabrication step that also the Ge layer freed from the SiGe cover inside a trench will be exposed to the etching plasma. To check the effect of surface etching on the photoluminescence of germanium we revert to the Ge/$Si_{10}Ge_{90}$ sample that has been part of the series of samples to study the effect of a potential barrier below the surface.

In this study, we use the following modifications of this sample the cross-sectional profiles of which are reported in FIG. 7-1:

- as grown
- sample with surface treated by reactive-ion etching (RIE)
- sample with RIE plus a subsequent treatment with H_2O_2 to smoothen the surface again
- sample with RIE plus deposition of SiO_2 to change the surface chemistry

Lodari from Politecnico di Milano etched the sample surface with RIE and studied the obtained surface roughnesses with an atomic force microscope. He finds that on a 5 × 5 µm area the root-mean-square roughness changes from 0.30 nm after sample growth to 0.36 nm after a RIE treatment for five seconds. The two further samples were subsequently etched with H_2O_2 for 20 s or 65 nm of thermal SiO_2 were deposited after the RIE treatment. The motivation is to smoothen the Ge surface again or to saturate dangling bonds at the surface, respectively.

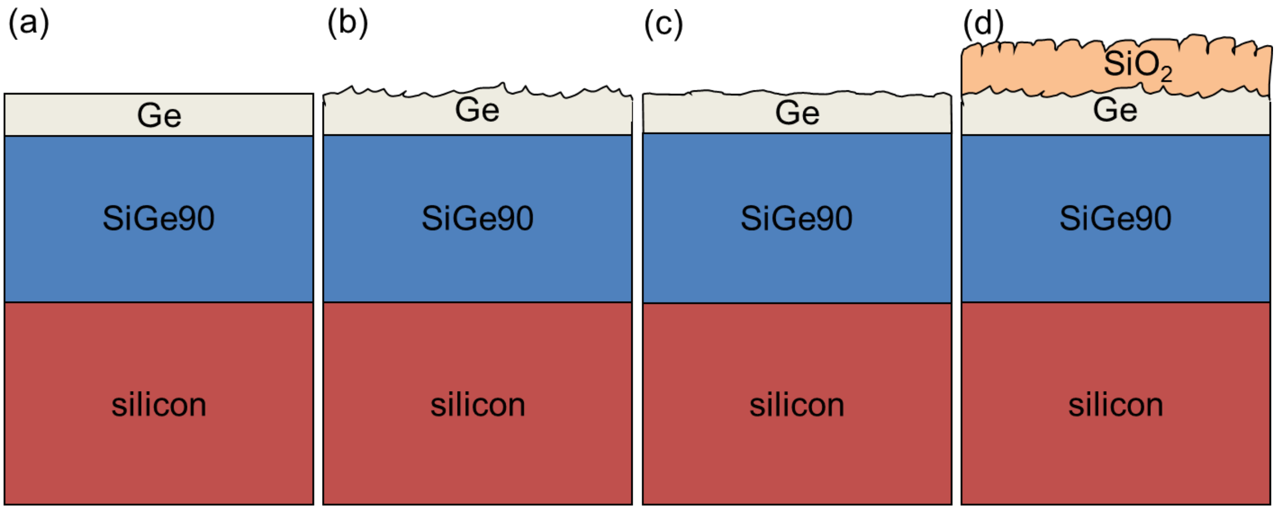

FIG. 7-1 Sketches of the samples prepared to study the effect of surface treatment on the PL from the top Ge layer. (a) as-grown, (b) reactive-ion etching (RIE) of the Ge surface, (c) RIE and subsequent etch with H_2O_2, and (d) RIE and subsequent deposition of SiO_2.

The photoluminescence results are shown in FIG. 7-2. In the as grown sample we can identify the strong emission from the top Ge layer at about 830 meV which constitutes the maximum of this spectrum. Like in the previous section we will focus on the discussion of the intensity of this emission band. The RIE treatment eliminates the emission from Ge completely. Subsequent etching with H_2O_2 recovers emission from the Ge layer. In fact, Lodari found that the surface roughness after H_2O_2 application is even less than in the as grown sample. However, the Ge signal is not recovered completely; we conclude that not only surface roughness matters, but also the changed chemistry of the surface: The etching processes could have led to an increased number of dangling bonds at the surface which are effective channels for non-radiative recombination.

The deposition of an thermal oxide on the surface etched with RIE might help to saturate dangling bonds and reduce the surface recombination velocity, but the effect of the oxide layer is just that of an anti-reflection coating: the spectrum from the sample with SiO_2 resembles in shape that one with the RIE treatment, but with increased intensity. The Ge signal is not recovered.

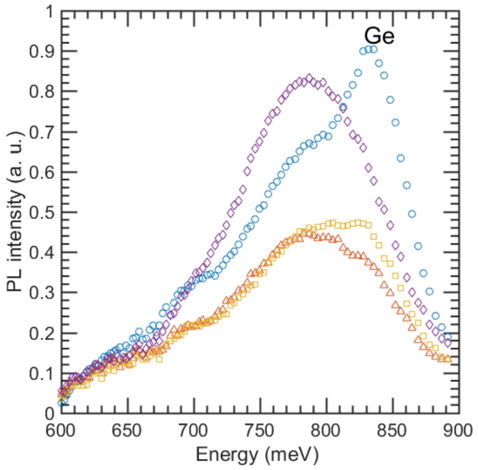

FIG. 7-2 Effect of different surface treatments on the photoluminescence intensity of a Ge layer grown on $Si_{10}Ge_{90}$. Shown are the PL spectra for an as-grown sample (○), for a sample with RIE etched surface (△), a sample with successive RIE and H_2O_2 treatment (□) as well as a sample with successive RIE etch and SiO_2 deposition (◊).

Reactive-ion etching was performed using a CF_4 (Freon-14/tetrafluoromethane) RF plasma. During reactive-ion etching several processes occur. CF_4 dissociates partially in the plasma, forming the highly reactive free radicals F and CF_x. These radicals adsorb to the sample surface and in a surface chemical reaction volatile products of the sample material are formed, thereby etching the surface chemically. In the case of a Ge surface, GeF_4 is formed that is subsequently removed by the pump system.

Besides this chemical etching, charged particles formed in the plasma impinge on the sample surface and corrode it by a physical sputtering process.

Consequently, in our case – the Ge surface is altered by chemical and physical processes that change the surface condition so that no epitaxial surface is present anymore. The altered surface may contain additional surface energy states through which non-radiative recombination of excited carriers occurs and hence quenches the PL from the Ge layer.

With the mere scope to give examples what may happen, we mention that in a plasma etch process the sample may be damaged by impinging ions, electrons, radicals, and photons.[181] Kusumandari et al. showed that with a CF_4 plasma electron and hole traps are created in germanium, that consist of divacancies, di-interstitials, interstitials or impurity-related defects.[182] They found that the traps can have a depth distribution of up to 3 µm into the sample bulk.[182] Moreover, byproducts from the chemical reaction may remain as a thin film on the surface.[183]

Besides smoothing the surface, on can think of the effect of the subsequent H_2O_2 treatment in restoring the original oxide terminating the Ge surface [184] or removing the layer of residual byproduct.

However, we point out – since the interaction of the plasma and the germanium surface is extremely complicated – that the experiments conducted in our study do not allow for a conclusion about the detailed processes that occur in our samples due to the RIE treatment. A more rigorous in-depth study applying further measurements techniques would be needed.

8 SiGe stressors on suspended Ge membranes

Our work so far has shown that we can induce high values of tensile strain in a Ge substrate with SiGe stressors, but that it is not possible to confine excited carriers to the volume of high strain that is close to the surface.
If we transferred the SiGe stressor method from bulk-like thick substrates material to suspended thin Ge micro-bridges, we may have two advantages:

(1) FEM simulations suggest that a thin suspended Ge layer with comparable thickness to the SiGe stressor layer can be strained to a higher degree. In turn, we can separate the perimeters of the SiGe stressors by a wider gap and still reach high strain values.
(2) In a thin suspended Ge layer, excited carriers are confined vertically by the limited thickness of the layer; air (vacuum) acts as a barrier.

In the following we present our first results of SiGe stressors on Ge micro-bridges and compare the obtained strain to the case of attached bulk-like Ge.

8.1 Sample preparation: Heteroepitaxy and Nanostructuration

The SiGe/Ge stack was grown by low-energy plasma-enhanced chemical vapor deposition (LEPECVD) on a Si (001) substrate.[98] Bridge and stressors are prepared by e-beam lithography and reactive ion etching (RIE). Potassium hydroxide (KOH) is used to suspend the SiGe/Ge bridge.
The actual samples were processed from a stack of nominally 50 nm SiGe with 60% Ge content on 100 nm Ge on Si(001) so that the SiGe stressor layer has a comparable thickness to the subsequently formed Ge bridge, see FIG. 8-1 (a). Material composition and strain were determined by x-ray diffraction (XRD). The Ge layer is slightly contaminated by Si (Ge content 98.6%) and exhibits an in-plane strain of $\varepsilon_{\|} = 0.05\%$ due to partial relaxation of thermally induced strain. The SiGe layer has a Ge content of 59.7% and the in-plane strain is determined to be $\varepsilon_{\|} = 1.64\%$. This strain value indicates coherent growth on Ge and corresponds to a stress of $\sigma_{\|} = 2.58$ GPa.

The creation of suspended SiGe/Ge bridges and the stressor pattern in the SiGe layer are described in detail in Ref. [185] and Ref. [59]. A key step for proper action of the stressor is that the etching of the trenches should stop exactly at the SiGe/Ge interface, in order to maximize the local stress applied to the Ge. FIG. 8-1 (b) shows the scanning electron micrograph (SEM) of a fully processed Ge bridge with cross stressors engraved into the SiGe top layer. The stressors on the suspended bridge can be recognized close to the center of the image (lighter color of suspended material), while at its ends the stressors on the bulk-like Ge can be seen. In the following we will refer to the different regions as “bridge” and “bulk”. The width W of one of the trenches is 230 nm and the length L = 1040 nm. A thin residual Ge hemline along the bridge borders remained, whose origin is linked to the protective coating that was applied during the bridge suspension.

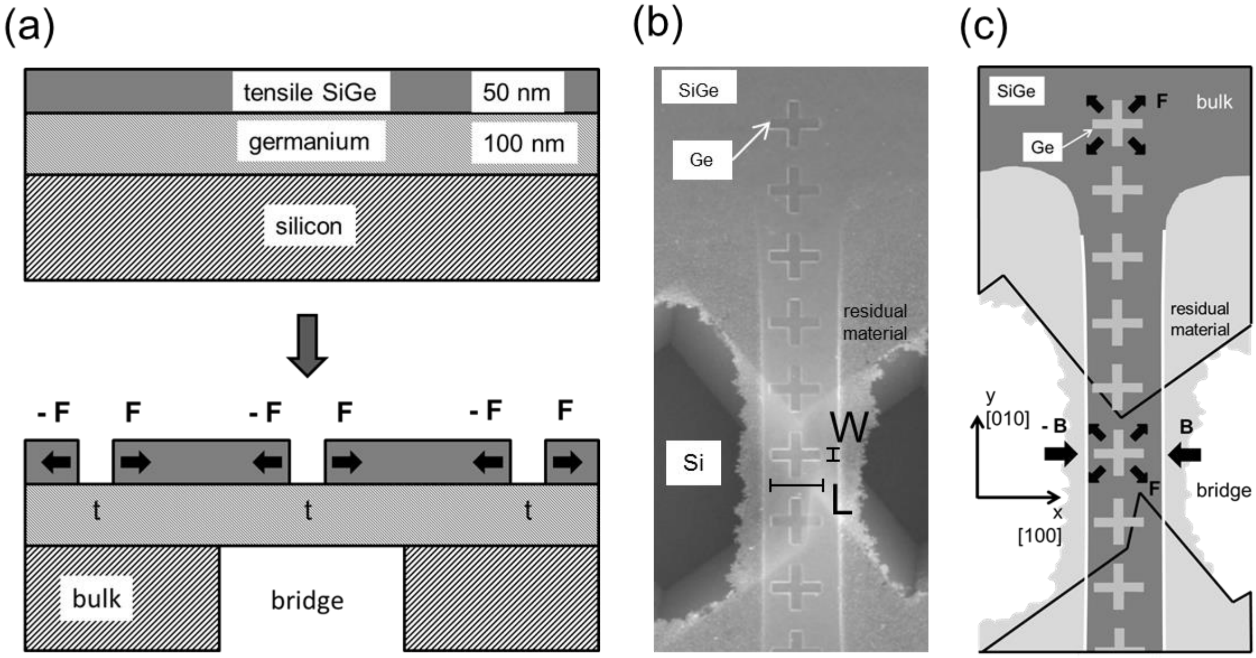

FIG. 8-1 (a) Sketches in cross section to illustrate the fabrication and working principle of the investigated system. The cross section is through the arms of the realized cross shaped patterns inside the SiGe layer. The perimeter forces at the side walls of the trenches (indicated by arrows) pull the Ge inside a trench resulting in tensile-strained Ge (indicated with the letter "t"). The sample features stressor structures on grounded ("bulk") and free standing ("bridge") Ge material.

(b) SEM image of the fabricated sample. The free-standing part can be recognized by the lighter color. The width of one trench is W = 230 nm and the length is L = 1040 nm.

(c) sketch in top view. The SiGe/Ge bridge is not constrained in the [100] direction, resulting in a compressive strain bias as indicated with arrows B. Arrows F illustrate the action of the cross stressors and are equivalent to the arrows in (a).

8.2 Raman strain analysis

We used a micro-Raman set-up in backscattering geometry equipped with a 100× 0.9 NA objective and 0.1 µm step positioning stage. A frequency-doubled Nd:YAG laser with 532 nm output wavelength was used, producing a spot size less than 1 µm on the sample. The choice of the excitation wavelength is justified by the vicinity of 532 nm wavelength to the Raman resonance in Ge [186] so that we could use a power of 0.05 mW, low enough to avoid heating artefacts in these structures characterized by low thermal dissipation.

The excitation was linearly polarized along *y*, while the collection was not polarized. With this experimental geometry, only the longitudinal-optical (LO) phonon can be probed. Even though in principle also transverse-optical (TO) modes could be collected through the marginal rays of an objective with high numerical aperture, their intensity is expected to be negligible with this unpolarized collection geometry.[187]

The system was calibrated with a reference bulk crystal to the Ge-Ge phonon mode at $\omega^0_{Ge-Ge} = 300.3\ \mathrm{cm}^{-1}$. The Raman shift value ω_{Ge-Ge} of the strained material was obtained from a fit of the acquired Raman spectrum to a simple model described in detail in the next section.

Since for symmetry the off-diagonal strain components are negligible, strain values ε were determined by setting up the strain tensor and using the relationship (Eq. (3-8))

$$\Delta\omega = \omega - \omega_0 = \frac{1}{2\omega_0}\left(q\varepsilon_{xx} + q\varepsilon_{yy} + p\varepsilon_{zz}\right)$$

where ω is the measured Raman shift, ω_0 is the Raman shift of the relaxed material and q and p are the deformation potentials for Ge as defined in Ref. [102], cf. sec. 3.3.

Information about the strain state of the Ge beneath a stressor can be obtained from the shift of its Raman band. Since the spot size of the scattered laser on the sample is larger than the width of the arms of the cross stressor and the 50 nm thick SiGe top layer is transparent at 532 nm wavelength (the penetration depth in SiGe with 60% Ge is estimated to be δ_{SiGe} = 90 nm, Ref. [159]), both SiGe layer and Ge layer are probed.

Let us first consider the unpatterned bulk, see FIG. 8-2 (a). The Ge band in this region is centered at 300.1 ± 0.1 cm^{-1}. This value is slightly red-shifted with respect to the reference in accordance with a slight tensile thermal strain.[157] The three prominent bands of the spectra originating from SiGe are related to the Ge-Ge, Si-Ge and Si-Si LO modes.[155]
In this work we will focus on the Ge-Ge mode since this is the most intense. The position of this band in the bulk is 284.0 ± 0.9 cm^{-1} which corresponds to (1.6 ± 0.2) % tensile strain. Both of these values are in agreement with XRD. We can compare these results to those related to the unpatterned SiGe/Ge bridge, cf. FIG. 8-2 (a).
Raman measurements on a suspended reference bridge without cross stressors revealed that the Ge layer is slightly compressed (Raman shift $\omega_{Ge\text{-}Ge}$ = 301.7 cm^{-1}, which corresponds to a strain of -0.3%) and that the SiGe layer is less tensile, i.e. partially relaxed, with Raman shift $\omega_{Ge\text{-}Ge}$ = 287.1 cm^{-1} which corresponds to 1.1% strain. This change in the strain is readily explained by a redistribution of the strain in the bilayered bridge. Due to the removal of the mechanical constraint perpendicular to the bridge (direction *x* in FIG. 8-2 (c)) transverse elastic relaxation of tensile stress in the SiGe layer is significant and the reduction of the tensile strain field in the SiGe layer causes a compression of the Ge layer. However, it is important to notice that SiGe is still in a highly tensile state, which is the prerequisite for it to be used to create nanostructured stressors.

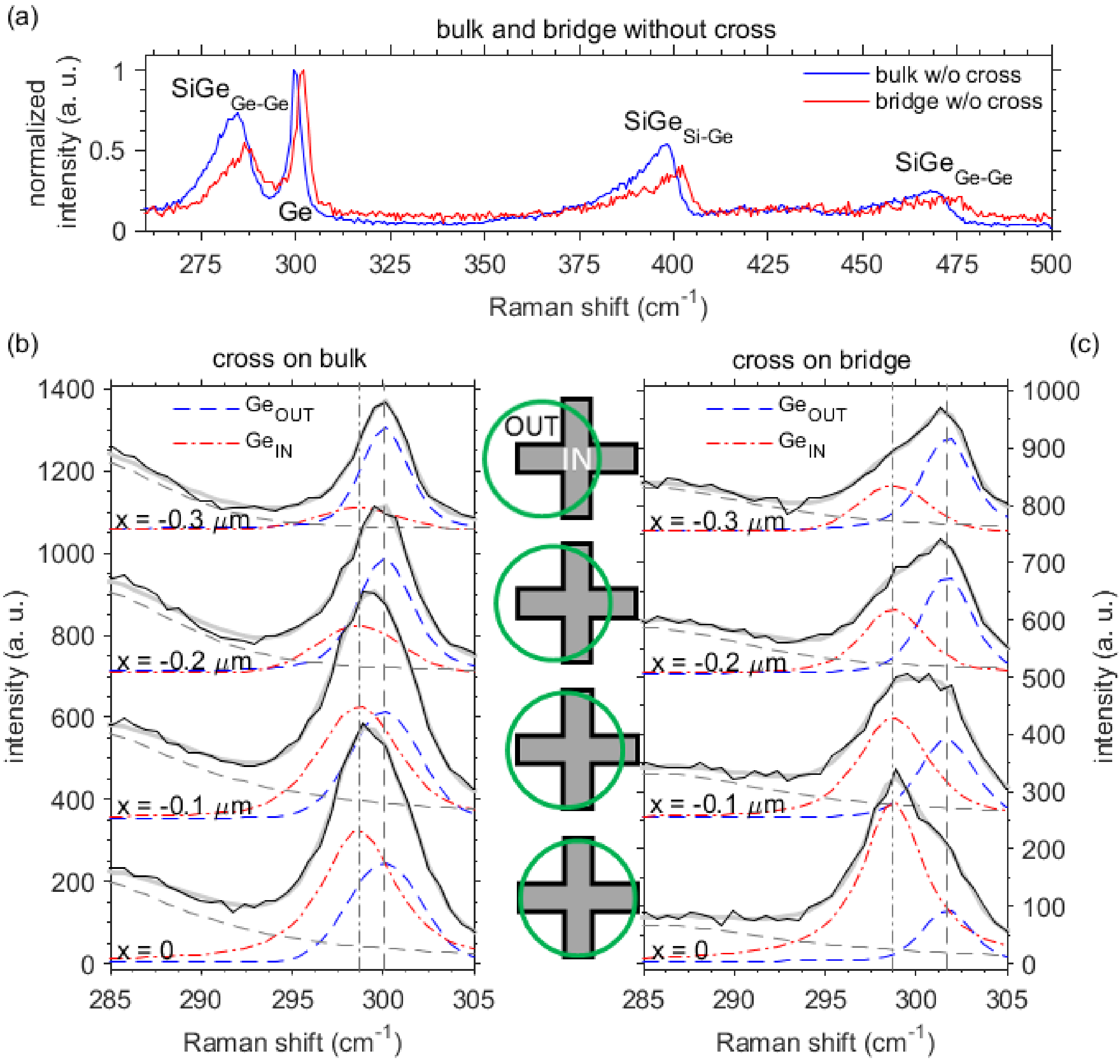

FIG. 8-2 Raman spectra of the bulk without cross (blue curve) and an unpatterned reference bridge (red curve). The different visible modes are labeled. The Raman spectra obtained from a line scan across a cross stressor on bulk and on the bridge along direction *x* (cf. FIG. 8-1 (c)) are shown in panels (b) and (c). The upper spectra of each series are taken from a position outside the center of the cross, whereas the position of the last spectra is in the center as indicated by the green circle in the sketches between panels (b) and (c). The data are fitted by the thick grey line, which is a combination of the single bands for Ge not altered by the cross stressor (blue dashed line), Ge altered by the stressor (red dash-dotted line) and the Ge-Ge mode of SiGe (grey dashed line).

We now investigate the effect of etching crossed trenches into the bulk and the bridge. The results are presented in FIG. 8-2 (b) and (c) for the bulk and bridge, respectively. With respect to the unpatterned case, these measurements are more critical since the nanostructures are of comparable size to the laser spot. For this reason, the effects related to the cross stressors can be better appreciated observing a line scan with steps of 0.1 µm running from outside (x = -0.3µm) towards the center of the cross (x = 0 µm), as depicted by the sketches in between the panels. Visual inspection of panel (b) shows a band at about 285 cm^{-1} from the SiGe stressor and a band at about 300 cm^{-1} from the Ge film. Moving towards the center of the cross we can see that the position of the Ge band moves towards tensile values. Visual inspection of panel (c) suggests that the Ge band features two components, whose relative intensity changes as we approach to the center of the cross. We interpret these two components as related to Ge outside the cross (Ge$_{OUT}$) and Ge inside the cross (Ge$_{IN}$). In the upper spectra the main contribution to Ge is from Ge$_{OUT}$. As we approach the center of the cross, the Ge_{IN} component from tensile Ge appears and overcomes the Ge_{OUT} component. The separation of the band into two components can be observed only in the cross on the bridge because in this case the strain induced by the cross is much higher than the case of the cross on bulk.

In order to consistently extract quantitative data, we fitted all the spectra from both bulk and bridge with the same model consisting of three peaks representing SiGe, Ge_{OUT}, and Ge_{IN}. We use two components for Ge to model what is in fact a complex distribution of strain because previous simulations [61] suggest that, within the small penetration depth of the laser (20 nm), in these structures there are indeed two regions with well separated values of strain: Inside the cross and outside the cross. In addition, a higher number of components would lead to an uncontrolled fit. For Illustration purposes, we replot the strain distribution inside a Ge bridge strained by a SiGe stressor as calculated by Scopece et al. with the finite element method. We point out that the calculation was performed for different geometrical and material parameters than used in this work.

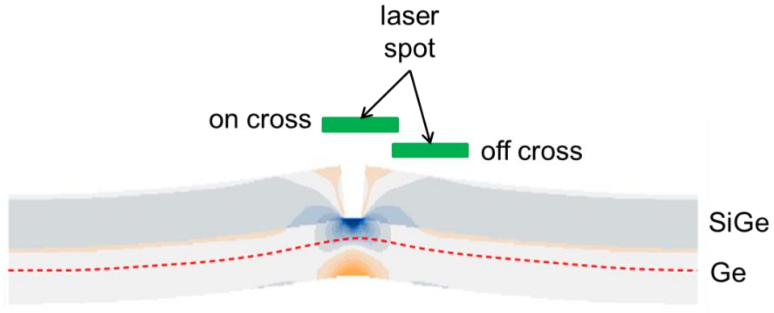

FIG. 8-3 Illustration of the strain distribution in a Ge bridge strained by a SiGe layer. The red dashed line indicates the penetration depth of the laser into the Ge layer. The laser spots on and off the stressor (trench of a cross) are drawn in scale to the gap width of *W* = 230 nm. In a situation with the laser spot off the cross, the relaxed / slightly compressed Ge is probed (orange colors). On the cross, exclusively the tensile strain induced by the SiGe stressor is probed.

In both FIG. 8-2 (b) and (c) the spectral position of the components was used as a global parameter for the simultaneous fitting of the spectra. For the bulk case, the fitted Ge_{IN} and Ge_{OUT} components are separated by 1.4 cm^{-1}, while for the bridge case they are separated by 3.0 cm^{-1}. As pointed out above, this increased splitting reflects the fact that on the bridge the strain induced by the cross is much higher than the case of the cross on bulk. For the bridge case, the SiGe can transfer more of its elastic energy to the underlying Ge so that the resulting strain is higher.[61]

We now proceed with the quantification of the strain. The cross stressors create biaxial strain in the center of the cross. However, the center of the cross, i.e. the intersection of the arms, is only 230 × 230 nm^2, too small to be resolved spatially. Since the area ratio of the center to the arms of the cross is about 1:6, what we detect with the Raman measurement stems mainly from the arms, which are under uniaxial strain. For the transformation of Raman shift into strain we have to consider the elements of the strain tensor ε in Eq. (3-8):

$$\varepsilon_{xx} = \varepsilon_{comp.\,bias} + \varepsilon_{therm} + \varepsilon_{xx,\,cross} \qquad (8\text{-}1)$$

$$\varepsilon_{yy} = \varepsilon_{therm} + \varepsilon_{yy,\,cross} \qquad (8\text{-}2)$$

$$\varepsilon_{zz} = -\frac{c_{12}}{c_{11}}\left(\varepsilon_{xx} + \varepsilon_{yy}\right) \qquad (8\text{-}3)$$

$\varepsilon_{comp.\ bias}$ is the compressive strain bias along direction x, ε_{therm} is the biaxial thermal strain originating in the growth of Ge on Si, $\varepsilon_{xx,\ cross}$ and $\varepsilon_{yy,cross}$ are the strain induced by the cross stressor along directions x and y, respectively, and C_{12} and C_{11} are the elastic stiffness constants of Ge. The strain values are then obtained by solving Eq. (3-8).

Since $\varepsilon_{comp.\ bias}$ and ε_{therm} are known from the independent measurements on the bulk and on the bridge, it is possible to calculate the strain in the material induced by the presence of the cross, $\varepsilon_{xx,\ cross}$, i. e. the additional strain relative to the Ge without crosses.

Table 8-1 shows a summary of the results in terms of Raman shift and obtained uniaxial strain values for absolute and relative ("cross induced") strain, demonstrating that the stressor on the bridge is more efficient than that on bulk material leading to twice the relative strain value. However, the strain induced by the stressors is nonuniform, because the stress forces act only at the perimeter of the cross, which means that the reported values give an average of the strain distribution. If we ascribe these average values to the arms and assume that each arm exerts an additive force on the center of the cross, it is possible to infer that the strain in the center of the cross will be biaxial and would reach at most 1.3%; only 0.6% would be reached by the same nanostructure in the bulk case. This value is lower than the 1.6% biaxial strain required to obtain direct gap material.[27] However, optimization of stressor geometry and process parameters could lead to increased tensile strain, as predicted by Ref. [61].

Table 8-1 Strain induced by the cross measured by Raman spectroscopy. ω_{IN} and ω_{OUT} are the spectral positions of the Ge_{IN} and Ge_{OUT} components. $\Delta\omega$ is the difference ω_{OUT} - ω_{IN}. $\varepsilon_{xx,\ cross}$ is the strain induced by the cross, ε_{xx} is the overall strain.

	ω_{OUT} (cm^{-1})	ω_{IN} (cm^{-1})	$\Delta\omega$ (cm^{-1})	$\varepsilon_{xx,\ cross}$ (%)	ε_{xx} (%)
bulk	300.1±0.2	298.7±0.7	-1.4±0.7	0.6±0.3	0.7±0.3
bridge	301.7±0.2	298.7±0.1	-3.0±0.2	1.3±0.1	0.7±0.1

We showed that the Ge inside a stressor is under tensile strain. Due to the compressive strain bias of the micro-bridge, the absolute strain values are of the order of 0.7% uniaxial strain for the micro-bridge. However, this strain value may be sufficient to be revealed in photo-luminescence experiments. This is discussed in the following section.

8.3 Photoluminescence of a Ge bridge strained by SiGe stressors

8.3.1 Germanium on Si substrate

We have seen that we can double the strain created by a SiGe stressor in germanium when we fabricate the stressor on a suspended thin Ge membrane with comparable thickness to the stressor layer instead on Ge bulk-like material. Besides this strain-sharing effect, the suspension of the Ge layer results in a Ge/air interface, so that photo-excited carriers in a photo-luminescence experiment are confined to the thin Ge membrane. Moreover, in section 5.5 we observed that photo-excited carriers thermalize only after a long distance of diffusion away from the surface where carrier photo-excitation happens; there is no “funneling” effect back to the highly strained Ge volume that is situated at the very Ge surface. In this respect, having a thin membrane may force the photo-excited carriers to stay in the highly strained region. However, photo-luminescence experiments failed. The only 100 nm thin, suspended Ge membrane has proven to be very heat sensitive. With respect to the bulk-like material we had to reduce the excitation-power by a factor of ~ ×20 to prevent destruction of the bridge (reduction of excitation-power density from 7.4×10^5 W/cm^2 to 0.4×10^5 W/cm^2). With this low excitation level the signal to noise ratio was not sufficient to draw any solid conclusions. The sample with the thin membrane has got two drawbacks in view of the exploitation as active material in luminescence experiments:

- the low layer thickness results in a low volume of active material which limits luminescence intensity
- the material quality is presumably low since the first nano-meters of hetero-epitaxial layers contain a larger number of defects. For example, the threading-dislocation density (TDD) of our thin Ge grown on Si is estimated to be ~10^9 cm^2.

8.3.2 Germanium on insulator (GeOI) substrate

To tackle the material quality issue, we tested the photoluminescence from a 50 nm germanium on insulator (GeOI) substrate wafer and compared it to the result of a 50 nm thick Ge layer grown on Si. GeOI substrates are germanium layers transferred on SiO_2 that in turn is fabricated on a silicon wafer. GeOI substrates are characterized by the extremely low threading dislocation density of their Ge layer. We used a die of a GeOI wafer manufactured by IQE Silicon Compounds Ltd. in the SmartCutTM process. The oxide layer is 200 nm thick and the Ge layer is 50 nm thick. The manufacturer states a dislocation density determined by TEM less than 1×10^5 cm^{-2} in our case,[188] which is several orders of magnitude less than the expected value in the 50 nm thick Ge on Si grown by LEPECVD.

FIG. 8-4 shows the PL spectra from the GeOI and the 50 nm Ge grown on Si with the same conditions like the bridge samples discussed previously. A discussion based on PL intensity is not constructive since the insulator layer may enhance PL intensity from the GeOI due to increased back-side reflectivity. Indeed, both spectra shown were acquired with different excitation power densities (3.6×10^5 W/cm^2 and 7.4×10^5 W/cm^2 for the GeOI and the Ge|Si, respectively). However, the PL spectra can be distinguished by their line-shape: The GeOI reveals the expected PL spectrum originating in a thin layer of Ge with the direct-gap band-transition at about 800 meV and a second band with peak energy of ~ 700 meV that can be attributed to the indirect-gap transition. The direct/indirect ratio is > 1 as expected for a thin layer of Ge. On the other hand, the PL spectrum from Ge on Si exhibits a broad band emission with peak energy between 700 meV and 750 meV. The direct-gap emission band is absent which is not expected for a thin layer of Ge investigated with a micro-PL set-up. Grzybowski et al. [82] as well as Pezzoli et al. [137] were not able to observe a PL signal from as-grown Ge on Si layers, i. e. samples without annealing steps. Also our sample did not undergo any post-growth treatment. The obtained PL signal may hence be attributed to originate in extended defects. Indeed, Arguirov et al. [189] also could observe emission at 720 meV in the luminescence from a Ge p-i-n LED grown on Si. They think that this feature is a result of a one dimensional dislocation band that is created by the modification of the Γ valley of the conduction band through the local strain field of the dislocations. Since – as already stated – we expect a poor Ge layer quality with high threading dislocation density, it is plausible that in PL experiments we can only observe dislocation related luminescence. Hence, it seems to be a viable path to produce SiGe stressors on GeOI substrates in future work. The use of a GeOI substrate may furthermore facilitate the fabrication of the germanium bridges, since the selective etching of SiO_2 in presence of SiGe and Ge is less critical than the selective removal of Si. However, growth of homo- and heteroepitaxial layers on GeOI substrates is not straight forward.

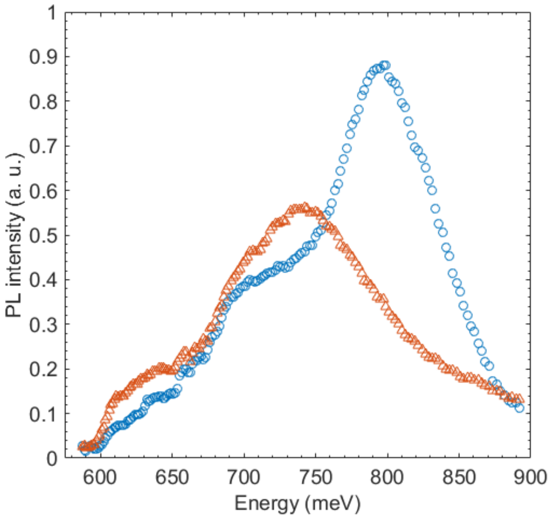

FIG. 8-4 Photo-luminescence spectra of 50 nm Ge on insulator (GeOI, ○) and 50 nm Ge grown directly on Si (△). The spectrum of GeOI has got the expected line-shape of Ge photoluminescence, whereas the luminescence from the thin layer directly grown on Si is attributed to the dislocation network in Ge.

9 Photoluminescence of phosphorous doped Ge on Si

So far, we have worked on the creation of tensile strain in germanium and have shown that with our SiGe stressor approach we are able to induce substantial strain values. Besides tensile strain, n-type doping is required to enhance the radiative recombination from germanium. Calculations for the threshold current density in Ge-on-Si laser structures revealed that if a sufficient strain value is reached, the doping level needed for an acceptable threshold current density may be well below 1×10^{19} cm^{-3},[62] which is a feasible doping level.
However, the strain values needed are still close to the indirect/direct bandgap transition in Ge. The drawback of high strain values in terms of applications is that the emission wavelength of the strained Ge laser is shifted to the mid-IR spectral region, because the bandgap in Ge shrinks with increasing strain; the laser would not match the transmission windows of optical fibers used in data-communication. From this point of view, it is interesting to investigate the effect of n-type doping on the emission spectra of Ge at higher doping concentrations in the range from 1×10^{19} cm^{-3} to 1×10^{20} cm^{-3}.

Doping is acknowledged as one route to enhance luminescence from Ge.[28] On the other hand, luminescence quenching was reported for doping levels larger than 3×10^{19} cm^{-3}.[65] Moreover, the dependence of carrier lifetimes on dopant concentration in Ge layers has not been addressed profoundly up until now. For these reasons, in the first part of our study we try to optimize the growth conditions for such highly doped Ge on Si samples with respect to photo-luminescence intensity and in the second part (sec. 10) we try to gain deeper inside into the effect of doping on carrier lifetimes by comparing experimental data with a sophisticated photoluminescence model. The work presented here was carried out at IHP GmbH, Frankfurt (Oder), under conduction of G. Capellini.

9.1 Growth condition study for photo-luminescence optimization of germanium

The growth of highly doped Ge on Si is challenging, since the impurity atoms have to be well incorporated in the Ge matrix. Moreover, there is a certain solubility limit of the dopant in Ge. We are going to use phosphorous (P) as dopant, since it is commonly used in CMOS technology. The solid solubility limit of P in Ge is 2×10^{20} P/cm^3.[190] In the first part of our study, we try to reveal trends in the multi-parameter space of growth parameters to find the maximum in terms of photoluminescence intensity, i. e. we perform a growth condition optimization to maximize PL. Thereby we take the following parameters into account that can be adjusted during sample growth:

- Deposition temperature T_{dep}
- Dopant flux Q_{PH_3}
- Postbake temperature T_{bake}

We start with an analysis of the deposition temperature T_{dep} and then investigate the effect of the dopant flux at selected deposition temperatures. Finally, we will choose the most promising combination of T_{dep} and dopant flux to investigate the effect of different postbake temperatures T_{bake}. With this optimization strategy, i. e. maximizing the first parameter and then keeping it fixed to change the second parameter and so forth, we are able to enhance PL intensity; it might be that the maximum we find is only a local one, though.

9.2 Selective growth of Ge on Si

Our final goal – however out of scope of this thesis – will be the monolithic integration of Ge into CMOS processing. Hence, the substrate will be silicon. The samples investigated so far were prepared starting with the deposition of an entire slab of Ge, covering the whole substrate. With the merger of germanium-based photonic functionality and standard CMOS microelectronic fabrication in mind, this is not a viable solution. Germanium as active material will be needed only in dedicated positions on a die.

For this reason, we have decided to deposit the highly doped Ge layers that we are going to investigate, selectively on Si. The approach is to cover the Si wafer with a SiO_2 mask and grow Ge on Si inside an opened window in SiO_2. The selectivity is given by the much higher desorption of Ge from the SiO_2 mask than from Si.[191]

Due to the large lattice mismatch of Ge with Si (4.2%), the formation of misfit dislocations at the Ge/Si interface to relax the epitaxial layer, as well as threading dislocations, are expected. Both provide non-radiative recombination channels for excited carriers and limit luminescence performance.[137, 142] Moreover, dislocations inside the Ge layer lead to a rough surface with cross-hatching like texture. To limit these side effects of the growth of Ge on Si, we have chosen to deposit a Ge buffer layer first that is subjected to an annealing step to gain a well suited Ge virtual substrate for subsequent growth of the actual Ge layer.

9.3 Sample preparation and analysis methods

The growth of all samples discussed in the entire chapter was accomplished by Y. Yamamoto and his co-worker A. Hesse at IHP GmbH, Frankfurt (Oder).

Germanium was grown selectively on Si in SiO_2 windows with reduced pressure chemical vapor deposition (RP-CVD, ASM Epsilon-2000 reactor). A 70 nm thick SiO_2 mask is created on a p-type Si (100) substrate (resistivity ~8–12 Ω cm) by oxide growth with CVD and patterning with standard lithography. The growth windows are opened into the SiO_2 layer by first removing the largest volume of SiO_2 with reactive ion etching (RIE) and then removing the residual SiO_2 using wet chemical etching with HF. After the HF dip a SiO_2 layer of about 50 nm thickness remained.

The Ge layer growth is divided into three sequential steps. After the growth of a 50 nm thin seed layer at 300 °C using GeH_4 with N_2 as carrier gas, a second 50 nm thin layer is grown at 550 °C in H_2 atmosphere and cyclic annealing performed at 800 °C. These two first steps create a 100 nm thick buffer layer for the subsequent growth and that helps reducing threading-dislocation density in the final layer.[192, 193] Due to the annealing step at 800 °C the buffer layer is under tensile strain. In case that the main Ge layer – see the third step – will be doped, the buffer layer is phosphorous (P) doped with dopant density of ~ 10^{19} cm^{-3}.

As the third growth step, the actual layer is deposited in which the different growth parameters are varied. Since the strain of the final Ge structure is determined by the strain in the buffer layer, it is the same for all samples that we have prepared. The growth time is kept constant for all samples, resulting in different final layer thicknesses reported in the respective sections.

Different doping of the final layer is achieved by changing the amount of PH_3 in the H_2-GeH_4-PH_3 gas mixture used for the hetero-epitaxial deposition.

The parameter postbake temperature T_{bake} varies from 500 °C to 800 °C. The postbake is carried out with and without an additional Si_3N_4 cover layer. The applied Si_3N_4 layer is 400 nm thick and its idea is to prevent desorption of phosphorous that diffuses to the sample surface during postbake.

Furthermore, samples with compressive Si_3N_4 top-layer are produced; the compressive Si_3N_4 induces tensile strain in the Ge structures. These Si_3N_4 layers deposited by plasma-enhanced chemical vapor deposition (PE-CVD) with precursors SiH_4 and NH_3 are about 400 nm thick and obtain different stress values ranging from 0.5 GPa to 2.3 GPa, depending on their actual growth condition. FIG. 9-1 (a) depicts schematic representations in cross section of the investigated samples.

Growth time was kept constant for all samples and resulting in different Ge film thicknesses reported separately in the corresponding discussion of each set of samples. As determined by X-ray diffraction measurements, all the Ge layers here investigated feature a $\varepsilon_{||}$ = 0.14% tensile in-plane strain due to the difference between the thermal expansion coefficient of the epilayer with that of the Si substrate.[194]

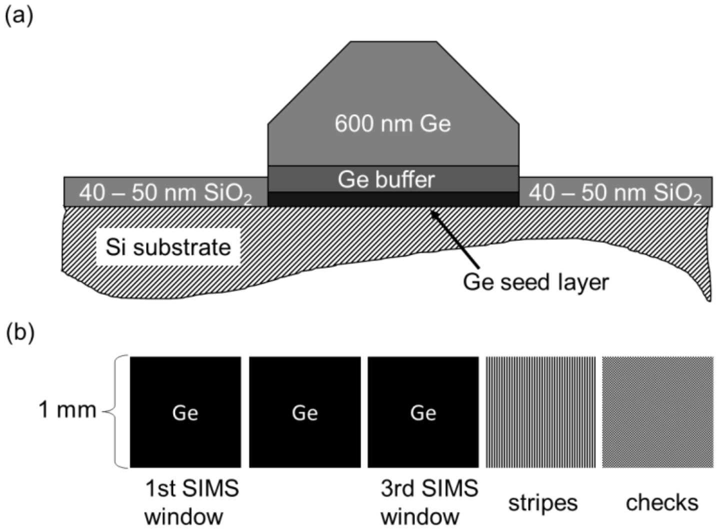

FIG. 9-1 Schematic representations of the general structure of the investigated samples. (a) Cross-section. Germanium is grown selectively in SiO_2 windows on a Si(001) substrate. The SiO_2 windows are prepared by means of lithography. The Ge growth consists of a three-step growth process including the deposition of a buffer layer. (b) Top-view. The sample features three different geometries of selectively grown Ge. Our investigation is mainly on the 1 mm × 1 mm windows that are also used for the SIMS analysis (SIMS windows). For selected samples we provide also data from the stripes that are 6 µm wide and 1 mm long and directed along the [110] crystallographic direction.

The surface morphology of the prepared samples is investigated using a scanning electron microscope (SEM). SEM images were prepared by G. Morgenstern and H. M. Krause at IHP GmbH, Frankfurt (Oder). The obtained chemical (i. e. total) dopant concentrations and concentration versus depth profiles are determined by secondary ion mass spectroscopy (SIMS) using a ^{74}Ge ^{31}P cluster. This work was delivered by F. Bärwolf and I. Costina from IHP GmbH, Frankfurt (Oder). The main PL analysis was carried out on the 1 mm × 1 mm quadratic Ge structures ("SIMS windows"), see FIG. 9-1 (b). In the study of the strain effect through external Si_3N_4 stressors, we will additionally investigate 6 µm wide and 1 mm long stripes, cf. FIG. 9-1 (b).

We used a micro-set-up in backscattering mode with 523 nm wavelength excitation laser focused to a spot of ~1 µm in diameter by a ×50 objective (N. A. = 0.65). Pump excitation densities *W*, measured close to the external sample surface, were of the order of 1 MW/cm^2. The emitted light was analyzed through an IR spectrometer and detected by an extended-InGaAs photo-diode array cooled with liquid nitrogen. A white-body lamp was used to determine the optical set-up response used for the spectra calibration. A LINKAM cryostat fueled with liquid nitrogen was used to access sample temperatures ranging from 80 K to 430 K within a ± 5 K accuracy for the study of the temperature behavior of PL.

9.4 Variation of deposition temperature T_{dep} at constant dopant flux

We start our study with a series of samples that differ in the deposition temperature T_{dep} of the main Ge layer. Since in our final application doping will be needed to pre-fill the L valleys so that injected carriers experience a smaller energy barrier between the conduction band valleys L and Γ, we immediately introduce impurity atoms during growth and investigate the influence of deposition temperature at a constant dopant flux of P = 1. The phosphine PH_3 flux Q_{PH_3} was kept constant in all samples to $Q_{PH_3} = 1$ P. Deposition temperature is likely to have an impact on crystalline quality that we can firstly assess through SEM images; Crystal defects can act as non-radiative recombination channels and are thus harmful to PL performance. Moreover, the incorporation of phosphorous into the Ge matrix changes with T_{dep}. This will give us hints on how growth temperature influences the incorporation and activation of dopants.

Samples were grown at deposition temperatures T_{dep} = 325 °C, 350 °C, 375 °C, 400 °C and 425 °C and phosphine flux $Q_{PH_3} = 1$ P. Growth time was kept constant for all samples and resulting in different Ge film thicknesses, because the growth rate is found to depend on the deposition temperature.[195]

9.4.1 variant T_{dep}: SEM analysis

FIG. 9-2 reports the SEM images of phosphorous doped Ge deposited selectively on Si at the deposition temperatures T_{dep} = 325 °C, 350 °C, 375 °C, 400 °C and 425 °C. We observe that all deposition temperatures T_{dep} enable selective growth of Ge inside the SiO_2 windows. Thicknesses are determined from the SEM images to be 450 nm, 560 nm, 600 nm, 710 nm and 700 nm, respectively. For the sake of completeness, the Ge layer thickness of an undoped reference sample grown with T_{dep} = 325 °C is 450 nm (no SEM image shown). Since the sample with T_{dep} = 325 °C and $Q_{PH_3} = 1$ P has got the same thickness, the introduction of impurities does not lead to a change in growth rate at 325 °C.

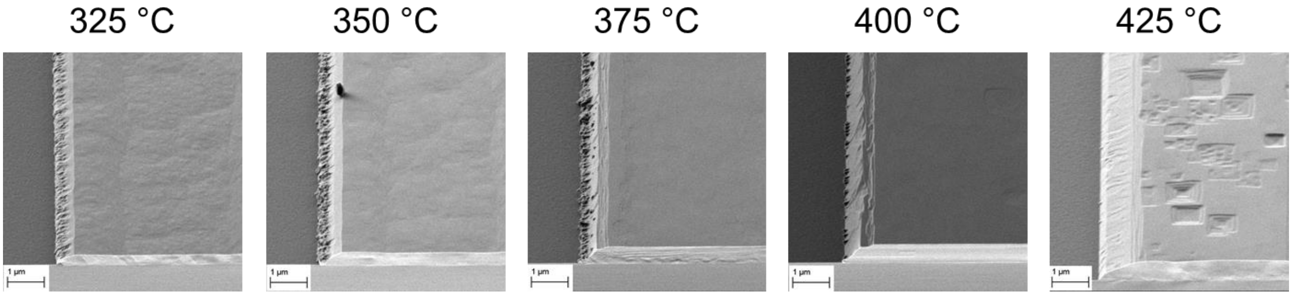

FIG. 9-2 SEM images of germanium grown selectively in SiO_2 windows at different deposition temperatures T_{dep}, ranging from 325 °C to 425 °C. The magnification is ×10,000.

The surface morphology of samples with T_{dep} = 325 °C and 350 °C is similar and exhibits a rough surface. For higher deposition temperatures T_{dep} the surface becomes smoother. However, in the 400 °C sample, quadratic notches in the surface are visible occasionally and at 425 °C these defects become widespread. The boundary to the SiO_2 mask becomes smoother in the samples with deposition temperatures 400 °C and 425 °C. From these observations, we conclude that crystal quality is improved with increasing deposition temperature, though it is degraded at 425 °C. This may be due to the increased deposition rate at 425 °C which leads to an accumulation of crystal imperfections, e. g. stacking vaults and vacancies.

9.4.2 variant T_{dep}: RT micro-photoluminescence

The luminescence spectra obtained at room temperature after photo-excitation in a micro-set-up are shown in FIG. 9-3. This figure reports the spectra of all deposition temperatures T_{dep} as well as the spectrum of an undoped reference sample with T_{dep} = 325 °C. All spectra are dominated by the direct-gap band located between 750 meV and 800 meV, see FIG. 9-3. The presence of photoluminescence of the undoped reference indicates its good crystal quality, see sec. 8.3 for a report on quenched PL from bad quality material. There is a clear trend in increasing intensity from the undoped reference sample to the samples at the three highest growth temperatures. To rule out a major effect of sample thickness on PL intensity, we cross-checked PL with samples of different thicknesses. We found that the effect of thickness on PL intensity is within the error of our PL measurements (± 5%). Note, that this is due to…

- …the very constricted penetration depth of the excitation laser into Ge (about ~17 nm with 532 nm excitation wavelength, see sec. 3.5)
- …limited diffusion of carriers because of…
    - …decreased carrier lifetime (see our discussion on the effect of doping on carrier lifetime, sec. 10) as well as
    - …decreased diffusion constant in doped Ge (the diffusion coefficient scales as the mobility (Einstein relationship) and the hole mobility decreases by more than two orders of magnitude in an ideal system
- …high radiative recombination rate for carriers in the Γ valley [69]

…so that the emitted luminescence originates not from the whole sample volume and carrier diffusion length is estimated to be in a range of 100 nm, which fits with the fact we have observed some variation (but little) going from 350 nm to 700 nm of thickness.

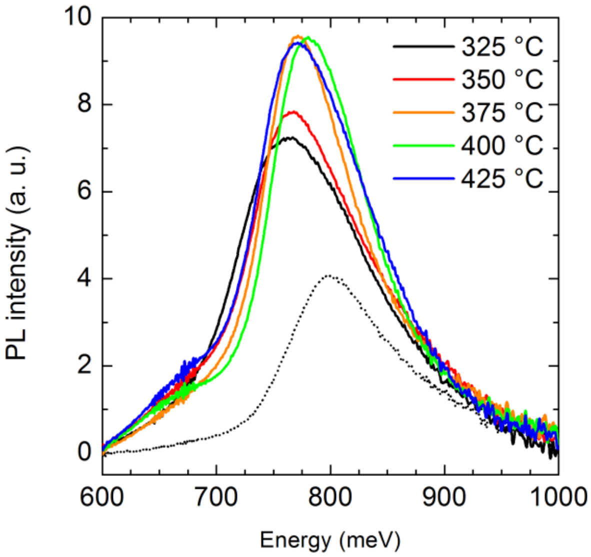

FIG. 9-3 Room temperature photoluminescence spectra of the sample series grown at deposition temperatures T_{dep} = 325 °C, 350 °C, 375 °C, 400 °C, and 425 °C. The PH_3 flux for all samples is Q_{PH_3} = 1 P. Also shown is an undoped reference sample grown at T_{dep} = 325 °C (dotted line) .

9.4.3 variant T_{dep}: PL intensity and Ge direct gap energy

The introduction of phosphine flux during the growth, i. e. doping of the samples, leads immediately to an peak PL increase of nearly a factor of ×2, see FIG. 9-4 (a). For T_{dep} = 350 °C the PL intensity increases further slightly and then distinctly for deposition temperatures larger than 375 °C. Moreover, the introduction of doping leads to a red-shift of the peak maxima of all samples. We determined the direct bandgap energy E_{dir} of the Ge layers with a fit of the direct gap luminescence band as described in sec. 4.2.4. The obtained values are reported in FIG. 9-4 (b). The direct bandgap of the undoped reference sample is 774 meV, which is lower than the direct bandgap of bulk Ge (800 meV). The lower bandgap compared to bulk is caused by tensile strain formation in the Ge layer due to the difference in thermal expansion coefficients of Si and Ge. It corresponds to a tensile in-plane strain $\varepsilon_{\|}$ of about ~ 0.2% (see Ref. [27]) in good agreement with the value obtained from the X-ray diffraction analysis ($\varepsilon_{\|}$ = 0.14%). By introducing phosphine during growth, the E_{dir} drops down to 732 meV. This band gap narrowing can be attributed to the electronic band renormalization due to the presence of dopant atoms.[125] There is no monotonous trend in band gap narrowing with deposition temperature.

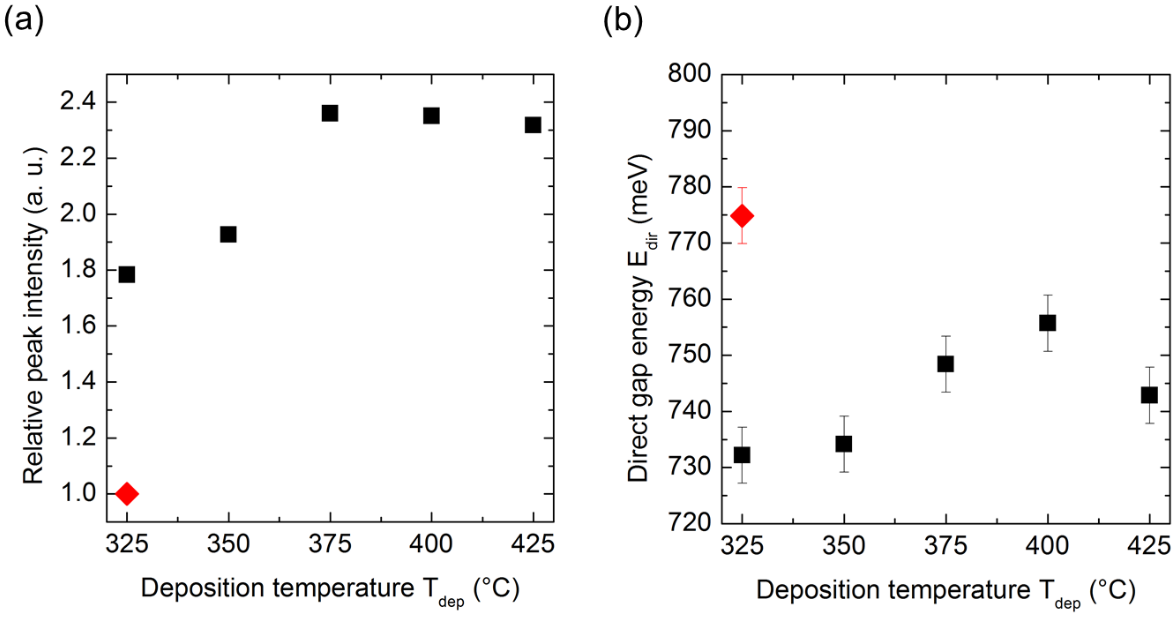

FIG. 9-4 Peak intensities (a) and direct gap energies (b) of the samples grown at different deposition temperatures T_{dep} at constant phosphine flux PH_3. Shown are also the values for an undoped Ge reference deposited at 325 °C (red diamond).

9.4.4 variant T_{dep}: n_{tot} and n_{act}

To gain deeper insight into the source of this behavior, we have determined the total concentration n_{tot} of phosphorous atoms inside the Ge layers with SIMS, FIG. 9-5. At Ge deposition temperatures T_{dep} = 325 °C and 350 °C, the obtained phosphorous concentration in the Ge layer is about ~3.2 $\times 10^{19}$ cm^{-3}. With increasing Ge deposition temperature from 350 °C to 400 °C the P concentration is decreased to ~1.4 $\times 10^{19}$ cm^{-3}. A further increase of T_{dep} to 425 °C leads again to an increase in incorporated phosphorous concentration.

The initial drop in P concentration can be explained with an enhanced P desorption from the growth surface with increased temperature. However, above 400 °C, a hydrogen free Ge surface can be reached,[196] and the incorporated P concentration increases at T_{dep} = 425 °C because the hydrogen free Ge surface allows for a higher P adsorption on the Ge surface during Ge growth. On the other hand, Hartmann et al. [128] report that they find an exponentially decrease of n_{tot} as the deposition temperature is increased from 400 °C to 750 °C. It is in all probability, that n_{tot} rises first when increasing T_{dep} from 400 °C to 425 °C because of the hydrogen free surface, but then decreases again at the temperatures used by Hartmann et al. which are quite a lot higher compared to 425 °C and may cause enhanced P surface desorption and out-diffusion.

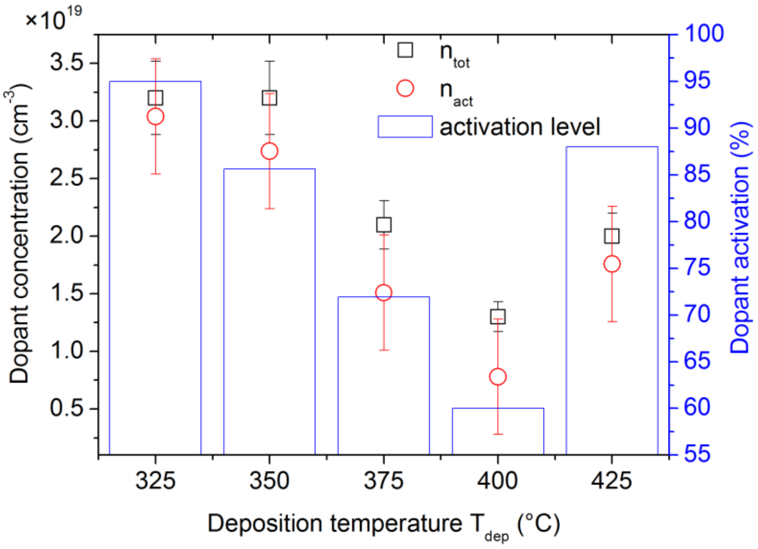

FIG. 9-5 Total dopant concentration n_{tot} revealed by secondary ion mass spectroscopy (SIMS) and the concentration of electrically activated donors n_{act} determined from band-gap narrowing (BGN) of the direct gap of Ge following the work of Camacho-Aguilera et al. [126] as a function of Ge deposition temperature T_{dep}. Moreover, the ratio n_{act}/n_{tot}, i. e. the activation level, is shown.

We conclude by noticing, that the number of total donors n_{tot} shows the inverse curve progression with T_{dep} of that of E_{dir} with T_{dep}. This is not surprising, since both are linked with each other through the narrowing of the direct gap energy in Ge that is caused by the electrically activated dopants with concentration n_{act}.

The value of n_{act} was obtained by subtracting the determined bandgap energy of the doped sample from that of the reference sample, resulting in the bandgap narrowing $\mathrm{BGN} = E_{\mathrm{gap}}(\mathrm{n_{act}} = 0) - E_{\mathrm{gap}}(\mathrm{n_{act}})$. In this manner, the effect of strain, which is present to the same extent in all samples, refer the section on the growth details, was annihilated. We followed the work of Camacho-Aguilera et al. [126] and linked the obtained values of BGN with the concentration of electrically activated donors, see also sec. 2.4.2. The results are also shown in FIG. 9-5. We find that from T_{dep} = 325 °C to 400 °C the incorporated donor concentration decreases by a factor of two. Concentration of activated donors also decreases from 325 °C to 400 °C, but more rapidly so that also the fraction of activated donors decreases from nearly 100% activation at 325 °C to 60% at 400 °C. Total P incorporation as well as activation level then increase for 425 °C: as discussed, desorption of hydrogen from the Ge surface during growth sets in so that Ge growth is not hindered due to H adsorption. Moreover, the higher growth temperature supports substitutional incorporation of phosphorous atoms P. Also Hartmann et al. [128] report that the level of ionized phosphorous we less for T_{dep} = 400 °C than for higher deposition temperatures.

The increased PL intensity of the samples with PH_3 flux can now be attributed unobjectionably to high doping with P concentrations larger than 1×10^{19} cm^{-3}. The peak positions and determined direct gap energies are in agreement with the total amount of incorporated dopants, showing that the incorporated impurity atoms are largely electrical active. For the sample with T_{dep} = 400 °C, the PL intensity is maximized despite the lowest concentrations of total n_{tot} and active n_{act} dopants. We hence conclude that this sample is of distinguished crystal quality. On the other hand, a further increase in deposition temperature T_{dep} leads to an increased dopant concentration (both n_{tot} and n_{act}), but PL intensity is rather decreased than further increased. We conclude, that crystal quality is degraded, a hint that we already got from inspection of the SEM images, cf. FIG. 9-2.

9.4.5 variant T_{dep}: FWHM of PL spectra

One measure for crystal quality is the width of the emission bands. The determined full width at half maximum (FWHM) of the direct gap emission is shown in FIG. 9-6 and substantiates our view that crystal quality is improved for deposition temperatures T_{dep} = 375 °C and 400 °C. However, FWHM is much larger than reported in other work of Ge/Si hetero-structures, e. g. the work of Sun et al. [124] that report a FWHM of 52 meV, close to the theoretical value of 45 meV. The larger width in our samples may have several reasons: The material of Sun et al. is grown at an elevated temperature of 650 °C which most likely improves quality of phosphorous doped Ge layers; furthermore, the material is subjected to a postbake and last but not least Sun et al. were able to detect photo-luminescence at excitation power densities several orders of magnitude lower.

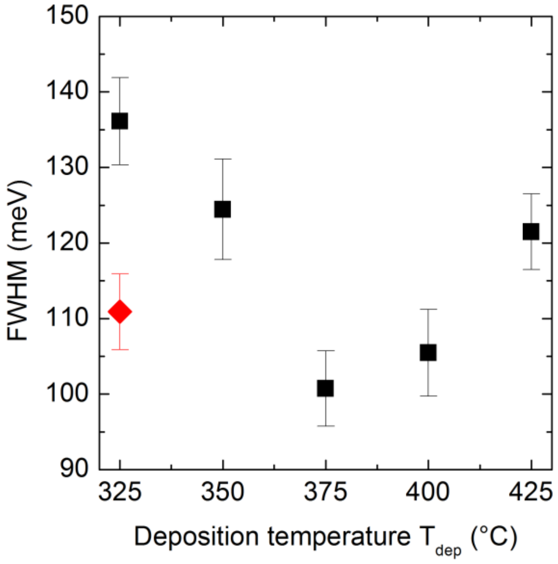

FIG. 9-6 Values for full width at half maximum (FWHM) of the direct gap luminescence band for the samples grown at different deposition temperatures T_{dep} at constant dopant flux.

One feature that contributes to the broadening of the direct gap luminescence band of Ge and that can be identified in the spectrum taken from the sample grown with T_{dep} = 325 °C, is the emission from point defects at about 720 meV that falls into the direct gap emission range and hence contributes to a substantial broadening.[176]

The 400 °C sample shows high PL despite low incorporation of dopants; since a large number of extrinsic carriers is prejudicial because eventually it can lead to increased losses, it is interesting to get high PL without high doping concentrations. For this reason, we will further investigate the 400 °C in varying the dopant flux; for comparison we shall do the same for the 350 °C growth process which shows high dopant incorporation and activation.

9.5 Variation of dopant flux Q_{PH3} at constant deposition temperature T_{dep}

The variation of the deposition temperature T_{dep} showed that growth at T_{dep} = 400 °C results in the best trade-off between reached doping level, crystal quality and photo-luminescence emission for a phosphorous doped sample with about ~ 1 $\times 10^{19}$ cm^{-3} dopant concentration. We are now interested in varying the dopant flux (at constant growth temperature) to further optimize the photo-luminescence efficiency.

The presence of donors causes the following main effects, which oppositely influence the light emission efficiency of Ge:

- a higher concentration of electrically active donors n_{act} induces an up-shift of the Fermi energy, easing the thermal excitation of electrons from the L_c valleys to the Γ_c valley, from where they can recombine directly with holes with a consequent increase of the photon emission rate.
- the non-radiative recombination rate through the Auger mechanism is proportional to the third power of the total carrier concentration (i. e., equilibrium plus the excess carrier density δn, cf. sec. 2.5.3), therefore a high dopant concentration may contribute to the quenching of the radiative emission due to a reduction of the non-radiative lifetime τ_{nr}.
- a high total density of donors n_{tot} can decrease the non-radiative recombination time τ_{nr} through two different mechanisms:
  - the reduced quality of the epitaxial material due to the increased density of point defects;
  - the electron-hole non-radiative recombination via Coulomb scattering of electrons with charged dopant ions
- The increased number of excess carriers may result moreover in an enhanced absorption of photons (free-carrier absorption (FCA))

9.5.1 variant P: sample preparation

To investigate the effect of the parameter dopant flux and hence the effect of phosphorous doping concentration on PL, we prepared two series of samples with different doping concentrations grown at deposition temperatures T_{dep} = 350 °C and T_{dep} = 400 °C. The different doping levels were accomplished by changing the phosphine flux Q_{PH_3} for in-situ doping during growth. Q_{PH_3} ranges from $Q_{PH_3} = 0$ (sample without doping, denominated w/o P) to a flux of $Q_{PH_3} = 8$ P (1 P is equal to a PH_3 mass flow of 20 sccm at reduced pressure using a PH_3/H_2 flow ratio of 4 $\times 10^{-7}$).

The work of Schwartz et al., who found an “optimum” donor density of ~ 3×10^{19} cm^{-3} to optimize electroluminescence from Ge LEDs set the framework for the targeted donor concentrations in our work, which are covered by the samples with Q_{PH_3} up to 2 P. In addition, we introduced with the 8 P sample a “corner DOE” sample to test an extreme case. As a matter of fact, too high doping can lead to clustering of P atoms and eventually to deactivation electrically active P^+ ions.

Growth time was kept constant for all samples and results in Ge film thicknesses from 485 nm to 718 nm for the series prepared at T_{dep} = 400 °C. The lowest sample thickness is obtained for the highest doped sample; this may indicate a reduced growth rate due to poisoning of the growth surface by the high amount of P atoms.[195]

9.5.2 variant P: SEM images

FIG. 9-7 shows scanning electron micrographs (SEM) from the obtained phosphorous doped Ge layers selectively grown in SiO_2-windows.

We find that in case of T_{dep} = 350 °C the border to SiO_2 seems to be very defective in all doped samples, whereas with T_{dep} = 400 °C a smooth but faceted edge toward the SiO_2 mask is obtained.

In the 350 °C series, the samples with PH3 flux Q_{PH_3} = ½ P and 1 P have got a quite smooth surface that has a wavy aspect. The undulation is more visible in the sample with 2 P and at 8 P deep funnel-shaped indentations occur.

For the 400 °C series, from the sample with PH3 flux Q_{PH_3} = ½ P to the sample with Q_{PH_3} = 2 P an increasing number of quadratic notches covers the surface. However, the surface seems to be smoother than in the 350 °C series, which may be a hint for a general higher crystal quality. The observed notches are more numerous with the higher phosphorus concentration, thus we link these notches to crystal defects introduced by the impurities (stacking faults, dislocations). The surface of the highest doped sample (8 P) has got a considerable surface roughness; single notches are not distinguishable anymore. It is doubted if the grown layer still can be attributed crystalline. The high phosphorus flux may have led to the agglomeration of P clusters. Dilliway et al. [195] in their study of atmospheric pressure CVD (APCVD) grown Ge layers (growth at 400 °C) with changing PH_3 flux also found a deterioration in surface roughness for a sample with 4× times higher PH_3 flux than a sample that still showed a smooth surface. They suggested that phosphorous starts to aggregate in larger structures than monomers or dimers.

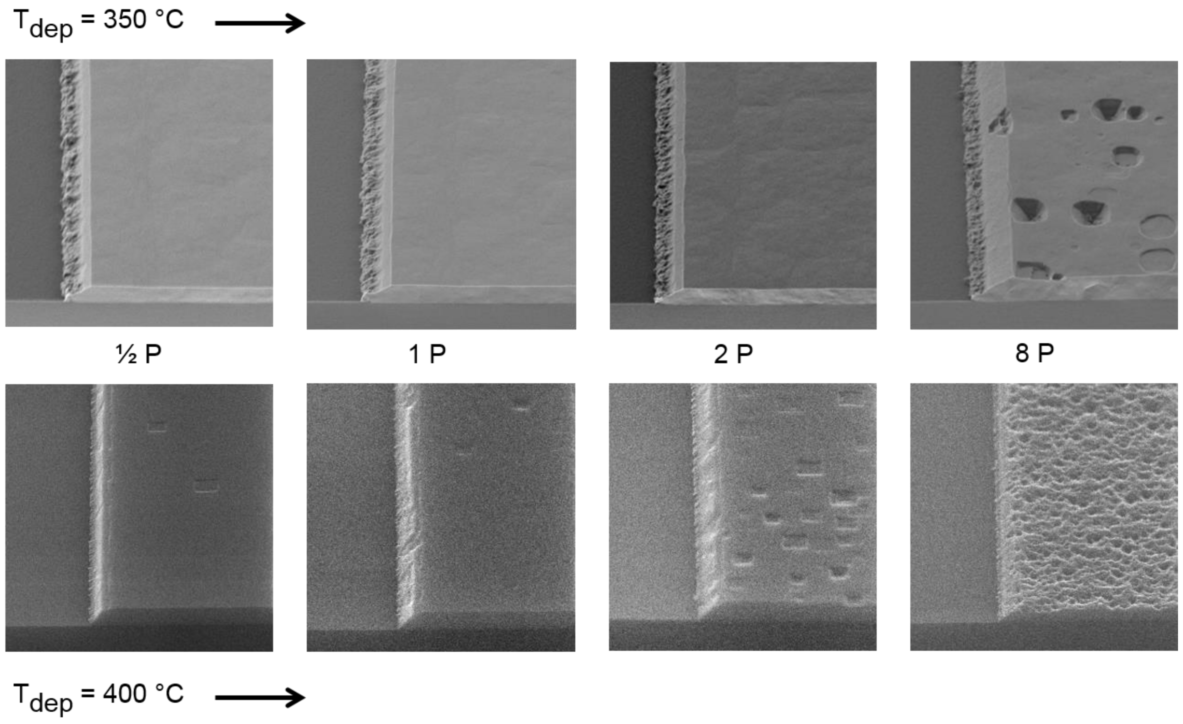

FIG. 9-7 Scanning electron micrographs (SEM) of the samples grown with different phosphine PH_3 flux for in-situ phosphorus doping at constant deposition temperature T_{dep} = 350 °C (top line of images) and 400 °C (bottom line). Depicted are the doped samples with phosphine PH_3 flux Q_{PH_3} from ½ to 8 P. Each micrograph shows the edge of a cut through the selectively grown Ge layer as well as its border to SiO_2. Micrographs as acquired at a magnification of ×10,000.

9.5.3 variant P: RT micro-photoluminescence

FIG. 9-8 presents the acquired photo-luminescence spectra at room temperature at constant pump power (1.1 $\times 10^6$ Wcm^{-2}). For comparison, we recorded the spectra of samples grown without PH_3 flux at 350 °C and 400 °C. All spectra are dominated by $\Gamma_c - \Gamma_v$ direct gap band-to-band radiative recombination which has got a peak energy of ~ 800 meV for the sample w/o P. With a check with samples grown with different growth times and hence resulting in different Ge layer thicknesses, we can exclude an effect of thickness on PL intensity larger than the present experimental error.

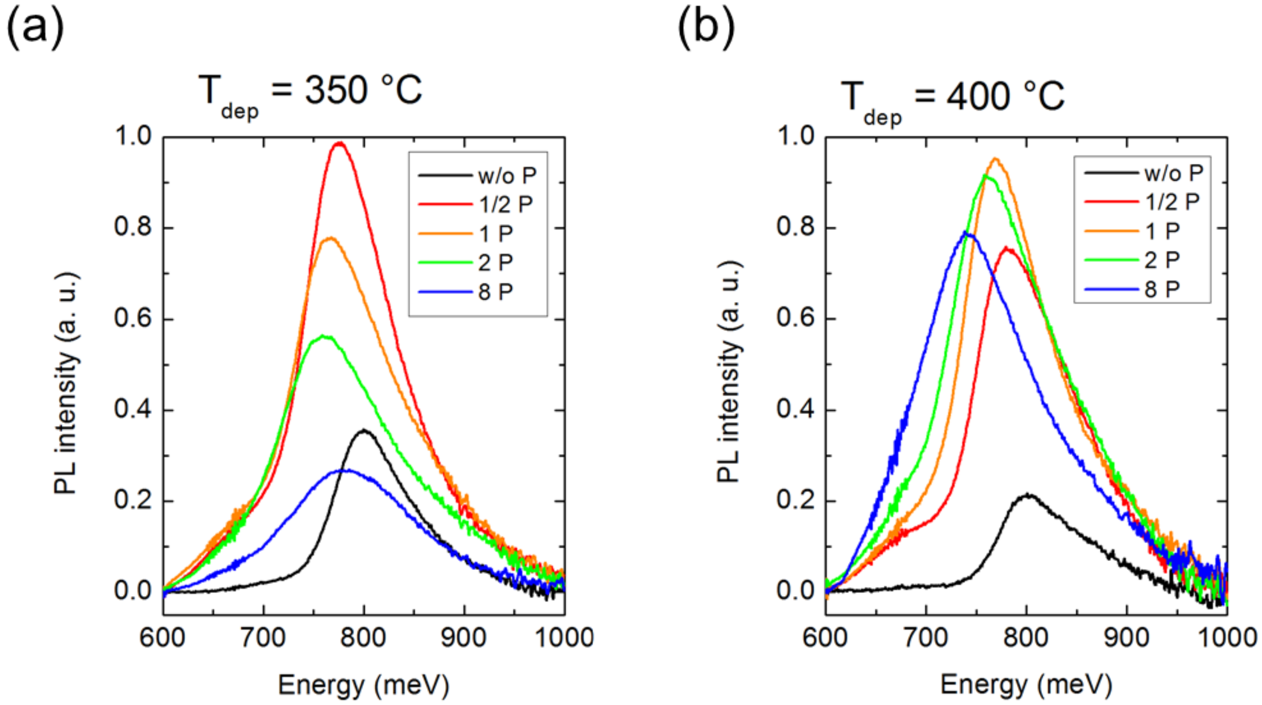

FIG. 9-8 Photoluminescence at room temperature of the investigated samples grown with varied phosphine PH_3 flux at the two deposition temperatures T_{dep} = 350°C (a) and 400 °C (b). The samples feature different phosphorous doping concentrations w/o P (undoped sample), ½ P, 1 P, 2 P, and 8 P.

The introduction of PH_3 during growth, i. e. the phosphorous doping of the Ge layer, leads to an immediate strong increase in PL intensity in case of both deposition temperatures. We note further, that for a certain PH_3 flux PL intensity is reduced again; in case of the 350 °C sample series, the highest flux Q_{PH_3} = 8 P leads to a strong reduction in PL intensity even below the intensity level of the undoped sample.

9.5.4 variant P: PL intensity and direct gap energy E_{dir}

This behavior is also shown in FIG. 9-9 (a) which reports the relative peak intensities in function of the phosphine flux Q_{PH_3} for both T_{dep} series. We find that the introduction of dopant atoms leads to a maximum relative PL enhancement of ×2.8 at sample ½ P for the series with T_{dep} = 350 °C and of ~ ×4.0 at for samples 1 P and 2 P in the T_{dep} = 400 °C series. For further increasing the dopant flux the PL intensity decreases.

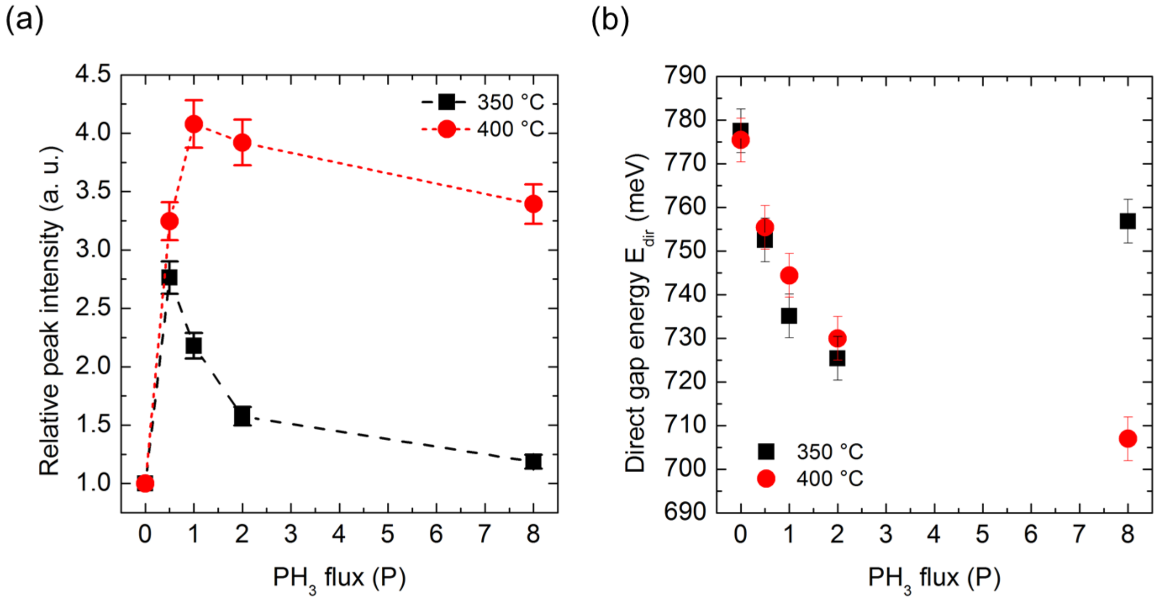

FIG. 9-9 (a) Relative peak intensities of the samples with grown with different PH_3 flux at deposition temperatures T_{dep} = 350 °C and 400 °C. After an initial raise, peak intensity decreases again for high values of PH_3 flux. The relative intensity increase due to doping is larger in the series grown at 400 °C. (b) Direct gap energies obtained from a fit of the direct gap luminescence band. The band gap gets narrower with increasing PH_3 flux, but for very high fluxes (8 P) in the series grown at 350 °C, the direct band gap energy is increased again.

The optimum dopant flux for growth at 400 °C lies hence between 1 P and 2 P, the resulting intensity values of which are comparable within the experimental error of PL measurements. Indeed, when considering integrated intensity instead of peak intensity in FIG. 9-9 (a), sample 2 P slightly performs better than sample 1 P and we observe an increase up to ×7 of the integrated PL intensity with respect to the undoped sample. This enhancement factor is little larger than these of integrated electroluminescence enhancements of n-type doped Ge-LEDs reported by Schwartz et al. (3.8 in Ref. [65]) and Schmid et al. (5.5 in Ref. [197]). Our findings come short compared to what reported by El Kurdi et al. on PL from doped GeOI (×20 at 1590 nm and ×10 at 1590 nm) and doped bulk material (×30 for integrated intensity).[67]

The photo-luminescence spectra for both deposition temperatures show a distinct difference in peak position for the doped samples with respect to the undoped reference samples; for the series at 400 °C there is a continuous red-shift from ~ 800 meV peak energy of the undoped sample to 740 meV in case of the sample with Q_{PH_3} = 8 P, whereas for the series at 350 °C the red-shift is not continuous and the sample with high dopant flux (P = 8) shows a reduced shift of peak energy. Numerical values for band gap energy obtained by the fit of the direct gap luminescence band as described in sec. 4.2.4, are given in FIG. 9-9 (b). The band gap narrowing is due to the band gap renormalization induced by the increased charge density due to the increased excess carrier density caused by the introduced impurity atoms.[127]

The PL spectra of the highly doped samples of both the 350 °C and the 400 °C series are visibly broadened with respect to the other spectra. This broadening can be attributed to defects introduced in the crystal by the high amount of dopant atoms that have to be incorporated in the Ge matrix. Most likely point defects with emission at about 720 meV are present that contribute to the broadening.[176]

9.5.5 variant P: Total and active dopant concentrations: n_{tot} and n_{act}

To gain deeper insight into the effect of changing the PH_3 flux during the Ge layer deposition, we plot the total amount of dopants n_{tot} determined with SIMS together with the active donors n_{act} as a function of phosphine flux Q_{PH_3} in FIG. 9-10. The fraction of activated donors is derived from the narrowing of the direct band gap energy (BGN) with respect to the undoped sample, featuring the same residual tensile strain, exploiting the relation proposed in Ref. [126] and as described in sec. 2.4.2. We can exclude that the doping introduced into the Ge buffer before growth of the main doped Ge layer has got a major effect on the thermal strain imposed on the main Ge layers, since the thermal expansion coefficient of Ge is changed only insignificantly with doping.[198] Hence, the values of band-gap narrowing (BGN) of the doped samples with respect to the undoped samples can be used to determined n_{act}.

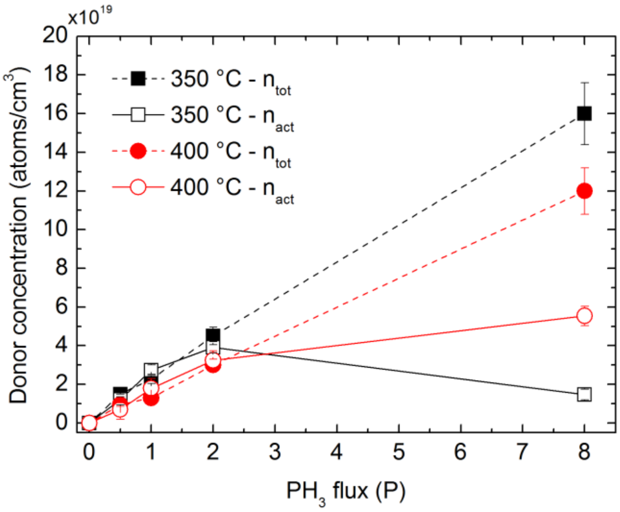

FIG. 9-10 Dopant concentrations versus phosphine PH_3 flux: total donor concentration is measured with secondary ion mass spectrometry (SIMS) and results linear with increasing PH_3 flux. Active donor concentration is retrieved from the band gap narrowing (BGN) of the direct energy gap. For high PH_3 fluxes the active donor concentration is less than the total dopant concentration.

The total dopant concentration n_{tot} is linear with PH_3 flux; for the 350 °C process the slope of the curve is steeper resulting in higher phosphor incorporation at the same flux than for the 400 °C process. In case of T_{dep} = 350 °C a total dopant concentration of $n_{tot} \approx 1.6 \times 10^{20}$ cm^{-3} is reached, whereas at T_{dep} = 400 °C n_{tot} is only about ~ 1.2×10^{20} cm^{-3} at the same flux of PH_3. From these two observations we conclude that phosphor desorption and surface segregation depend linearly on flux and is less for 350°C; the results of Hartmann et al. suggest that this trend is continued to higher deposition temperatures, finding a decrease of $n_{tot} = 3.6 \times 10^{20}$ cm^{-3} at T_{dep} = 400 °C to n_{tot} = 1.0 $\times 10^{19}$ cm^{-3} at T_{dep} = 750 °C.[128] Their result for n_{tot} at 400 °C is different from ours, because of the choice of different process parameters, i. e. most likely they have used a higher flux of PH_3.

For low PH_3 fluxes the concentration of electrically activated dopants n_{act} follows the linear trend and coincides with the total dopant concentration n_{tot}; an activation level of ~ 100% can be assumed up to a dopant concentration of ~3 $\times 10^{19}$ cm^{-3} for both deposition temperatures. However, for high flux (Q_{PH_3} = 8 P) the trend for active donors deviates strongly from the linear increase of total P. In the case of the 350 °C we even find a slope inversion. The deposition temperature of 350 °C may be too low to incorporate the high flux of P well, so that phosphorous atoms occupy interstitial positions in the crystalline matrix and/or phosphor clusters are formed.

Donor activation in the highest doped sample 8 P is reduced to ~ ×0.1 in the 350 °C process and to ~ ×0.5 in the 400 °C process. The curve progression of the T_{dep} = 400 °C series seems to be logarithmical and results to be linear to good approximation in a double-logarithmical plot. This agrees with the findings of Vincent et al. who investigated the active dopant concentration (determined by micro four point probe measurement, four point probe measurement, or Hall measurement) as a function of the PH_3 partial pressure during growth of in-situ doped Ge on GaAs at 425°C.[199]

The observation of a saturation like behavior of active donor concentration n_{act} with increasing total dopant concentration n_{tot} is in good agreement with Vanhellemont and Simoen, Ref. [200], who argue that in n-type doped Ge, the higher Fermi energy due to an increased electron density leads to a higher concentration of double negatively charged vacancies V^{2-} which pair with positively charged substitutional donors P^{+} and hence lead to donor de-activation. Furthermore, the $P^{2}V$ complex can act as a seed for even larger clusters $P^{m}V^{n}$ leading to deactivation of further donors.[201] This brings about a donor de-activation leading to the experimentally observed maximum active donor concentration of n_{act} ~ 5 ×10^{19} cm^{-3}.[200] Indeed, in the T_{dep} = 400 °C series, albeit the 8 P sample shows a de-activation due to the pairing mechanism, its active donor concentration is evaluated to be ~ 5.5 ×10^{19} cm^{-3}, in good agreement the maximum density above reported.

In case of T_{dep} = 400 °C we could explain the limitation in active dopant concentration n_{act} with the intrinsic saturation mechanism of active donors described previously. In case of sample growth at 350 °C we do not observe a saturation in n_{act}, but an inversion of the trend in n_{act} eventually resulting in n_{act}(8 P) ≈ 2 ×10^{19} cm^{-3}, a value that is lower than the maximum reached n_{act} in varying Q_{PH_3}. We think that at this lower deposition temperature, n_{act} is limited “extrinsically” by a lower concentration of P atoms incorporated at proper lattice sites of the Ge matrix.[195] The “deterioration” of the crystal quality brought about by an excessive doping is also responsible for the broadening of the PL spectral features at lower energies, as can be observed in the PL spectra of FIG. 9-8.

With the new knowledge, that n_{tot} is linearly proportional to Q_{PH_3}, FIG. 9-9 (b) also shows the dependence of the direct gap energy E_{dir} on n_{tot}. Up to Q_{PH_3} = 2 P, which corresponds to n_{tot} = 4.5 ×10^{19} cm^{-3} for T_{dep} = 350 °C and n_{tot} = 3.0 ×10^{19} cm^{-3} for T_{dep} = 400 °C, we can assume a linear behavior of E_{dir} with n_{tot} within the expected uncertainties. However, including the data points at Q_{PH_3} = 8 P (n_{tot} = 1.6 ×10^{20} cm^{-3} and n_{tot} = 1.2 ×10^{20} cm^{-3} for T_{dep} = 350 °C and T_{dep} = 400 °C, respectively), the dependence of E_{dir} on n_{tot} seems to be rather logarithmic than linear. It is hence questionable if we can extent the linear relationship between BGN and – please note – active dopant concentration n_{act} derived by Camacho-Aguilera et al. that applied their formula to data with up to ~ 4.5 ×10^{19} cm^{-3} (note, that Camacho-Aguilera et al. found full electrical activation for their samples and thus n_{tot} and n_{act} are equal).[126] The data points at Q_{PH_3} = 8 P would fit well into the dependence of BGN on doping concentration derived by Jain and Roulston which contains terms of $(n)^{1/2}$, $(n)^{1/3}$ and $(n)^{1/4}$.[127] By applying the linear relation of Camacho-Aguilera et al., the obtained value of n_{act} constitutes a lower limit.

9.5.6 variant P: PL intensity as function of n_{act}

We use the active donor concentration n_{act} derived from band gap narrowing of the direct energy gap, to discuss PL intensity in function of n_{act}. The expected effect is that extrinsic electrons provided by electrically activated dopants fill the L valleys in the conduction band so that the Γ valley population can be increased after photo-excitation and direct gap recombination and hence PL intensity are enhanced.

In the previous section we have seen that n_{act} – up to a certain point – is an increasing function for increasing PH_3 flux. However, the PL intensity does not follow n_{act}. FIG. 9-11 shows the peak PL intensity relative to the undoped samples for the two series with T_{dep} = 350 °C and T_{dep} = 400 °C. After a drastic increase of the PL intensity when increasing n_{act} up to $n_{act} = 1 – 1.5 \times 10^{19}$ cm^{-3} for T_{dep} = 350 °C and $n_{act} = 2 - 3 \times 10^{19}$ cm^{-3} for T_{dep} = 400 °C, PL starts to decrease. This results in an "optimum" donor concentration, pointing to a simultaneous increase of the non-radiative recombination rate with increasing doping. This might be an increased impact of non-radiative Auger processes as speculated by Schwartz et al. [65] or by a strongly shortened Shockley–Read–Hall lifetime that even may reach the same range as the Auger recombination time, as pointed out by Boucaud et al..[63] We shall discuss this issue in the next section about the donors' impact on non-radiative lifetime (see sec. 10), where we compare experimental data with a numerical model to quantify the discussion. Sample 350 °C|8 P has got a comparable active donor concentration n_{act} to sample 350°C|½ P, but its peak intensity is only a fraction of that of sample ½ P. In this case, the deterioration of crystal quality due to excessive doping clearly affects PL emission efficiency.

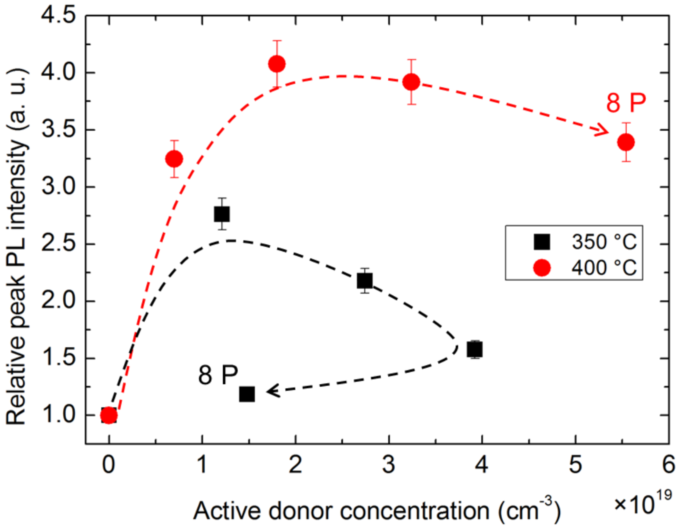

FIG. 9-11 Relative peak intensity normalized to the undoped sample (w/o P) for the series of PH_3 flux variation at sample growth at T_{dep} = 350 °C and 400 °C. Data is plotted versus active donor concentration. The optimum donor concentration for maximum PL intensity is different for the two deposition temperatures T_{dep}. The dashed arrows connecting the data points indicate increasing PH_3 flux from 0 (w/o P) to 8 P.

The observation of an optimum doping concentration to achieve the maximum in luminescence and the resulting harmfulness of too high doping is also known from III-V semiconductors, as for example reported in Ref. [202] on the cathodoluminescence spectra of Zn-doped GaAs.

9.5.7 variant P: PL in function of lattice temperatures T_L

The acquisition of PL spectra in function of the lattice temperature T_L of the sample allows to trace the evolution of emission features and to disclose the details not visible at one temperature only. FIG. 9-12 reports the PL spectra of a temperature series in the range from 80 K to 430 K at constant pump power excitation density of 1.1×10^6 Wcm^{-2} for the samples with different doping concentration and the two deposition temperatures T_{dep} = 350 °C and T_{dep} = 400 °C considered.

All the samples show an increase of the spectral intensity with temperature – due to the thermal excitation of electrons from the L to the Γ conduction valley. At low temperatures the population of the direct gap valley in the zone center (Γ) and hence direct gap emission is reduced, since at low temperatures thermal promotion of carriers from L to Γ is less efficient. Moreover, the barrier between the fundamental conduction band valley located in point L of the Brillouin zone and Γ depends on lattice temperature T_L and is reduced for higher temperatures.[129] At room temperature the barrier between L and Γ amounts to $E_{L/\Gamma} \approx 140$ meV. Samples 350 °C | 2P and 400 °C | 8 P show PL quenching in the high temperature regime. All samples show a constant red-shift of the PL peak energy due to the temperature-induced band gap shrinking.

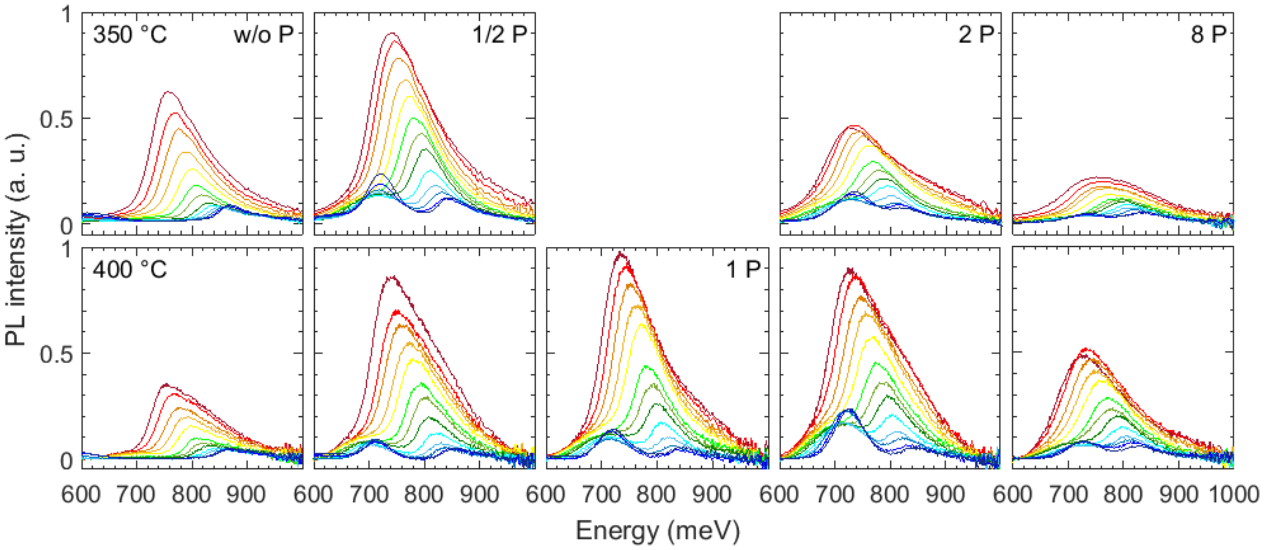

FIG. 9-12 Photoluminescence spectra obtained at different lattice temperatures T_L and constant laser excitation power. The upper row shows samples grown with deposition temperature T_{dep} = 350 °C, the lower row shows the samples prepared with T_{dep} = 400 °C. Samples were grown with different phosphine fluxes Q_{PH_3}, ranging from an undoped sample (w/o P) to samples with Q_{PH_3} = 8 P.

As we already have seen, there is a positive impact of doping on PL intensity up to sample 1/2 P in the 350 °C series and up to sample 2 P within the 400 °C series. In sec. 10 we are going to better discuss the impact of doping when comparing measurements of the 400 °C series with numerical data. On the other hand, samples with Q_{PH_3} = 8 P display broader and less intense PL signals over the entire temperature range.

The low temperature spectra of the undoped samples do not exhibit visible indirect transitions $L_c \rightarrow \Gamma_v$ but are dominated by direct band gap emission, whereas all the doped samples show a predominance of the $\Gamma_c \rightarrow \Gamma_v$ non-direct recombination at lattice temperatures below T_L = 160 K.
In a similar work by Virgilio et al., thin undoped Ge on Si layers were dominated by the indirect-gap transitions also at low temperatures in contrast to this work.[69]
The fact, that in our samples the indirect gap emission band in the intrinsic sample is strongly suppressed at the lowest measurement temperatures and that a dislocation emission band is visible below ~ 650 meV, indicates that material quality may be worse than in the study of Virgilio et al. and that dislocations may play a more important role, because the radiative lifetime for the indirect transition $L_c \rightarrow \Gamma_v$ is much longer than that for the direct transition $\Gamma_c \rightarrow \Gamma_v$ so that indirect gap transitions will be killed first by a non-radiative channel provided by the dislocation related energy states in the forbidden band gap.

On the other hand, we may explain the presence of the direct gap emission from the intrinsic sample with the quite high excitation power density of 1.1 $\times 10^6$ $\mathrm{Wcm^{-2}}$ which may cause local heating and promotion of excited electrons from the L to the Γ valley. Another mechanism for Γ valley population at low temperatures may be the one proposed by Klingenstein and Schweizer. They found that electron-electron interaction can populate the Γ-valley, namely when they observed direct gap emission at low temperature mediated by Auger-scattering caused by the high sample excitation power.[203]

Different from the intrinsic samples, the rationale for the appearance of strong indirect transition luminescence in all the doped samples is that in the doped samples the electron momentum required in an indirect radiative recombination process can be provided not only via electron-phonon interaction, but also by means of an extrinsic mechanism of Coulomb scattering with charged impurities.[125] According to Ref. [125], in heavily doped Ge electron-electron scattering may also contribute to assist second order radiative transitions, owing to the large carrier density featured by this material.

Having a close look at the indirect gap emission intensities, we can trace donor activation and deactivation: While in the undoped samples no indirect gap emission is visible, it raises in case of the doped samples, because activated donors constitute Coulomb scattering centers and the Fermi level E_F is raised close to the indirect conduction band edge so that dislocation energy states within the forbidden band gap are filled and cannot empty the L band anymore.
The highest doped samples then show a reduction of indirect gap emission at low temperatures. In case of the 350 °C series, we know that the number of active donors n_{act} is even decreased and we can explain the decrease in indirect emission band with a decrease of n_{act} which results in a reduction of Coulomb scattering centers and Fermi level.
On the other hand, sample 350 °C | 2 P as well as the highest doped sample with Q_{PH_3} = 8 P of the 400 °C series, have got the highest $\mathrm{n_{act}}$. However, the indirect emission band is reduced in intensity. This fact points out, that there must be a mechanism related to total donor concentration n_{tot} that increases the non-radiative lifetime and reduces PL intensity. We will get back to this point in sec. 10.

9.5.8 variant P: Indirect gap luminescence at 80 K

Let us have a closer look at the PL spectra acquired at 80 K, see FIG. 9-13. We find a red-shift of the direct-gap peak positions in both series in good agreement with the BGN determined at room temperature. This confirms that BGN does not depend on the lattice temperature T_L in the temperature interval of our study, in accordance with Haas [125]. Moreover, direct-gap emission increases, indicating more electron scattering into Γ, because increased doping elevates the Fermi-level E_F and thus reduces the energy difference between the L and Γ valleys.

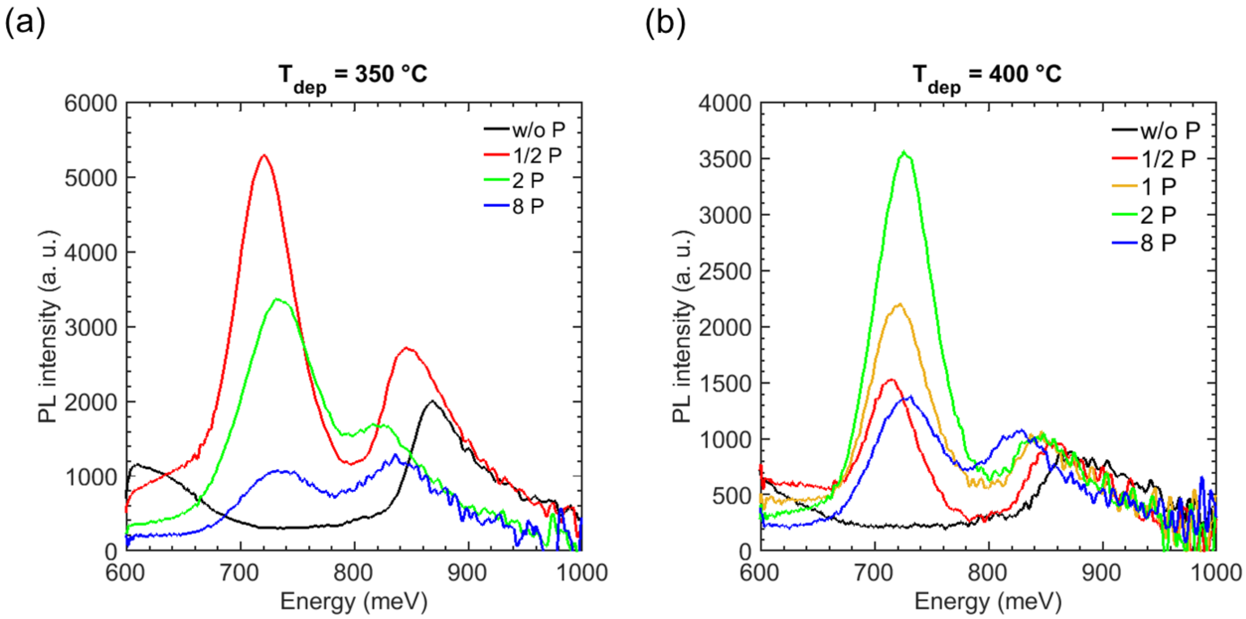

FIG. 9-13 PL spectra of series of samples with varying dopant concentration acquired at 80 K. (a) Spectra for the series grown at a deposition temperature T_{dep} = 350 °C. (b) Spectra for the series grown at a deposition temperature T_{dep} = 400 °C.

In addition, the order of increased indirect transition intensities in both sets of samples is in accordance with the obtained integrated PL intensities at room temperature: In the T_{dep} = 350 °C series, the ½ P sample performs best at RT and has got highest indirect gap emission at 80 K. In case of T_{dep} = 400 °C, integrated PL at RT increases up to the 2 P sample and the indirect gap emission intensity at 80 K also increases up to the 2 P sample.

The peak energies of the indirect transition samples fit to the following picture which assumes the presence of defects as non-radiative channels that have discrete energy levels within the forbidden energy gap of Ge. In the intrinsic sample, radiative indirect transitions are strongly suppressed because non-radiative recombination via the defect states is much faster. In case of the doped samples, the Fermi energy E_F is raised due to the presence of extrinsic carriers. For the lower doping levels, the defect energy states are filled partially and the effectiveness of these non-radiative channels is limited. Indirect transitions via electron-phonon scattering are now viable. Further increase of doping leads to a major contribution of indirect transitions of elastic electron-donors scattering. This can be well observed by the blue-shift of the indirect emission in the 400 °C series, because the no-phonon line corresponding to the elastic scattering is at higher spectral energies than the line corresponding to the scattering and emission of a LA phonon.[168]

This leads us to the point to discuss the peak intensity ratio Γ/L of the 80 K spectra in detail. Interestingly, we find that best performing samples at room temperature have got the smallest Γ/L ratios at 80 K, as shown in FIG. 9-14. This shows that there is a high electron density in the L valleys which (1) helps to preserve momentum for indirect transitions by electron-electron scattering (increased L-band peak) and (2) raises the Fermi level in the conduction band; this second effect will help to promote electrons to Γ. At 80 K this promotion is still limited due to the high energy barrier between L and Γ. However, when increasing the temperature the elevated Fermi-level is fully exploited and samples will show best PL at room temperature.

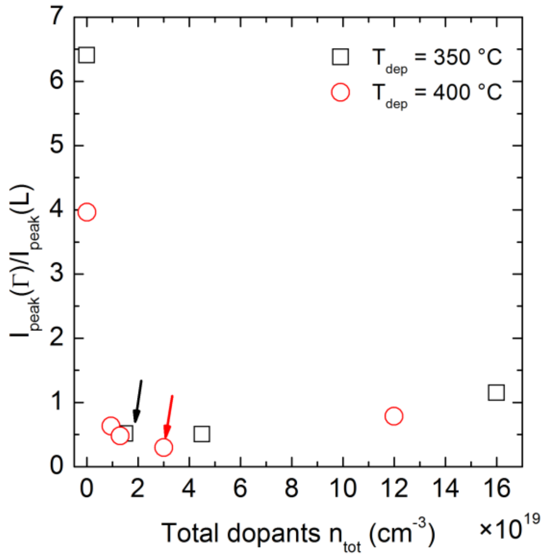

FIG. 9-14 Ratio of peak photoluminescence intensity from direct gap and indirect gap transitions $I_{peak}(\Gamma)/I_{peak}(L)$ of the spectra acquired at T_L = 80 K; arrows indicate best performing samples at room temperature.

Moreover, we would like to mention, that the high indirect transition intensity (higher or comparable to the Γ-band peak intensity) shows that most electrons end up in the L-valleys after thermalization to the conduction band edge when exciting with a 532 nm laser source. Sakamoto et al. suggest direct pumping into L with a 532 nm laser source.[170]

9.5.9 variant P: direct/indirect gap PL intensity ratio and electron temperature T_{el}

In FIG. 9-15 we present contour plots of PL intensity for each lattice temperature T_L, obtained from the spectra shown in FIG. 9-12. The integrated intensity of each spectrum was normalized to 1 to highlight the evolution of the direct/non-direct transition ratio. As discussed previously, in the case of doped samples indirect gap emission is clearly visible at temperatures below 190 K. Above 190 K, all spectra are dominated by direct gap recombinations. The thermal excitation of carriers from L to Γ is now efficient.

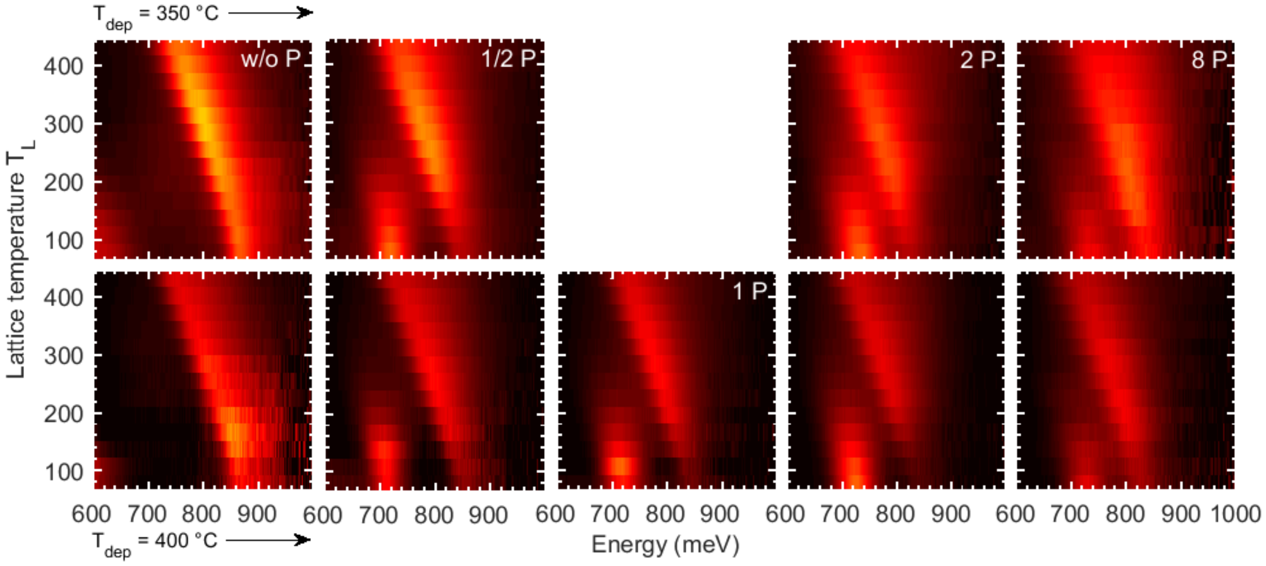

FIG. 9-15 Contour plots of the PL spectra shown in FIG. 9-12; The sample series grown with deposition temperature T_{dep} = 350 °C is shown in the upper row, the series with T_{dep} = 400 °C is shown in the lower row. The integrated intensity of each spectrum was normalized to unity to highlight the evolution of the spectral features.

We determined the direct band gap energies E_{dir} of all the samples w/o P, ½ P, 1 P, 2 P and 8 P from the lattice temperature dependent PL measurements. Again, we used the fitting procedure that has already been described. The results are shown in FIG. 9-16 together with a fit of the Varshni formula that describes energy gap dependence on temperature, to the data. It seems, that the decrease of E_{dir} as a function of doping with respect to the undoped sample is rather independent of the temperature, because at 80 K as well as at 430 K the BGN of the 8 P sample with respect to the w/o P sample amounts in both cases to about 40 meV. This shows that in all doped samples the doping level is so high that there are no discrete donor levels anymore. Haas, who derived the band gap narrowing in phosphorous doped Ge from absorption measurements, came to the same conclusion for his measurements at temperatures from 80 K to 295 K.

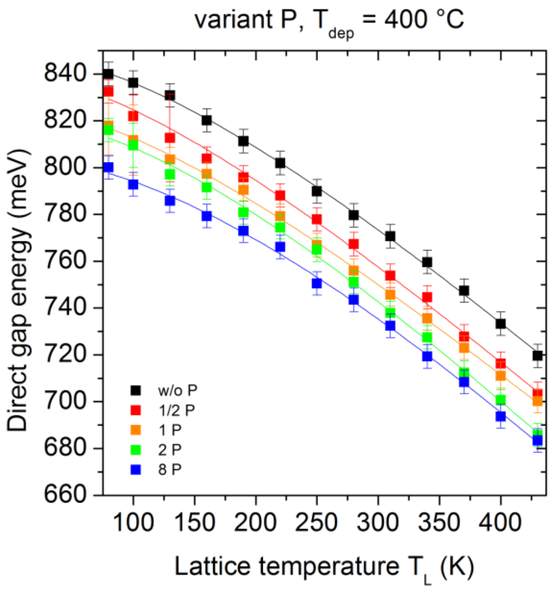

FIG. 9-16 Direct band gap energies E_{dir} of the samples w/o P, ½ P, 1 P, 2 P and 8 P grown at T_{dep} = 400 °C in dependence of the lattice temperature T_L.

As already discussed and contrary to the expectations, in the contour plots in FIG. 9-15 we also observe that at low temperature (80 K) there is some direct band gap recombination in all the samples. As we already have seen in the methods section (cf. sec. 4.2.3) and as will be discussed in more detail in the section about the impact of donors on the non-radiative lifetimes in Ge (sec. 10), the occurrence of direct gap emission at a sample temperature of 80 K is not expected with our experimental configuration (532 nm laser).

Klingenstein and Schweizer report luminescence from the Γ valley even at 2 K using a pulsed 1064 nm laser with 0.8 kW/cm^2 incident power on the sample. They explain their data with Auger scattering mechanisms that can assist transfer of electrons from the L valley to the Γ valley under sufficient optical pumping.[203]

Grzybowski et al. investigated the intensity ratio $I_{\text{dir}}/I_{\text{ind}}$ of the direct and indirect photoluminescence band of Ge under continuous photo-excitation. In thin Ge on Si films, $I_{\text{dir}}/I_{\text{ind}}$ was higher than expected by theory, taking into account temperature and strain.[82] They concluded that an additional contribution may be needed to explain the elevated experimental $I_{\text{dir}}/I_{\text{ind}}$ ratio in an intrinsic Ge-on-Si sample and suggested that quasi-equilibrium conditions between the L and Γ valleys may not prevail in the conduction band of photoexcited intrinsic Ge-on-Si films. Grzybowski et al. could explain the departure from the quasi-equilibrium as caused by the very short effective lifetime of carriers due to recombination at the interface of the Ge film with Si or at the Ge surface. The overall excited carrier concentration is reduced, but the ratio n_Γ/n_L is increased, explaining the increased intensity ratio $I_{\text{dir}}/I_{\text{ind}}$.

Grzybowski et al. argue that in the case of doped Ge with doping levels close to 10^{19} cm^{-3}, the ratio of electron concentration in Γ and in L n_Γ/n_L should be determined by standard equilibrium conditions between the two valleys and not by the dynamics of photo-excited excess carriers.

However, comparing our experimental data to a theoretical model assuming quasi-equilibrium between L and Γ, see sec. 10, we find that in our experiments the ratio $I_{\text{dir}}/I_{\text{ind}}$ is underestimated by the model not only in the intrinsic case, but also in our doped samples. For this reason, we suggest here that an excess in the electron gas temperature T_{el} with respect to lattice temperature T_L is the origin of the increased I_{dir}. Indeed, from the fit of the direct gap emission band with formula (4-1) (cf. sec. 4.2.4) that is also used to determine the direct gap energy, we find that the electron temperature T_{el} is larger than the lattice temperature T_L under continuous wave photo-excitation with 1.1 MW/cm^2, as shown in FIG. 9-17.

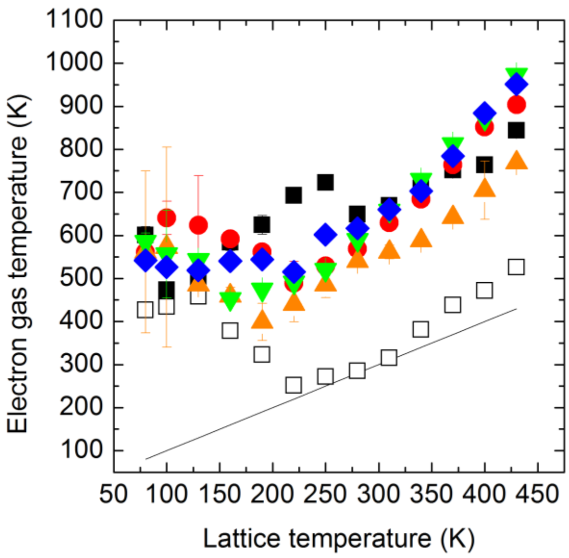

FIG. 9-17 Electron gas temperatures T_{el} resulting from the fit of the direct gap emission band in the photoluminescence spectra of the samples w/o P (full □), ½ P (full ○), 1 P (full △), 2 P (full ▽) and 8 P (full ◊). The power density was 1.1 MW/cm^2 in all measurements. In addition, data obtained for a Ge bulk crystal are shown (open □). The obtained data gives an indication on the effective electron temperature that differs the most from lattice temperature T_L at $T_L < 200$ K.

The obtained electron temperature T_{el} value from the fit originates in the slope of the high energy tail of the direct band emission. We point out that – in the case the indirect gap emission is in close proximity to the direct gap band – the high energy slope of the direct gap band may be affected by the very tail of the indirect gap band. In addition to the data from our Ge films, we show the data obtained from PL measurements on a Ge bulk crystal. The power density was 1.1 MW/cm^2 in all measurements.

The obtained data gives an indication on the effective electron temperature that differs the most from lattice temperature at $T_L < 200$ K. For higher lattice temperatures, the electron temperature seems to follow the increase in T_L. The elevated electron gas temperature may explain the presence of direct gap emission at 80 K in the following way: The quasi-Fermi distribution of electrons in the conduction band extends to higher energies and scattering of excited electrons from L to Γ may be facilitated.

Moreover, the data seems to suggest that the established electron gas temperature under continuous laser excitation is higher in case of the Ge layers than in a bulk crystal. It may be that in case of the Ge layers heat conduction is worse than in a bulk crystal due to the increased number of dislocations disturbing the spread of phonons.

Our investigation of the influence of deposition temperature T_{dep} and phosphine flux Q_{PH_3} on photoluminescence properties of in-situ phosphorous-doped Ge on Si layers revealed so far that T_{dep} = 400 °C and Q_{PH_3} = 1 P lead to the largest relative increase in peak PL intensity with respect to an undoped sample prepared at the same T_{dep}.

In the following we are interested in what are the right conditions of an additional postbake treatment to further increase the relative PL enhancement.

9.6 Effects of postbake condition on PL performance

We continue our investigation with the final growth parameter "postbake temperature" T_{bake}. The postbake is an additional heat treatment at elevated temperature after the actual sample growth. Due to the elevated temperature that is higher than the actual deposition temperature T_{dep}, diffusion of impurity atoms is activated which can result in additional electrical activation of donors by putting them into substitutional sites of the crystal lattice. Moreover, the rearrangement of atoms at the postbake temperature T_{bake} enables to remove defects. For example, threading dislocations will move and can be driven out of the crystal region of interest, hence improving crystal quality.

In the following, we are going to investigate the effects of different postbake conditions on photoluminescence intensity. We shall recourse to the 400 °C | 1 P sample which showed strong PL with low total P concentration n_{tot} and a level of activation slightly below 100%, see sec. 9.4.4. Since postbake treatments are known to not only improve crystalline quality but also electrically activate dopant atoms we expect this sample to have a strong potential for further PL increase.

Postbake was accomplished at the temperatures T_{bake} = 500 °C, 600 °C, 700 °C and 800 °C. Moreover, we performed the postbake with and without the deposition of an additional Si_3N_4 capping layer. We are interested if the Si_3N_4 capping layer could prevent the phosphorous atoms from desorbing from the Ge surface and hence limit out-diffusion of P.[204] The Si_3N_4 capping layer is stripped after the postbake.

Photoluminescence spectra were acquired at room temperature using the micro-setup in Frankfurt (Oder). In FIG. 9-18 we present the obtained spectra together with a reference sample without postbake. To check the effect of applying and stripping the Si_3N_4 capping layer, we performed these steps also with one reference sample without postbake.

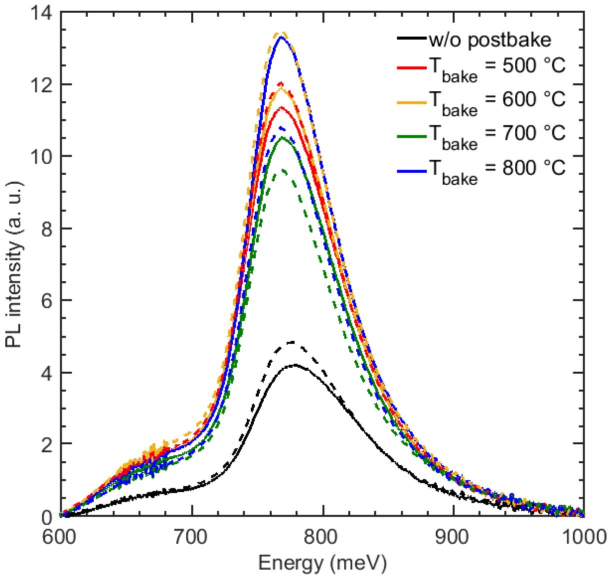

FIG. 9-18 Representative PL spectra of samples with different postbake treatment; postbake is performed at temperatures T_{bake} = 500 °C, 600 °C, 700 °C, and 800°C without (solid lines) or with Si_3N_4 capping layer (dashed lines).

In general, the comparison of the PL spectra from a sample without postbake and the samples with postbake shows strongly enhanced PL intensity. There is no clear trend regarding the postbake temperature T_{bake} and the application of a Si_3N_4 capping layer. FIG. 9-19 (a) summarized the integrated intensities compared to a sample without doping. As we already have seen, the introduction of doping leads to a first strong increase in PL. The postbake treatment leads to a further increase of a factor of 2.0 - 2.5 for all T_{bake}. We conclude, that 500 °C are already sufficient to improve PL and that no further improvements are obtained with higher T_{bake}.

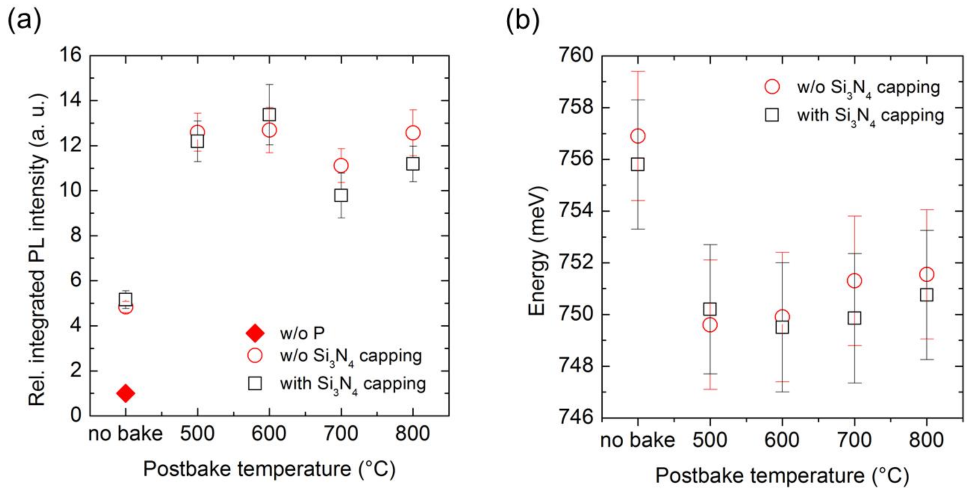

FIG. 9-19 (a) Relative integrated PL of P doped Ge layers as-deposited and after postbake treatmenet of temperatures of T_{bake} = 500 °C, 600 °C, 700 °C and 800 °C, normalized to the intensity value of a reference sample without doping.

(b) Direct energy gap E_{dir} in function of the postbake temperature T_{bake}. For all temperatures the direct band gap is reduced by the a virtually by the same amount with respect to the samples without postbake.

FIG. 9-19 (b) reports the direct band gap energies obtained by fitting the PL spectra (cf. sec. 4.2.4). The samples with postbake treatment show a slightly reduced band gap of about ~ 5 meV. This band gap narrowing cannot be ascribed to an increased thermal strain, since the strain in the Ge layers is determined by the cyclic annealing at 800 °C during Ge buffer growth. We hence conclude that it stems from electrical activation of additional dopant atoms.

For a deeper analysis we compare in FIG. 9-20 (a) the total donor concentration n_{tot} obtained from SIMS with the active donor concentration n_{act} derived from BGN with respect to a sample without doping, for the samples without and with postbake treatment. Considering n_{tot} first, no change is observed for the samples without postbake and the samples after postbake at 500 °C, 600 °C and 700 °C with and without Si_3N_4 capping layer. The total P concentration stays within the ~ 1.4×10^{19} cm^{-3} to ~ 1.5×10^{19} cm^{-3} interval. At 800 °C, however, we observe a slight decrease of n_{tot} that we explain with a partial desorption and out-diffusion of phosphorous from the Ge surface during the postbake. Within the errorbars, this decrease is the same for the samples with and without Si_3N_4 capping layer. The slightly lower decrease for the sample with Si_3N_4 capping layer may indicate the effectiveness of the Si_3N_4 capping layer.

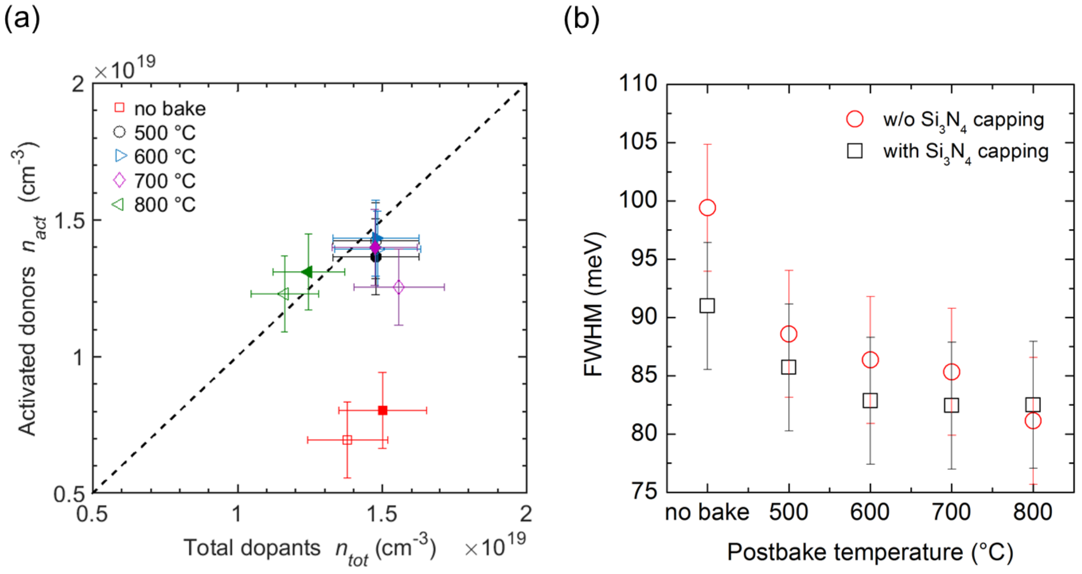

FIG. 9-20 (a) Total n_{tot} versus active n_{act} donor concentration after postbake treatment: open symbols represent data from postbake without Si_3N_4 capping layer, full symbols is data from postbake with Si_3N_4. The dashed line has got a slope equal to 1 and indicates 100% electrical activation of dopants.

(b) Full width at half maximum (FWHM) of the photo-luminescence spectra of the samples without postbake and postbake at temperatures T_{bake} = 500 °C, 600 °C, 700 °C, and 800 °C. The postbake treatment reduces the width of the direct gap emission band.

Regarding the active donor concentration, we find a value of about ~0.8×10^{19} cm^{-3} for the as-deposited sample. Electrical activation of donors is hence less than 100% and a part of the phosphorous in Ge remains electrically inactive. Already with a postbake temperature T_{bake} = 500 °C, n_{act} raises up to ~ 1.5×10^{19} cm^{-3} and full donor activation in the Ge layer is achieved. The higher values of T_{dep} lead to the same result of 100% electrical donor activation.

We are now able to attribute the increase in PL after postbake to the increased number of ionized donors that further fill up the L-valleys and ease thermal excitation in the Γ-valley. The increase active donor concentration indicates that also an improved crystallinity is achieved due to the improved incorporation of P atoms in the Ge matrix. To support this view, we determined the full width at half maximum (FWHM) of the luminescence peaks. FIG. 9-20 (b) shows that after the postbake treatment indeed a reduction in FWHM is achieved for all T_{bake}. It is most likely that the postbake improved crystallinity and hence caused a decrease of the PL luminescence stemming from point defects at the spectral position of about ~ 720 meV [176] which eventually results in the observed reduced FWHM.

Effect of postbake treatment on PL at low lattice temperature

In sec. 9.5.8 we observed that samples with the lowest intensity ratio of direct to indirect gap emission Γ/L at 80 K showed highest PL at room temperature. Our argumentation has been as follows: high direct gap PL at RT can be traced back to high indirect gap emission at 80 K; the electrons undergoing an indirect gap transition will be pumped into the direct gap valley when the energy barrier between L and Γ is reduced at higher temperatures.
We would like to verify this presumption for a sample that experienced a postbake treatment at T_{bake} = 500 °C that has proven to be sufficient to gain 100% electrical activation of donors and to improve crystallinity; as we have seen, with higher T_{bake} no further improvement was reached.

FIG. 9-21 shows the PL spectra of the sample with postbake at lattice temperatures T_L = 80 K and T_L = 310 K, and compares it to the case without postbake. As a matter of fact, we find a much smaller peak intensity ratio Γ/L at 80 K for a sample that underwent a postbake treatment. The ratio is reduced from ~ 0.5 in case of the sample without postbake to only ~ 0.1.

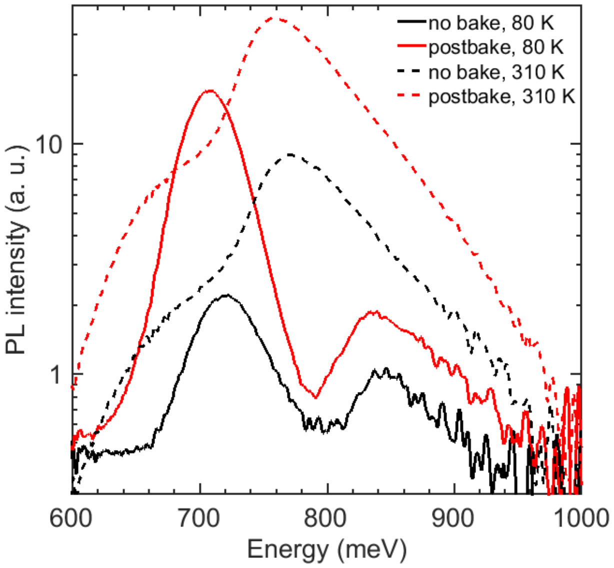

FIG. 9-21 Photoluminescence spectra of a sample with postbake treatment at T_{bake} = 500 °C in comparison to a sample without postbake. Apart from the postbake both samples were prepared with the same growth parameters. Spectra are acquired at lattice temperatures T_L = 80 K and T_L = 310 K. The sample with postbake shows a largely decreased peak intensity ratio of the direct to indirect gap transitions at 80 K with respect to the sample without postbake treatment.

9.7 Effect of Si_3N_4 stressors on Ge photoluminescence

We would like to complete our discussion on the effect of the different sample growth parameters by a short excursion on the effect of strain on PL. We remind the reader here, that up until now the strain inside the Ge layers has been determined by the cyclic-annealing during the preparation of the Ge buffer initially in the growth procedure. This annealing step was performed at 800 °C which also has been the highest temperature used in the postbake treatment discussed above.

To quickly check the influence of additional strain in Ge, we rely on the simplest external stressors that can be fabricated: we deposit an additional layer of compressed Si_3N_4 on top of the Ge structures, see FIG. 9-22 for a schematic cross section of a sample with Si_3N_4 top layer. Since the Ge layers grown selectively inside the SiO_2 windows have got a larger thickness than the SiO_2 mask, there is a step at the edge of a Ge layer, which is then also present in the Si_3N_4 layer.

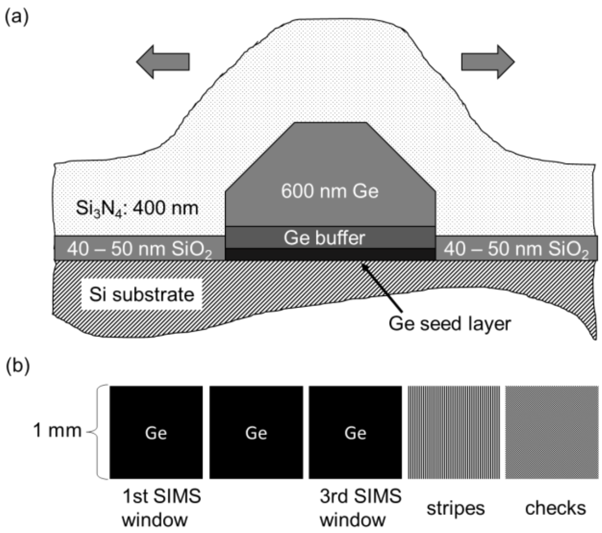

FIG. 9-22 Schematic representations of the general structure of the investigated samples. (a) Cross-section. The Si_3N_4 top layer is about 400 nm thick and acts as external stressor; arrows indicate forces exerted on the Ge structure by the Si_3N_4 layer. (b) Top-view. We study the effect of the Si_3N_4 layer both on the 1 mm x 1 mm SIMS windows and the 6 µm wide and 1 mm long stripes on which the effect is expected to the larger.

The compressive strain field stored inside the Si_3N_4 layer can be tuned by the Si_3N_4 deposition conditions and can relax at the edges formed at the borders of the Ge structures, like indicated by the arrows in FIG. 9-22. The Ge layer beneath is consequently exposed to a pulling force that creates tensile strain inside it.

The use of compressive Si_3N_4 as external stressors for tensile strain creation in Ge is well known. Recently, El Kurdi et al. even achieved direct gap material using Si_3N_4 as wrapped around stressors of suspended Ge micro-disks.[119]

Also Capellini et al. have already reported on the investigation of Ge micro-structures strained by Si_3N_4 top layers, comprising results of Raman spectroscopy and photoluminescence measurements.[49, 53]

Hence, the scope of this investigation is to finalize our Ge optimization for PL enhancement taking into account also the effect of additional strain, that – as we have seen – will be of paramount importance to reduce the threshold current density in a laser application.

Also in this study we rely on the main growth procedure with T_{dep} = 400 °C and phosphine flux Q_{PH_3} = 1 P that features the cyclic annealing at 800 °C after Ge buffer layer deposition. The resulting thickness of the whole Ge layer is 700 nm. The silicon nitride Si_3N_4 layer is deposited by plasma CVD at 380 °C and is about 400 nm thick. We have prepared three samples with stresses $\sigma_{\mathrm{Si_3N_4}}$ = 0.5 GPa, 1.5 GPa and 2.3 GPa inside the Si_3N_4 layer.

The obtained micro-photoluminescence spectra are shown in FIG. 9-23 (a). Measurements were performed on the 1 mm × 1 mm Ge window and on 6 µm wide and 1 mm long stripes. We have to point out immediately that we had no control of the Si_3N_4 layer thickness in the various samples. Since Si_3N_4 acts as an anti-reflection layer, slight differences in thickness can change in a large deviation in reflectance from the samples surface and hence excitation power density on the sample is changed (a change in Si_3N_4 thickness of about ~ 25 nm – which is within the error when growing the Si_3N_4 layer – leads to a change in reflectance of more than 20 percentage points at 532 nm. The change in reflectance at 1600 nm is negligible, hence, the influence of the Si_3N_4 layer in the spectral range of emitted PL is within the experimental error and the change in collected PL intensity is due to the change in excitation power). Consequently we are not able to compare PL intensities of the samples and the discussion of the influence of strain is limited to the direct gap energies.

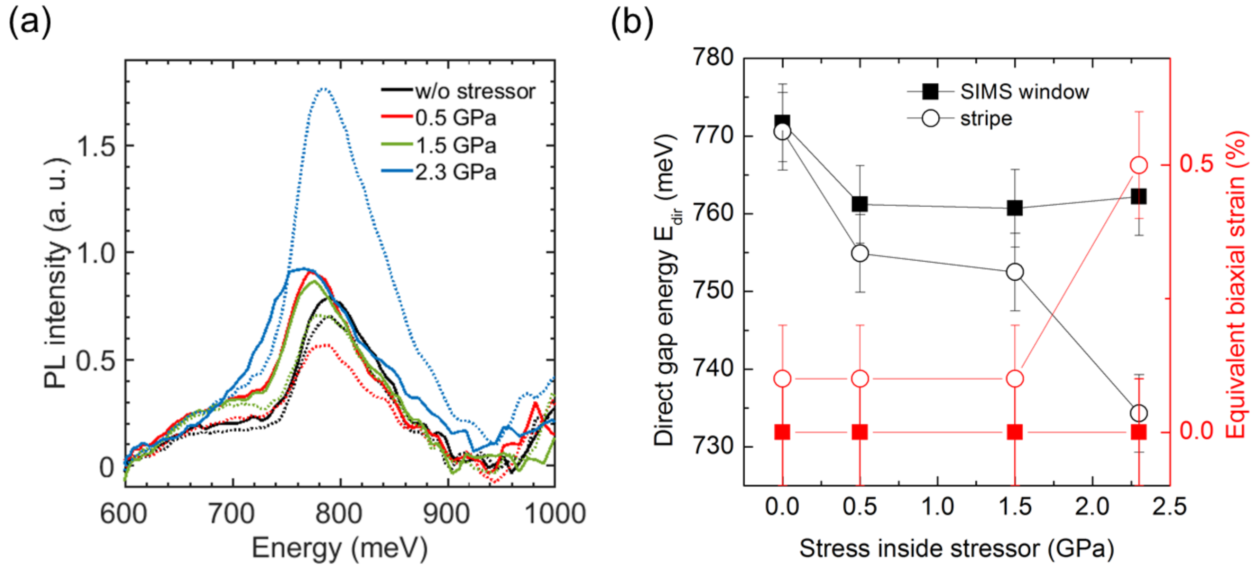

FIG. 9-23 (a) Photo-luminescence spectra of 1 mm × 1mm Ge layers ("SIMS window", dotted lines) and 6 µm wide and 1 mm long stripes (solid lines) featuring a Si_3N_4 stressor layer. Spectra are collected at room temperature. The Si_3N_4 layer is deposited by plasma CVD with varying stress ranging from 0.5 GPa to 2.3 GPa.

(b) Direct bandgap energy obtained from PL spectra from 1 mm × 1mm Ge layers ("SIMS window", □) and 6 µm wide and 1 mm long stripes (○) as a function of strain in the Si_3N_4 stressor. The right axis of ordinate reports equivalent biaxial strain values as obtained from micro-Raman measurements.

Direct gap energies are obtained by a fit of the direct gap luminescence band as descripted in sec. 4.2.4 and results are displayed in FIG. 9-23 (b). For the reference sample without Si_3N_4 stressor, the direct bandgap energy is ~ 770 meV for both the Ge window and the stripe. This is in agreement with the thermal strain that is induced into the structures during growth and is of the same amount for the larger window and the narrow stripes. The application of the Si_3N_4 stressor leads to a further reduction in direct bandgap energy for both the Ge window and the stripes. This proves, that the external Si_3N_4 stressors induce further strain into the Ge layers. We observe, that in case of the Ge window the direct bandgap energy is shifted by ~ 10 eV to E_{dir} = 760 meV for all Si_3N_4 layers. On the other hand, the band gap measured on the stripes is continuously reduced to 735 meV when increasing the stress in the Si_3N_4 stressor from 0.5 GPa to 2.3 GPa.

In case of the Ge window, the strongest effect of the stressor layer is at the border of the structure where the Si_3N_4 stressor can expand and thereby strain the Ge layer. However, excitation and collection of photo-luminescence is executed in the center of the window where the effect of the stressor is less. Indeed, the fact that the band gap energy is constant for all stressors shows that the stressor effect “saturates” in the center of the Ge windows with 1 mm side length, i. e. the elastic deformation of Ge at the center is restricted because the sidewall of the Ge is not close enough to realize the elastic deformation.

On the contrary, the 6 µm wide stripes are narrow enough to observe a band gap energy change in function of the stressor load. The observation of decreasing band gap with increasing stress in the stressor is in perfect accordance with our picture that the compressed Si_3N_4 stressor transfers its elastic energy to the Ge stripes. The higher stress values in Si_3N_4 result in higher strain in Ge and hence in a smaller Ge band gap in the stripes. Using Micro-Raman spectroscopy, we could prove that the strain in the sample featuring the Si_3N_4 layer with highest stress (2.3 GPa) is increased significantly with respect to the other sample configurations. The detected strain amounts to 0.5% equivalent biaxial strain, see FIG. 9-23 (b).

10 Donors’ impact on recombination mechanisms in n-type Ge

In our previous study on the influence of deposition temperature T_{dep} and dopant concentration on photoluminescence emission from in-situ phosphorous-doped (P doped) Ge grown selectively on Si, cf. sec. 9, we found that Ge growth at 400 °C enables selective growth and leads to the best trade-off between dopant activation and good crystal quality resulting in relatively high PL intensity that is maximized for a dopant concentration in the range of 1.8 – 3.2 10^{19} cm^{-3}. Higher doping levels did not further improve PL intensity but led to a deterioration of light emission.

At first sight, doping appears to be a viable option to tackle the issue of indirect band gap in germanium: A higher concentration of electrically active donors n_{act} raises the Fermi energy and promotion of electrons into the Γ valley by thermal excitation is facilitated.
On the other hand, doping has also its drawbacks, with free carrier absorption and its role on the recombination dynamics. Different mechanisms of this impact of doping on the recombination dynamics have been discussed in the literature.

In order to contribute to a better understanding, we compare the results of our photoluminescence (PL) experiments conducted at different lattice temperatures T_{L}, cf. sec. 9.5.7, with the corresponding PL spectra computed using a numerical model. We shall see that with a proper calibration procedure of the model parameters to the experimental PL data, the model provides a solid estimation of the relative donor impact on non-radiative lifetime τ_{nr} at the nanosecond scale. Moreover, the model implementation allows us to differentiate between the different non-radiative channels in vigor.

10.1 Experimental methods

In this study, we focus on the series of phosphorous-doped Ge samples grown at 400 °C that we have already introduced in the previous section and that lead to the best trade-off between growth selectivity, surface morphology, dopant activation, and crystal quality. These samples were prepared by selective growth of Ge on Si in 1 mm × 1mm large SiO_2 windows at 400 °C using reduced pressure chemical vapor deposition (RP-CVD) with GeH_4 as germanium source. Different doping levels were accomplished by in-situ phosphorous doping and changing the phosphine PH_3 flux during growth. We have prepared undoped samples without PH_3 flux (w/o P) and samples with fluxes of ½ P, 1 P, 2 P and 8 P. The unit 1 P is equal to a PH_3 mass flow of 20 sccm at reduced pressure using a PH_3/H_2 flow ratio of 4 $\times 10^{-7}$. Growth time was kept constant for all samples and results in Ge film thicknesses from 485 nm to 718 nm. Details of the sample preparation can also be found in Ref. [205].

The high quality buffer layer allows to have a higher quality of the doped Ge layer, in spite of the rather low deposition temperature of 400 °C. However it is recognized that the grown Ge material may not be the best result ever achievable for Ge grown on Si since T_{dep} is comparably low and there are no annealing cycles to improve crystal quality. Nonetheless low growth temperature conditions allow for very high concentrations of substitutional P atoms in the Ge matrix as well as electrically active P^+ donors.[128]

Micro-PL spectra are collected using the set-up in Frankfurt (Oder) as described in sec. 4.4 with a 532 nm excitation laser. Using a LINKAM cryostat fueled with liquid nitrogen we could access sample temperatures ranging from 80 K to 430 K to study the temperature behavior of the luminescence.

Like we have argued in sec. 9.5, we can rule out a corruption of obtained PL intensities due to the different sample thicknesses by comparison of PL intensity of differently thick samples featuring the same growth parameters deposition temperature T_{dep} and phosphine flux Q_{PH_3}.

10.2 Numerical model for PL spectrum computation

To quantify the relative impact of dopant concentration on the non-radiative lifetimes in highly phosphorous doped Ge on Si layers and to discriminate the most efficient non-radiative recombination channel, we compare our experimental PL data with computed spectra.
To this aim, we adopt the multi-valley self-consistent effective mass numerical model developed mainly by M. Virgilio (Pisa) and G. Pizzi (Lausanne) which has already been used in Refs. [27, 37, 53, 69].
The model permits to calculate PL spectra from Ge as a function of pump power excitation level, residual strain in the Ge layer, and lattice temperature.
In short, the model takes into account …

- …the multi-valley nature of the Ge band structure by taking into account the Γ_c and L_c valleys of the conduction band and the heavy hole (HH), light hole (LH) and split-off (SO) valence bands
- …effect of strain on the effective masses of carriers in the bands and consequentially the effect of strain on the band structure and the dipole matrix elements
- …temperature-driven band gap shrinkage according to Varshni's law

Electron and hole relaxation after photo-excitation are modelled considering…

- …excitation power density and energy of the excitation source
- …steady state equilibrium rate equation for the excess carriers δn taking into account both radiative and non-radiative contributions to the recombination rate:
  - radiative contributions:
    - direct gap transitions
    - phonon absorption/emission for indirect transitions
    - considering both energy-resolved direct and indirect electron-hole recombination rates estimated by means of first and second order perturbation theory, respectively
  - non-radiative contributions:
    - defect related Shockley-Read-Hall (SRH) lifetime τ_{SRH}
    - non-radiative Auger recombination
- …charge distribution inside the bands and resulting Fermi energy E_F
- …spatially resolved self-absorption effects of the emitted photons

The model allows to calculate internal recombination rates and the number of emitted photons, each calculated per unit of time, volume, energy, emission angle, and polarization of the emitted photon.

Moreover, in their recent work on strained Ge microstripes (Ref. [69]), Virgilio et al. included the temperature effects on the non-radiative dynamics by introducing a linear dependence of the SRH related lifetime on inverse temperature β: $\tau_{\mathrm{SRH}}(\beta) = \tau_{\mathrm{RT}} \cdot [1 + \gamma \cdot (\beta - \beta_{\mathrm{RT}})]$, where γ is a positive number. Hence, τ_{SRH} becomes shorter with increasing temperature. This feature is present also in this work and adjusted to the new conditions in our samples.

Furthermore, in this work, a spatially homogeneous distribution of the excess carrier density is assumed due to the small thickness of the Ge layers (~ 450 nm) featured by our samples. To describe in-plane diffusion we assumed in our calculation that the photo-generated carriers are uniformly distributed within a radius of 40 µm from the excitation spot.

Most importantly, in the present work, the model is updated to take into account the influence of dopants considering…

- …the narrowing of the indirect and direct gap as a function of n_{act} at a given lattice temperature T_L
- …the effect on the non-radiative recombination dynamics.
- …that elastic scattering with the ionized dopants can result in radiative transitions across the indirect gap (no-phonon line).

A high total density of donors n_{tot} can decrease the non-radiative recombination time τ_nr through two different mechanisms:

- the reduced quality of the epitaxial material due to the increased density of point defects;
- the electron-hole non-radiative recombination via Coulomb scattering of electrons with charged dopant ions

These two effects are accounted for by the impact of the doping concentration on the SRH rate as will be discussed in the following.

10.3 Experimental results

We summarize the results obtained so far and refer to FIG. 9-8 (b) of sec. 9.5.3 where we displayed the room temperature (RT) PL emission spectra of the investigated samples grown at 400 °C at constant pump power of 1.1×10^6 $\mathrm{Wcm^{-2}}$. We noticed that the spectral shape was dominated by the emission coming from $\Gamma_\mathrm{c} - \Gamma_\mathrm{v}$ direct band-to-band recombination and that the integrated PL intensity increased with increasing $\mathrm{PH_3}$ flux up to the 2 P sample and then decreased. The maximum increase of the integrated PL intensity with respect to the undoped sample has been of a factor of up to ×7.

Furthermore, we determined the active donor concentration n_{act} in our samples following the approach of Camacho-Aguilera et al.[126]. These values are shown together with the total donor concentration n_{dop} as measured by SIMS in FIG. 9-10 where we observe full activation of the co-deposited donors up to a concentration of $\sim 3 \times 10^{19}$ $\mathrm{cm^{-3}}$ (sample 2 P), while donor activation in the highest doped sample 8 P is reduced to ~ ×0.5. As we shall discuss in the following, an “excessive doping” leads to a deterioration of the crystal quality responsible for the broadening of the PL spectral features at lower energies and for the decreased intensity.

10.4 Temperature dependent PL

To better understand the influence of the doping on the recombination mechanisms, in the panels of FIG. 10-1 (a) we replot the micro-PL spectra acquired in the 80 K - 430 K lattice temperature range at constant pump power excitation density of 1.1 ×10^6 Wcm^{-2} that we have already presented in FIG. 9-12 of sec. 9.5.7.

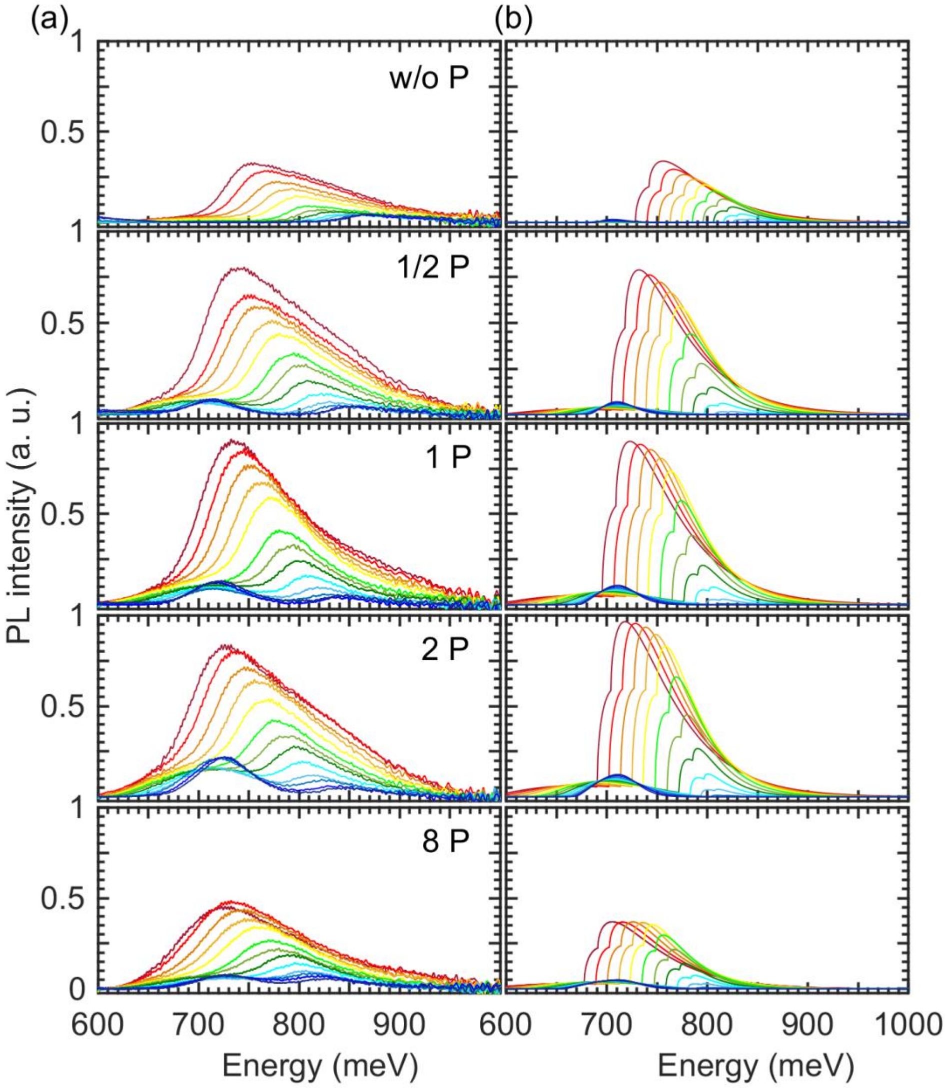

FIG. 10-1 (a) Experimental and (b) simulated PL spectra in the 80 K (dark blue color) to 430 K (dark red color) temperature range for each of the five samples with different doping concentrations achieved by variation of the phosphine flux Q_{PH_3}. The following samples were prepared: undoped sample (w/o P) and samples with Q_{PH_3} = ½ P, 1 P, 2 P, and 8 P..

We had seen, that all the samples show an increase of the spectral intensity with temperature – due to the thermal excitation of electrons from the L to the Γ conduction valley, and that this increase is accompanied by a red-shift of the PL peak energy due to the temperature-induced band gap shrinking. Moreover, as better discussed in the following when comparing measurements with numerical data, we observe a positive impact of doping up to sample 2 P on both the peak and integrated PL intensity. On the other hand, sample 8 P, albeit featuring the highest active dopant concentration, displays a broader and less intense PL signal.

The low temperature spectra of the intrinsic sample are dominated by direct band gap emission while all the doped samples show a predominance of the $L_c - \Gamma_v$ non-direct recombination at low lattice temperature T_L. We pointed out that in the doped samples there is an additional mechanism besides electron-phonon scattering to change electron momentum required in an indirect radiative recombination process. The electron momentum change can also be provided by means of Coulomb scattering of excited electrons with charged impurities present in the doped samples and moreover, in heavily doped Ge, electron-electron scattering may also contribute to assist second order radiative transitions, owing to the large carrier density featured by this material.[125] In line with these considerations, we observe that in general the intensity of the indirect transition increases, as well as the indirect-to-direct gap transitions intensity ratio as the activated donor density increases.

In FIG. 10-1 (b) we display theoretical PL spectra calculated by M. Virgilio. As input parameters we used the measured pump power density and the n_{dop} and n_{act} values obtained from experiment. In our simulations, the narrowing of the indirect and direct band as a function of n_{act} at a given lattice temperature T_L was implemented by linear interpolation of the low and room temperature results of Refs. [126] and [125], while temperature-driven band gap shrinkage has been implemented using Varshni's law to fit our temperature-dependent PL spectra.

Moreover, we have included in the present version of our numerical modeling, besides phonon absorption/emission, an elastic mechanism to describe the non-radiative part of the second-order recombinations across the indirect gap (indirect radiative transitions with an elastic scattering from L_c to the Brillouin zone center followed by a radiative transition). This elastic process phenomenologically takes into account the carriers scattering with charged ions and its coupling strength is assumed to be proportional to n_{act}. This coupling is temperature-independent, since in the explored temperature range and at the adopted doping concentrations, which are well above the Mott transition in germanium, the amount of ionized impurities does not vary with temperature. The value of the elastic scattering coupling constant has been calibrated to reproduce the measured ratio between the indirect and direct PL peaks at intermediate lattice temperatures for sample 1 P.

Spatially- and energy-dependent self-absorption effects, which in principle may influence the spectral shape, have also been considered. However, due to the relative small thickness of the investigated samples, we have found that the external PL spectra closely mimic the shape of the spectrum associated to the internal recombination rate.

In order to calculate the PL spectra for a given excitation density, we first evaluate the pump-induced equilibrium excess carrier concentration δn by numerically solving the relative steady state rate equation. To this aim, we assumed a spatially-homogeneous carrier distribution population and took into account both radiative and non-radiative recombination processes. In the former case we use for the direct and indirect radiative recombinations coefficients involving L_c and Γ_c excess electrons the values 1.3×10^{-10} cm^3 s^{-1} and 5.1×10^{-15} cm^3 s^{-1}, respectively.[28] We considered the non-radiative rates due to the Auger mechanism ($C_{nnp} = 3 \times 10^{-32}$ cm^6 s^{-1} and $C_{ppn} = 7 \times 10^{-32}$ cm^6 s^{-1}, Ref. [28]) and SRH-like electron-hole recombinations. As in the previous work by Virgilio et al., Ref. [69], for the SRH lifetime at room temperature $\tau_{SRH} = 30$ ns is assumed. This estimation was performed based on the relationship found in literature connecting the non-radiative recombination time to threading dislocation density (TDD).[126, 206]

Moreover, we considered the relation derived in Virgilio et al., Ref. [69], see also the model description at the beginning of this discussion (sec. 10.2), to account for the dependence of τ_{SRH} on the lattice temperature T_L. However, a lower value of the γ parameter entering the relation reported there ($\gamma = 10$ instead of $\gamma = 34$) has been used here to describe the temperature variation of the SRH lifetime in the sample w/o P. This choice corresponds to a weaker dependence on temperature and is suggested by the absence of strong PL quenching in the high temperature regime observed in this new set of intrinsic samples.

Comparing the top left and right plot in FIG. 10-1 we see that the numerical data well reproduce the experimental PL spectral shape and its enhancement observed increasing the lattice temperature. Nevertheless, if we do not account for the impact of the dopants on τ_{SRH}, we find that the model largely overestimates the PL increase observed in doped samples (a factor of $\times 10^3$ instead of ×3.5 for the RT enhancement of the PL peak when comparing the w/o and ½ P samples. This large discrepancy indicates that doping significantly affects τ_{SRH}. Moreover, it also implies that even in heavily doped samples where Auger rates are assumed to be very fast, the SRH recombination remains the dominant non-radiative mechanism which controls the excess carrier lifetime and density.

10.5 Model implementation of donors' impact on τ_{SRH}

The reduction of τ_{SRH} is due to non-radiative recombinations related to crystal defects associated with the dopant atoms, induced by the in-situ-doping process which worsens the crystal quality. To account for this effect, we propose for the dependence of the Shockley-Read-Hall recombination rate R_{SRH} ($\propto \tau_{\mathrm{SRH}}^{-1}$) on the total (i. e., active and non-active) doping concentration n_{tot} a natural and simple linear dependence:

$$R_{\mathrm{SRH}}(\mathrm{n_{dop}}) = R_{\mathrm{SRH}}^{\mathrm{int}} \cdot (1 + \kappa \cdot n_{\mathrm{tot}}), \qquad (10\text{-}1)$$

where $R_{\mathrm{SRH}}^{\mathrm{int}}$ is the RT rate of the intrinsic material and κ a phenomenological proportionality constant the value of which can be estimated calibrating the model with experimental PL data. The linear dependence on total doping concentration mirrors the idea that every impurity atom can contribute to a change in lifetime, including also those which are not electrically active. Note that this expression is compatible with a bulk-like non-radiative recombination process and not with non-radiative recombination via surface or interface scattering centers, as instead claimed by Geiger et al. in Ref. [66] where lifetimes of the order of 1 ns are measured both in intrinsic and heavily doped samples and are attributed to processes occurring at the very defective Ge/Si interface.

Using the 1 P sample as reference, we extract from the fit of the model to the experimental data $\kappa = 3 \times 10^{-17}$ cm^3. This results in a reduction of the RT lifetime from 30 ns for the intrinsic case to ~ 0.1 ns at a doping level of 1×10^{19} cm^{-3}. Despite this large drop of τ_{SRH} and the related dramatic decrease of the excess carrier density, a more intense PL signal is measured in the doped samples since the larger equilibrium carrier density is responsible for an upward shift of the quasi-Fermi level in the conduction band E_{Fc} which eases the population of the Γ_c valley.

Nevertheless it is worth to notice that the observed experimental enhancement (×3.5 for the peak PL signal at RT in the ½ P sample) is by far smaller than what we would estimate from the model if the doping did not affect τ_{SRH} (we would obtain a factor ×1000). The reason for this limited enhancement is a relevant reduction (two orders of magnitude) of the steady state excess carrier density. Indeed, setting τ_{SRH} = 30 ns we estimate at the adopted pump power density of 1.1 MW/cm^2 an excess carrier density in the w/o sample of $\delta n = 2 \times 10^{16}$ cm^{-3}. Neglecting the doping induced reduction of τ_{SRH}, this value remains practically unchanged for active donor concentrations in the 10^{19} cm^{-3} range.

On the other hand, taking into account the impact of doping on the lifetime one obtains for instance τ_{SRH} ~ 0.1 ns at a doping level of $n_{tot} \approx 1 \times 10^{19}$ cm^{-3} (sample ½ P, non-radiative lifetime reduced by a factor of ×300) and a related excess carrier density of $\delta n = 2 \times 10^{14}$ cm^{-3} only. Geiger et al. report a decrease in lifetime by a factor of 5 (0.4 ns instead of 2 ns, Ref. [66]) when performing time-resolved measurements on intrinsic Ge on Si and n-doped (10^{19} cm^{-3}) samples. It is likely, that their material has got a different quality resulting in a shorter non-radiative recombination time than we observe in our intrinsic samples, reversely causing a smaller reduction factor.

To better appreciate the huge impact of donor density on τ_{SRH}, we observe that neglecting the doping induced reduction of τ_{SRH} has often led to a large overestimation of the excess carrier density in excited heavily doped Ge in the recent literature about optical gain in Ge. For instance, De Kersauson et al.,[50] although using a much lower pump power density with respect to the one adopted for the present investigation, estimate the excess carrier density in optically pumped tensile heavily doped Ge wires at 1 – 2 $\times 10^{19}$ cm^{-3}, based on Auger recombination as the sole non-radiative channel (caution is recommended in comparing these results with present data, because De Kersauson et al. investigated uni-dimensional wires whereas our study is on Ge films of comparable thickness, thus surface recombination is expected to play a less important role in our case, whereas the wire geometry could enhance the excess carrier density by limiting carrier diffusion). Similarly, SRH-like non-radiative recombination through defects was not considered also in an earlier work of this group.[67]

Finally, in the pioneering paper by Liu et al. [28] a value of 100 ns for τ_{SRH}, which in light of the present results appears quite unrealistic, has been used to calculate optical gain in heavily doped Ge. Only in more recent years, the relevance of a sound estimation for τ_{SRH}, which indeed represents a key physical parameter to model and understand optical emission in Ge, has been recognized and critically addressed, as for instance reported in Refs. [66, 207-209]. Also Boucaud et al. have recently pointed out the importance of a τ_{SRH} decrease induced by doping, stating that the SRH rate could be even faster than Auger recombination.[63] El Kurdi et al. from Paris in fact implemented a τ_{SRH} that resulted slightly shorter than τAuger in their model to explain experimental PL data in one of their recent works, Ref. [119]:

$$\frac{1}{\tau_{nr}} = \frac{1}{\tau_{SRH}(N_D)} + \frac{1}{\tau_{Auger}(N_D)} \qquad (10\text{-}2)$$

with τ_{SRH} = 2.6 ns and τ_{Auger} = 14 ns for a dopant density $N_D \sim 1 \times 10^{19}$ cm^{-3}.

After the calibration of κ, our model reproduces the PL intensity in all the other doped samples consistently. This fact indicates that, thanks to the adopted calibration procedure we get a sound estimation of the impact of doping on excess carrier lifetime. To put more evidence in favor of this statement, we notice that the obtained value for κ is essentially identical to the one ($\kappa = 2.5 \times 10^{-17}$ cm^3) proposed in Ref. [68], where the same empirical relation was introduced to phenomenologically describe the δn decay transients in moderately and heavily p-type doped bulk Ge, observed by means of time-resolved optical measurements. Indeed, the inverse constant κ^{-1} corresponds to the threshold doping density introduced by Gaubas and Vanhellemont and gives a critical value for the onset of doping-induced traps. Furthermore, the agreement of our estimation for κ with the one reported in Ref. [68] where bulk Ge has been investigated, confirms that in doped Ge layers grown on Si the carrier lifetime is not limited by recombinations occurring at the defective Ge/Si interface, but by a “bulk” effect instead.

We point out that in agreement with our results, Gaubas and Vanhellemont [68] found a relative decrease of τ_{SRH} by a factor larger than ×100 when the donor density was increased from intrinsic material to 10^{19} cm^{-3}, independently of the excess carrier density δn.

Finally, we notice that the same authors also conclude that Auger recombination in doped Ge plays a negligible role in limiting the lifetime with respect to SRH scattering, even for doping concentrations in the 10^{19} cm^{-3} range.[68]

For the sake of completeness, we wish to mention here that also an alternative interpretation of the PL data reported in FIG. 10-1 may be considered. In this alternative scenario, the modest increase of the PL signal experimentally observed in doped samples can be reproduced by the model also assuming much higher excess carrier densities (~10^{19} cm^{-3}), as resulting from a lateral diffusion of the carriers of the order of ~1 μm only, together with a much lower impact of the dopants on τ_{SRH}. However, in this case our model predicts a PL spectral shape for the w/o P sample at low and intermediate temperatures clearly incompatible with the experimental results since it features a single broad band, extending from ~ 700 to ~ 950 meV. Moreover, at this high excitation levels the Auger recombination rate competes with the SRH one, thus leading to a lower value for the scaling exponent for the integrated PL signal as a function of the pump power, which is incompatible with our observations (see the discussion below). We believe that time resolved measurements could be used to unambiguously assess which scenario better describes the system here investigated, and to shed more light on the discrepancy existing between the data presented in literature (e. g. Refs. [210] and [66]).

While the indirect recombination contribution to the low temperature PL intensity of the intrinsic sample is due to phonon assisted processes, from our model we obtain that the main source for the indirect signal in the doped samples is related to second order recombinations where the missing momentum is provided by L_c-Γ_c Coulomb elastic scattering. This can also be identified in the experimental data (cf. FIG. 9-13 in sec. 9.5.8) and is in agreement with mobility studies, where the large momentum ion scattering at impurity concentrations of about ~10^{19} cm^{-3} is shown to be the dominant factor limiting the carrier mobility.[211]

Although the overall temperature-driven increase of the PL intensity displayed in FIG. 10-1 is correctly reproduced by the model, at low temperatures the predicted intensity ratio between the direct- and indirect recombination bands underestimates the experimental value. It is worth to notice that also in Ref. [82] the predicted direct/indirect intensity ratio is well below the measured one, despite the fact that a different theoretical approach has been used to interpret PL in Ge, see also sec. 9.5.9.

10.6 Effect of pump induced heating

To better evidence this observation, in FIG. 10-2 we compare the experimental and simulated spectra as a function of lattice temperature T_L. By normalizing the integrated intensity of each spectrum to unity we can highlight the evolution of the direct/non-direct transition ratio. The underestimation of the direct/indirect PL signal ratio obtained by theoretical models based, as in the present case, on the assumption that the energy distributions of Γ_c and L_c conduction band carriers are characterized by a common quasi-Fermi level, has been addressed in Ref. [82]. The authors, studying both doped and undoped samples, hypothesize that the excess carrier distribution in the conduction band valleys of optically-excited Ge is out of equilibrium. As a consequence, a larger fraction of the overall reduced electron population is to be expected for the Γ_c valley. This out of equilibrium effect should be less relevant in heavily doped samples thanks to the fast intervalley scattering between Γ_c and L_c caused by the presence of charged impurities.[82]

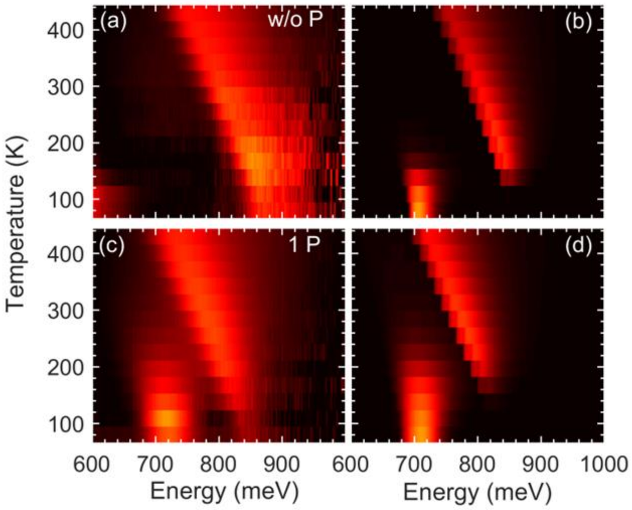

FIG. 10-2 Contour plots of the experimental (a, c) and simulated (b, d) intensity of the spectra from the temperature series from 80 K to 430 K. Shown are the data for the intrinsic (upper panels) and 1 P (lower panels) samples. Integrated intensities of all the spectra are normalized to 1.

However, since in our experiments the numerical underestimation of the direct/indirect PL signal ratio is observed also in doped samples, we suggest here an alternative effect to account for this discrepancy. Indeed a larger direct/indirect signal ratio, close to the experimental values, can be obtained if pump-induced electron heating effects are incorporated in the model. To this aim, we have carried out simulations assuming a thermalized electron distribution sharing the same quasi-Fermi level E_{Fc} in the L_c and Γ_c valleys with an electron temperature T_{el} slightly larger than the lattice temperature T_L. We find that an excess in the electron temperature of ~ 30 K is enough to reproduce the correct vales for the direct/indirect PL signal measured in the low temperature range.

10.7 Integrated intensity change with temperature

In FIG. 10-1 (a) we compare the experimental and simulated integrated PL intensities as a function of lattice temperature T_L. We can distinguish a high temperature region ($0.027\ \text{meV}^{-1} < \beta = 1/(k_B T_L) < 0.05\ \text{meV}^{-1}$) where the spectra are dominated by radiative recombination from Γ_c (cf. FIG. 10-2). In this region an Arrhenius-like behavior is observed and well reproduced by the model. This is consistent with the picture that electrons recombining from Γ_c need to be thermally activated above the Γ_c - L_c energy barrier.

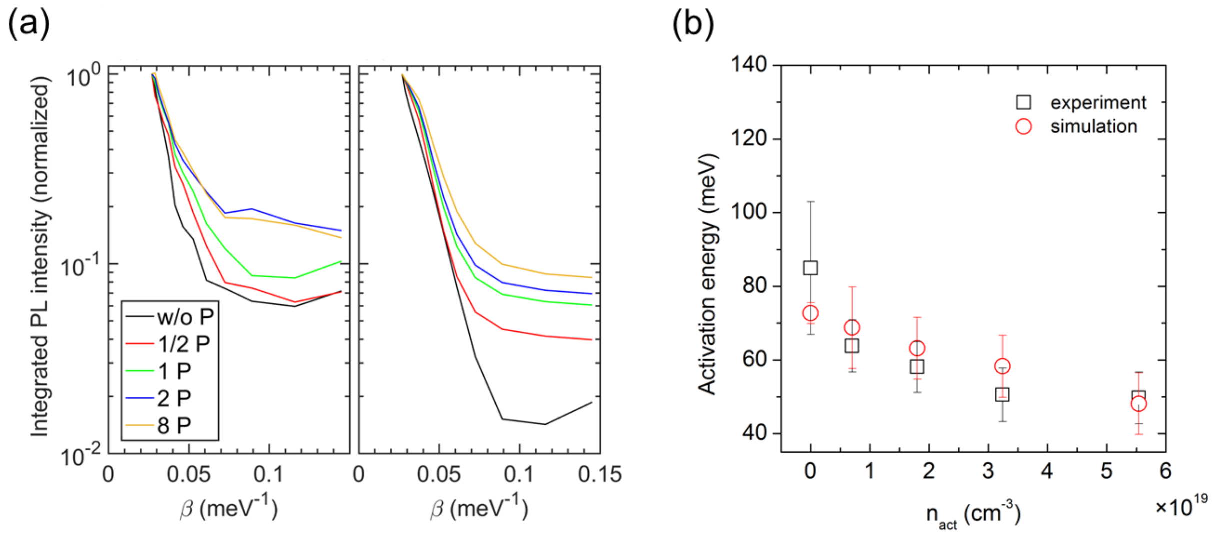

FIG. 10-3 (a) Temperature dependence of the integrated PL intensity shown in an Arrhenius plot. Experimental (left panel) and simulated (right panel) data taken from the temperature series from T_L = 80 K to 430 K are plotted versus $\beta = 1/(k_B T_L)$. Intensities are normalized to the integrated intensity at T_L = 430 K. In the simulations the electron temperature T_{el} equals the lattice temperature T_L.

(b) Activation energies obtained from the Arrhenius plot in (a) in function of the density of activated donors nact of the different samples with Q_{PH_3} = w/o P, ½ P, 1 P, 2 P, and 8 P.

From the fitted slope of the Arrhenius-like region we obtain for the experimental data an activation energy in the intrinsic sample of 85 meV which compares well with the value of 73 meV for the simulated data, see FIG. 10-3 (b). This value is consistent with the empty-band energy difference between the L_c and Γ_c band edges which we calculated to be $\Delta E_{\Gamma L}$ = 125 meV for a residual thermal strain of $\varepsilon_{\|} \sim 1.5 \times 10^{-3}$ and which is reduced due to continuous wave pumping. Owing to the reduced barrier height, due to filling of the L valleys with extrinsic electrons from donors, both the experimental and theoretical activation energy decreases monotonically upon increasing the doping concentration, reaching in the 8P sample the values of about 50 and 48 meV, respectively.

In the low T region ($\beta > 0.05$ meV^{-1}) we find a weaker dependence of the integrated PL as a function of T_L, similarly to what was previously observed for intrinsic, tensilely strained Ge micro-stripes in Ref. [69]. This is in agreement with simulations, albeit the theoretical intensities appear slightly under-estimated. This underestimation is probably due to the role of electron heating effects (neglected in the simulations) which at low temperature may enhance the direct feature of the PL signal. Nevertheless, in the low-temperature regime the dominant spectral feature is due to indirect transitions while thermally activated direct recombinations play a minor role. In line with this observation, we find that in this temperature region, the w/o P, ½ P, and 1 P intensities are slightly increasing with β, as is typical in single valley semiconductors. This enhancement is entirely controlled by an increase of τ_{SRH} for decreasing T, as already predicted for the intrinsic case in Ref. [69]. Finally, we notice that the increase with β in Ge systems at low temperatures has been observed also by Pezzoli et al..[137, 142] Again, these features are well reproduced by our model with Shockley-Read-Hall recombination as dominant non-radiative mechanism.

10.8 Excitation power dependent PL

The comparison between the experimental and numerical PL spectra has indicated that the SRH dominates the Auger non-radiative recombination. To give further support to this conclusion we have studied the scaling of the integrated PL signal as a function of the pump power density.
In sec. 2.5.5, we have shown how this scaling can be related with the non-radiative dynamics. For $\tau_{SRH} >> \tau_{Auger}$, the rate equation which describes the excess carrier dynamics is linear in δn. Consequently, in intrinsic material, the integrated PL spectrum is expected to be a quadratic function of the pump power density. In fact, PL is roughly proportional to the product of the excess hole and electron densities and both increase linearly with the pump power W. On the other hand, if the Auger mechanism is the fastest non-radiative recombination channel, $\tau_{SRH} << \tau_{Auger,}$ the rate equation for the excess carriers contains terms in δn up to the third power. It follows that in intrinsic materials the integrated PL scales sublinearly with the excitation density, as $W^{2/3}$.

Following the same line of reasoning for the n-type material, and considering that in our doped samples we expect an excess carrier density much lower than that of the equilibrium conditions so that radiative recombination is limited by the minority carrier density, we concluded that when SRH is the fastest recombination mechanism, the scaling exponent for the integrated PL as a function of the excitation power W is 1, whereas in case that Auger is dominating, PL scales with $W^{1/3}$.

Before comparing the above expected values for the scaling exponents with those observed experimentally or predicted numerically by our model, we show in the left panels of FIG. 10-4 (a) PL data acquired at room temperature from the w/o P and 1P samples, using different excitation powers in the 0.2-1.5 MW/cm^2 range. For comparison, we report in the right panels of Fig. 5 also simulated spectra, normalized using as reference the PL signal at 1.5 MW/cm^2 measured on the w/o P sample at RT. Numerical and experimental spectra of FIG. 10-4 (a) are in good agreement, and both indicate that RT PL is dominated by direct recombinations for all the investigated excitation densities.

On the other hand, the spectral feature due to indirect transitions can be clearly distinguished at lower T_L, cf. FIG. 10-1 and FIG. 10-2. For instance, in the doped samples and at $T_L = 190$ K we can resolve a low energy shoulder at around 700 meV. The intensity of this spectral feature is comparable with the one related to the direct gap and it is well reproduced by the model, assuming an excess electron temperature of 30 K with respect to $T_L = 190$ K (not shown).
Moreover, we observe that at this intermediate T_L the ratio between the direct and indirect peaks increases by increasing the pump density. Again, these two facts suggest the presence of a pump-induced electron heating effect which enhances the population of Γ_c electrons, while the lattice temperature seems to be affected only negligibly by the absorption of pump photons.

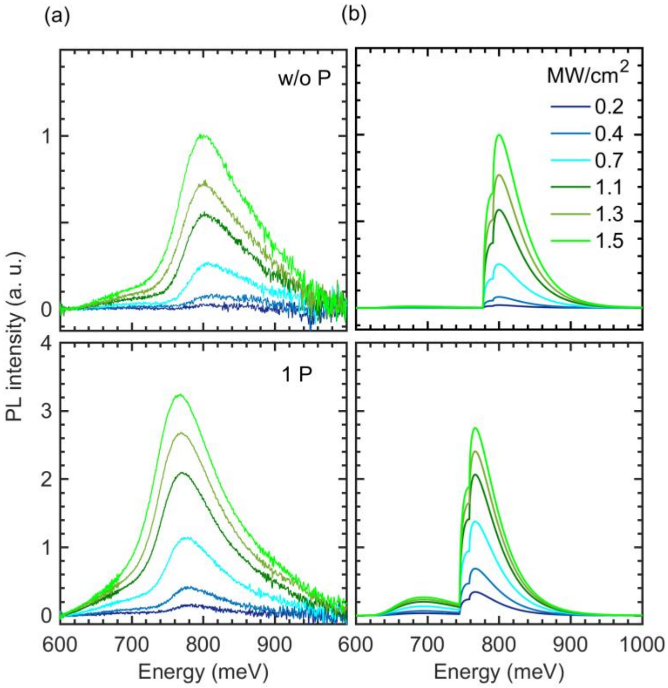

FIG. 10-4 Room temperature experimental (a) and simulated (b) spectra under different excitation powers in the 0.2-1.5 MW/cm^2 range, for the undoped (upper panels) and for the 1 P (lower panels) sample. Numerical data have been normalized to reproduce the peak intensity observed in the undoped sample at the highest excitation power.

Finally, we notice that the pump-induced increase of the direct/indirect intensity ratio in our doped samples cannot be attributed to an increase of the quasi-Fermi energy E_{Fc} associated to a larger δn population and responsible for a reduction of the effective height of the $\Gamma_c - L_c$ energy barrier, as elsewhere suggested in the literature.[212]

In fact, as shown previously, numerical data indicate that, due to the very fast non-radiative dynamics, the excess carrier density in doped samples is much lower than the equilibrium one for the entire explored range of pump power density. It follows that the quasi-Fermi energy in the conduction band is practically insensitive to an increase of W.

FIG. 10-5 shows the integrated PL intensity at room temperature versus excitation power density. Experimental and numerical data are shown in the left and right plot, respectively. We can observe in the left panel of FIG. 10-5 that all the doped samples share the same scaling exponent which is significantly lower than the one which describes the behavior of the intrinsic Ge layer. We determine for this latter quantity a value of 2.0 ± 0.1 which is in perfect agreement with 2.0, as resulting from the fitting of the numerical data in the right plot. From our discussion of the influence of the different non-radiative mechanisms on PL scaling with excitation power, it follows that the scaling observed for the intrinsic material is incompatible with the dominance of the Auger rate in the non-radiative dynamics, and that we can then conclude that SRH mechanism controls the excess carrier population in undoped Ge.

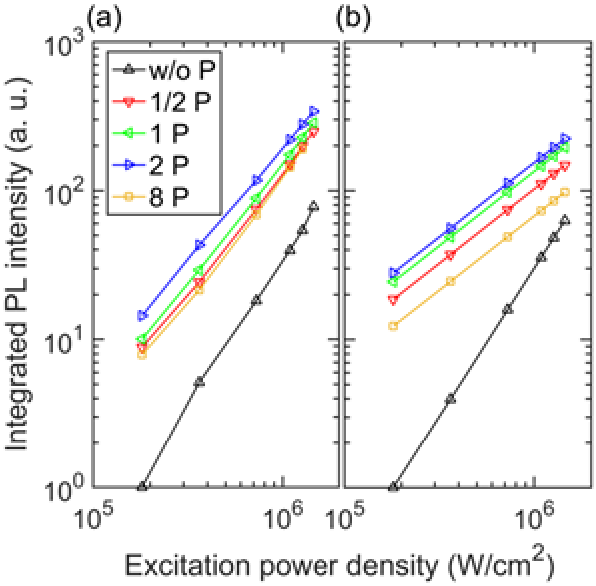

FIG. 10-5 Integrated PL intensity as a function of excitation power density *W* at room temperature for all investigated samples. Experimental and numerical data are shown in panel (a) and (b), respectively.

In the doped samples experimental values for the scaling span the 1.5 – 1.6 interval when the active dopant concentration range between 0.7 $\times 10^{19}$ cm^{-3} and 5.5 $\times 10^{19}$ cm^{-3}. These values, although lower than the corresponding quantity measured in the undoped case, are significantly larger than 1, which is the scaling predicted by our model. As a matter of fact, our simulations, as already stated, indicate that due to the reduction of τ_{SRH} caused by impurity defects, the SRH recombination dominates over the Auger mechanism and hence, it follows that the integrated PL is expected to be simply proportional to *W*. Again, we attribute the discrepancy between the higher experimental value and theory to electron heating effects which, enhancing the direct feature of the PL spectrum, induce a steeper increase with pump power of the PL signal. For instance, we notice that strong pump-induced heating effects are at the basis of the huge scaling exponent of 7, observed in Ge suspended membranes (Ref. [213]**)** and as commented in Ref. [214].

We point out that, when comparing the scaling in intrinsic and doped samples, one has to remember that the electron heating influence on the PL signal is expected to be relevant only in the latter case. This is due to the larger conduction quasi-Fermi energy E_{Fc} featured by the doped material. As a matter of fact, at room temperature E_{Fc} is close to the L_c band edge while in the w/o P sample it is estimated to be 6 × k_BT below the L_c energy. It follows, that the enhancement of the c_Γ carrier density, due to pump-induced electron heating in the intrinsic material is negligible and then the theoretical and experimental values of the scaling exponent are found to be in good agreement, especially because in agreement with the simulative results also the experimentally obtained scaling exponents for the doped samples are basically equal.

Finally, to confirm that the discrepancy between the experimental (~ 1.5 – 1.6) and theoretical (~1) scaling exponents in doped samples can be attributed to electron heating effects, the scaling of the integrated PL against pump power density has been measured at different lattice temperatures in the 80 K - 430 K range. The rationale for this is that the relative importance of pump-induced electron heating effects on the PL signal should decrease increasing T_L. The resulting scaling exponents are shown in FIG. 10-6. In agreement with our consideration we find that the scaling exponents of the doped samples decrease from about 1.7 – 2.1 at T_L = 100 K down to 1.3 – 1.4 at T_L = 430 K, approaching the theoretical limit value of 1, strengthening the role of SRH as the non-radiative mechanism governing the carrier dynamics also in heavily doped Ge on Si layers.

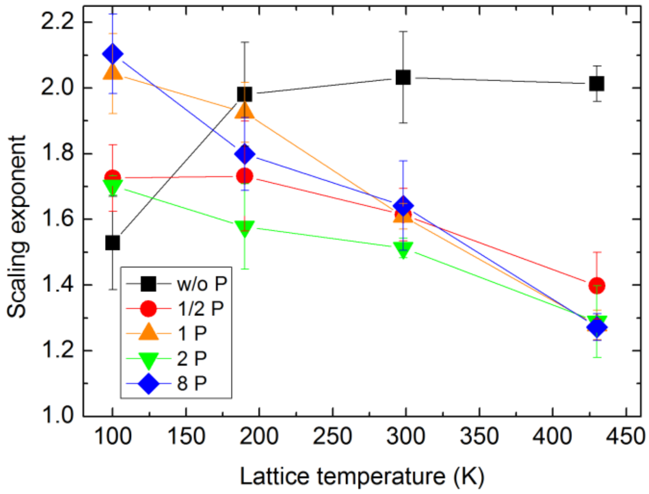

FIG. 10-6 Power scaling exponents versus lattice temperature T_L for the undoped (w/o P) and doped samples (1 P to 8 P) of the sample series grown at T_{dep} = 400 °C. The influence of a pump induced electron heating effect on the scaling exponent is less at higher T_L and the observed values approach the theoretically expected values in a SRH governed regime of 2 for the undoped sample and 1 for the doped samples.

11 Summary and conclusions

In this thesis, we have dealt with the two main ingredients to enhance light emission from Ge hetero-epitaxial layers grown on silicon: Strain and n-type doping. The Ge-based lasing devices presented so far by Camacho-Aguilera et al. [32] and Koerner et al.,[33] suffered from high threshold current densities (J_{th} > 100 kA/cm^2).

We have proposed an alternative approach to induce tensile strain in Ge based on the top-down fabrication of SiGe nano-stressors. This approach exploits the lattice mismatch of SiGe and Ge and elastic energy transfer from SiGe to Ge upon patterning of the SiGe layer. We have applied this method to bulk-like, 1 µm thick Ge layers and fabricated SiGe stripe stressors with compositions $Si_{50}Ge_{50}$ and $Si_{60}Ge_{40}$.

The SiGe epilayers were grown coherently on Ge and hence are under high tensile strain with negligible relaxation. The in-plane strain obtained from XRD and micro-Raman spectroscopy are 2.1% and 2.5% for the $Si_{50}Ge_{50}$ and $Si_{60}Ge_{40}$ layer, respectively.

By means of micro-Raman spectroscopy we showed that – after engraving several tens of nanometers wide parallel trenches into the SiGe layers – the so created SiGe stripe stressors relaxed their elastic energy and transferred it to the Ge layer beneath. Due to the Raman polarization selection rules the analysis was limited to stripe stressors oriented along the crystallographic direction <110>.

Micro-Raman spectroscopy is the only method with which the strain induced to the Ge layer may be detected, since the strained volume has to be discriminated from the vast bulk material. For this reason and due to the sample geometry measurements are sophisticated.

The Ge region in the gap between two SiGe stripe stressors is found to be under uniaxial tensile strain and the induced strain depends on the gap width between two stripes. With $Si_{50}Ge_{50}$ stressors and a gap width of 20 nm we could reveal uniaxial tensile strain up to 4%, the highest uniaxial strain level obtained at the time of publication. This strain value is close to what has been calculated by other groups for an indirect/direct gap transition, see sec. 2.3.3 for a review of threshold strain values published in literature. However, the strain is induced only locally close to the Ge surface.

For this reason, the verification of the tensile strain in Ge by means of micro-photoluminescence spectroscopy was complicated. Excited electrons in Γ_c are subject to fast intervalley scattering into the neighboring non-direct valleys.[123] For the realization of a Ge based electrically pumped it hence seems necessary to find a method to provide carrier injection into the Γ valley by appropriate tuning of the electric contacts.

However, we investigated the photoluminescence emission of a SiGe stressor sample with laser sources of 1064 nm, 532 nm, and 457.9 nm wavelength at different lattice temperatures T_L. The 1064 nm laser source was best suited to obtain Ge direct gap luminescence, since it provides direct electron pumping into the Γ conduction band valley Γ_c. It was possible to discriminate luminescence from the strained Ge volume at ~ 80 K using this laser source.

Moreover, we found that diffusion of excited carriers into the large bulk of Ge layer, away from the sample surface, limited the PL intensity originating in the highly strained region. No funneling effect could be revealed. By investigating a dedicated set of samples, we could show that carrier diffusions length exceeds 500 nm in an intrinsic Ge/$Si_{10}Ge_{90}$ stack. We explained this by an increased diffusion constant of hot carriers, as presented by Othonos in Ref. [162].

In addition, we revealed that roughening of the Ge surface through reactive-ion etching quenches direct gap PL completely. It cannot be excluded that during the SiGe stressor fabrication the Ge surface is damaged considerably.

To enlarge the relative volume of tensile Ge and to confine excited carriers, we transferred the SiGe stressor approach to a thin Ge bridge of 100 nm thickness. Large vertical carrier diffusion is prevented by the limited thickness of the bridge. SiGe stressors on the bridge and on Ge still attached to the Si substrate were fabricated by etching crossed trenches (crosses) into the top SiGe layer with x = 60% Ge content. Simulations of such a structure showed that in the intersection of the two trenches, i. e. in the middle of the cross, biaxial strain is created.[61]

Using micro-Raman spectroscopy, we could determine the strain created by the SiGe stressor. These measurements proved to be even more difficult compared to the SiGe stressors on bulk-like substrates, since the Ge bridges resulted to be extremely heat-sensitive.

A comparison between the effect of the stressor on the bridge and the same stressor on the Ge layer attached to the substrate demonstrated that suspension of the Ge layer doubled the strain that could be reached. The obtained strain values induced into Ge by the SiGe stressor are (1.3 ± 0.1) % and (0.6 ± 0.3) % uniaxial for the suspended and attached case, respectively. Assuming superposition of the cross arms, the SiGe stressor induced 1.3% biaxial tensile strain in the center of the cross on the Ge bridge, which is close to the calculated biaxial strain for an indirect/direct gap transition (1.6% - 1.9%).

However, we found that the bridge was under a compressive strain bias in its initial state due to the partial transverse relaxation of the SiGe top layer. Hence, the absolute strain value reached in Ge comes short with only (0.7 ± 0.1) % uniaxial strain in the arms of the cross or ~ 0.7% biaxial strain in its center.

Due to the low absolute strain value reached and the low resistance of the Ge bridge to heat induced by the laser source, it was not possible to obtain a meaningful PL spectrum from the strained region on the bridge.

N-type doping is commonly accepted to be one core ingredient to reach optical gain in Ge. Gain calculations for strained and doped Ge show that also with high strain levels close to the indirect/direct bandgap transition, doping levels of ~ $\times 10^{19}$ cm^{-3} are required to reduce the high threshold current densities from which the Ge-based lasers suffered so far.[62]

Thus, the challenge is to grow highly doped Ge with good crystal quality. For this reason, we investigated the effects of different growth parameters on the PL intensity of selectively grown phosphorous in-situ doped Ge to reveal trends for optimized growth of n-type doped Ge on Si.

By changing the deposition temperature T_{dep} of Ge at constant in-situ doping, we found that PL intensity is increased from T_{dep} = 325 °C to 400 °C despite a decrease in phosphorous atoms incorporated into the Ge matrix. We explain this result with improved crystal quality for growth at 400 °C. This part of the work has been performed at IHP GmbH (Frankfurt (Oder)) under the supervision of G. Capellini.

The variation of the dopant flux (PH_3 pressure) during in-situ doping at Ge deposition temperatures T_{dep} = 350 °C and 400 °C revealed that initially PL intensity is increased and reaches an optimum doping concentration resulting in maximum PL. Maximum PL peak intensity is observed for activated donor concentrations $n_{act} = 1 – 1.5 \times 10^{19}$ cm^{-3} for T_{dep} = 350 °C and $n_{act} = 2 - 3 \times 10^{19}$ cm^{-3} for T_{dep} = 400 °C. Relative enhancements of PL peak intensity with respect to an undoped sample were ×2.8 and ~ ×4.0 for the series with T_{dep} = 350 °C and that with T_{dep} = 400 °C series, respectively. Further doping leads to a decrease in PL which can be attributed to an increased point defect concentration and degraded crystallinity.

Furthermore, a red shift of PL is observed with increasing doping concentration by bandgap narrowing. In case of T_{dep} = 350 °C, the red-shift was not continuous but for the highest doping concentration the red-shift was reduced again due to donor deactivation through P clustering.

The variation of postbake temperature T_{bake} from 500 °C to 800 °C was performed on samples with T_{dep} = 400 °C and fixed dopant flux. As grown samples as well as samples with additional silicon nitride Si_3N_4 capping layer to hinder potential phosphorous out-diffusion were treated.

The photoluminescence analysis showed that PL intensity is further increased by a factor of 2.0 - 2.5 for all T_{bake}. We could show that this can be ascribed to enhanced donor activation and improved crystal quality.

Results of the phosphorous concentration obtained by SIMS showed that phosphorous out-diffusion is considerable for T_{bake} = 800 °C only and is slightly higher in the sample without Si_3N_4 capping layer.

We found that growth at 400 °C led to the best trade-off between high dopant concentration and crystal quality. To gain deeper insight in the impact of doping on the PL and to understand better the physical mechanism limiting the emission performances of P-doped Ge layers, we used the series of samples with different doping concentrations grown at this temperature to study their recombination dynamics.

Therefore, we have linked the active donor concentration n_{act} and total dopant concentrations n_{tot} to the radiative and non-radiative recombination mechanisms in heavily doped Ge/Si heterostructures featuring n-type doping densities in the $[1 – 10] \times 10^{19}$ cm^{-3} range.

This was done by comparing experimental PL data with the theoretical model proposed by Virgilio et al. in Ref. [69]. This model already took into consideration the effects of strain and temperature on the band structure and recombination rates and was expanded for the effects of doping. In particular, we have added a linear dependence of the non-radiative Shockley-Read-Hall recombination rate on total dopant density n_{tot}. The model parameters are calibrated to one experimental spectrum only. The model then reproduces correctly all the spectral features occurring in the experimental data obtained at lattice temperatures from 80 K to 430 K, as well as for different excitation power densities. Furthermore, the model output results in an increase of the SRH rate by a factor of ~ ×300 for dopant concentrations in the 10^{19} cm^{-3} range. This is accompanied by a reduction of the SRH related lifetime from ~ 30 ns in the intrinsic case to ~ 0.1 ns in the doped case. Alternative deposition and doping techniques could lead to different non-radiative carrier recombination rates.

The SRH lifetime was shorter than the Auger lifetime in all the doped samples investigated here, hence the SRH recombination dominates the Auger recombination mechanism for the excess carrier density evaluated in our experiments.

In conclusion, we have proposed a top-down approach to create SiGe stressors for tensile strain generation in Ge. This approach relies on materials and technologies that are fully compatible with modern silicon micro-technology. The variation of the gap size between SiGe stressors gives the possibility to control the induced strain in a germanium layer.

The transfer of a SiGe stressor on a suspended membrane doubled the strain generated in Ge. Boztug et al. showed that optical gain can be obtained from Ge nano-membranes and pointed out that gain is already achieved at strain values below the indirect/gap transition.[44] In this respect, our method may be used to pattern Ge membranes with SiGe stressors.

Previous calculations showed that in principle it is possible to raise the strain values obtained with SiGe stressors by improving the fabrication, especially the etching step. Fabrication of membranes from germanium on insulator substrates (GeOI) may be a promising solution to enhance the light emission from Ge strained by SiGe stressors. Furthermore, the application of SiGe stressors to doped material could also improve light emission from strained Ge. A beneficial side effect of the n-type doping may be a reduction of excited carrier diffusion out of the highly strained volume.

Moreover, we revealed trends for optimized growth of n-type doped Ge on Si. We have shown that the impact of the doping atoms on non-radiative lifetime is a bulk-effect that reduces the SRH lifetime by two orders of magnitude. This leads to the limitation of the positive effect of n-type doping on PL emission intensity and results in an optimum dopant concentration. The impact of doping on the SRH-like recombination rate should be accounted for in future laser gain calculations, since the shorter the non-radiative carrier lifetime, the higher the threshold current density to achieve population inversion and optical gain.

Combining hypothetically the strain value achieved with SiGe stressors on a Ge bridge with the optimum phosphorous doping that we have revealed, and taking the threshold current density calculations of Sukhdeo et al., Ref. [62], we could have reached a threshold current density reduction by two orders of magnitude.

Acknowledgements

Doing research is like playing in an orchestra. My most profound thanks to my PhD supervisor E. Bonera (Università degli Studi di Milano-Bicocca, Milan) and all the ensemble members:

Idea and overall direction of the strain project:
E. Bonera (Università degli Studi di Milano-Bicocca, Milan)

Idea and overall direction of the doping project:
G. Capellini (IHP GmbH, Frankfurt (O.))

Heteroepitaxial growth:
D. Chrastina (Politecnico di Milano, Como)
J. Frigerio (Politecnico di Milano, Como)
Y. Yamamoto (IHP GmbH, Frankfurt (O.))
A. Hesse (IHP GmbH, Frankfurt (O.))

Nanostructuration:
M. Bollani (IFN-CNR, Como)
V. Mondiali (Politecnico di Milano, Como)
M. Lodari (Politecnico di Milano, Como)
M. Borriello (Politecnico di Milano, Como)

X-ray diffraction measurements:
D. Chrastina (Politecnico di Milano, Como)
Y. Yamamoto (IHP GmbH, Frankfurt (O.))
A. Hesse (IHP GmbH, Frankfurt (O.))

SIMS measurements:
F. Bärwolf (IHP GmbH, Frankfurt (O.))
I. Costina (IHP GmbH, Frankfurt (O.))

SEM images:
V. Mondiali (Politecnico di Milano, Como)
M. Lodari (Politecnico di Milano, Como)
M. Borriello (Politecnico di Milano, Como)
H. M. Krause (IHP GmbH, Frankfurt (O.))
G. Morgenstern (IHP GmbH, Frankfurt (O.))

Numerical modelling:
M. Virgilio (IHP GmbH, Frankfurt (O.))

Moreover, I am grateful to T. Schroeder (IHP GmbH, Frankfurt (O.)) and G. Capellini (IHP GmbH, Frankfurt (O.)) who gave me the possibility to come and join IHP for several months. Many thanks to N. Taoka (now AIST, Nagoya) who has always been helpful to resolve problems in the lab and to discuss experimental issues and to all the other colleagues from IHP, especially V. Schlykow, F. Akhtar, R. Delgado, J. Dabrowski, M. Kazmierczak, D. Kot, G. Lippert, G. Kissinger, M. Lukosius,

P. Zaumseil, O. Skibitzki, B. Kuck, H. M. Krause, Y. Dedkov, E. Pérez, C. A. Chavarin, and M. Cirillo for their sympathy, support and the nice time spent together in Frankfurt.

Grazie mille ai colleghi della Bicocca: E. Gatti, F. Pezzoli, A. Giorgioni, S. De Cesari, F. Basso Basset, E. Vitiello, L. Rossetto for all the discussions and support, also to resolve everyday problems in Milan and Sesto San Giovanni.
I am also deeply grateful to E. E. Grilli (Università degli Studi di Milano-Bicocca, Milan) sharing all his knowledge, especially his practical skills.

Last, but of tremendous importance, I acknowledge financial support from “fondo giovani” of Ministero dell'istruzione, dell'università e della ricerca (MIUR).

Vergelt's Gott!

List of scientific contributions

Research articles in scientific journals:

M. R. Barget, M. Lodari, M. Borriello, V. Mondiali, D. Chrastina, M. Bollani and E. Bonera
``Tensile strain in Ge membranes induced by SiGe nanostressors,"
Applied Physics Letters **109**, 133109 (2016).

M. Bollani, D. Chrastina, L. Gagliano, L. Rossetto, D. Scopece, **M. Barget**, V. Mondiali, J. Frigerio, M. Lodari, F. Pezzoli, F. Montalenti and E. Bonera ``Local uniaxial tensile strain in germanium of up to 4% induced by SiGe epitaxial nanostructures," Applied Physics Letters 107, 083101 (2015).

F. Isa, A. Jung, M. Salvalaglio, Y. A. R. Dasilva, I. Marozau, M. Meduňa, **M. Barget**, A. Marzegalli, G. Isella, R. Erni, F. Pezzoli, E. Bonera, P. Niedermann, O. Sereda, P. Gröning, F. Montalenti and H. von Känel
``Strain Engineering in Highly Mismatched SiGe/Si Heterostructures ,"
Materials Science in Semiconductor Processing (2016).

F. Isa, M. Salvalaglio, Y. A. R. Dasilva, M. Meduňa, **M. Barget**, A. Jung, T. Kreiliger, G. Isella, R. Erni, F. Pezzoli, E. Bonera, P. Niedermann, P. Gröning, F. Montalenti and H. von Känel
``Highly Mismatched, Dislocation-Free SiGe/Si Heterostructures,"
Advanced Materials **28**, 884 (2015).

V. Mondiali, M. Lodari, D. Chrastina, **M. Barget**, E. Bonera and M. Bollani
``Micro and nanofabrication of SiGe/Ge bridges and membranes by wet-anisotropic etching ,"
Microelectronic Engineering **141**, 256 (2015).

V. Schlykow, W. M. Klesse, G. Niu, N. Taoka, Y. Yamamoto, O. Skibitzki, **M. R. Barget**, P. Zaumseil, H. von Känel, M. A. Schubert, G. Capellini and T. Schroeder
``Selective growth of fully relaxed GeSn nano-islands by nanoheteroepitaxy on patterned Si(001),"
Applied Physics Letters **109**, 202102 (2016).

Y. Yamamoto, **M. R. Barget**, G. Capellini, N. Taoka, M. Virgilio, P. Zaumseil, A. Hesse, T. Schroeder and B. Tillack
``Photoluminescence of Phosphorous Doped Ge on Si (100),"
Materials Science in Semiconductor Processing (2016).

Congress contributions:

Barget, M; Lodari, M; Mondiali, V; Chrastina, D; Bollani, M; Bonera, E
SiGe nanostructures inducing tensile strain in suspended germanium membranes.
Oral presentation @ E-MRS Fall Meeting 2016, Warsaw, Poland

Barget, M; Bollani, M; Chrastina, D; Gagliano, L; Rossetto, L; Scopece, D; Mondiali, V; Frigerio, J; Borriello, M; Lodari, M; Pezzoli, F; Montalenti, F; Bonera, E
SiGe nano-stressors for Ge strain-engineering

Oral presentaion @ 12th International Conference on Nanosciences & Nanotechnologies (NN15), Thessaloniki, Greece

Gagliano, L; Rossetto, L; Scopece, D; Mondiali, V; Lodari, M; Barget, M; De Cesari, S; Pezzoli, F; Bollani, M; Chrastina, D; Montalenti, F; Bonera, E
Local Uniaxial Tensile Deformation of Germanium up to the 4% Threshold by Epitaxial Nanostructures.
Poster @ Summer School Silicon Photonics 2014, Gent, Belgium

Bibliography

[1] Jürgen Jahns. *Photonik*. Oldenbourg Wissenschaftsverlag GmbH, 2001.

[2] Gerhard Abstreiter. Engineering the future of electronics. *Physics World*, 5 (3): 36, 1992. URL http://stacks.iop.org/2058-7058/5/i=3/a=29.

[3] R. A. Soref. Silicon-based optoelectronics. *Proceedings of the IEEE*, 81 (12): 1687, 1993. doi: 10.1109/5.248958.

[4] C. Gunn. CMOS photonics for high-speed interconnects. *IEEE Micro*, 26 (2): 58, 2006. ISSN 0272-1732. doi: 10.1109/MM.2006.32.

[5] Roel Baets, Ananth Z. Subramanian, Ashim Dhakal, Shankar K. Selvaraja, Katarzyna Komorowska, Frédéric Peyskens, Eva Ryckeboer, Nebiyu Yebo, Gunther Roelkens, and Nicolas Le Thomas. Spectroscopy-on-chip applications of silicon photonics. *Proc. SPIE*, 8627: 86270I–1, 2013. doi: 10.1117/12.2010498.

[6] Advantages and disadvantages of monolithic ICs. URL http://electronicspost.com/-advantages-and-disadvantages-of-monolithic-ics/.

[7] G. T. Reed, G. Mashanovich, F. Y. Gardes, and D. J. Thomson. Silicon optical modulators. *Nat Photon*, 4 (8): 518, 2010.

[8] Jurgen Michel, Jifeng Liu, and Lionel C. Kimerling. High-performance Ge-on-Si photodetectors. *Nature Photonics*, 4 (8): 527, 2010.

[9] Papichaya Chaisakul, Delphine Marris-Morini, Jacopo Frigerio, Daniel Chrastina, Mohamed-Said Rouifed, Stefano Cecchi, Paul Crozat, Giovanni Isella, and Laurent Vivien. Integrated germanium optical interconnects on silicon substrates. *Nat Photon*, 8 (6): 482, 2014.

[10] Nobuyoshi Koshida and Hideki Koyama. Visible electroluminescence from porous silicon. *Applied Physics Letters*, 60 (3): 347, 1992. doi: 10.1063/1.106652.

[11] P. Vogl, Martin M. Rieger, J. A. Majewski, and G. Abstreiter. How to convert group-IV semiconductors into light emitters. *Physica Scripta*, T49: 476, 1993. doi: 10.1088/0031-8949/1993/T49B/017.

[12] C. S. Peng, Q. Huang, W. Q. Cheng, J. M. Zhou, Y. H. Zhang, T. T. Sheng, and C. H. Tung. Optical properties of Ge self-organized quantum dots in Si. *Phys. Rev. B*, 57: 8805, 1998. doi: 10.1103/PhysRevB.57.8805.

[13] B. Zheng, J. Michel, F. Y. G. Ren, L. C. Kimerling, D. C. Jacobson, and J. M. Poate. Room-temperature sharp line electroluminescence at λ=1.54 from an erbium-doped, silicon light-emitting diode. *Applied Physics Letters*, 64 (21): 2842, 1994. doi: 10.1063/1.111977.

[14] Haisheng Rong, Ansheng Liu, Richard Jones, Oded Cohen, Dani Hak, Remus Nicolaescu, Alexander Fang, and Mario Paniccia. An all-silicon Raman laser. *Nature*, 433 (7023): 292, 2005.

[15] Haisheng Rong, Richard Jones, Ansheng Liu, Oded Cohen, Dani Hak, Alexander Fang, and Mario Paniccia. A continuous-wave Raman silicon laser. *Nature*, 433 (7027): 725, 2005.

[16] Martin Kittler and Vitaly V. Kveder. Dislocations in silicon and D-band luminescence for infrared light emitters. *Materials Science Forum*, 590: 29, 2008. doi: 10.4028/www.scientific.net/MSF.590.29.

[17] Martin Kittler and Manfred Reiche. Dislocations as active components in novel silicon devices. *Adv. Eng. Mater.*, 11 (4): 249, 2009. ISSN 1527-2648.

[18] S. Saito, T. Takahama, K. Tani, M. Takahashi, T. Mine, Y. Suwa, and D. Hisamoto. Stimulated emission of near-infrared radiation in silicon fin light-emitting diode. *Applied Physics Letters*, 98 (26): 261104, 2011. URL http://scitation.aip.org/content/aip/journal/apl/-98/26/10.1063/1.3605255.

[19] Andrew Lee, Qi Jiang, Mingchu Tang, Alwyn Seeds, and Huiyun Liu. Continuous-wave InAs/GaAs quantum-dot laser diodes monolithically grown on Si substrate with low threshold current densities. *Opt. Express*, 20 (20): 22181, 2012. doi: 10.1364/OE.20.022181.

[20] S. Wirths, R. Geiger, N. von den Driesch, G. Mussler, T. Stoica, S. Mantl, Z. Ikonic, M. Luysberg, S. Chiussi, Hartmann J. M., H. Sigg, J. Faist, D. Buca, and D. Grützmacher. Lasing in direct-bandgap GeSn alloy grown on Si. *Nature Photonics*, 9 (2): 88, 2015.

[21] Martyna Grydlik, Florian Hackl, Heiko Groiss, Martin Glaser, Alma Halilovic, Thomas Fromherz, Wolfgang Jantsch, Friedrich Schäffler, and Moritz Brehm. Lasing from glassy Ge quantum dots in crystalline Si. *ACS Photonics*, 3 (2): 298, 2016. doi: 10.1021/acsphotonics.5b00671.

[22] Minjoo L. Lee, Eugene A. Fitzgerald, Mayank T. Bulsara, Matthew T. Currie, and Anthony Lochtefeld. Strained Si, SiGe, and Ge channels for high-mobility metal-oxide-semiconductor field-effect transistors. *Journal of Applied Physics*, 97 (1): 011101, 2005.

[23] P. Narozny, H. Dambkes, H. Kibbel, and E. Kasper. Si/SiGe heterojunction bipolar transistor made by molecular-beam epitaxy. *IEEE Transactions on Electron Devices*, 36 (10): 2363, 1989. doi: 10.1109/16.40923.

[24] IBM research blog advancing toward 7nm. URL https://www.ibm.com/blogs/research/-2016/12/advancing-toward-7nm/.

[25] Ravi Pillarisetty. Academic and industry research progress in germanium nanodevices. *Nature*, 479 (7373): 324, 2011.

[26] T. P. McLean. The absorption edge spectrum of semiconductors. *Progress in Semiconductors*, 5: 53, 1960.

[27] M. Virgilio, C. L. Manganelli, G. Grosso, G. Pizzi, and G. Capellini. Radiative recombination and optical gain spectra in biaxially strained n-type germanium. *Phys. Rev. B*, 87: 235313, 2013. doi: 10.1103/PhysRevB.87.235313.

[28] Jifeng Liu, Xiaochen Sun, Dong Pan, Xiaoxin Wang, Lionel C. Kimerling, Thomas L. Koch, and Jurgen Michel. Tensile-strained, n-type Ge as a gain medium formonolithic laser integration on Si. *Opt. Express*, 15 (18): 11272, 2007. doi: 10.1364/OE.15.011272.

[29] Peng Huei Lim, Sungbong Park, Yasuhiko Ishikawa, and Kazumi Wada. Enhanced direct bandgap emission in germanium by micromechanical strain engineering. *Optics Express*, 17 (18): 16358, 2009. doi: 10.1364/OE.17.016358.

[30] Jifeng Liu, Xiaochen Sun, Lionel C. Kimerling, and Jurgen Michel. Direct-gap optical gain of Ge on Si at room temperature. *Optics Letters*, 34 (11): 1738, 2009. doi: 10.1364/OL.34.001738.

[31] Jifeng Liu, Xiaochen Sun, Rodolfo Camacho-Aguilera, Lionel C. Kimerling, and Jurgen Michel. Ge-on-Si laser operating at room temperature. *Opt. Lett.*, 35 (5): 679, 2010. doi: 10.1364/OL.35.000679.

[32] Rodolfo E. Camacho-Aguilera, Yan Cai, Neil Patel, Jonathan T. Bessette, Marco Romagnoli, Lionel C. Kimerling, and Jurgen Michel. An electrically pumped germanium laser. *Opt. Express*, 20 (10): 11316, 2012. doi: 10.1364/OE.20.011316.

[33] Roman Koerner, Michael Oehme, Martin Gollhofer, Marc Schmid, Konrad Kostecki, Stefan Bechler, Daniel Widmann, Erich Kasper, and Joerg Schulze. Electrically pumped lasing from Ge fabry-perot resonators on Si. *Opt. Express*, 23 (11): 14815, 2015. doi: 10.1364/OE.23.014815.

[34] Lee Carroll, Peter Friedli, Stefan Neuenschwander, Hans Sigg, Stefano Cecchi, Fabio Isa, Daniel Chrastina, Giovanni Isella, Yuriy Fedoryshyn, and Jérôme Faist. Direct-gap gain and optical absorption in germanium correlated to the density of photoexcited carriers, doping, and strain. *Phys. Rev. Lett.*, 109: 057402, 2012. doi: 10.1103/PhysRevLett.109.057402.

[35] B. Dutt, D.S. Sukhdeo, D. Nam, B.M. Vulovic, Ze Yuan, and K.C. Saraswat. Roadmap to an efficient germanium-on-silicon laser: Strain vs. n-type doping. *Photonics Journal, IEEE*, 4 (5): 2002, 2012. doi: 10.1109/JPHOT.2012.2221692.

[36] David Sukhdeo, Donguk Nam, Ze Yuan, Birendra (Raj) Dutt, and Krishna C. Saraswat. Toward an efficient germanium-on-silicon laser: Ultimate limits of tensile strain and n-type doping. In *CLEO: 2013*, page JTh2A.109. Optical Society of America, 2013. doi: 10.1364/CLEO_QELS.2013.JTh2A.109.

[37] M. Virgilio, C. L. Manganelli, G. Grosso, T. Schroeder, and G. Capellini. Photoluminescence, recombination rate, and gain spectra in optically excited n-type and tensile strained germanium layers. *Journal of Applied Physics*, 114 (24): 243102, 2013.

[38] B. M. Haugerud, L. A. Bosworth, and R. E. Belford. Mechanically induced strain enhancement of metal-oxide-semiconductor field effect transistors. *Journal of Applied Physics*, 94 (6): 4102, 2003. doi: 10.1063/1.1602562.

[39] P. R. Chidambaram, C. Bowen, S. Chakravarthi, C. Machala, and R. Wise. Fundamentals of silicon material properties for successful exploitation of strain engineering in modern CMOS manufacturing. *IEEE Transactions on Electron Devices*, 53 (5): 944, 2006. ISSN 0018-9383. doi: 10.1109/TED.2006.872912.

[40] Yasuhiko Ishikawa, Kazumi Wada, Douglas D. Cannon, Jifeng Liu, Hsin-Chiao Luan, and Lionel C. Kimerling. Strain-induced band gap shrinkage in Ge grown on Si substrate. *Applied Physics Letters*, 82 (13): 2044, 2003.

[41] T.-H. Cheng, K.-L. Peng, C.-Y. Ko, C.-Y. Chen, H.-S. Lan, Y.-R. Wu, C. W. Liu, and H.-H. Tseng. Strain-enhanced photoluminescence from Ge direct transition. *Applied Physics Letters*, 96 (21): 211108, 2010.

[42] M. El Kurdi, H. Bertin, E. Martincic, M. de Kersauson, G. Fishman, S. Sauvage, A. Bosseboeuf, and P. Boucaud. Control of direct band gap emission of bulk germanium by mechanical tensile strain. *Applied Physics Letters*, 96 (4): 041909, 2010. doi: 10.1063/1.3297883.

[43] J. R. Sánchez-Pérez, C. Boztug, F. Chen, F. F. Sudradjat, D. M. Paskiewicz, R. Jacobson, M. G. Lagally, and R. Paiella. Direct-bandgap light-emitting germanium in tensilely strained nanomembranes. *Proceedings of the National Academy of Sciences*, 108 (47): 18893, 2011. doi: 10.1073/pnas.1107968108.

[44] C. Boztug, J. R. Sánchez-Pérez, F. F. Sudradjat, R. B. Jacobson, D. M. Paskiewicz, M. G. Lagally, and R. Paiella. Tensilely strained germanium nanomembranes as infrared optical gain media. *Small*, 9 (4): 622, 2013. doi: 10.1002/smll.201201090.

[45] J. Menéndez and J. Kouvetakis. Type-I Ge/$Ge_{1-x-y}Si_xSn_y$ strained-layer heterostructures with a direct Ge bandgap. *Appl. Phys. Lett.*, 85 (7): 1175, 2004. doi: 10.1063/1.1784032.

[46] Y.-Y. Fang, J. Tolle, R. Roucka, A. V. G. Chizmeshya, John Kouvetakis, V. R. D’Costa, and José Menéndez. Perfectly tetragonal, tensile-strained Ge on $Ge_{1-y}Sn_y$ buffered Si(100). *Appl. Phys. Lett.*, 90 (6): 061915, 2007. doi: 10.1063/1.2472273.

[47] R. Jakomin, M. de Kersauson, M. El Kurdi, L. Largeau, O. Mauguin, G. Beaudoin, S. Sauvage, R. Ossikovski, G. Ndong, M. Chaigneau, I. Sagnes, and P. Boucaud. High quality tensile-strained n-doped germanium thin films grown on InGaAs buffer layers by metal-organic chemical vapor deposition. *Appl. Phys. Lett.*, 98 (9): 091901, 2011. doi: 10.1063/1.3559231.

[48] A. Ghrib, M. de Kersauson, M. El Kurdi, R. Jakomin, G. Beaudoin, S. Sauvage, G. Fishman, G. Ndong, M. Chaigneau, R. Ossikovski, I. Sagnes, and P. Boucaud. Control of tensile strain in germanium waveguides through silicon nitride layers. *Applied Physics Letters*, 100 (20): 201104, 2012. doi: 10.1063/1.4718525.

[49] G. Capellini, G. Kozlowski, Y. Yamamoto, M. Lisker, C. Wenger, G. Niu, P. Zaumseil, B. Tillack, A. Ghrib, M. de Kersauson, M. El Kurdi, P. Boucaud, and T. Schroeder. Strain analysis in SiN/Ge microstructures obtained via Si-complementary metal oxide semiconductor compatible approach. *Journal of Applied Physics*, 113 (1): 013513, 2013.

[50] M. de Kersauson, M. El Kurdi, S. David, X. Checoury, G. Fishman, S. Sauvage, R. Jakomin, G. Beaudoin, I. Sagnes, and P. Boucaud. Optical gain in single tensile-strained germanium photonic wire. *Opt Express*, 19 (19): 17925, 2011.

[51] Donguk Nam, Devanand Sukhdeo, Arunanshu Roy, Krishna Balram, Szu-Lin Cheng, Kevin Chih-Yao Huang, Ze Yuan, Mark Brongersma, Yoshio Nishi, David Miller, and Krishna Saraswat. Strained germanium thin film membrane on silicon substrate for optoelectronics. *Opt Express*, 19 (27): 25866, 2011. doi: 10.1364/OE.19.025866.

[52] A. Ghrib, M. El Kurdi, M. de Kersauson, M. Prost, S. Sauvage, X. Checoury, G. Beaudoin, I. Sagnes, and P. Boucaud. Tensile-strained germanium microdisks. *Applied Physics Letters*, 102 (22): 221112, 2013.

[53] G. Capellini, C. Reich, S. Guha, Y. Yamamoto, M. Lisker, M. Virgilio, A. Ghrib, M. El Kurdi, P. Boucaud, B. Tillack, and T. Schroeder. Tensile Ge microstructures for lasing fabricated by means of a silicon complementary metal-oxide-semiconductor process. *Opt. Express*, 22 (1): 399, 2014. doi: 10.1364/OE.22.000399.

[54] Qinglei Guo, Miao Zhang, Zhongying Xue, Jing Zhang, Gang Wang, Da Chen, Zhiqiang Mu, Gaoshan Huang, Yongfeng Mei, Zengfeng Di, and Xi Wang. Uniaxial and tensile strained germanium nanomembranes in rolled-up geometry by polarized Raman scattering spectroscopy. *AIP Advances*, 5 (3): 037115, 2015.

[55] M. J. Süess, R. Geiger, R. A. Minamisawa, G. Schiefler, J. Frigerio, D. Chrastina, G. Isella, R. Spolenak, J. Faist, and H. Sigg. Analysis of enhanced light emission from highly strained germanium microbridges. *Nature Photonics*, 7: 466, 2013. doi: 10.1038/nphoton.2013.67.

[56] David S. Sukhdeo, Donguk Nam, Ju-Hyung Kang, Mark L. Brongersma, and Krishna C. Saraswat. Direct bandgap germanium-on-silicon inferred from 5.7% <100> uniaxial tensile strain [invited]. *Photon. Res.*, 2 (3): A8, 2014. doi: 10.1364/PRJ.2.0000A8.

[57] G.O. Dias, D. Rouchon, J. Widiez, J.M. Hartmann, D. Fowler, A. Chelnokov, V. Reboud, A. Gassenq, S. Tardif, K. Guiloy, N. Pauc, J. Escalante, I. Duchemin, Y.-M. Niquet, F. Rieutord, V. Calvo, J. Faist, R. Geiger, T. Zabel, and H. Sigg. Design rules to control the tensile strain in Ge μ-membranes fabricated from GeOI substrates for photonics applications. In *Group IV Photonics (GFP), 2015 IEEE 12th International Conference on*, page 133, 2015. doi: 10.1109/Group4.2015.7305988.

[58] A. Gassenq, K. Guilloy, G. Osvaldo Dias, N. Pauc, D. Rouchon, J.-M. Hartmann, J. Widiez, S. Tardif, F. Rieutord, J. Escalante, I. Duchemin, Y.-M. Niquet, R. Geiger, T. Zabel, H. Sigg, J. Faist, A. Chelnokov, V. Reboud, and V. Calvo. 1.9% bi-axial tensile strain in thick germanium suspended membranes fabricated in optical germanium-on-insulator substrates for laser applications. *Applied Physics Letters*, 107 (19): 191904, 2015.

[59] V. Mondiali, M. Lodari, M. Borriello, D. Chrastina, and M. Bollani. Top-down SiGe nanostructures on Ge membranes realized by e-beam lithography and wet etching. *Microelectronic Engineering*, 153: 88, 2016.

[60] Monica Bollani, Daniel Chrastina, Luca Gagliano, Lidia Rossetto, Daniele Scopece, Michael Barget, Valeria Mondiali, Jacopo Frigerio, Mario Lodari, Fabio Pezzoli, Francesco Montalenti, and Emiliano Bonera. Local uniaxial tensile strain in germanium of up to 4% induced by SiGe epitaxial nanostructures. *Applied Physics Letters*, 107 (8): 083101, 2015.

[61] Daniele Scopece, Francesco Montalenti, Monica Bollani, Daniel Chrastina, and Emiliano Bonera. Straining Ge bulk and nanomembranes for optoelectronic applications: a systematic numerical analysis. *Semiconductor Science and Technology*, 29 (9): 095012, 2014. URL http://iopscience.iop.org/article/10.1088/0268-1242/29/9/095012

[62] David S. Sukhdeo, Yeji Kim, Shashank Gupta, Krishna C. Saraswat, Birendra Raj Dutt, and Donguk Nam. Anomalous threshold reduction from <100> uniaxial strain for a low-threshold Ge laser. *Optics Communications*, 379: 32, 2016. doi: http://dx.doi.org/10.1016/j.optcom.2016.05.030.

[63] P. Boucaud, M. El Kurdi, A. Ghrib, M. Prost, M. de Kersauson, S. Sauvage, F. Aniel, X. Checoury, G. Beaudoin, L. Largeau, I. Sagnes, G. Ndong, M. Chaigneau, and R. Ossikovski. Recent advances in germanium emission [invited]. *Photon. Res.*, 1 (3): 102, 2013. doi: 10.1364/PRJ.1.000102.

[64] Vinod Kumar Khanna. Physical understanding and technological control of carrier lifetimes in semiconductor materials and devices: A critique of conceptual development, state of the art and applications. *Progress in Quantum Electronics*, 29 (2): 59, 2005. URL http://www.sciencedirect.com/science/article/pii/S0079672705000030.

[65] Bernhard Schwartz, André Klossek, Martin Kittler, Michael Oehme, Erich Kasper, and Jörg Schulze. Electroluminescence of germanium LEDs on silicon: Influence of antimony doping. *physica status solidi (c)*, 11 (11-12): 1686, 2014. ISSN 1610-1642. doi: 10.1002/pssc.201400056.

[66] R. Geiger, J. Frigerio, M. J. Süess, D. Chrastina, G. Isella, R. Spolenak, J. Faist, and H. Sigg. Excess carrier lifetimes in Ge layers on Si. *Applied Physics Letters*, 104 (6): 062106, 2014. URL http://scitation.aip.org/content/aip/journal/apl/104/6/10.1063/1.4865237.

[67] M. El Kurdi, T. Kociniewski, T.-P. Ngo, J. Boulmer, D. Débarre, P. Boucaud, J. F. Damlencourt, O. Kermarrec, and D. Bensahel. Enhanced photoluminescence of heavily n-doped germanium. *Applied Physics Letters*, 94 (19): 191107, 2009. URL http://scitation.aip.org/content/aip/journal/apl/94/19/10.1063/1.3138155.

[68] E. Gaubas and J. Vanhellemont. Dependence of carrier lifetime in germanium on resisitivity and carrier injection level. *Applied Physics Letters*, 89 (14): 142106, 2006. URL http://scitation.aip.org/content/aip/journal/apl/89/14/10.1063/1.2358967.

[69] M. Virgilio, T. Schroeder, Y. Yamamoto, and G. Capellini. Radiative and non-radiative recombinations in tensile strained Ge microstrips: Photoluminescence experiments and modeling. *Journal of Applied Physics*, 118: 233110, 2015. URL http://scitation.aip.org/content/aip/journal/jap/118/23/10.1063/1.4938026.

[70] Herbert Stöhr and Wilhelm Klemm. Über Zweistoffsysteme mit Germanium. I. Germanium/Aluminium, Germanium/Zinn und Germanium/Silicium. *Z. Anorg. Allg. Chem.*, 241 (4): 305, 1939. URL http://dx.doi.org/10.1002/zaac.19392410401.

[71] Carl D. Thurmond. Equilibrium thermochemistry of solid and liquid alloys of germanium and of silicon. I. the solubility of Ge and Si in elements of groups III, IV and V. *The Journal of Physical Chemistry*, 57 (8): 827, 1953. doi: 10.1021/j150509a019.

[72] F. X. Hassion, A. J. Goss, and F. A. Trumbore. On the germanium-silicon phase diagram. *The Journal of Physical Chemistry*, 59 (10): 1118, 1955. doi: 10.1021/j150532a037.

[73] Otfried Madelung. *Semiconductors Data Handbook*. Springer-Verlag Berlin Heidelberg, 3 edition, 2004. doi: 10.1007/978-3-642-18865-7.

[74] L. Vegard. Die Konstitution der Mischkristalle und die Raumfüllung der Atome. *Zeitschrift für Physik*, 5 (1): 17, 1921.

[75] J. P. Dismukes, L. Ekstrom, and R. J. Paff. Lattice parameter and density in germanium-silicon alloys. *J. Phys. Chem.*, 68 (10): 3021, 1964. doi: 10.1021/j100792a049.

[76] V. K. Yang, M. Groenert, C. W. Leitz, A. J. Pitera, M. T. Currie, and E. A. Fitzgerald. Crack formation in GaAs heteroepitaxial films on Si and SiGe virtual substrates. *Journal of Applied Physics*, 93 (7): 3859, 2003. doi: 10.1063/1.1558963.

[77] G. Dolling. Lattice vibrations in crystals with the diamond structure. In *Inelastic Scattering of Neutrons in Solids and Liquids*, volume II, page 37. International Atomic Energy Agency, 1963.

[78] G. Nilsson and G. Nelin. Study of the homology between silicon and germanium by thermal-neutron spectrometry. *Phys. Rev. B*, 6: 3777, 1972. doi: 10.1103/PhysRevB.6.3777.

[79] Electronic archive new semiconductor materials. Characteristics and properties. online. URL http://www.ioffe.ru/SVA/NSM/Semicond/index.html.

[80] Riccardo Tubino, Luigi Piseri, and Giuseppe Zerbi. Lattice dynamics and spectroscopic properties by a valence force potential of diamondlike crystals: C, Si, Ge, and Sn. *The Journal of Chemical Physics*, 56 (3): 1022, 1972. URL http://scitation.aip.org/content/aip/-journal/jcp/56/3/10.1063/1.1677264.

[81] Werner Weber. Adiabatic bond charge model for the phonons in diamond, Si, Ge, and α-Sn. *Phys. Rev. B*, 15: 4789, 1977. doi: 10.1103/PhysRevB.15.4789.

[82] G. Grzybowski, R. Roucka, J. Mathews, L. Jiang, R. T. Beeler, J. Kouvetakis, and J. Menéndez. Direct versus indirect optical recombination in Ge films grown on Si substrates. *Physical Review B*, 84 (20): 205307, 2011. doi: 10.1103/PhysRevB.84.205307.

[83] Mikhail I. Dyakonov. Basics of semiconductor and spin physics. In Mikhail I. Dyakonov, editor, *Spin Physics in Semiconductors*, volume 157 of *Springer Series in Solid-State Sciences*, page 1. Springer Berlin Heidelberg, 2008.

[84] Lok C. Lew Yan Voon and Morten Willatzen. *The k ·p method*. Springer-Verlag Berlin Heidelberg, 2009.

[85] Peter Y. Yu and Manuel Cardona. *Fundamentals of Semiconductors*. Springer-Verlag Berlin Heidelberg, 4 edition, 2010.

[86] Rubin Braunstein, Arnold R. Moore, and Frank Herman. Intrinsic optical absorption in germanium-silicon alloys. *Phys. Rev.*, 109: 695, 1958. doi: 10.1103/PhysRev.109.695.

[87] James S. Kline, Fred H. Pollak, and Manuel Cardona. Electroreflectance in Ge-Si alloys. *Helvetica Physica Acta*, 41: 968, 1968.

[88] J. A. Venables, G. D. T. Spiller, and M. Hanbucken. Nucleation and growth of thin films. *Reports on Progress in Physics*, 47 (4): 399, 1984. URL http://stacks.iop.org/0034-4885/47/-i=4/a=002.

[89] Jayesh Bharathan, Honghui Zhou, Jagdish Narayan, George Rozgonyi, and Gary E. Bulman. Thermal misfit strain relaxation in Ge/(001)Si heterostructures. *Journal of Electronic Materials*, 43 (9): 3196, 2014. doi: 10.1007/s11664-014-3247-6.

[90] Douglas J Paul. Si/SiGe heterostructures: from material and physics to devices and circuits. *Semiconductor Science and Technology*, 19 (10): R75, 2004. doi: 10.1088/0268-1242/19/10/R02.

[91] Leo Miglio, Roberto Bergamaschini, Anna Marzegalli, Fabio Isa, Daniel Chrastina, Giovanni Isella, Philippe Niedermann, Alex Dommann, Claudiu V. Falub, Elisabeth Müller, and Hans; von Känel. ”devide et impera” in detector technology. *Il Nuovo Saggiatore*, 29 (3-4): 7, 2013.

[92] J. H. van der Merwe. Structure of epitaxial crystal interfaces. *Surface Science*, 31: 198, 1972. URL http://www.sciencedirect.com/science/article/pii/0039602872902610.

[93] J.W. Matthews and A.E. Blakeslee. Defects in epitaxial multilayers. *Journal of Crystal Growth*, 27: 118, 1974. URL http://www.sciencedirect.com/science/article/pii/-S0022024874800552.

[94] Martin L. Hammond. *Handbook of Thin Film Deposition*, chapter Silicon Epitaxy by Chemical Vapor Deposition, page 45. Elsevier, 2nd edition, 2001.

[95] C. Rosenblad, H. R. Deller, A. Dommann, T. Meyer, P. Schroeter, and H. von Känel. Silicon epitaxy by low-energy plasma enhanced chemical vapor deposition. *Journal of Vacuum Science & Technology A*, 16 (5): 2785, 1998. URL http://scitation.aip.org/content/avs/-journal/jvsta/16/5/10.1116/1.581422.

[96] G. Isella, D. Chrastina, B. Rössner, T. Hackbarth, H.-J. Herzog, U. König, and H. von Känel. Low-energy plasma-enhanced chemical vapor deposition for strained Si and Ge heterostructures and devices. *Solid-State Electronics*, 48 (8): 1317, 2004. URL http://-www.sciencedirect.com/science/article/pii/S0038110104000565.

[97] M. Kummer, C. Rosenblad, A. Dommann, T. Hackbarth, G. Höck, M. Zeuner, E. Müller, and H von Känel. Low energy plasma enhanced chemical vapor deposition. *Materials*

Science and Engineering: B, 89 (1-3): 288 - 295, 2002. URL http://www.sciencedirect.com/-science/article/pii/S0921510701008017.

[98] Jacopo Frigerio, Mario Lodari, Daniel Chrastina, Valeria Mondiali, Giovanni Isella, and Monica Bollani. Metastability and relaxation in tensile SiGe on Ge(001) virtual substrates. *Journal of Applied Physics*, 116 (11): 113507, 2014. URL http://scitation.aip.org/content/-aip/journal/jap/116/11/10.1063/1.4896076.

[99] Claudiu V Falub, Hans von Känel, Fabio Isa, Roberto Bergamaschini, Anna Marzegalli, Daniel Chrastina, Giovanni Isella, Elisabeth Müller, Philippe Niedermann, and Leo Miglio. Scaling hetero-epitaxy from layers to three-dimensional crystals. *Science*, 335 (6074): 1330, 2012. doi: 10.1126/science.1217666.

[100] Fabio Isa, Marco Salvalaglio, Yadira Arroyo Rojas Dasilva, Mojmír Meduna, Michael Barget, Arik Jung, Thomas Kreiliger, Giovanni Isella, Rolf Erni, Fabio Pezzoli, Emiliano Bonera, Philippe Niedermann, Pierangelo Gröning, Francesco Montalenti, and Hans von Känel. Highly mismatched, dislocation-free SiGe/Si heterostructures. *Advanced Materials*, 28 (5): 884, 2015. doi: 10.1002/adma.201504029.

[101] O. D. Trapp, Larry J. Lopp, and Richard A. Blanchard. *Semiconductor Technology Handbook*. Components Technology Institute, Inc., 6th edition, 2000.

[102] F. Cerdeira, C. Buchenauer, Fred Pollak, and Manuel Cardona. Stress-induced shifts of first-order Raman frequencies of diamond- and zinc-blende-type semiconductors. *Physical Review B*, 5 (2): 580, 1972. doi: 10.1103/PhysRevB.5.580.

[103] J. Bardeen and W. Shockley. Deformation potentials and mobilities in non-polar crystals. *Phys. Rev.*, 80: 72, 1950. doi: 10.1103/PhysRev.80.72.

[104] Chris Van de Walle and Richard Martin. Theoretical calculations of heterojunction discontinuities in the Si/Ge system. *Physical Review B*, 34 (8): 5621, 1986. doi: 10.1103/PhysRevB.34.5621.

[105] Chris G. Van de Walle. Band lineups and deformation potentials in the model-solid theory. *Phys. Rev. B*, 39: 1871, 1989. doi: 10.1103/PhysRevB.39.1871.

[106] M. V. Fischetti and S. E. Laux. Band structure, deformation potentials, and carrier mobility in strained Si, Ge, and SiGe alloys. *Journal of Applied Physics*, 80 (4): 2234, 1996. URL http://scitation.aip.org/content/aip/journal/jap/80/4/10.1063/1.363052.

[107] Moustafa El Kurdi, Guy Fishman, Sébastien Sauvage, and Philippe Boucaud. Band structure and optical gain of tensile-strained germanium based on a 30 band k·p formalism. *Journal of Applied Physics*, 107 (1): 013710, 2010. URL http://scitation.aip.org/content/aip/journal/-jap/107/1/10.1063/1.3279307.

[108] Kevin Guilloy, Nicolas Pauc, Alban Gassenq, Yann-Michel Niquet, Jose-Maria Escalante, Ivan Duchemin, Samuel Tardif, Guilherme Osvaldo Dias, Denis Rouchon, Julie Widiez, Jean-Michel Hartmann, Richard Geiger, Thomas Zabel, Hans Sigg, Jerome Faist, Alexei Chelnokov, Vincent Reboud, and Vincent Calvo. Germanium under high tensile stress: Nonlinear dependence of direct band gap vs strain. *ACS Photonics*, 3 (10): 1907, 2016. doi: 10.1021/acsphotonics.6b00429.

[109] Cicek Boztug, José R. Sánchez-Pérez, Francesca Cavallo, Max G. Lagally, and Roberto Paiella. Strained-germanium nanostructures for infrared photonics. *ACS Nano*, 8 (4): 3136, 2014. doi: 10.1021/nn404739b.

[110] E. Vitiello, M. Virgilio, A. Giorgioni, J. Frigerio, E. Gatti, S. De Cesari, E. Bonera, E. Grilli, G. Isella, and F. Pezzoli. Spin-dependent direct gap emission in tensile-strained Ge films on Si substrates. *Phys. Rev. B*, 92: 201203, 2015. doi: 10.1103/PhysRevB.92.201203.

[111] Li Liu, Miao Zhang, Lijuan Hu, Zengfeng Di, and Shi-Jin Zhao. Effect of tensile strain on the electronic structure of Ge: A first-principles calculation. *Journal of Applied Physics*, 116 (11): 113105, 2014. URL http://scitation.aip.org/content/aip/journal/jap/116/11/10.1063/-1.4896253;jsessionid=ZN_VVhY6mHk5BJJtritWtLo4.x-aip-live-02.

[112] Richard Soref. Mid-infrared photonics in silicon and germanium. *Nature Photonics*, 4 (8): 495, 2010. doi: 10.1038/nphoton.2010.171.

[113] Arthur L. Ruoff. On the ultimate yield strength of solids. *Journal of Applied Physics*, 49 (1): 197, 1978. doi: 10.1063/1.324321. URL http://aip.scitation.org/doi/abs/10.1063/1.324321.

[114] David Roundy and Marvin L. Cohen. Ideal strength of diamond, Si, and Ge. *Phys. Rev. B*, 64: 212103, 2001. doi: 10.1103/PhysRevB.64.212103.

[115] Feng Zhang, Vincent H. Crespi, and Peihong Zhang. Prediction that uniaxial tension along <111> produces a direct band gap in germanium. *Phys. Rev. Lett.*, 102: 156401, 2009. doi: 10.1103/PhysRevLett.102.156401.

[116] O. Aldaghri, Z. Ikonić, and R. W. Kelsall. Optimum strain configurations for carrier injection in near infrared Ge lasers. *Journal of Applied Physics*, 111 (5): 053106, 2012. doi: 10.1063/1.3691790.

[117] H. Tahini, A. Chroneos, R. W. Grimes, U. Schwingenschloegl, and A. Dimoulas. Strain-induced changes to the electronic structure of germanium. *Journal of Physics: Condensed Matter*, 24 (19): 195802, 2012. URL http://stacks.iop.org/0953-8984/24/i=19/a=195802.

[118] S. W. Chang and S. L. Chuang. Theory of optical gain of Ge-$Si_xGe_ySn_{1-x-y}$ quantum-well lasers. *IEEE Journal of Quantum Electronics*, 43 (3): 249, 2007. doi: 10.1109/JQE.2006.890401.

[119] Moustafa El Kurdi, Mathias Prost, Abdelhamid Ghrib, Sébastien Sauvage, Xavier Checoury, Grégoire Beaudoin, Isabelle Sagnes, Gennaro Picardi, Razvigor Ossikovski, and Philippe Boucaud. Direct band gap germanium microdisks obtained with silicon nitride stressor layers. *ACS Photonics*, 3 (3): 443, 2016. doi: 10.1021/acsphotonics.5b00632.

[120] D. Peschka, M. Thomas, A. Glitzky, R. Nürnberg, K. Gärtner, M. Virgilio, S. Guha, T. Schroeder, G. Capellini, and T. Koprucki. Modeling of edge-emitting lasers based on tensile strained germanium microstrips. *Photonics Journal, IEEE*, 7 (3): 1, 2015. doi: 10.1109/JPHOT.2015.2427093.

[121] M. El Kurdi, M. Prost, A. Ghrib, A. Elbaz, S. Sauvage, X. Checoury, G. Beaudoin, I. Sagnes, G. Picardi, R. Ossikovski, F. Boeuf, and P. Boucaud. Tensile-strained germanium microdisks with circular bragg reflectors. *Applied Physics Letters*, 108 (9): 091103, 2016. URL http://scitation.aip.org/content/aip/journal/apl/108/9/10.1063/1.4942891.

[122] A. John Peter. Metal-insulator transition in many valley semiconductors in the spirit of the hubbard model. *Solid State Communications*, 129 (3): 169, 2004. URL http://-www.sciencedirect.com/science/article/pii/S0038109803008809.

[123] Fabio Pezzoli, Lan Qing, Anna Giorgioni, Giovanni Isella, Emanuele Grilli, Mario Guzzi, and Hanan Dery. Spin and energy relaxation in germanium studied by spin-polarized direct-gap photoluminescence. *Phys. Rev. B*, 88: 045204, 2013. doi: 10.1103/PhysRevB.88.045204.

[124] Xiaochen Sun, Jifeng Liu, Lionel C. Kimerling, and Jurgen Michel. Direct gap photoluminescence of n-type tensile-strained Ge-on-Si. *Applied Physics Letters*, 95 (1): 011911, 2009. doi: 10.1063/1.3170870.

[125] C. Haas. Infrared absorption in heavily doped n-type germanium. *Phys. Rev.*, 125: 1965, 1962. doi: 10.1103/PhysRev.125.1965.

[126] Rodolfo Camacho-Aguilera, Zhaohong Han, Yan Cai, Lionel C. Kimerling, and Jurgen Michel. Direct band gap narrowing in highly doped Ge. *Applied Physics Letters*, 102 (15): 152106, 2013. URL http://scitation.aip.org/content/aip/journal/apl/102/15/10.1063/-1.4802199.

[127] S.C. Jain and D.J. Roulston. A simple expression for band gap narrowing (BGN) in heavily doped Si, Ge, GaAs and Ge_xSi_{1-x} strained layers. *Solid-State Electronics*, 34 (5): 453, 1991. URL http://www.sciencedirect.com/science/article/pii/003811019190149S.

[128] J. M. Hartmann, J. P. Barnes, M. Veillerot, J. M. Fédéli, Q. Benoit A La Guillaume, and V. Calvo. Structural, electrical and optical properties of in-situ phosphorous-doped Ge layers.

Journal of Crystal Growth, 347 (1): 37, 2012. URL http://www.sciencedirect.com/science/article/pii/S0022024812002060.

[129] Y.P. Varshni. Temperature dependence of the energy gap in semiconductors. *Physica*, 34 (1): 149, 1967. URL http://www.sciencedirect.com/science/article/pii/0031891467900626.

[130] P. B. Allen and M. Cardona. Theory of the temperature dependence of the direct gap of germanium. *Phys. Rev. B*, 23: 1495, 1981. doi: 10.1103/PhysRevB.23.1495.

[131] Robert W. Keyes. Electronic effects in the elastic properties of semiconductors. Volume 20 of *Solid State Physics*, pages 37 - 90. Academic Press, 1968. URL http://www.sciencedirect.com/science/article/pii/S0081194708602179.

[132] D. K. Ferry. Energy-gap narrowing and state filling in semiconductors under intense laser irradiation. *Phys. Rev. B*, 18: 7033, 1978. doi: 10.1103/PhysRevB.18.7033.

[133] R. N. Hall. Recombination processes in semiconductors. *Proceedings of the IEE - Part B: Electronic and Communication Engineering*, 106 (17): 923, 1959. ISSN 0369-8890. doi: 10.1049/pi-b-2.1959.0171.

[134] E. Fred Schubert. *Light-Emitting Diodes*. Cambridge University Press, 2nd edition, 2006.

[135] R. N. Hall. Electron-hole recombination in germanium. *Phys. Rev.*, 87: 387, 1952. doi: 10.1103/PhysRev.87.387.

[136] W. Shockley and W. T. Read. Statistics of the recombinations of holes and electrons. *Phys. Rev.*, 87: 835, 1952. doi: 10.1103/PhysRev.87.835.

[137] F. Pezzoli, F. Isa, G. Isella, C. V. Falub, T. Kreiliger, M. Salvalaglio, R. Bergamaschini, E. Grilli, M. Guzzi, H. von Känel, and L. Miglio. Ge crystals on Si show their light. *Phys. Rev. Applied*, 1: 044005, 2014. doi: 10.1103/PhysRevApplied.1.044005.

[138] B. Mroziewicz, M. Bugajski, and W. Nakwaski. *Physics of Semiconductor Lasers*. North Holland, 1991.

[139] R. Conradt and J. Aengenheister. Minority carrier lifetime in highly doped Ge. *Solid State Communications*, 10 (3): 321, 1972. URL http://www.sciencedirect.com/science/article/pii/0038109872900166.

[140] Bibhu P. Swain, Hidetaka Takato, Zhengxin Liu, and Isao Sakata. Ambient stability of wet chemically passivated germanium wafer for crystalline solar cells. *Solar Energy Materials and Solar Cells*, 95 (1): 84, 2011. URL http://www.sciencedirect.com/science/article/pii/S0927024810002941.

[141] A. B. Sproul. Dimensionless solution of the equation describing the effect of surface recombination on carrier decay in semiconductors. *Journal of Applied Physics*, 76 (5): 2851, 1994. doi: 10.1063/1.357521.

[142] Fabio Pezzoli, Anna Giorgioni, Kevin Gallacher, Fabio Isa, Paolo Biagioni, Ross W. Millar, Eleonora Gatti, Emanuele Grilli, Emiliano Bonera, Giovanni Isella, Douglas J. Paul, and Leo Miglio. Disentangling nonradiative recombination processes in Ge micro-crystals on Si substrates. *Applied Physics Letters*, 108 (26): 262103, 2016. URL http://scitation.aip.org/content/aip/journal/apl/108/26/10.1063/1.4955020.

[143] Jacques I. Pankove. *Optical Processes in Semiconductors*. Prentice-Hall, Inc., Englewood Cliffs, New Jersey, 1971.

[144] W. G. Spitzer, F. A. Trumbore, and R. A. Logan. Properties of heavily doped n-type germanium. *Journal of Applied Physics*, 32 (10): 1822, 1961. URL http://scitation.aip.org/content/aip/journal/jap/32/10/10.1063/1.1728243.

[145] F. Pezzoli, E. Bonera, E. Grilli, M. Guzzi, S. Sanguinetti, D. Chrastina, G. Isella, H. von Känel, E. Wintersberger, J. Stangl, and G. Bauer. Phonon strain shift coefficients in $Si_{1-x}Ge_x$ alloys. *Journal of Applied Physics*, 103 (9): 093521, 2008. URL http://scitation.aip.org/content/aip/journal/jap/103/9/10.1063/1.2913052.

[146] J. S. Reparaz, A. Bernardi, A. R. Goni, M. I. Alonso, and M. Garriga. Composition dependence of the phonon strain shift coefficients of SiGe alloys revisited. *Applied Physics*

Letters, 92 (8): 081909, 2008. URL http://scitation.aip.org/content/aip/journal/apl/92/8/-10.1063/1.2884526.

[147] E. Bonera, M. Bollani, D. Chrastina, F. Pezzoli, A. Picco, O. G. Schmidt, and D. Terziotti. Substrate strain manipulation by nanostructure perimeter forces. *Journal of Applied Physics*, 113 (16): 164308, 2013. doi: 10.1063/1.4802686.

[148] C. V. Raman and K. S. Krishnan. A new type of secondary radiation. *Nature*, 121 (3048): 501, 1928.

[149] C. V. Raman. A change of wave-length in light scattering. *Nature*, 121 (3051): 619, 1928.

[150] G. Landsberg and L. Mandelstam. Eine neue Erscheinung bei der Lichtzerstreuung in Krystallen. *Naturwissenschaften*, 16 (28): 557, 1928. doi: 10.1007/BF01506807.

[151] Ingrid De Wolf. Micro-Raman spectroscopy to study local mechanical stress in silicon integrated circuits. *Semiconductor Science and Technology*, 11 (2): 139, 1996. URL http://-stacks.iop.org/0268-1242/11/i=2/a=001.

[152] Charles Kittel. *Einführung in die Festkörperphysik*. Oldenbourg Wissenschaftsverlag GmbH, München, 14 edition, 2013.

[153] O. Pagès, J. Souhabi, V. J. B. Torres, A. V. Postnikov, and K. C. Rustagi. Re-examination of the SiGe Raman spectra: Percolation/one-dimensional-cluster scheme and *ab initio* calculations. *Phys. Rev. B*, 86: 045201, 2012. doi: 10.1103/PhysRevB.86.045201.

[154] M. Franz, K. F. Dombrowski, H. Rücker, B. Dietrich, K. Pressel, A. Barz, U. Kerat, P. Dold, and K. W. Benz. Phonons in $Ge_{1-x}Si_x$ bulk crystals. *Phys. Rev. B*, 59: 10614, 1999. doi: 10.1103/PhysRevB.59.10614.

[155] M. I. Alonso and K. Winer. Raman spectra of c-$Si_{1-x}Ge_x$ alloys. *Phys. Rev. B*, 39: 10056, 1989. doi: 10.1103/PhysRevB.39.10056.

[156] F. Pezzoli, Lucio Martinelli, E. Grilli, M. Guzzi, S. Sanguinetti, M. Bollani, H. D. Chrastina, G. Isella, H. von Känel, E. Wintersberger, J. Stangl, and G. Bauer. Raman spectroscopy of $Si_{1-x}Ge_x$ epilayers. *Materials Science and Engineering: B*, 124 - 125: 127, 2005. URL http://www.sciencedirect.com/science/article/pii/S0921510705005313.

[157] F. Pezzoli, E. Bonera, E. Grilli, M. Guzzi, S. Sanguinetti, D. Chrastina, G. Isella, H. von Känel, E. Wintersberger, J. Stangl, and G. Bauer. Raman spectroscopy determination of composition and strain in $Si_{1-x}Ge_x$/Si heterostructures. *Materials Science in Semiconductor Processing*, 11 (5 - 6): 279, 2008. URL http://www.sciencedirect.com/science/article/pii/-S1369800108000693.

[158] A. Gassenq, S. Tardif, K. Guilloy, G. Osvaldo Dias, N. Pauc, I. Duchemin, D. Rouchon, J.-M. Hartmann, J. Widiez, J. Escalante, Y.-M. Niquet, R. Geiger, T. Zabel, H. Sigg, J. Faist, A. Chelnokov, F. Rieutord, V. Reboud, and V. Calvo. Accurate strain measurements in highly strained Ge microbridges. *Applied Physics Letters*, 108 (24): 241902, 2016. URL http://scitation.aip.org/content/aip/journal/apl/108/24/10.1063/1.4953788.

[159] J. Humlícek, M. Garriga, M. I. Alonso, and M. Cardona. Optical spectra of Si_xGe_{1-x} alloys. *Journal of Applied Physics*, 65 (7): 2827, 1989. URL http://scitation.aip.org/content/aip/-journal/jap/65/7/10.1063/1.342720.

[160] J. Humlícek. *Optical functions of the relaxed SiGe alloy*, chapter 5.6, page 249. INSPEC, The Institution of Electrical Engineers, London, United Kingdom, 2000.

[161] Hubert H. Burke and Irving P. Herman. Temperature dependence of Raman scattering in $Ge_{1-x}Si_x$ alloys. *Phys. Rev. B*, 48: 15016, 1993. doi: 10.1103/PhysRevB.48.15016.

[162] Andreas Othonos. Probing ultrafast carrier and phonon dynamics in semiconductors. *Journal of Applied Physics*, 83 (4): 1789, 1998. URL http://scitation.aip.org/content/aip/journal/jap/-83/4/10.1063/1.367411.

[163] Ahmet Elci, Marlan O. Scully, Arthur L. Smirl, and John C. Matter. Ultrafast transient response of solid-state plasmas. I. germanium, theory, and experiment. *Phys. Rev. B*, 16: 191, 1977. doi: 10.1103/PhysRevB.16.191.

[164] H. Roskos, B. Rieck, A. Seilmeier, and W. Kaiser. Cooling of a carrier plasma in germanium investigated with subpicosecond infrared pulses. *Applied Physics Letters*, 53 (24): 2406, 1988. URL http://scitation.aip.org/content/aip/journal/apl/53/24/10.1063/-1.100244;jsessionid=mB-ZR-G2E6XwXF8ksvPkOH-b.x-aip-live-06.

[165] R. J. Elliott. Intensity of optical absorption by excitons. *Phys. Rev.*, 108: 1384, 1957. doi: 10.1103/PhysRev.108.1384.

[166] G. A. Thomas, E. I. Blount, and M. Capizzi. Indirect recombination mechanisms in germanium. *Phys. Rev. B*, 19: 702, 1979. doi: 10.1103/PhysRevB.19.702.

[167] C. Benoît à la Guillaume and M. Voos. Electron-hole drops in doped Ge. *Solid State Communications*, 11 (11): 1585, 1972. URL http://www.sciencedirect.com/science/article/-pii/0038109872905248.

[168] R. R. Lieten, K. Bustillo, T. Smets, E. Simoen, J. W. Ager, E. E. Haller, and J.-P. Locquet. Photoluminescence of bulk germanium. *Physical Review B*, 86 (3): 035204, 2012. doi: 10.1103/PhysRevB.86.035204.

[169] J. Haynes. New radiation resulting from recombination of holes and electrons in germanium. *Physical Review*, 98 (6): 1866, 1955. doi: 10.1103/PhysRev.98.1866.

[170] Tetsuya Sakamoto, Shuhei Hayashi, Yuhsuke Yasutake, and Susumu Fukatsu. An alternative route for efficient optical indirect-gap excitation in Ge. *Applied Physics Letters*, 105 (4): 042101, 2014. URL http://scitation.aip.org/content/aip/journal/apl/105/4/10.1063/-1.4891755.

[171] W. van Roosbroeck and W. Shockley. Photon-radiative recombination of electrons and holes in germanium. *Phys. Rev.*, 94: 1558, 1954. doi: 10.1103/PhysRev.94.1558.

[172] H.Barry Bebb and E.W. Williams. Chapter 4 photoluminescence I: Theory. In R. K. Willardson and Albert C. Beer, editors, *Semiconductors and Semimetals*, volume 8 of *Semiconductors and Semimetals*, pages 181 - 320. Elsevier, 1972. URL http://-www.sciencedirect.com/science/article/pii/S0080878408623455.

[173] J. A. Van Vechten and M. Wautelet. Variation of semiconductor band gaps with lattice temperature and with carrier temperature when these are not equal. *Phys. Rev. B*, 23: 5543, 1981. doi: 10.1103/PhysRevB.23.5543.

[174] Monica Bollani, Daniel Chrastina, Valeria Montuori, Daniela Terziotti, Emiliano Bonera, Giovanni M Vanacore, Alberto Tagliaferri, Roman Sordan, Corrado Spinella, and Giuseppe Nicotra. Homogeneity of Ge-rich nanostructures as characterized by chemical etching and transmission electron microscopy. *Nanotechnology*, 23 (4): 045302, 2012. URL http://-stacks.iop.org/0957-4484/23/i=4/a=045302.

[175] N. L. Rowell, J. M. Baribeau, and D. C. Houghton. Photoluminescence of MBE grown $Si_{1-x}Ge_x$ films. *Journal of The Electrochemical Society*, 135 (11): 2841, 1988. doi: 10.1149/1.2095444.

[176] Tzanimir Arguirov, Oleg Vyvenko, Michael Oehme, Jörg Schulze, and Martin Kittler. Dislocation luminescence in highly doped degenerated germanium at room temperature. *physica status solidi (c)*, 10 (1): 56, 2013. doi: 10.1002/pssc.201200395.

[177] Fabio Pezzoli, Anna Giorgioni, David Patchett, and Maksym Myronov. Temperature-dependent photoluminescence characteristics of GeSn epitaxial layers. *ACS Photonics*, 3 (11): 2004, 2016. doi: 10.1021/acsphotonics.6b00438.

[178] S. Roy Morrison. Recombination of electrons and holes at dislocations. *Phys. Rev.*, 104: 619, 1956. doi: 10.1103/PhysRev.104.619.

[179] T. Figielski. Recombination at dislocations. *Solid-State Electronics*, 21 (11): 1403, 1978. URL http://www.sciencedirect.com/science/article/pii/0038110178902162.

[180] Michele Virgilio and Giuseppe Grosso. Type-I alignment and direct fundamental gap in SiGe based heterostructures. *Journal of Physics: Condensed Matter*, 18 (3): 1021, 2006. doi: 10.1088/0953-8984/18/3/018.

[181] Koji Eriguchi and Kouichi Ono. Quantitative and comparative characterizations of plasma process-induced damage in advanced metal-oxide-semiconductor devices. *Journal of Physics D: Applied Physics*, 41 (2): 024002, 2008. URL http://stacks.iop.org/0022-3727/41/i=2/a=024002.

[182] Kusumandari, N. Taoka, W. Takeuchi, M. Fukudome, M. Sakashita, O. Nakatsuka, and S. Zaima. Broad defect depth distribution in germanium substrates induced by CF_4 plasma. *Applied Physics Letters*, 103 (3): 033511, 2013. doi: 10.1063/1.4815925.

[183] T. S. Kim, H. Y. Yang, Y. H. Kil, T. S. Jeong, S. Kang, and K. H. Shim. Dry etching of germanium by using inductively coupled CF_4 plasma. *J. Korean Phys.Soc.*, 54 (6): 2290, 2009.

[184] Sandrine Rivillon, Yves J. Chabal, Fabrice Amy, and Antoine Kahn. Hydrogen passivation of germanium (100) surface using wet chemical preparation. *Applied Physics Letters*, 87 (25): 253101, 2005. doi: 10.1063/1.2142084.

[185] V. Mondiali, M. Lodari, D. Chrastina, M. Barget, E. Bonera, and M. Bollani. Micro and nanofabrication of SiGe/Ge bridges and membranes by wet-anisotropic etching. *Microelectronic Engineering*, 141: 256, 2015. URL http://www.sciencedirect.com/science/article/pii/S0167931715002117.

[186] A. Picco, E. Bonera, E. Grilli, M. Guzzi, M. Giarola, G. Mariotto, D. Chrastina, and G. Isella. Raman efficiency in SiGe alloys. *Phys. Rev. B*, 82: 115317, 2010. doi: 10.1103/PhysRevB.82.115317.

[187] Emiliano Bonera, Marco Fanciulli, and David N. Batchelder. Raman spectroscopy for a micrometric and tensorial analysis of stress in silicon. *Applied Physics Letters*, 81 (18): 3377, 2002. URL http://scitation.aip.org/content/aip/journal/apl/81/18/10.1063/1.1519105.

[188] Product data sheet germanium on insulator (GeOI). URL www.iqep.com/media/122900/GeOI2.pdf.

[189] T. Arguirov, M. Kittler, and N. V. Abrosimov. Room temperature luminescence from germanium. *Journal of Physics: Conference Series*, 281 (1): 012021, 2011. URL http://stacks.iop.org/1742-6596/281/i=1/a=012021.

[190] Jeehwan Kim, Stephen W. Bedell, and Devendra K. Sadana. Multiple implantation and multiple annealing of phosphorus doped germanium to achieve n-type activation near the theoretical limit. *Applied Physics Letters*, 101 (11): 112107, 2012. doi: 10.1063/1.4751845.

[191] Darin Leonhardt and Sang M. Han. Energetics of Ge nucleation on SiO_2 and implications for selective epitaxial growth. *Surface Science*, 603 (16): 2624, 2009. URL http://www.sciencedirect.com/science/article/pii/S0039602809004580.

[192] Yuji Yamamoto, Grzegorz Kozlowski, Peter Zaumseil, and Bernd Tillack. Low threading dislocation Ge on Si by combining deposition and etching. *Thin Solid Films*, 520 (8): 3216, 2012. URL http://www.sciencedirect.com/science/article/pii/S0040609011018359.

[193] Yuji Yamamoto, Peter Zaumseil, Tzanimir Arguirov, Martin Kittler, and Bernd Tillack. Low threading dislocation density Ge deposited on Si (100) using RPCVD. *Solid-State Electronics*, 60 (1): 2, 2011. URL http://www.sciencedirect.com/science/article/pii/S0038110111000499.

[194] G. Capellini, M. De Seta, P. Zaumseil, G. Kozlowski, and T. Schroeder. High temperature x-ray diffraction measurements on Ge/Si(001) heterostructures: A study on the residual tensile strain. *Journal of Applied Physics*, 111 (7): 073518, 2012. URL http://scitation.aip.org/content/aip/journal/jap/111/7/10.1063/1.3702443.

[195] Gabriela Dilliway, Ruud Van Den Boom, Alain Moussa, Frederik Leys, Benny Van Daele, Brigitte Parmentier, Trudo Clarysse, Eddy R. Simoen, C. Defranoux, Marc M. Meuris, Alessandro Benedetti, Olivier Richard, and Hugo Bender. In situ phosphorus doping of germanium by APCVD. *ECS Transactions*, 3 (7): 599, 2006. doi: 10.1149/1.2355857.

[196] S. Shimokawa, A. Namiki, M. N.-Gamo, and T. Ando. Temperature dependence of atomic hydrogen-induced surface processes on Ge(100): Thermal desorption, abstraction, and

collision-induced desorption. *The Journal of Chemical Physics*, 113 (16): 6916, 2000. URL http://scitation.aip.org/content/aip/journal/jcp/113/16/10.1063/1.1311783.

[197] Marc Schmid, Michael Oehme, Martin Gollhofer, Roman Körner, Mathias Kaschel, Erich Kasper, and Joerg Schulze. Effect of heavy doping and strain on the electroluminescence of Ge-on-Si light emitting diodes. *Thin Solid Films*, 557: 351, 2014. URL http://-www.sciencedirect.com/science/article/pii/S0040609013013333.

[198] V. V. Zhdanova and T. A. Kontorova. *Sov. Phys. Solid State*, 7: 2685, 1966.

[199] B. Vincent, A. Firrincieli, W.-E. Wang, N. Waldron, A. Franquet, B. Douhard, W. Vandervorst, T. Clarysse, G. Brammertz, R. Loo, J. Dekoster, M. Meuris, and M. Caymax. Ge chemical vapor deposition on GaAs for low resistivity contacts. *Journal of The Electrochemical Society*, 158 (3): H203, 2011. URL http://jes.ecsdl.org/content/158/3/-H203.abstract N2 - This paper reports the two-dimensional epitaxial growth of thin intrinsic Ge and in-situ doped n-Ge on GaAs substrates by atmospheric pressure chemical vapor deposition. High quality Ge growth on GaAs is activated almost instantly by an optimized pregrowth procedure. Ga autodoping is found to occur within the first Ge monolayers close to the.

[200] Jan Vanhellemont and Eddy Simoen. On the diffusion and activation of n-type dopants in Ge. *Materials Science in Semiconductor Processing*, 15 (6): 642, 2012. URL http://-www.sciencedirect.com/science/article/pii/S1369800112001564.

[201] A. Chroneos. Dopant-vacancy cluster formation in germanium. *Journal of Applied Physics*, 107 (7): 076102, 2010. URL http://scitation.aip.org/content/aip/journal/jap/107/7/10.1063/-1.3361115.

[202] J. I. Pankove. *J. Phys. Soc. (Japan)*, 21 - supplement: 298, 1966.

[203] Werner Klingenstein and Heinz Schweizer. Direct gap recombination in germanium at high excitation level and low temperature. *Solid-State Electronics*, 21 (11-12): 1371, 1978. doi: 10.1016/0038-1101(78)90210-1.

[204] A. Satta, T. Janssens, T. Clarysse, E. Simoen, M. Meuris, A. Benedetti, I. Hoflijk, B. De Jaeger, C. Demeurisse, and W. Vandervorst. P implantation doping of Ge: Diffusion, activation, and recrystallization. *Journal of Vacuum Science & Technology B: Microelectronics and Nanometer Structures Processing, Measurement, and Phenomena*, 24 (1): 494, 2006. doi: 10.1116/1.2162565.

[205] Yuji Yamamoto, Michael Reiner Barget, Giovanni Capellini, Noriyuki Taoka, Michele Virgilio, Peter Zaumseil, Anne Hesse, Thomas Schroeder, and Bernd Tillack. Photoluminescence of phosphorous doped Ge on Si (100). *Materials Science in Semiconductor Processing*, 2016. submitted.

[206] R. M. Sieg, J. A. Carlin, J. J. Boeckl, S. A. Ringel, M. T. Currie, S. M. Ting, T. A. Langdo, G. Taraschi, E. A. Fitzgerald, and B. M. Keyes. High minority-carrier lifetimes in GaAs grown on low-defect-density Ge/GeSi/Si substrates. *Applied Physics Letters*, 73 (21): 3111, 1998. doi: 10.1063/1.122689.

[207] S. Sukhdeo. PhD thesis, Stanford University, 2015.

[208] David S. Sukhdeo, Shashank Gupta, Krishna C. Saraswat, Birendra (Raj) Dutt, and Donguk Nam. Impact of minority carrier lifetime on the performance of strained germanium light sources. *Optics Communications*, 364: 233, 2016. URL http://www.sciencedirect.com/-science/article/pii/S003040181530314X.

[209] Dirk Peschka, Marita Thomas, Annegret Glitzky, Reiner Nürnberg, Michele Virgilio, Subhajit Guha, Thomas Schroeder, Giovanni Capellini, and Thomas Koprucki. Robustness analysis of a device concept for edge-emitting lasers based on strained germanium. *Optical and Quantum Electronics*, 48 (2): 1, 2016. doi: 10.1007/s11082-016-0394-4.

[210] E. Gaubas and J. Vanhellemont. Comparative study of carrier lifetime dependence on dopant concentration in silicon and germanium. *Journal of The Electrochemical Society*, 154 (3): H231, 2007. doi: 10.1149/1.2429031.

[211] V. I. Fistul', M. I. Iglitsyn, and É. M. Omel'yanovskii. Mobility of electrons in germanium strongly doped with arsenic. *Soviet Physics / Solid State*, 4 (4): 784, 1962.

[212] T.-H. Cheng, C.-Y. Ko, C.-Y. Chen, K.-L. Peng, G.-L. Luo, C. W. Liu, and H.-H. Tseng. Competitiveness between direct and indirect radiative transitions of Ge. *Applied Physics Letters*, 96 (9): 091105, 2010. URL http://scitation.aip.org/content/aip/journal/apl/96/9/-10.1063/1.3352048.

[213] Jinendra Raja Jain, Aaron Hryciw, Thomas M. Baer, David A. B. Miller, Mark L. Brongersma, and Roger T. Howe. A micromachining-based technology for enhancing germanium light emission via tensile strain. *Nat Photon*, 6 (6): 398, 2012. doi: 10.1038/nphoton.2012.111.

[214] P. Boucaud, M. El Kurdi, S. Sauvage, M. de Kersauson, A. Ghrib, and X. Checoury. Light emission from strained germanium. *Nat Photon*, 7 (3): 162, 2013. URL http://dx.doi.org/-10.1038/nphoton.2013.12.